eman ta zabal zazu

Universidad del País Vasco
Euskal Herriko Unibertsitatea

Synaptic dysfunction in Parkinson´s Disease: functional and ultrastructural study of the striatal synapses in an animal model of progressive parkinsonism

LEYRE MERINO GALÁN

AÑO 2021

Synaptic dysfunction in Parkinson´s Disease: functional and ultrastructural study of the striatal synapses in an animal model of progressive parkinsonism

Leyre Merino Galán

Directoras:
Dra. María Cruz Rodríguez Oroz
Dra. Ana Quiroga Varela

Memoria presentada para optar al título de Doctor por
La Universidad del País Vasco
Departamento de Neurociencias

TESIS DOCTORAL

Donostia-San Sebastián, 2021

A mis padres

A mi hermano y a mi tía

El verdadero viaje de descubrimiento no consiste en buscar nuevos paisajes,
sino en mirar con nuevos ojos

Marcel Proust

The research work presented in this doctoral thesis was developed at the Health Research Institute Biodnostia (IIS Biodonostia), the Center for Applied Medical Research (CIMA-Universidad de Navarra), Columbia University and the University of the Basque Country (UPV/EHU) under the supervision of Dr. María Cruz Rodríguez Oroz and Dr. Ana Quiroga Varela, and was supported by a grant of the predoctoral program for training of research personnel at the UPV/EHU from 2015 call, by a grant for the mobility of research staff of the UPV/EHU from 2019 call, by a travel grant of Boehringer Ingelheim Fonds, and by Carlos III Health Institute (PI14 / 00763).

SUMMARY

La enfermedad de Parkinson (EP) es un trastorno neurodegenerativo con una prevalencia global estimada del 0.3% que aumenta drásticamente con la edad. La EP se manifiesta clínicamente con la presencia de signos motores (temblor de reposo, rigidez y bradicinesia). Se caracteriza histopatológicamente por una degeneración gradual de las neuronas dopaminérgicas de la sustancia negra *pars compacta* (SN_{pc}) que proyectan al área motora del estriado, dando lugar a alteraciones en la fisiología de los ganglios basales, y por consiguiente, a la aparición de trastornos relacionados con el control de movimiento. Los estudios de imagen y *post-mortem* de pacientes con EP muestran que los signos motores clásicos de la EP aparecen cuando la depleción dopaminérgica en el estriado es del 60-70% y la pérdida de neuronas dopaminérgicas de la SN_{pc} es alrededor del 50%. Así mismo, estudios epidemiológicos indican que el diagnostico de EP está precedido en muchas ocasiones por una fase prodrómica o premotora de años o incluso décadas en los que la degeneración dopaminérgica ya se ha iniciado. Esta fase se caracteriza por síntomas no-motores específicos como hiposmia o alteraciones del sueño entre otras. Histopatológicamente la EP se caracteriza por la presencia de cuerpos de Lewy y neuritas de Lewy, que son inclusiones eosinofílicas que se encuentran en el citoplasma y neuritas, respectivamente. Estas inclusiones contienen agregados proteicos, siendo su principal componente la proteína α-sinucleina (α-syn). Estas inclusiones se encuentran en la SN_{pc} en el momento del diagnóstico, pero a medida que la enfermedad progresa se propagan a otras regiones del cerebro. Los estudios genéticos y epidemiológicos han descrito que la expresión elevada de α-syn (duplicaciones o triplicaciones en su gen) o las mutaciones en el mismo son un factor que contribuye a la aparición y progresión de la enfermedad. Aunque la función fisiológica de α-syn no se conoce completamente, se ha descrito que se localiza principalmente en los terminales presinápticos donde cumple varias funciones, incluida la modulación de la liberación de dopamina y el mantenimiento de la homeostasis sináptica. En este sentido, la disfunción sináptica está emergiendo como uno de los eventos neurobiológicos tempranos y principales en la EP. Varias líneas de investigación han proporcionado evidencias sólidas de que la acumulación de α-syn en terminales presinápticos juega un papel clave en este proceso. Así, varios estudios clínicos y experimentales muestran que la acumulación de α-syn en los terminales presinápticos precede a la de los cuerpos celulares, y que este depósito patológico representa un factor determinante en la alteración de la homeostasis y función sináptica, apuntando de esta forma a las sinapsis como región de inicio de la patología en la EP.

Además, se ha propuesto que el proceso de patogénesis subyacente a la EP puede presentar un mecanismo de degeneración celular retrógrado (*dying-back*), en el que la muerte celular es consecuencia del deterioro temprano de la función sináptica y degeneración de

axones, y de la consiguiente progresión retrógrada de la patología. Sin embargo, la secuencia de eventos sinápticos y la identificación de los mecanismos subyacentes a la disfunción sináptica, que eventualmente dan lugar al inicio del proceso neurodegenerativo, continúan siendo una incógnita.

Nuestra hipótesis es que el inicio del proceso de degeneración dopaminérgica nigroestriatal en la EP está relacionado con una disfunción sináptica causada por la acumulación de agregados de α-syn a nivel presináptico. Esta anomalía funcional, da lugar a posteriores cambios ultraestructurales que conducen a la degeneración de los terminales dopaminérgicos, y en último término a una alteración de las espinas dendríticas postsinápticas y a la muerte neuronal. Por tanto, los cambios funcionales y ultraestructurales serían dos pasos de un mismo proceso. Así, las intervenciones terapéuticas tempranas en la primera etapa (disfunción sináptica) podrían prevenir o retrasar el desarrollo de la degeneración dopaminérgica, evitando la progresión de la EP.

El objetivo general de esta tesis doctoral es estudiar la secuencia temporal de eventos sinápticos tempranos, a nivel funcional y ultraestructural, que tienen lugar en el estriado en un modelo experimental de parkinsonismo progresivo inducido por la sobreexpresión de α-syn humana (hα-syn) con la mutación A53T inoculada bilateralmente en la SN_{pc} mediante un vector viral adenoasociado (rAAV). Para llevar a cabo este objetivo, se ha estudiado la sinpasis estriatal a diferentes tiempos post-inoculación (p.i.) del rAAV que sobreexpresa hα-syn: 24 h, 72 h, 1, 2 y 4 semanas. Únicamente en la semana 4 p.i existía una degeneración dopaminérgica significativa, que por otra parte no se asoció con signos motores parkinsonianos, por lo que los cambios detectados en esta tesis doctoral corresponden a fases prodrómicas de la enfermedad. El estudio funcional bioenergético utilizando Seahorse XF96, y el estudio proteómico mediante SWATH-MS, se han llevado a cabo en sinaptosomas aislados del estriado, y nos han permitido obtener una secuencia de eventos a nivel funcional. Se han detectado alteraciones en la respiración mitocondrial y flexibilidad metabólica, así como una desregulación en la expresión de proteínas y los procesos biológicos relacionados a nivel sináptico. El estudio ultraestructural del estriado mediante microscopía electrónica nos ha permitido conocer alteraciones tanto en las fibras dopaminérgicas de las neuronas de la SN_{pc}, como mecanismos compensatorios en las sinapsis glutamatérgicas de neuronas de la corteza motora y el tálamo. En el estriado, los terminales dopaminérgicos convergen con los terminales glutamatérgicos en las espinas dendríticas de las neuronas de proyección espinosas (SPNs) y un correcto equilibrio entre dopamina y glutamato juega un papel esencial en la activación de las SPNs para un control motor normal. Por último, se ha llevado a cabo un estudio morfológico en tres dimensiones de las

espinas dendríticas de las SPNs estriatales mediante microscopía confocal de alta resolución. Esto nos ha permitido observar los cambios de la densidad y la morfología del principal componente postsináptico de las sinapsis estriatales, en el punto temporal en el que ya existe una degeneración dopaminérgica significativa.

Hasta la fecha, muy pocos estudios han analizado las anomalías sinápticas que tienen lugar en el inicio del proceso neurodegenerativo en la EP, antes de que se produzcan los singos motores de la enfermedad. La mayoría de los estudios en modelos animales de EP se han realizado utilizando modelos tradicionales mediante el uso de neurotoxinas que inducen una pérdida aguda de las neuronas dopaminérgicas y carecen de un fenotipo progresivo, descartando su validez para estudiar la fase premotora de la enfermedad. Otros estudios se han realizado en modelos transgénicos de sobreexpresión de α-syn nativa o mutada donde no se observa una neurodegeneración dopaminérgica o ésta no ha sido evaluada, las alteraciones motoras son cuestionables debido a la ausencia de neurodegeneración y no se observan inclusiones de α-syn en el sistema nigroestriatal.

Los resultados del presente trabajo muestran que la inoculación bilateral de rAAV-A53T-hα-syn provoca una expresión progresiva de hα-syn en la SN_{pc} a partir de las 72 h y en el estriado a partir de la 1ª semana p.i. Paralelamente, se observa una pérdida bilateral leve y progresiva de neuronas dopaminérgicas en la SN_{pc} siendo significativa a la 4ª semana p.i., así como una pérdida progresiva significativa de las fibras TH^+ y DAT^+ en el estriado a partir de la 2ª semana en adelante, junto a una morfología hinchada y distrófica de las fibras TH^+ que permanecen a la 4ª semana p.i. Interesantemente, esta pérdida dopaminérgica no está asociada con el deterioro de la actividad motora en ninguno de los puntos temporales estudiados. En este sentido el modelo bilateral de rata rAAV-hα-syn escogido para los objetivos de esta tesis doctoral, es un modelo bien establecido y la mejor opción en el que investigar los eventos sinápticos que tienen lugar en el inicio de la degeneración dopaminérgica, mimetizando la etapa más temprana de la EP, donde los sujetos aún no muestran alteraciones motoras aunque el proceso neurodegenerativo ya se ha iniciado y la pérdida celular es mínima.

Los resultados del estudio muestran que la sobreexpresión de hα-syn en los somas dopaminérgicos de la SN_{pc} influye de manera inicial (72 h p.i.) en el estado fisiológico de las terminales sinápticas estriatales, observada por la desregulación de proteínas que afectan principalmente al metabolismo celular. De manera interesante, aunque el desequilibrio metabólico parece estar comenzando, observamos una función bioenergética intacta. Esta

alteración proteica podría ser el inicio de cambios funcionales y estructurales observados en los puntos posteriores.

Posteriormente a la semana 1 p.i, observamos un daño mitocondrial sináptico *in vivo* con una reducción de la respiración y un aumento de proteínas desreguladas en relación con la mitocondria, sin que existan defectos ultraestructurales en las mitocondrias ni degeneración dopaminérgica. Estos hallazgos confirman que las alteraciones bioenergéticas en este punto temporal se deben a una alteración funcional en la respiración y no a cambios en el contenido o estructura mitocondrial, precediendo a la misma. Además, a partir de la semana 1 p.i. existe una desregulación proteica en procesos biológicos relacionados con la morfogénesis celular, el metabolismo y el flujo autofágico. Estas alteraciones proteicas van seguidas de un incremento en el número de vesículas electroclaras a partir de la 2ª semana p.i. que colocaliza con un aumento de LC3 y Rab5 en las fibras dopaminérgicas hinchadas a las 4 semanas p.i. Esto podría sugerir que las estructuras electroclaras observadas podrían corresponder a vesículas del sistema autofágico o endocítico, lo que a su vez está apoyado por los resultados proteómicos que muestran una desregulación proteica en estos procesos, aunque se necesitan más estudios para dilucidar los mecanismos específicos subyacentes.

A las 4 semanas p.i., coincidiendo con una muerte celular dopaminérgica significativa en la SN_{pc}, así como con la denervación máxima de las fibras dopaminérgicas en el estriado, observamos una disminución de la respiración máxima y la capacidad respiratoria de reserva. Estos datos indican que los sinaptosomas estriatales no pueden alcanzar la tasa máxima de respiración, sugiriendo que las mitocondrias sinápticas están funcionalmente dañadas, lo que probablemente compromete la funcionalidad sináptica y la supervivencia de esas sinapsis, conduciendo a la muerte celular. Además, nuestros datos muestran claramente una capacidad energética defectuosa en los sinaptosomas estriatales para adaptarse a situaciones de estrés, observada por una capacidad glicolítica disminuida, revelando su escasa flexibilidad metabólica.

A nivel ultraestructural, se confirmó una pérdida progresiva de axones dopaminérgicos a partir de la 2ª semana p.i y que las fibras dopaminérgicas restantes adquieren una conformación patológica con una morfología hinchada y abultada. Por otro lado, también se han observado mecanismos compensatorios de plasticidad sináptica dentro de las sinapsis glutamatérgicas, tales como incremento en la densidad de sinapsis perforadas y en el número de mitocondrias presinápticas, así como una disminución en la proporción de sinapsis axoespinosas. Estos mecanismos compensatorios podrían inicialmente favorecer la eficacia sináptica en un intento de compensar la incipiente pérdida de señalización dopaminérgica, y así permitir el correcto

funcionamiento del circuito motor evitando la expresión de anomalías motoras. Sin embargo, mantenidos en el tiempo podrían aumentar progresivamente la transmisión glutamatérgica estriatal, produciendo una muerte neuronal por excitotoxicidad, junto con una actividad anormal del circuito de los ganglios basales, lo que finalmente daría como resultado la aparición de los signos motores parkinsonianos. Dichos mecanismos compensatorios descritos están respaldados por el aumento observado en el tamaño de la cabeza de las espinas dendríticas como consecuencia de la disminución de la densidad de las espinas dendríticas de tipo delgado (inmaduras) a las 4 semanas p.i., ya que una posible disminución en el remplazo de espinas podría dar lugar a una potenciación de las espinas ya existentes, y de este modo mantener la transmisión sináptica normalizada, a pesar de la degeneración dopaminérgica significativa.

Por último, es importante destacar que las alteraciones sinápticas del estriado observadas en este estudio no están asociadas con el desarrollo de signos motores parkinsonianos, por lo que representan alteraciones de la etapa premotora y, por lo tanto, abren la puerta a nuevas investigaciones que ahonden en su estudio para una posible intervención terapéutica temprana dirigidas a dianas sinápticas a nivel funcional que podrían ralentizar el proceso neurodegenerativo desde las primeras etapas (antes de la lesión dopaminérgica clínicamente relevante).

Abbreviations

3D	Three dimension
6-OHDA	6-hydroxydopamine
α-syn	α-synuclein
AAV	Adeno associated virus
ABC	Avidin biotin complex
ALS	Autophagy lysosomal system
AP	Anterior-posterior
AS	Asymmetric synapse
ATP	Adenosine triphosphate
au	Arbitrary units
BAC	Bacterial artificial chromosome
BCA	Bicinchoninic acid
BSA	Bovine serum albumin
CBA	Chicken β-actin
ChI	Cholinergic interneuron
CMV	Cytomegalovirus
CNS	Central nervous system
CPu	Caudate putamen
CSF	Cerebrospinal fluid
D_1R/D_2R	Dopamine receptors
DA	Dopamine
DAB	3,3'-diaminobenzidine tetrahydrochloride
DAPI	4',6-diamidino-2-fenilindol
DAT	Dopamine transporter
DLS	Dorsal lateral striatum
DMS	Dorsal medial striatum
DV	Dorsal ventral
ECAR	Extracellular acidification rate
ER	Endoplasmic reticulum
ETC	Electron transport chain
EVV	Empty viral vector
FCCP	Carbonyl cyanide-4-(trifluoromethoxy) phenylhydrazone
$_f$MRI	Functional magnetic resonance imaging
GABA	γ-aminobutiric acid
GBA	Glucocerebrosidase
gc/ml	Genome copies per ml
GP	Globus pallidus
GP_e	External globus pallidus
GP_i	Internal globus pallidus
GWAS	Genome-wide association study
h	Hour
H^+	Proton
hα -syn	Human α-synuclein
$_i$PD	Incidental Parkinson´s Disease
KO	Knock-out
Lamp1	Lysosomal-associated membrane protein
LB	Lewy body
LC3B	Microtubule-associated proteins 1A/1B light chain 3B
L-DOPA	L-3,4 dihydroxyphenylalanine

LN	Lewy neurite
LRKK2	Leucine-rich repeat kinase 2
LTD	Long-term depression
LTP	Long-term potentiation
MCI	Mild cognitive impairment
ML	Medial-lateral
MPTP	1-methyl-4-phenyl-1,2,3,6-tetrahydropyridine
MS	Mass spectrometry
NAc	Nucleus accumbens
NDS	Normal donkey serum
NHS	Normal horse serum
NRS	Normal rabbit serum
ns	Not significant
OCR	Oxygen consumption rate
OF	Open field
p.i.	Post-inoculation
PB	Phosphate buffer
PBS	Phosphate buffer saline
PD	Parkinson´s Disease
PDD	Parkinson´s disease with dementia
PEI	Polyethyleneimine
PET	Positron emission tomography
PFA	Paraformaldehyde
PFF	Preformed fibril
PGK	Phosphoglycerate kinase
PSD	Postsynaptic density
rAAV	Recombinant adeno associated viral vectors
RBD	REM sleep behaviour disorder
REM	Rapid eye movement
ROD	Relative optical density
ROS	Reactive oxygen species
RT	Room temperature
SEM	Standard error of the mean
SN	Substantia nigra
SN_{pc}	Substantia nigra *pars compacta*
SPN	Spiny projection neuron
SS	Symmetric synapse
STN	Subthalamic nucleus
SV	Synaptic vesicle
SVE	Synaptic vesicle endocytosis
SWASH-MS	Sequential window acquisition of all theoretical mass spectra mass spectrometry
TBS	Tris buffered saline
TH	Tyrosine hydroxylase
UPS	Ubiquitin proteasome system
VMS	Ventral medial striatum
VP	Ventral pallidum
VTA	Ventral tegmental area
w	Week
WPRE	Woodchuck hepatitis post-transcriptional regulatory element
WT	Wilde-type

TABLE OF CONTENTS

INTRODUCTION

1. Parkinson´s Disease

1.1 Epidemiology

Parkinson´s disease (PD) is the second most common neurodegenerative disorder with an estimated global prevalence of 0.3% that increases sharply with age. It affects 1% of people older than 60 years and 3% of people over 80 years of age (Pringsheim et al., 2014). The global incidence of PD ranges from 5 to 35 new cases per 100.000 person-years (Lee and Gilbert, 2016; Simon et al., 2020). In Spain, the incidence of PD was estimated at 187 per 100.000 person-years between 65 and 85 years (Benito-León et al., 2004). It is noteworthy that the number of cases with PD is expected to double by 2030, due to the increment in the current life expectancy of our society. This will lead to a high health system burden and socioeconomic repercussion becoming this disorder a serious public health problem (Dorsey et al., 2007).

Regarding distribution among sex, PD is twice more common in men than in women in most populations (Benito-León et al., 2004; Cerri et al., 2019; Pringsheim et al., 2014). A protective effect of female sex hormones, a sex-associated genetic mechanism or sex-specific differences in exposure to environmental risk factors might explain this male preponderance, although disparities in health care could also contribute (Cerri et al., 2019).

1.2 Clinical features and diagnosis

The first description of the disease was made by James Parkinson in 1817 in an essay entitled "*An essay on the Shaking Palsy*" (Parkinson, 1817). In this essay he described a handful of patients who showed resting tremor and gait disturbances in his daily walks in London, leading to the characterization of the motor signs of the disease. Since the original descriptions, the conceptualization and clinical spectrum of the disease continue to evolve and nowadays in addition to the motor signs, numerous non-motor manifestations are also recognized to be related to the neurodegenerative process of the disease (Postuma and Berg, 2019). However, the initially described motor signs persist as the essential basis of the current clinical diagnostic criteria (Postuma et al., 2015).

Classical diagnosis of PD occurs with the onset of motor signs (early-stage PD). At this moment the loss of dopaminergic terminals is 50-75% (Cheng et al., 2010). Thus, the diagnosis of PD is preceded by a prodromal phase of years or even decades, which is characterized by specific non-motor symptoms (Berg et al., 2015; Postuma et al., 2012) (Figure 1). In this sense, several studies point that the neurodegenerative process of the SN_{pc} could antedate in 12-14

years the occurrence of parkinsonian motor signs (Postuma et al., 2012; Postuma and Berg, 2019). Thus, this prodromal period could provide a potential temporal window to study pathological events leading to massive dopaminergic degeneration. In addition, during this period, a disease-modifying therapy, once it becomes available, could be administered to prevent or delay the neuronal degeneration and the development of the disease (Siderowf and Lang, 2012). Besides, over the course of the illness (mild and late-stage PD), there is an emergence of complications related to the progression of the neurodegeneration and the long-term dopaminergic treatment, including both motor and non-motor symptoms (Hely et al., 2005) (Figure 1).

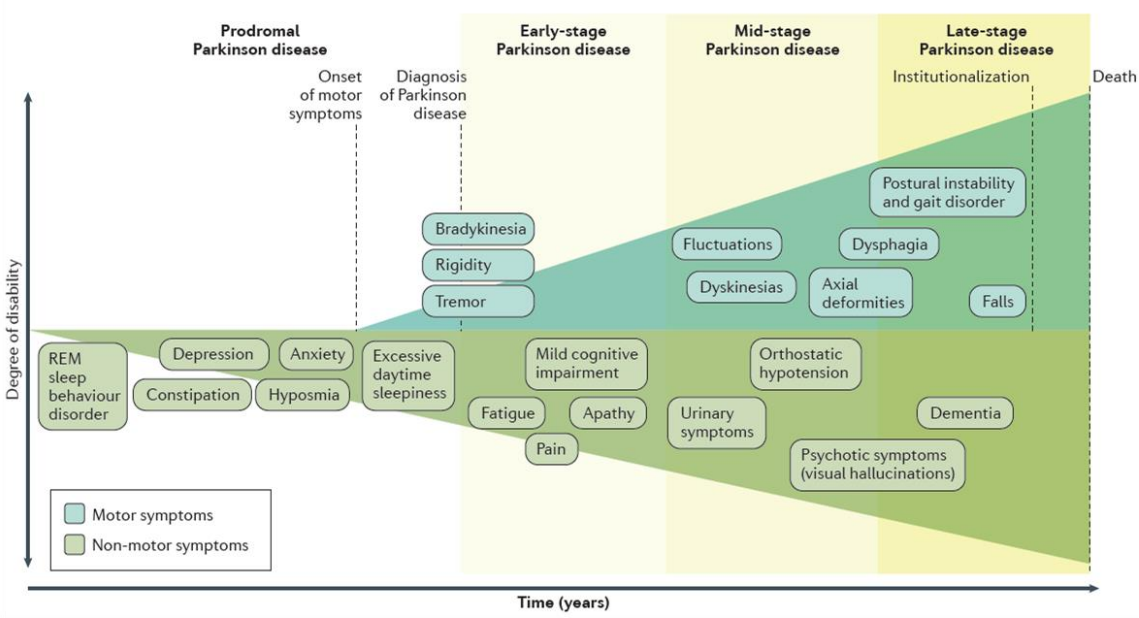

Figure 1: Clinical symptoms and time course of Parkinson's disease progression.

Diagnosis of PD occurs with the onset of motor signs (bradykinesia, rigidity and tremor) but it can be preceded by a prodromal phase of several years. This prodromal phase is characterized by specific non-motor symptoms (REM sleep behaviour disorder (RBD), depression, anxiety, constipation and hyposmia). Additional non-motor symptoms such as MCI, dementia, fatigue, pain, apathy and urinary symptoms develop following diagnosis and with disease progression, causing clinically significant disability. Long-term complications of dopaminergic therapy, including fluctuations, dyskinesia, and psychosis, also contribute to disability. Axial motor signs, such as postural instability with frequent falls and freezing of gait, tend to occur in advanced disease. EDS, excessive daytime sleepiness. MCI, mild cognitive impairment. RBD, sleep behaviour disorder. From Poewe and coworkers (Poewe et al., 2017).

1.2.1 Motor signs

PD is clinically characterized by the presence of motor signs, such as resting tremor, rigidity and bradykinesia (Jankovic, 2008; Postuma et al., 2015). These motor manifestations, called cardinal signs of the disease, appear because of the progressive loss of the dopaminergic neurons of the SN_{pc} that lead to dopaminergic denervation of the striatum (Dickson et al., 2009; Rodriguez-Oroz et al., 2009). As indicated, these cardinal motor signs appear when there is about 30–60% of dopaminergic neuron loss and 70–80% of striatal dopamine (DA) depletion and 50–75% neurite degeneration (Cheng et al., 2010).

The disease has usually an asymmetric onset, with unilateral signs in one limb. As the neurodegeneration progresses, they spread to the other ipsilateral limb and, subsequently, the contralateral hemibody is affected. In addition, since the onset of the disease, axial involvement occurs in the form of facial hypomimia, decreased blinking, or hypophonia (abnormal weakness of the volume or timbre of voice) (DeMaagd and Philip, 2015; Postuma et al., 2015).

Resting tremor is present in about 70% of PD patients at the time of diagnosis, although most patients will develop this motor sign during the progression of the disease (Rajput et al., 1991). This tremor in PD occurs at rest when the majority of patients show a typical movement of the fingers known as “pill-rolling” that consists of a tendency to join the thumb and index and perform semi-circular movements. Tremor increases with distraction manoeuvres and disappears with the execution of voluntary movements with the affected limb or during sleep (Jankovic, 2008).

Rigidity is the persistent resistance and difficulty for passive movement of the joints of limbs, caused by an increased muscular tone or an excessive and continuous muscular contraction. The rigidity of limbs can be uniform or show increased or decreased tone and it increases when other body parts are moved or when talking (Jankovic, 2008).

Bradykinesia (slow execution of movements) and hypokinesia (reduction of movements) are the motor signs that mostly impair PD patients, as they interfere with the activities that require precise movement control. These motor signs consist of a difficulty to perform the whole movement process, from planning to execution and encompass the loss of facial expressiveness, decreased arm swing when walking, or reduction of voluntary or automatic movements (Berardelli et al., 2001; Rodriguez-Oroz et al., 2009).

Other motor aspects that stand out in these patients but not at the diagnosis and late in the progression are the gait disturbances and postural instability, which leads to impaired

balance and frequent falls. PD patients present failure of postural reflexes, they walk with short steps, shuffling and with difficulty in the initiation, turning around, or approaching a destination (freezing of gait), being the latter a manifestation of more advanced stages of the disease. Other signs also frequent in the evolution of the disease are difficulty to swallow food (dysphagia) and speech disorders (dysarthria), which can be very disabling (Jankovic, 2008).

1.2.2 Non-motor symptoms

Non-motor symptoms can be present to a variable degree throughout all stages of PD. Some of them are also frequently present in PD even before the onset of the cardinal motor signs (Postuma et al., 2012; Postuma and Berg, 2019) (Figure 1). During the prodromal phase these symptoms can be characterized by impaired olfaction (hyposmia) (Doty, 2012), constipation (Goldman and Postuma, 2014), neuropsychiatric disturbances such as mood disorders (depression and apathy) (Aarsland et al., 2009; Pagonabarraga et al., 2016), sleep-wake cycle disorders (Chahine et al., 2017) and rapid eye movement (REM) sleep behaviour disorder (RBD) (Postuma et al., 2012). In the early-stages of PD it is frequent the presence of fatigue, mild cognitive impairment affecting early executive functions (MCI) (Aarsland et al., 2017; Delgado-Alvarado et al., 2016), apathy and pain (Conte et al., 2013; Khoo et al., 2013). As the disease advances, non-motor symptoms become increasingly prevalent and obvious and represent a substantial challenge in the clinical management of these patients (Hely et al., 2005). Autonomic dysfunction, such as urinary incontinence, constipation, orthostatic hypotension (Pfeiffer, 2020), hallucinations and other psychotic manifestations are common non-motor features in the late-stages of PD (Ffytche et al., 2017). Dementia is also particularly prevalent, occurring in 83% of patients with PD at 8-12 years of disease evolution (Aarsland et al., 2017; Hely et al., 2005). These non-motor symptoms directly contribute to the deterioration of the quality of life of PD patients. In fact, 28% of patients indicated in one study that non-motor abnormalities were more disabling than motor signs (Barone et al., 2009).

1.3 Neuropathology of PD

1.3.1 Neurodegeneration of nigrostriatal dopaminergic system

The major pathological hallmark of PD is the selective and progressive neurodegeneration of the nigrostriatal dopaminergic system. This neural pathway provides the connection between the SN_{pc} and the striatum as dopaminergic neurons located in the ventrolateral and caudal part of the SN_{pc} (A9 area; Figure 2a) project their axons to the motor part of the striatum (rostral and dorsal areas of the caudate and putamen) (Björklund and Dunnett, 2007; Dickson et al., 2009).

The progressive loss of dopaminergic neurons of the SN_{pc} (Figure 2a-d) and the subsequent reduction of striatal dopaminergic innervation in PD patients causes a decrease in striatal DA concentration and leads to a dysregulation of the basal ganglia circuitry and consequently, to the appearance of the cardinal motor signs of the disease (Dickson et al., 2009; Rodriguez-Oroz et al., 2009).

1.3.2 Lewy Pathology

The other pathological hallmark of PD is the presence of concentric eosinophilic hyaline intracytoplasmic inclusions known as Lewy bodies (LBs) and Lewy neurites (LNs) that are found in the neuronal cell soma and processes, respectively (Lewy, 1912; Figure 2e-g). The LBs are morphologically characterized for representing spherical cytoplasmic inclusions that show three different eosinophilic layers (nucleus, core and halo). They are composed of misfolded or aggregated proteins that cellular degradation and reparation systems are not able to eliminate. The main component of these inclusions is the protein α-synuclein (α-syn), although other proteins such as ubiquitin and proteins of the neurofilament including Tau protein are also present (Irizarry et al., 1998; Spillantini et al., 1998). Interestingly, in a recent study LBs were found to wrap and encase vesicles, lysosomes, dysmorphic mitochondria, and disrupted cytoskeletal elements (Shahmoradian et al., 2019). LBs are mainly located in the dopaminergic neurons of the SN_{pc} and the *locus coeruleus*, although they have also been observed in other brain structures like the basal nucleus of Meynert, hypothalamus, the dorsal raphe nucleus, dorsal motor nucleus of vagus and pedunculopontine nucleus and even in limbic and neocortical brain regions (Braak et al., 2003; Sulzer and Surmeier, 2013). Thus, apart from nigrostriatal dopaminergic system pathology, extensive extranigral pathology is also observed in PD that leads to the dysregulation of other neurotransmitter systems (Hornykiewicz, 1998; Moghaddam et al. 2017), which may play a significant role in some of the non-motor symptoms of PD (Postuma et al., 2012).

Lewy pathology has been hypothesized to progress in a stereotyped pattern over the course of PD (Braak et al., 2003) (Figure 2h). Braak and coworkers performed α-syn immunohistochemistry in a large number of autopsy cases and suggested that toxic species of α-syn progressively reach different brain regions in a caudal-to-rostral direction that would explain the clinical-pathological progression of the disease. Based essentially on Lewy pathology, they suggested a six-stage scheme in which the pathology begins first at the olfactory bulb and the dorsal vagal nucleus and gradually follows an ascending course through the central

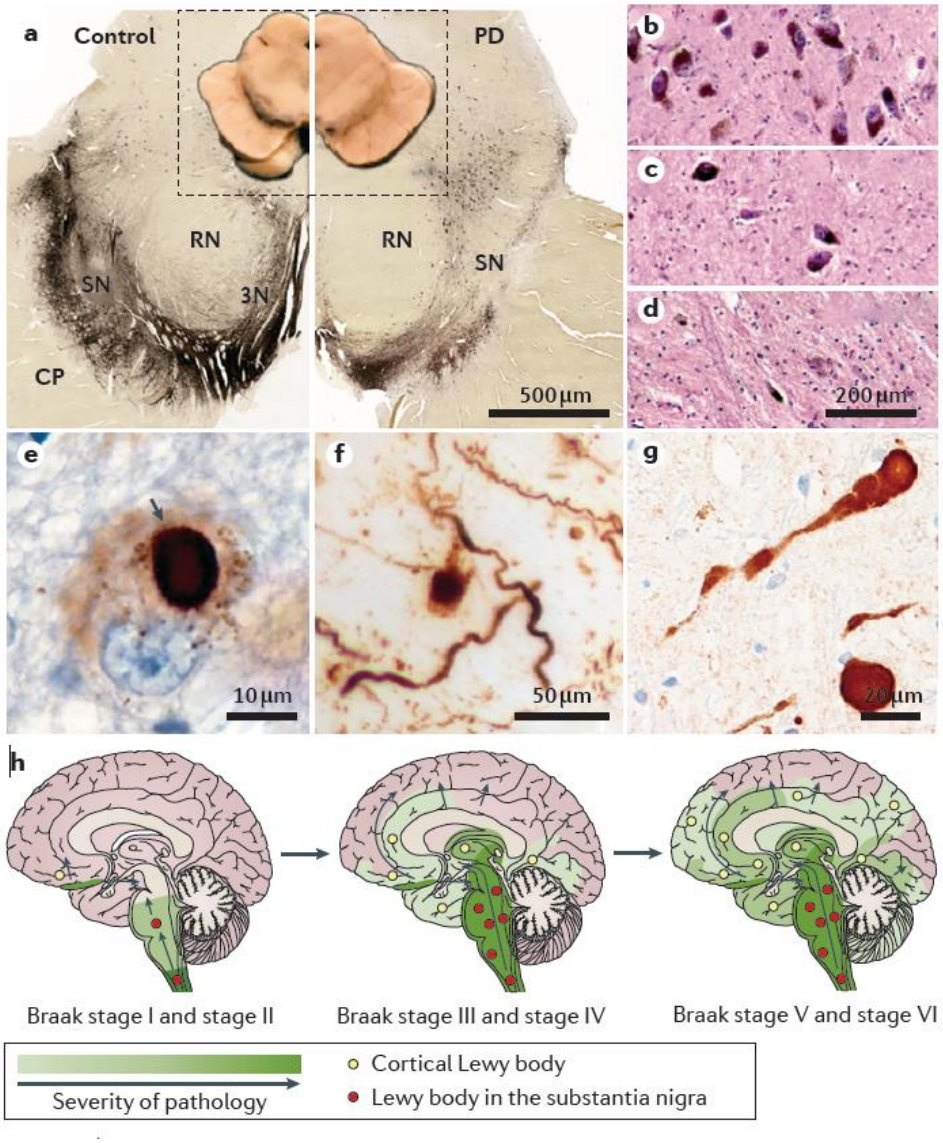

Figure 2: The main anatomical pathologies of Parkinson´s Disease. (**A**) Macroscopical and transverse sections of the midbrain upon immunohistochemical staining for tyrosine hydroxylase from a healthy control (left panel) and a PD patient (right panel). Selective loss of the ventrolateral parts of the SN is evident in the histological section from the PD patient. (**B-D**) Hematoxylin and eosin staining of the ventrolateral region of the SN showing a normal distribution of pigmented neurons in (**B**) a healthy control and diagnostically significant (**C**) moderate or (**D**) severe pigmented cell loss in PD. (**E-G**) Immunohistochemical staining of α-synuclein shows the round, intracytoplasmic Lewy bodies (arrow in **e**), more diffuse, granular deposits of α-syn (**E-F**), deposits in neuronal cell processes (**F**), extracellular dot-like α-syn structures (**F**) and α-syn spheroids in axons (**G**). (**H**) The Braak theorized the progression of α-syn aggregation in PD. α-syn inclusions occur in cholinergic and monoaminergic lower brainstem neurons in asymptomatic cases (Braak stage I and stage II), infiltrate similar neurons in the midbrain and basal forebrain in those with the motor symptoms of PD (Braak stage III and stage IV), and then are found later in limbic and neocortical brain regions with disease progression (Braak stage V and stage VI). From Poewe and coworkers (Poewe et al., 2017).

brainstem that reaches the SN_{pc}, culminating in widespread α-syn pathology at later stages and involving associative cortical regions.

However, there has been criticism against the Braak hypothesis, as it appears to hold up for the majority, but not all of cases, examined in large cohorts. On one hand, it does not always correlate with the clinical severity or with the neuronal loss (Jellinger, 2009). In addition, there are genetic forms of PD in which α-syn aggregates are absent (Schneider and Alcalay, 2017) and it does not explain the absence of clinical symptoms in subjects who on autopsy have widespread α-syn pathology (incidental PD) (Dalfó et al., 2005). On the other hand, it has to be mentioned that these protein aggregates are not exclusive to PD, as they can be observed in other neurodegenerative synucleinopathies such as dementia with Lewy bodies and multiple system atrophy (Peelaerts et al., 2018).

1.4 Etiology

Although time has elapsed since the first description of PD, the etiology of the disease remains largely unknown. Continuous and intense efforts have been undertaken to improve our incomplete comprehension of the disease. In this context, a complex interaction between multiple factors is postulated to take place in the etiology of PD including aging, environmental factors and genetic predisposition (Pang et al., 2019) (Figure 3).

1.4.1 Aging

Age is considered the major known risk factor for the development of PD. The prevalence and incidence of PD increase nearly exponentially with age and peak after 80 years of age (Chesnokova et al., 2019; Pringsheim et al., 2014). Aging is an evolutionarily conserved natural process that involves dysregulation of several pathways such as mitochondrial dysfunction, oxidative stress and impairment in protein degradation systems, which are also involved in the pathogenesis of PD (Kaushik and Cuervo, 2015; Vanni et al., 2020). During aging, the reduction in protein clearance systems is consistent with observations of increased levels of α-syn in nigral dopaminergic neurons (Chu and Kordower, 2007). Moreover, the vulnerability of dopaminergic neurons increases with the age making them more susceptible to silent toxics (Surmeier et al., 2017; Vila, 2019). Thus, the combination of aging and the pathological mechanisms associated with PD could lead to a cellular stress condition that leads to the onset of the disease.

1.4.2 Environmental Factors

Environmental exposure to several factors also represents a risk factor for the development of PD (Bellou et al., 2016; Noyce et al., 2012). Epidemiological studies associate a higher incidence of PD in rural areas and a positive association between PD and environmental toxin exposure such as MPTP or pesticides like rotenone or paraquat have been described (Pang et al., 2019). Indeed, these toxins inhibit complex I of the mitochondrial electron transport chain (ETC) and/or produce an alteration in the mitochondrial membrane potential. As a result, this leads to a decrease in the production of adenosine triphosphate (ATP), which is associated with an increase in levels of reactive oxygen species (ROS) and free radicals, which ultimately lead to cell death (Huang et al., 2016). Interestingly, other environmental factors have also been found to be associated with a decreased risk for developing PD including tobacco smoking, coffee drinking, non-steroidal anti-inflammatory drug use and calcium channel blocker intake (Noyce et al., 2012). The exact mechanisms behind these associations are not known, but coffee and cigarette smoke contain possible neuroprotective compounds such as caffeine and nicotine, respectively. These compounds bind to adenosine A receptors, which could mediate these neuroprotective effects (Scheperjans et al., 2015).

1.4.3 Genetic Factors

During the last 20 years, genetic research has played a key role in elucidating the pathogenesis of the disease. The contribution of genetics to PD was suggested by the increased risk of disease associated with a family history of PD or tremor (Noyce et al., 2012). The most convincing evidence came with the discovery of monogenic forms of PD that helped to deepen the understanding of the pathogenesis, making the genetic factor more relevant. However, patients with genetic PD only account for about 5-10% of all PD cases, while the majority of cases belong to idiopathic PD, whose causes are largely unknown (Cherian and Divya, 2020). Until this date, a total number of 23 loci and 19 causative genes have been associated with PD, yet with a certain degree of heterogeneity regarding phenotypes, age-onset and inheritance mode (Del Rey et al., 2018).

The first gene identified to be associated with inherited PD was *SNCA* (*PARK1/4*), which encodes the protein α-syn. Disease-causing mutations of this gene include missense mutations and duplications or triplications that render α-syn prone to aggregation and are associated with autosomal dominant parkinsonism (Cherian and Divya, 2020). The first mutation in this gene associated with PD was the A53T (Polymeropoulos et al., 1997). Since then, other pathogenic missense mutations in the *SNCA* gene such as A30P, E46K, H50Q, G51D and A53E have been

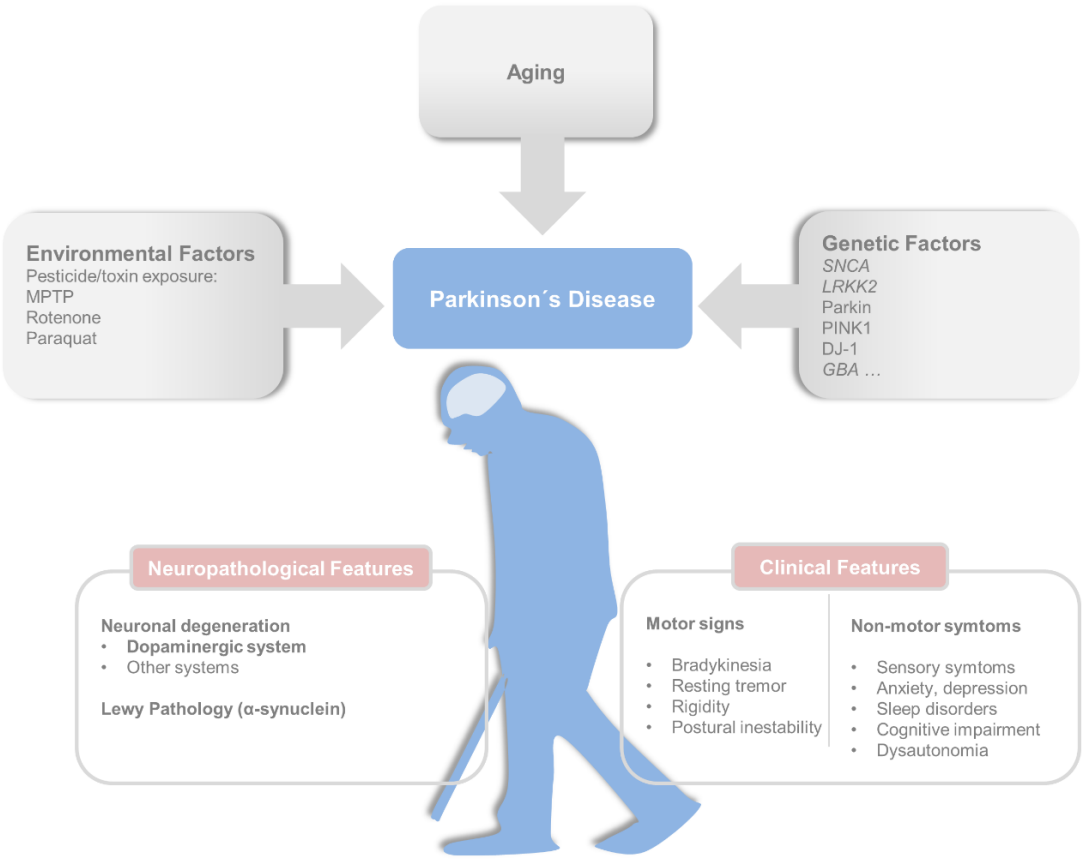

Figure 3: Etiology and key pathological and clinical features of Parkinson´s Disease. A complex interaction between multiple factors is postulated to take place in the etiology of PD including aging, environmental and genetic factors. PD is pathologically characterized by the neurodegeneration of the dopaminergic system and Lewy pathology, and it is clinically characterized by the presence of cardinal motor signs and a variety of non-motor symptoms.

identified (Del Rey et al., 2018). The subsequent identification of families with duplication or triplication of the *SNCA* gene strengthened the link between α-syn and PD and indicated that increased concentrations of even wild-type (WT) protein alone can cause the disease (Chartier-Harlin et al., 2004; Singleton, 2003). Furthermore, the clinical phenotype of patients with *SNCA* triplication is more severe than in those with *SNCA* duplication, suggesting a dose-dependent association between disease severity and *SNCA* gene dosage (Chartier-Harlin et al., 2004). On the other hand, genome-wide association studies (GWAS) have shown that single nucleotide polymorphisms in this gene increase the risk of developing sporadic PD (Koprich et al., 2017). Recognition of *SNCA* mutations as a genetic cause of PD led to another pioneering study where the protein α-syn was identified as the major component of LBs and LNs in PD patients (Spillantini et al., 1998). Thus, genetic studies of the *SNCA* gene helped to establish the link between α-syn and PD and showed that α-syn is significantly implicated in the pathogenesis of both familial and sporadic cases of PD (Dehay et al., 2015). Later on, other genes associated with genetic PD have also been described. The most common causes of genetic PD are the mutations

in *LRRK2* (*PARK8*) gene that are associated with autosomal dominant parkinsonism (Cherian and Divya, 2020). *LRRK2* encodes the leucine-rich repeat kinase 2, a large multidomain protein involved in multiple cellular processes, including neurite outgrowth and synaptic morphogenesis, membrane trafficking, autophagy, and protein synthesis and phosphorylation (Rosenbusch and Kortholt, 2016). At least eight disease-causing mutations in *LRRK2* have been identified (G2019S, R1441C/G/H, I2020T y Y1699C) all mostly clustered within the catalytic domains of the protein (Zhao et al., 2018). The most common *LRRK2* mutation results in a G2019S amino acid substitution, which increases the kinase activity of the protein. This mutation is especially prevalent among Ashkenazi Jews, representing 30% of familial PD and 13% of sporadic PD (Ozelius et al., 2006). Regarding our region, the R1441G mutation in *LRRK2* is especially prevalent in the Basque Country, representing 40% of familial PD cases (Ruiz-Martínez et al., 2010). In addition, mutations in the *VPS35* (*PARK17)* gene have also been associated with autosomal dominant PD, which encode vesicle protein sorting 35 (Cherian and Divya, 2020). This protein is localized at early endosomes and acts as the central hub of the retromer cargo recognition complex, as Vps35 is necessary for the adhesion of the complex to the endosomal membrane. The retromer complex mainly controls the trafficking of cargo proteins from early endosomes to the plasma membrane for recycling, to the trans-Golgi network for retrieval, or to lysosomes for degradation (Eleuteri and Albanese, 2019). Moreover, it mediates vesicular transport from mitochondria to peroxisomes. Therefore, mutation in this gene have been suggested to influence the endosomal system and mitochondrial homeostasis (Cutillo et al., 2020).

Several other genes have also been associated with autosomal recessive forms of PD, which include *PARKIN* (*PARK2*), *DJ-1* (*PARK7*) and *PINK1* (*PARK6*) and are frequently associated with early-onset PD (age less than 40 years) (Cherian and Divya, 2020; Kasten et al., 2018). Interestingly, the proteins encoded by these genes are all implicated in mitochondrial health. Parkin, an E3 ubiquitin ligase, and PINK1, a serine-threonine protein kinase, cooperate in the clearance of damaged mitochondria through mitophagy. The function of DJ-1 is less well characterized, but it seems to protect mitochondria from oxidative stress (Blesa et al., 2015). The convergence of all these proteins on mitochondrial dynamics provided additional support to the idea that mitochondrial failure and the consequent oxidative stress are key events in PD pathogenesis.

In recent years, a high worldwide prevalence of mutations in the gene *GBA,* encoding the lysosomal enzyme β-glucocerebrosidase, have also been described in PD patients. In homozygosity, mutations in this gene cause the lysosomal storage disorder Gaucher´s disease,

but subjects with a single allele affected are at increased risk (30% at 80 years of age) of developing PD (O'Regan et al., 2017). These advances support the idea that alterations in the autophagy lysosomal pathways have important consequences in the clearance of pathological proteins involved in the pathogenesis of PD. Unlike other genetic forms of PD, *GBA* mutations are relatively common in the global population with a prevalence ranging from 2.3% to 9.4% (Sidransky and Lopez, 2012).

Besides genetics, epigenetic alterations such as DNA methylation, histone modifications or microRNAs have also been suggested to play a role in the pathogenesis of PD in recent years (Pavlou and Outeiro, 2017), opening a new venue of epigenetic research in PD.

1.5 Pathogenesis

Although the mechanisms of degeneration and death of dopaminergic neurons are not well known, substantial advances in understanding the pathogenesis of PD have resulted from the epidemiological findings, pathological observations and genetic discoveries described above. The evidence accumulated to date suggests that PD etiology is probably a combination of aging and multiple pathological mechanisms underlying dopaminergic degeneration. These pathological mechanisms that lead to cell death affect mainly the mitochondrial function and oxidative stress, protein degradation via the ubiquitin-proteasome system (UPS) and autophagy lysosomal system (ALS), protein aggregation, glutamate receptor mediated neuronal excitotoxicity, neuroinflammation and, the most relevant for this doctoral thesis, the synaptic dysfunction (Figure 4), which will be detailed in the next section (Poewe et al., 2017).

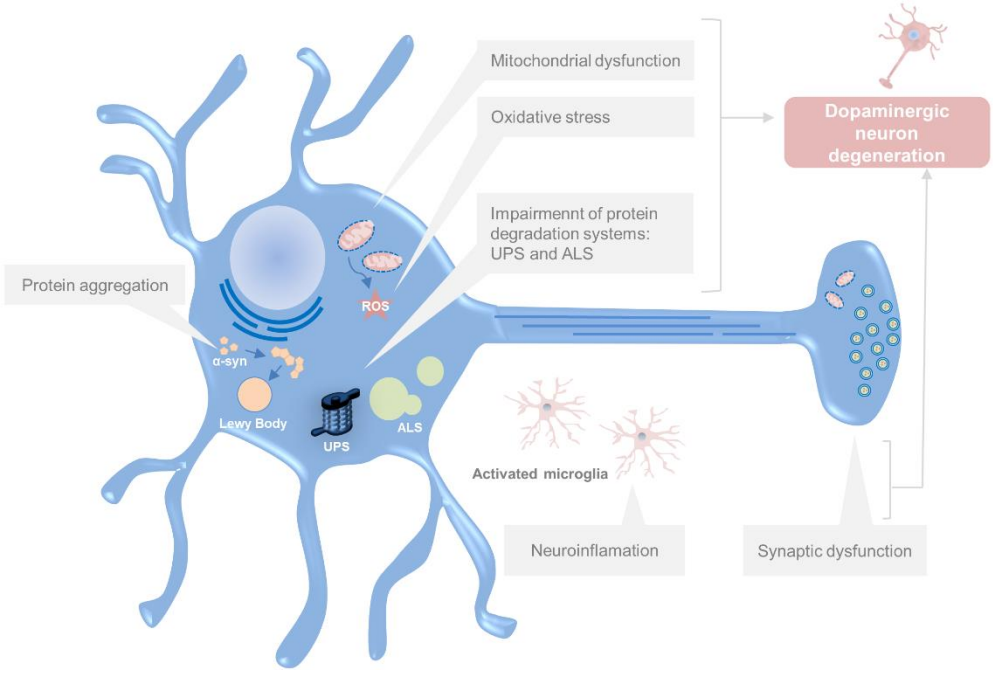

Figure 4. Pathological mechanisms involved in Parkinson´s Disease. Schematic diagram depicting major pathological mechanisms that are implicated in the pathogenesis of PD. Abbreviations: α-syn, α-synuclein; ALS, autophagy lysosomal system; ROS, reactive oxygen species; UPS, ubiquitin-proteasome system.

1.6 Treatment

The reality is that PD lacks preventive or neuroprotective treatment, meaning that progressive decline remains inevitable. Effective symptomatic therapy is available in order to alleviate the motor signs and improve the quality of life of PD patients (Schapira, 2009). In current clinical management, conventional PD therapy focuses on the pharmacological treatment by the replacement of the dopaminergic function using drugs that enhance intracerebral DA concentrations or stimulate DA receptors to alleviate the motor signs. The most effective symptomatic therapy for the treatment of PD remains to be L-DOPA (the precursor of DA), although it is also used in combination with other classes of medications including DA agonists, monoamine oxidase type B inhibitors, inhibitors of COMT (catechol-o-methyl transferase) and, less commonly, amantadine. However, after prolonged periods of use these drugs are known to cause side effects and can become ineffective (de Bie et al., 2020; Kalia and Lang, 2015). Surgical options such as deep brain stimulation also have an important role for a subset of patients with PD and help to reduce some motor signs of PD, such as stiffness, tremor and slowness of movement and motor complications (Rodriguez-Oroz, 2010). Recently, exciting cutting-edge approaches with less invasive technologies such as gamma knife or magnetic resonance-guided focused ultrasound for the treatment of motor symptoms in PD have been advanced (Martínez-Fernández et al., 2018).

A major goal of PD research is the development of disease-modifying therapies that slow or halt the underlying neurodegenerative process. However, as the underlying causes of the disease are unknown, multiple cellular processes are variably involved in the pathogenesis and the disease is diagnosed once the neurodegenerative process is advanced, finding a neuroprotective or disease-modifying strategy results a challenge. Many efforts are concentrated on decoding the presymptomatic phases and turning scientific progress into disease-modifying therapies for PD (Del Rey et al., 2018).

2. Basal Ganglia

The basal ganglia are an interconnected group of grey matter nuclei located in the deep encephalon, compromising the striatum, globus pallidus (GP), subthalamic nucleus (STN), *substantia nigra* (SN) and the ventral tegmental area (VTA).

2.1 Striatum

The striatum is the main nucleus of the basal ganglia and it is functionally implicated in motor planning, action selection, reward-guided learning, and other motivated behaviours and cognitive processes (Burke et al., 2017).

2.1.1 Striatal subregions

In humans, the striatum is comprised of a complex consisting of the caudate nucleus and putamen (dorsal striatum); and ventral caudate nucleus, ventral putamen and the nucleus accumbens (NAc) (ventral striatum) (Baliki et al., 2013; Grahn et al., 2009).

In rodents, the striatum corresponds to a unique entity and it is traditionally subdivided into two regions based on gross anatomical localization and divergent connectivity. The dorsal striatum is a single mass of grey matter that includes the caudate and putamen. The ventral striatum consists of the NAc, the ventromedial parts of the caudate and putamen (VMS), and the striatal part of the olfactory tubercle. These dorsal and ventral regions contain additional subdivisions based on their inputs and immunohistochemical markers (Burke et al., 2017). The dorsal striatum can be divided into the dorsal lateral striatum (DLS) and the dorsal medial striatum (DMS), based on the functional and topographic organization of the cortical glutamatergic afferences. The NAc can be further subdivided into core (dorsal and central parts) and shell (rostral-most, medial, lateral, and ventral parts) (Gonzales and Smith, 2015) (Figure 5A).

The striatal subregions are also functionally segregated. In general, the dorsal striatum is involved in motor planning, action selection, and stimulus-response habit learning, while the NAc plays a role in processing motivated behaviour and reward-related learning (Burke et al., 2017; Isomura et al., 2013).

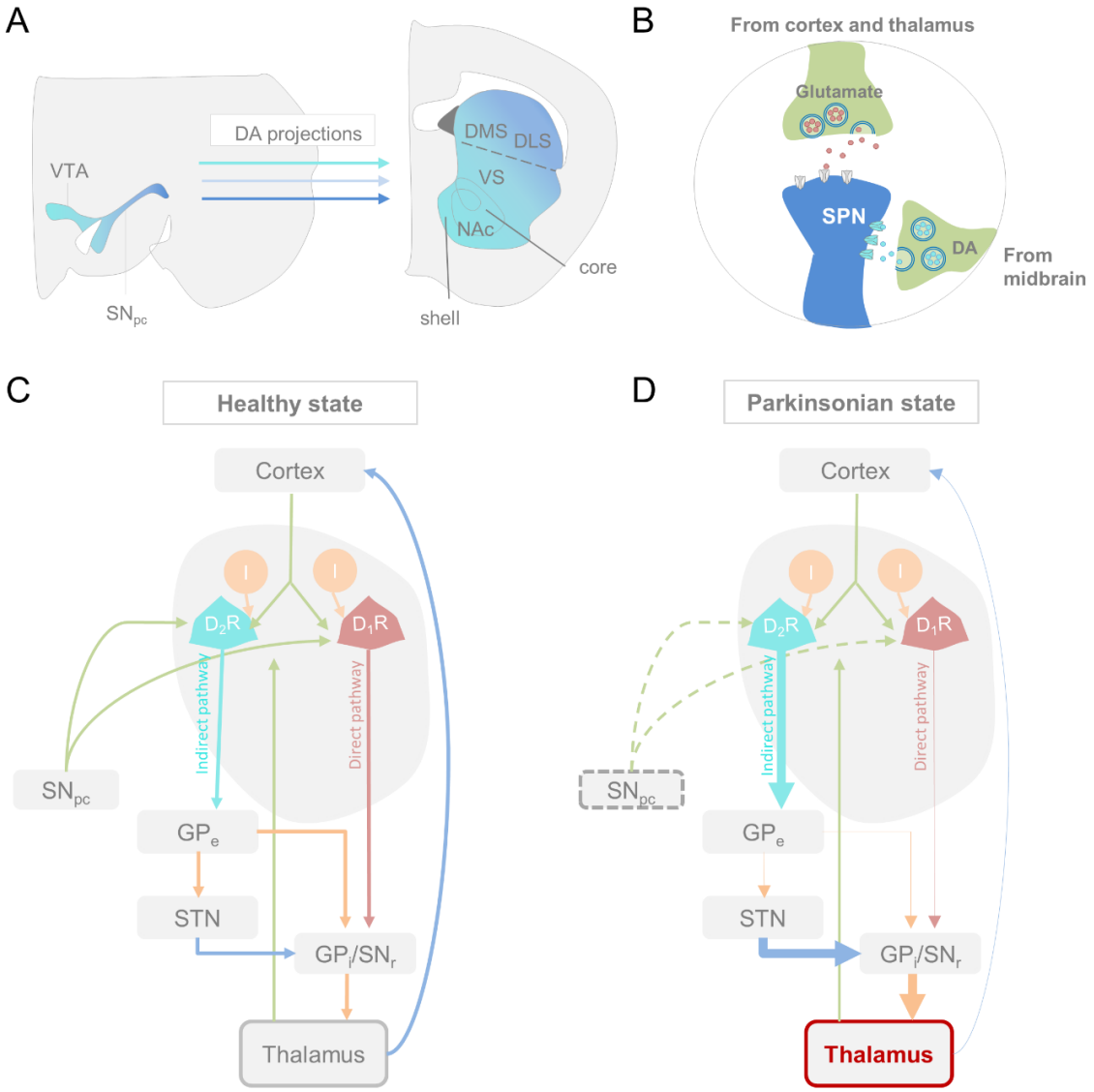

Figure 5: Basal Ganglia circuitry. (**A**) The dopaminergic projections to the striatum in the rat brain. The ventrolateral region of the SN_{pc} projects to dorsal areas of the striatum (motor striatum), mainly to the dorsolateral striatum (DLS); while caudomedial SN_{pc} neurons projects to the ventral and medial part of the striatum (associative and limbic striatum). (**B**) Glutamatergic terminals make synapses mainly with SPNs at the head of their dendritic spines, while dopaminergic terminals make synapses in the neck of those dendritic spines. (**C-D**) Basal ganglia circuitry in (**C**) healthy state and (**D**) parkinsonian state. Green arrows represent input projections to the striatum, dark blue arrows excitatory projections and orange arrows inhibitory projections. $_{d}$SPNs (red) express mainly D_1Rs and form the direct pathway (red arrow), whereas $_{i}$SPNs (light blue) express mainly D_2Rs and form the indirect pathway (light blue arrow). (**D**) The degeneration of the nigrostriatal pathway leads to an imbalance in the activity of $_{d}$SPNs and $_{i}$SPNs, potentiating the indirect pathway and debilitating the direct pathway. This deregulation ultimately inhibits thalamic neurons and thus, suppress motor activity. Abbreviations: DA, dopamine; DLS, dorsolateral striatum; DMS, dorsomedial striatum; D_1R, D_1 DA receptor; D_2R, D_2 DA receptor; GP_e, external globus pallidus; GP_i, internal globus pallidus; I, inhibitory neuron; NAc, nucleus accumbens; SN_{pc}, substantia nigra *pars compacta*; SN_r, substantia nigra *reticulata;* SPN, spiny projection neuron; STN, subthalamic nucleus; VS, ventral striatum; VTA, ventral tegmental area.

2.1.2 Main inputs to the striatum

The striatum is considered the major input nucleus of the basal ganglia and receives two main types of inputs: glutamatergic and dopaminergic. By receiving glutamatergic and dopaminergic inputs, the striatum acts as an integrative hub that assists in the selection of appropriate behaviours through its outputs to downstream basal ganglia structures (Redgrave et al., 1999). Specifically, in humans and rodents the striatum integrates information from different parts of the cortex, thalamus, pedunculopontine nucleus and the dopaminergic system including SN_{pc}, ventral tegmental area (VTA) and retrobrural field (RRF). Glutamatergic projections arise from cortical and thalamic regions. Among the dopaminergic pathway, the ventrolateral region of the SN_{pc} projects mainly to rostral and dorsal areas of the striatum (motor striatum), whereas the VTA, mid-central SN_{pc} and RRF neurons project mainly to the ventral and medial part of the striatum and NAc (associative and limbic striatum) (Hegarty et al., 2013; Joel and Weiner, 2000) (Figure 5A).

2.1.3 Cell types

The striatum itself entails a degree of cellular heterogeneity but the principal neurons in the striatum are the GABAergic spiny projection neurons (SPNs), which comprise over 95% of total striatal neurons and constitute the main cellular input as well as the only output of the striatum (Burke et al., 2017; Gerfen and Surmeier, 2011). These SPNs have dendritic arbors heavily populated with spines (Villalba and Smith, 2010, 2013) and are classically divided into two populations based on their output projection patterns and DA receptor expression profile (Gerfen et al., 1990). Direct pathway SPNs ($_{d}$SPN) represent approximately half of the SPN population, mainly express D_1 DA receptors (D_1Rs), and send dense projections to the SN *pars reticulata* (SN_r) and internal globus pallidus (GP_i) (or entopeduncular nucleus in rodents) forming the direct pathway of the basal ganglia. D_1Rs in $_{d}$SPNs are coupled to $G_{s/olf}$, which increases intrinsic excitability and promotes long-term potentiation (LTP). By contrast, indirect pathway SPNs ($_{i}$SPN) mainly express D_2 DA receptors (D_2Rs) and project to the external GP (GP_e; or GP in rodents) and the ventral pallidum (VP) forming the indirect pathway (Figure 5C). In $_{i}$SPNs D_2Rs activation engages $G_{i/o}$ proteins that decrease intrinsic excitability and promote long-term depression (LTD) (Surmeier et al., 2014). However, this classic segregation of SPNs is oversimplified and incomplete. A small fraction of SPNs co-expresses both D_1Rs and D_2Rs and constitutes a distinct population that is differentially altered in PD (Surmeier et al., 1996). Nevertheless, this dichotomy has proven extremely useful for advancing our understanding of this brain region and the function of the basal ganglia as a whole.

The remaining 5% of striatal neurons are either cholinergic and GABAergic interneurons. Until about 10 years ago, these striatal interneurons were classified in four well-characterized types: cholinergic interneurons (ChIs), fast-spiking interneurons, calretinin-expressing interneurons, and the neuropeptide Y/somatostatin/NOS-expressing and persistent and low threshold spiking interneurons (Burke et al., 2017). Since then, thanks to the development of new tools and optogenetic methods, additional interneuron types have been identified and characterized (Assous et al., 2017). Striatal interneurons are integral players in striatal function, exerting cholinergic or GABAergic inhibition and neuromodulation of SPNs. All types of interneurons express differential combinations of DA receptors, adding extra layers of complexity to how striatal network activity is regulated by DA (Zhai et al., 2018).

2.1.4 Dysregulation of the motor circuit in PD

In summary, classical models of basal ganglia function postulate that activation of $_{d}$SPNs disinhibits principal thalamic neurons that lead to the activation of the motor cortex to facilitate motor action. On the other hand, activation of $_{i}$SPNs ultimately inhibits thalamic neurons that lead to a lack of activation of the motor cortex and consequently suppress motor behaviour (Albin et al., 1989) (Figure 5C). The release of DA at the striatum from nigrostriatal neurons plays a differential modulatory effect on the SPNs at the origin of both direct and indirect pathways (Gerfen, 2000). Thus, the DA input exerts a facilitatory effect on $_{d}$SPNs, while it promotes an inhibitory effect on $_{i}$SPNs, with a net effect of increasing facilitatory inputs to the motor cortex to allow the execution of the desired movement (Gerfen and Surmeier, 2011; Obeso et al., 2002).

The degeneration of the nigrostriatal dopaminergic pathway leads to significant morphological and functional changes in the striatal neuronal circuitry that conduce to an imbalance in the activity of $_{i}$SPNs and $_{d}$SPNs (Gerfen, 2000; Gerfen et al., 1990). $_{i}$SPNs, whose activation promotes movement suppression become hyperactive, whereas $_{d}$SPNs, whose activation promotes movement initiation, become hypoactive, reducing the stimulation of the motor cortex, which is thought to be the underlying cause of motor impairment in PD (Albin et al., 1989; Kravitz et al., 2010; Obeso et al., 2002; Surmeier et al., 2014)(Figure 5D).

2.1.5 Functional overview of the dorsal striatal synapses

This doctoral thesis focuses on synaptic changes within the dorsal striatum, as it is the main striatal subregions, which undergoes progressive DA depletion leading to the hallmark motor signs of PD.

In the dorsal striatum, glutamatergic projections arise from cortical and thalamic regions. In addition, the dorsal striatum is densely innervated by dopaminergic neurons arising from the SN_{pc} (Gerfen and Surmeier, 2011; Guo et al., 2015). Dopaminergic terminals converge with glutamatergic terminals at the dendritic spines of both types of striatal SPNs. Glutamatergic terminals make synapses mainly with SPNs at the head of their dendritic spines, while dopaminergic terminals make synapses in the neck of those dendritic spines (Yao et al., 2008) (Figure 5B).

Glutamate inputs drive SPN firing and, without these excitatory inputs, SPNs are quiescent and their membrane potential is very hyperpolarized. During a desirable action, DA is thought to modulate the neuronal excitability to acutely raise the signal-to-noise ratio through activation of D_1Rs on $_d$SPNs and D_2Rs on $_i$SPNs, as well as by triggering synaptic plasticity and inducing changes in gene expression. Accordingly, the strength of corticostriatal inputs that drives SPNs firing is modulated by DA and, thus, an integrated crosslink between DA and glutamate plays an essential role in driving a physiological motor behaviour (Gerfen and Surmeier, 2011).

Furthermore, in response to the loss of DA signaling, SPNs undergo homeostatic changes that involve intrinsic excitability and synaptic plasticity that tend to restore the balance. In experimental animal models using a neurotoxic agent that causes a striatal DA depletion, $_i$SPNs hyperactivity triggered by the loss of D_2R signaling leads to reduced intrinsic excitability over time. In parallel, loss of D_1R signaling in $_d$SPNs leads to a compensatory elevation in intrinsic excitability (Fieblinger et al., 2014). In addition to these adaptations in intrinsic excitability, synaptic homeostatic plasticity is also engaged as SPNs undergo substantial dendritic spine pruning in PD models (Fieblinger et al., 2014; Suarez et al., 2016). However, the strength of the remaining synapses is increased (Fieblinger et al., 2014; Suarez et al., 2016), which could be explained, at least in part, to the fact that the loss of D_2R signaling promotes LTP (Shen et al., 2008). Nevertheless, what these studies demonstrate is that striatal cells and circuits compensate for the loss of DA signaling by manifesting both intrinsic and synaptic homeostatic plasticity. This plasticity should lessen the consequences of DA depletion in the early stages of the disease and could help explain why well over half of the dopaminergic innervation of the striatum needs to be lost before parkinsonian signs become obvious (Bernheimer et al., 1973).

3. The synapse

Santiago Ramón y Cajal proposed that neurons are not continuous throughout the body, they communicate with each other instead, an idea known as the neuron doctrine (Jones, 1999). However, the term "synapse" was not introduced until 1897 by the neurophysiologists Foster and Sherrington (Foster and Sherrington, 1897). Synapses are now described as the intercellular junctions between a presynaptic neuron and a postsynaptic neuron (Südhof, 2012). They are used to transmit signals between neurons in the central nervous system (CNS) allowing an organized flux of information through the brain and are considered highly dynamic structures in terms of number, structure, molecular constituents and functional properties (Lepeta et al., 2016).

There are two fundamentally different types of synapses: electrical and chemical synapses. In an electrical synapse, the presynaptic and postsynaptic cell membranes are connected by special channels termed gap junctions that are capable of rapid transfer of electric current. However, these synapses are not prevalent in the mammalian CNS. Chemical synapses are composed of a presynaptic terminal, the synaptic cleft and the postsynaptic terminal and are based on the release of neurotransmitters, which require a complex and tight regulation for proper neurotransmission to occur (Sudhof and Rizo, 2011) (Figure 6).

3.1 The presynaptic terminal

The presynaptic nerve terminal is a specialized secretory machinery that releases neurotransmitters by synaptic vesicles (SV) exocytosis in response to an action potential. By receiving an action potential, Ca^{2+} channels open, thereby allowing an influx of Ca^{2+} into the presynaptic terminal that promotes the assembly of the SNARE complex (Südhof, 2013). Ultimately, this molecular machinery will trigger SV trafficking from the closest pool, the readily releasable pool, to be tethered, docked and fused to the presynaptic terminal called the active zone, for subsequent releases of neurotransmitter in the synaptic cleft (Südhof, 2012; Sudhof and Rizo, 2011). In addition to the SNARE complex, a subfamily of highly conserved small GTPases called Rab are implicated in intracellular trafficking of vesicles and the recruitment of SVs in the active zone (Binotti et al., 2016). After exocytosis, the SV membrane is retrieved from the synaptic cleft by endocytosis, either via clathrin-dependent slow or via clathrin-independent fast modes of endocytosis (Saheki and De Camilli, 2012). The SVs are locally loaded with neurotransmitters, hence being recycled to allow another round of exo-endocytotic membrane cycle. This mechanism allows the neurons to sustain a high firing rate without depletion of the

SV pools (Gross and von Gersdorff, 2016; Saheki and De Camilli, 2012) (Figure 6). According to the type of neurotransmitter released, chemical synapses can be further classified including glutamatergic, dopaminergic, GABAergic, cholinergic, etc. (Graybiel, 1990). Of note, α-syn maintains neurotransmitter homeostasis by regulating different steps of this exo-endocytic cycle (Bridi and Hirth, 2018), as it will be detailed in section 4.2.

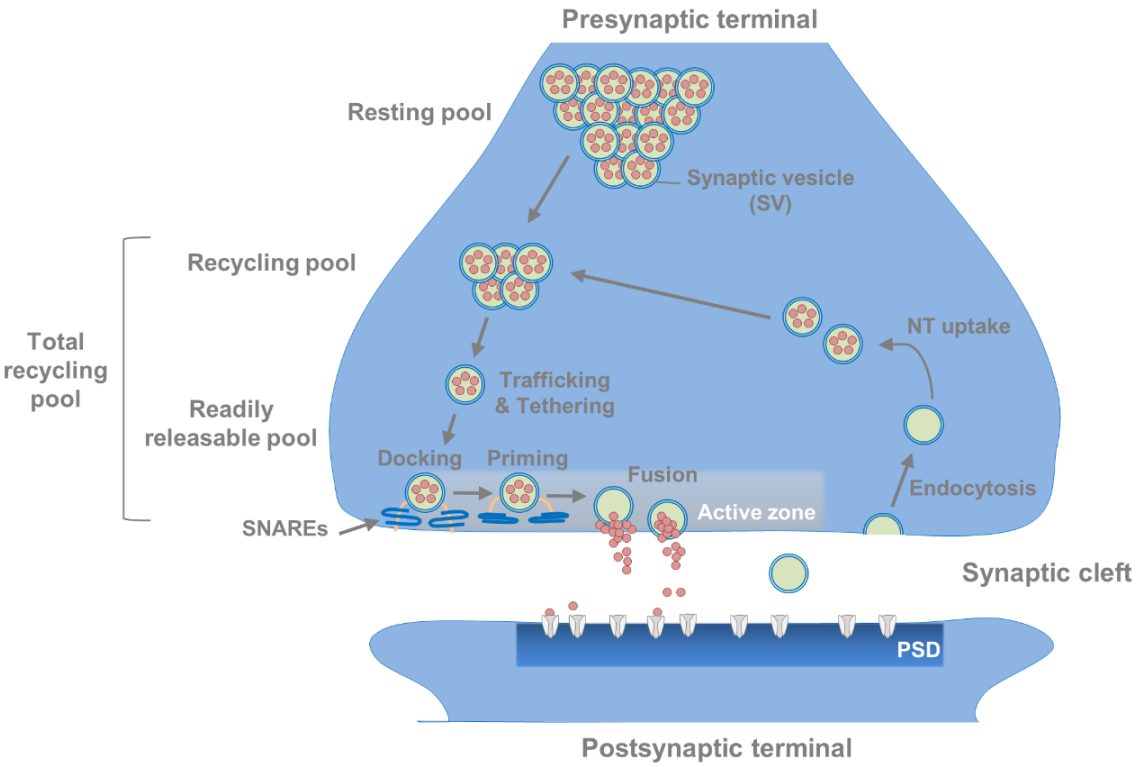

Figure 6: The presynaptic exo-endocytotic cycle regulating neurotransmitter release. Upon an incoming action potential, Ca^{2+} channels become permeable to Ca^{2+} entry in the presynaptic terminal. This activates a molecular machinery including the SNARE complex proteins that recruit SVs from the proximal resting and recycling pools via trafficking and tethering to form the readily releasable pool. After docking and priming, the ready realisable pool of vesicles undergoes SNARE-mediated membrane fusion at the active zone, ultimately leading to neurotransmitter release into the synaptic cleft. After exocytosis, the SV membrane is retrieved to the presynaptic terminal via endocytosis, to be filled with neurotransmitter (NT uptake) and re-enter the exo-endocytotic cycle, thereby granting the neuron its ability to sustain high firing rates. The neurotransmitters bind to receptor channels that are embedded at the postsynaptic density (PSD) of the postsynaptic terminal.

3.2 The postsynaptic terminal

The postsynaptic terminal is specialized to receive the neurotransmitter signal and transduce it into electrical and biochemical changes in the postsynaptic cell, that may either excite or inhibit them, allowing further classification of synapses as excitatory and inhibitory synapses, respectively. The neurotransmitters bind to receptor channels that are concentrated at the postsynaptic membrane and are embedded in a dense and rich protein network comprised of anchoring and scaffolding molecules, signaling enzymes, cytoskeletal components, as well as other membrane proteins, which is known as the postsynaptic density (PSD) (Sheng and Kim, 2011). PSDs typically have a disc-like shape, although they can also be irregular or perforated (Harris and Weinberg, 2012). Apart from clustering receptors, PSDs are involved in the activation of postsynaptic receptors that induce biochemical signaling events in the postsynaptic neuron. In addition, when examined under an electron microscope, synapses can be classified as asymmetric or symmetric. This classification is based mainly on the width of pre- and postsynaptic densities associated with the synaptic junction (Gray, 1959; Harris and Weinberg, 2012).

Asymmetric synapses (AS) are formed by axon terminals that contain spherical synaptic vesicles and are characterized by a prominent electron-dense PSD that is thicker than the presynaptic one (Figure 7A). The PSDs of ASs are highly heterogeneous in size with a diameter of 200–800 nm and thickness of 30–60 nm. ASs are formed mainly on tiny protrusions of the postsynaptic neuron called dendritic spines, although they can also target dendritic shafts and the cell bodies of inhibitory neurons. ASs, which are considered excitatory in function, predominate and account for about 80% of the total population of synapses (Sheng and Hoogenraad, 2007; Sheng and Kim, 2011).

In contrast, symmetric synapses (SS) are less common and are inhibitory in function. SSs are formed by axon terminals that contain pleomorphic synaptic vesicles and are characterized by a thin PSD that is of the same width as the presynaptic density (Figure 7B). The postsynaptic elements at such synapses include mainly dendritic shafts, the cell bodies of both excitatory and inhibitory neurons and axon initial segments, and less commonly dendritic spines. Thus, the postsynaptic side of excitatory synapses differs from inhibitory synapses not only in their content of neurotransmitter receptors but also in their morphology and molecular composition and organization (Sheng and Kim, 2011).

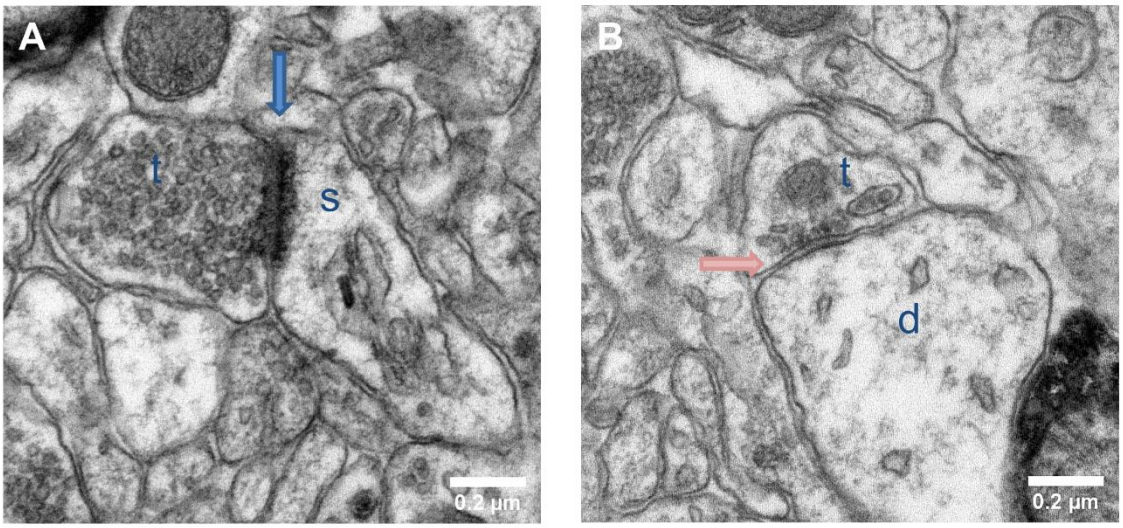

Figure 7: Two categories of CNS synapses. Representative photomicrographs of (**A**) asymmetric synapse (AS) and (**B**) symmetric synapse (SS). ASs are mainly excitatory, contain spherical synaptic vesicles and a prominent PSD, whereas SSs are usually inhibitory and contain pleomorphic synaptic vesicles and a thin PSD. Abbreviations: d, dendritic shaft; s, dendritic spine; t, presynaptic terminal. Original images obtained from our electron microscopy assessment.

3.3 Structural synaptic plasticity

Activity-dependent remodeling of synaptic efficacy and neuronal connectivity is a remarkable property of synaptic transmission and a characteristic of plastic events in the CNS. Synapses are extremely dynamic structures that are constantly being formed, eliminated and reshaped. In fact, adaptive reorganization of neuronal connectivity, which allows the acquisition of new information, both during development and in the mature brain, is based upon the strengthening of existing synapses, the formation of new synapses and the destabilization of previously established synaptic contacts (Holtmaat and Caroni, 2016). However, the delicate balance between stabilization and destabilization might also provide the basis for an increasing rate of failure. The effects of synaptic plasticity can, therefore, lead to either positive or negative changes. On one hand, synaptic plasticity may lead to beneficial modifications as may occur in learning and, on the other hand, it may lead to detrimental effects as neurodegeneration and cell death. Indeed, plastic changes have also been observed in relation to a variety of neurodegenerative diseases and experimental manipulations (Herms and Dorostkar, 2016; Villalba and Smith, 2018). Synaptic plasticity involves not only changes in functional activity but also conformational changes in synaptic structure. Structural characteristics identified as synaptic plasticity events are produced in both presynaptic and postsynaptic compartments of the synapse and include alteration in the morphology of presynaptic terminals, the number of

presynaptic vesicles of the active zone, length and thickness of the PSD and the presence of perforations within them, size and shape of the postsynaptic spine head and length of the postsynaptic spine neck (Wefelmeyer et al., 2016). Of note, during synaptic plasticity, the surface area of the PSD of ASs usually correlates with the dendritic spine head volume in which they are located, as well as with the abundance of postsynaptic glutamate receptors, consistent with the idea that bigger synapses are stronger synapses (Borczyk et al., 2019; Rochefort and Konnerth, 2012).

4. α-synuclein

4.1 Structure and location of α-synuclein

α-syn is a small (14 kDa), 140 aminoacidic protein, encoded by the *SNCA* gene (located in the 4q21.3-q22 chromosome) and is considered an intrinsically disordered protein. It is structurally divided into three regions with distinct physicochemical properties: (1) an amphipathic N-terminal domain (residues 1-60), containing apolipoprotein lipid-binding motifs that are predicted to form α-helical structures that interact with lipid membranes. Several known clinical mutations found in familial PD (A53T, E46K, A30P) are located in this region, indicating the importance of membrane binding for the function of α-syn; (2) a central hydrophobic core (residues 61-95) containing the non-amyloid β component (NAC) region that presents high propensity to form β-rich conformation and is involved in protein aggregation; (3) an acidic C-terminal region (residues 96-140) that is highly negatively charged, which is a common characteristic found in intrinsically disordered proteins to maintain solubility (Lashuel et al., 2013; Wang et al., 2016)(Figure 8A).

It is noteworthy that α-syn is an evolutionarily conserved protein. The amino acid sequences of the mouse (*Mus musculus*) and rat (*Rattus norvegicus*) α-syn are 95.3% similar to those of the human α-syn (Lavedan, 1998). Therefore, it can be considered that rodents are suitable models for the study of the functions of α-syn.

α-syn is a member of the synuclein family of proteins, which also include β and γ-synuclein. What largely sets apart α-syn from the other members structurally is the NAC region. All three members of the family are predominantly neuronal proteins that under physiological conditions localize preferentially to presynaptic terminals (George, 2002). However, α-syn is the only protein of the synuclein family to be found in LBs and LNs and to be implicated in the pathogenesis of PD (Goedert and Compston, 2018; Lashuel et al., 2013).

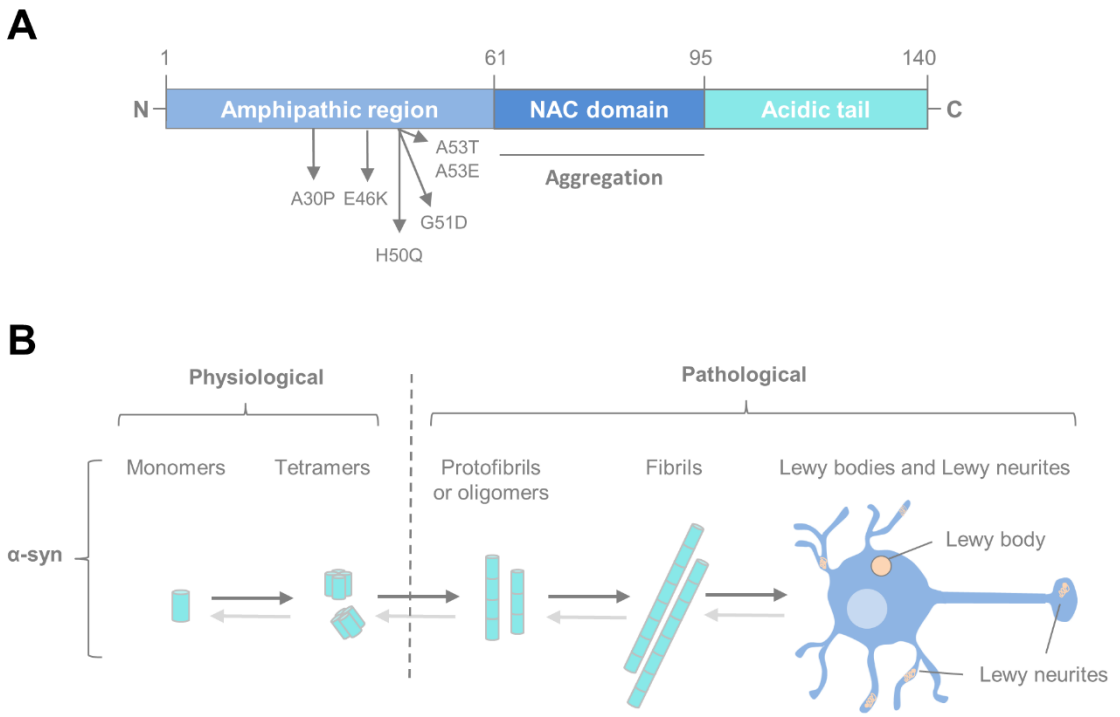

Figure 8: α-synuclein structure. (**A**) α-syn structure with its main protein domains: the N-terminal amphipathic region, a NAC domain and a C-terminal acidic tail. Several dominant missense mutations have been identified in the amphipathic region causing early-onset PD, whereas the NAC domain has been implicated in α-syn aggregation. (**B**) Physiological and pathological structures of α-syn. Under physiological conditions, α-syn is considered to natively exist as an unfolded monomer or tetramer in a dynamic equilibrium between a soluble and a membrane-bound state. Under pathological conditions, α-syn monomers interact and aggregate into multiple soluble oligomeric species, progress to protofibrils and finally to insoluble amyloid-like fibrils that ultimately accumulate and form LBs and LNs.

The expression and localization of α-syn are developmentally regulated. Although it is expressed in various peripheral tissues during human fetal development, in adults it is predominantly found in the nervous system and, for unclear reasons, in certain blood cells such as erythrocytes and platelets (Barbour et al., 2008).

In neurons, the α-syn expression is induced following the determination of neuronal phenotype and establishment of synaptic connections and lags behind the induction of other presynaptic proteins. It is initially detected throughout the soma and neuronal processes, but it eventually becomes predominantly localized at presynaptic terminals in the postnatal brain at several neurotransmitter systems. In this sense, *post-mortem* studies have shown that α-syn aggregates are located in synaptosomal protein extracts and that α-syn pathology prominently involves synaptic compartments (Schulz-Schaeffer, 2010). Despite its ubiquitous distribution through many brain areas, α-syn pathology does not impact on all brain sites of expression but

rather shows a prevalent effect in selectively vulnerable sites such as the nigrostriatal dopaminergic system (Wang et al., 2016).

Specifically, α-syn is localized to presynaptic boutons due to its preference for membranes with high curvature (Middleton and Rhoades, 2010), determined by a characteristic lipid-binding domain composed of six copies of a tandem 11 residues in the N-terminal domain that determines the binding affinity of α-syn to membranes (Jensen et al., 2011). This property results in the structural transition from random coil to α-helix, which mediates the reversible protein´s binding to lipid rafts present in synaptic membranes and to synaptic vesicles. Although α-syn exhibits a strong membrane-binding capacity, evidence shows that α-syn dominantly exists in a soluble state in cytosol instead (Theillet et al., 2016). Thus, under physiological conditions, α-syn is considered to natively exist as an unfolded monomer in a dynamic equilibrium between a soluble and a membrane-bound state (Burré, 2015). Moreover, several studies also report the formation of α-syn tetramers and high-order multimers like octamers (Burré et al., 2014), suggesting significant morphological plasticity of α-syn on its native state (Figure 8B).

4.2 Physiological function of α-synuclein

Although the exact physiological function of α-syn is not fully understood, studies have suggested that by its prevalent location at the presynaptic fraction, α-syn function is crucial in various aspects of synaptic transmission and maintaining neurotransmitter homeostasis. Deficiencies in neurotransmitter release and synaptic function have been observed in experimental studies in response to both knock-down or overexpression of α-syn (Abeliovich et al., 2000; Chandra et al., 2004; Greten-Harrison et al., 2010; Nemani et al., 2010; Vargas et al., 2017). Indeed, mice lacking the *SNCA* gene show impaired stimulated release of DA (Abeliovich et al., 2000), mice lacking both α-syn and β-syn show reduced brain levels of DA (around 20%) (Chandra et al., 2004), and mice lacking all three synuclein family members (α, β and γ) show reduced excitatory synapse size and reduced synaptic function with age (Greten-Harrison et al., 2010). Overexpression of α-syn has been shown to reduce DA release and induce synaptic alterations in transgenic mice and viral vector models (Garcia-Reitböck et al., 2010; Gaugler et al., 2012; Janezic et al., 2013; Lundblad et al., 2012; Nemani et al., 2010), which will be detailed in-depth in section 6. Furthermore, α-syn also plays a key role in controlling the synthesis of DA by interacting with the rate limiting enzyme tyrosine hydroxylase (TH) responsible for the synthesis of DA. Overexpression of α-syn in mouse models decreased TH activity (Kirik et al.,

2002; Masliah, 2000) and *in vitro* reduced the phosphorylation state of TH, stabilizing it in its inactive state (Peng, 2005).

Regarding mechanism, α-syn has found to regulate SNARE complex assembly and the consequent SV fusion, to organize the distinct synaptic vesicle pools, to interact with Rabs and regulate their function in SV trafficking and to regulate DA homeostasis and SV endocytosis (Bridi and Hirth, 2018; Burré, 2015; Scott and Roy, 2012).

More specifically, α-syn has been found to facilitate neuronal SNARE complex assembly, by its direct interaction with VAMP-2, a key component of the v-SNARE residing on the synaptic vesicles. The binding between α-syn and VAMP-2 ultimately leads to the formation of the SNARE complex through the recruitment of the t-SNARE membrane proteins SNAP-25 and syntaxin-1. The formation of the SNARE complex is required for vesicle fusion to the presynaptic plasma membrane and consequently, for neurotransmitter release. Thus, it has been hypothesized that α-syn can act as a neuroprotective chaperone to assessing the fusion of the SNARE complex and maintaining its function (Burre et al., 2010). Besides functioning as a chaperone, α-syn is also important for the maintenance and distribution of the SNARE complex. Evidence from transgenic mouse models and PD patients demonstrates that accumulated α-syn alters the levels and localization of SNARE proteins at the striatal presynaptic nerve terminals (Garcia-Reitböck et al., 2010). Further investigation revealed that synucleins are important mediators of the presynaptic terminal size and organizers of distinct synaptic vesicle pools by specifically regulating synaptic vesicle tethers to the plasma membrane and each other (Vargas et al., 2017). However, the possible role of α-syn in regulating synaptic homeostasis is not exclusively related to its direct interaction with synaptic vesicles. α-syn also interacts with synaptic proteins controlling the trafficking of synaptic vesicle within the presynaptic terminal to recruit them from the SV pools into the active zone and facilitate exocytosis. These synaptic proteins include several members of the highly conserved small GTPase family called Rab (Abeliovich and Gitler, 2016). In addition, α-syn promotes neurotransmitter reuptake and vesicle filling by modulating the activity of neurotransmitter transporters such as monoamine transporter 2 (VMAT2) as well as dopamine transporter (DAT); supporting the notion that α-syn is a general modulator of DA homeostasis (Butler et al., 2015; Guo et al., 2008).

Together, these observations indicate that α-syn has an important role in maintaining neurotransmitter homeostasis by regulating synaptic vesicle fusion, clustering, and trafficking between the reserve and the readily releasable pool, as well as in endocytosis and

neurotransmitter reuptake and vesicle filling by interacting with neurotransmitter membrane transporters and other synaptic proteins (Figure 6).

4.3 α-synuclein aggregation

An increasing body of evidence from studies carried out in animal models and PD patients supports the hypothesis that the processes underlying α-syn aggregation have central roles in the pathogenesis of PD. However, the molecular mechanism of α-syn structural transformation and the relation between different structural species and their functional and pathogenic roles in neuronal function and PD remains unknown.

Under pathological conditions, monomeric α-syn misfolds and aggregates into multiple soluble oligomeric species, which then progress to protofibrils and finally to insoluble amyloid-like fibrils that accumulate forming LBs and LNs (Calo et al., 2016; Ghiglieri et al., 2018)(Figure 8B). The pathological relevance of the different α-syn species has been extensively debated as conflicting results have been described. It has been proposed that toxic species could be insoluble amyloid-like fibrils, which were identified as a prominent component of LBs, although more recent evidence would support a key role for soluble oligomers or protofibrils (Melki, 2015). Nevertheless, the general concept is that α-syn exists under various conformational shapes and oligomeric states in a dynamic balance, modulated by factors that either accelerate or inhibit fibril formation. Conditions that promote α-syn aggregation include genetic mutations, molecular crowding induced by high concentrations of macromolecules or increased α-syn protein levels, impairment of α-syn degradation systems, oxidative conditions and post-translational modifications (Ghiglieri et al., 2018). In this line, several post-transcriptional modifications of α-syn have been characterized and their presence has been noted in LB pathology, which includes phosphorylation, oxidation, nitrosylation, glycation, glycosylation and truncation. These post-translational modifications offer more chance for aggregation by potentially promoting conformational changes that make α-syn more prone to aggregation (Uversky, 2007). Of all modifications, the best studied is S129 phosphorylation, which has been suggested to induce α-syn oligomerization and neurotoxicity (Chen et al., 2009; Chen and Feany, 2005), but its pathological significance is still unclear. Although the conditions that favor α-syn aggregation have been characterized, the precise mechanisms that promote aggregation are unknown. Several studies point that shifting the structure of α-syn to an unfolded or partially folded state, results in increased exposure of the amyloidogenic NAC core of α-syn, thereby proving a seed for templating and initiating the aggregation process (Uversky, 2007).

4.4 α-synuclein propagation

Based on Braak staging hypothesis that postulates that α-syn pathology spreads throughout the brain of PD patients in a spatially and temporally stereotypic pattern (Braak et al., 2003), a growing body of evidence suggests that α-syn pathology may progressively spread from cell-to-cell between interconnected brain regions through a prion-like manner (Olanow and Brundin, 2013). The "prion hypothesis" is based on the concept that toxic α-syn species may spread from cell-to-cell to other brain interconnected regions through intra-axonal transport, be released into the extracellular space, be taken up by neighboring neurons and seed aggregation of endogenous α-syn once inside their new cellular host. This ability to self-propagate and spread within host cells underlines the transmissible nature of prion diseases (Scheckel and Aguzzi, 2018). This hypothesis of α-syn propagation was postulated more than a decade ago after several observations and independent experimental findings. Evidence from *post-mortem* studies reported the development of LB-like structures in grafted DA neurons of PD patients who received transplantation of embryonic mesencephalic grafts more than 10 years earlier. These LB-like structures were composed of aggregated α-syn, suggesting that misfolded or aggregated α-syn from the patients´ brains had infiltered the grafts, potentially serving as templates to initiate aberrant folding and accumulation of normal and endogenous α-syn expressed by the engrafted neurons (Kordower et al., 2008; Li et al., 2008). This host-to-graft transmission of pathological α-syn was also replicated in a transgenic mouse model of PD (Desplats et al., 2009). Thus, initial α-syn misfolding in a small number of cells could progressively lead to the spread of α-syn aggregates to multiple brain regions over years or decades following the initial insult. A recent study shows that the inoculation of preformed fibrils of α-syn into the gut can spread to the brain via the vagus nerve with a progressive pattern causing loss of dopaminergic neurons and motor and non-motor symptoms. Interestingly, truncal vagotomy and the α-syn deficiency (α-syn null mice) prevented the gut-to-brain spread of α-syn and associated neurodegeneration and behavioural deficits (Kim et al., 2019), supporting the Braak hypothesis and reinforcing the concept that sequestration of endogenous α-syn into aggregates appears to be critical for the propagation of the pathology and defects in neuronal function. This is consistent with the Braak hypothesis that the first sites of α-syn aggregation might be in the gut enteric nerves and the olfactory bulb (stage I), secondly achieving the dorsal nucleus of the vagus nerve (stage II), where they underlie the non-motor symptoms associated with prodromal PD. Indeed, with the progression of the disease, these pathologic α-syn aggregates would spread, eventually leading to motor dysfunction once the SN_{pc} becomes involved (stage III; Figure 2h) (Braak et al., 2003). However, the detailed cellular mechanism involved in the propagation

of pathological α-syn is not fully established. Cell culture studies have demonstrated that α-syn can be secreted into the extracellular space through exosomes and endocytosis is a key mechanism of uptake of extracellular α-syn (Fussi et al., 2018; Gustafsson et al., 2018; Lee et al., 2008). However, although this cell-to-cell transmission of α-syn has been recapitulated in cell cultures and animal models (Volpicelli-Daley et al., 2011), this area of research remains contentious as not all researchers concur with a model by which cell-to-cell transfer of pathological α-syn causes disease. An alternative hypothesis is that the α-syn protein travels to distant neuronal nuclei in white matter tracts, thus inducing aggregation in the distant brain regions in the absence of cell-to-cell transfer (Benskey et al., 2016).

5. Synaptic dysfunction in Parkinson´s Disease

Synaptic dysfunction is emerging as one of the early and major neurobiological events in PD and several lines of evidence suggest that accumulation of α-syn in presynaptic terminals plays a central role in this process. In fact, numerous recent reports show aggregation of α-syn at synapses and, consequent alterations in synaptic function and structure confirm synaptic α-synucleinopathy as a primary event in the pathogenesis of PD (Bridi and Hirth, 2018; Calo et al., 2016; Ghiglieri et al., 2018). However, there are remaining gaps in our understanding of the time sequence of synaptic events that lead to synaptic dysregulation and their underlying molecular mechanisms, as well as the exact point in the cascade in which aberrant α-syn assumes its neurotoxic potential before causing neuronal degeneration. In the following section, we focus on the key synaptic biological processes in the context of this doctoral thesis that might contribute to PD pathogenesis (Figure 9).

5.1 Dysfunction of the synaptic vesicle endocytosis

Multiple PD-linked genes have been recently identified to be involved in synaptic vesicle endocytosis (SVE), suggesting that defective SVE plays an important role in PD pathogenesis. These include mutations in *DNAJC6* (auxilin), *SYNJ1* (synaptotajin 1) and *SH3GL2* (endophilin A1) which are key synaptic proteins involved in clathrin-mediated endocytosis. Animal knockout mouse models of *DNAJC6, SYNJ1* and *SH3GL2* have all exhibited endocytic defects at the synapse that lead to dystrophic axons, highlighting the importance of proper SVE control in maintaining axonal terminal integrity. Furthermore, other PD genes including *LRRK2*, *VPS35* and *PARKIN* have also been pointed as potential regulators of SVE (Nguyen et al., 2019).

Regarding the role of α-syn in SVE regulation, recent studies showed that acute injection of human WT α-syn into lamprey synaptic terminals coupled with an intense stimulation of

neurons significantly reduce endocytic rates leading to accumulation of clathrin-coated vesicles (Busch et al., 2014). Moreover, a triple-knockout mouse model of all synuclein isoforms affected the kinetics of SVE leading to impaired endocytic capacity at steady states (Vargas et al., 2014). On the other hand, acute overexpression of α-syn was found to induce DA leakage from synaptic vesicles. This suggests that a defect in SVE in dopaminergic terminals could lead to improper packaging of DA into vesicles leading to increased cytosolic DA, which is subject to oxidation, ultimately contributing to dopaminergic neurodegeneration that begins at the synaptic terminals (Plotegher et al., 2017). Together, these studies suggest that α-syn has an important role in endocytosis by mediating SVE following neuronal stimulation.

5.2 Dysfunction of mitochondria and mitophagy at the synapse

Numerous observations based on susceptibility to mitochondrial toxic agents, mutations in mitochondrial proteins (PINK1, Parkin, DJ-1) responsible for familial forms of PD and PD patients *post-mortem* studies support the strong link between PD and mitochondrial function (see sections 1.5.2 and 1.5.3).

The synapse is the most physiologically active neuronal compartment, which requires a correct mitochondrial function to provide ATP to power SVE that replenishes synaptic vesicles to sustain repeated releases of neurotransmitters. Thus, the abnormal interactions of aggregated α-syn with mitochondria at the synapse could form the molecular basis for functional deficits that can compromise nigrostriatal dopaminergic function. In this sense, the SN_{pc} dopaminergic neurons and specifically their mitochondria possess at least two characteristics that make them particularly vulnerable to toxic insults, such as α-syn aggregation. First, these neurons display an extensive length of branched axons that offer a high number of transmitter release sites. A high oxidative phosphorylation activity is required to support their multiple active axon terminals, which increases levels of ROS that contribute to oxidative damage in the synaptic terminals. Second, dopaminergic neurons also have spontaneous activity and act as autonomous pacemakers, which modulates the sustained release of DA to the striatum. The maintenance of this physiological activity leads to large influxes of Ca^{2+} into the synapse, which requires strict control, promoting Ca^{2+} entry into the mitochondria when cytosolic levels are high. Of note, increased mitochondrial Ca^{2+} stores have been shown to lead to mitochondrial dysfunction, suggesting that ROS accumulation and Ca^{2+} buffering by mitochondria may together compromise synaptic mitochondria and consequently nigrostriatal dopaminergic function (Nguyen et al., 2019; Zaichick et al., 2017).

High-resolution microscopy studies of dopaminergic fibers within the caudate nucleus of *post-mortem* PD brain has revealed an increase in mitochondrial density and higher expression of mitochondrial complexes I and IV within dopaminergic axons of the striatum, but not within dopaminergic synaptic terminals (Reeve et al., 2018). In addition, marked decreases in mitochondrial complex I activity have been widely found in the striatum of PD patients (Flønes et al., 2018; Schapira et al., 1990).

Data from studies link the protein α-syn to mitochondria as α-syn contains a cryptic mitochondrial targeting signal at the N-terminal domain (residues 1-32), which makes a fraction of α-syn associates to mitochondria (Martin et al., 2006). Interestingly, the extent to which synuclein and mitochondria associate appears quite dynamic and can be increased markedly by a range of stressors, such as decreased cytosolic pH (Cole et al., 2008). In this sense, numerous studies have documented that α-syn protein is imported and accumulates in the SN and striatal mitochondria of PD patients, where it inhibits complex I activity (Devi et al., 2008; Keeney et al., 2006; Mizuno et al., 1989; Schapira et al., 1990). Notably, mitochondria isolated from PD patients have also a much higher content of synuclein than those from age-matched controls (Devi et al., 2008). In addition, mitochondrial dysfunction and abnormalities in morphology have been reported in several transgenic models overexpressing human α-syn (hα-syn) in the SN and striatum (Bido et al., 2017; Chinta et al., 2010; Giasson et al., 2002; Martin et al., 2006). However, there is a lack of studies focused on the study of the timing of synaptic mitochondrial abnormalities and whether they are first evidence before neuronal degeneration.

Moreover, several groups have shown that overexpression of α-syn increases ROS production (Chinta et al., 2010; Devi et al., 2008). This effect can cause the accumulation of numerous mitochondrial DNA mutations, lipid peroxidation and protein insults (protein oxidative damage and protein nitration) that further disrupts the mitochondrial function, thereby potentiating a vicious cycle. Damaged or dysfunctional mitochondria are cleared by an autophagic degradation process termed mitophagy (Haelterman et al., 2014). However, evidence from cellular and animal models suggests that overexpression of α-syn may inappropriately induce mitophagy, thus leading to further mitochondrial dysfunction (Chinta et al., 2010; Choubey et al., 2011). When mitochondrial dysfunction reaches a level in which mitophagy is impaired, also other cellular autophagic processes and the UPS are compromised, which ultimately leads to cell death (Haelterman et al., 2014).

5.3 Dysfunction of autophagy at the synapse

Several mutations recognized as genetic causes or risk factors for PD have been identified in genes associated with autophagy, supporting the strong link between neuronal clearance systems and PD. Some of these genes encode lysosomal enzymes (e.g. GBA1, ATP13A2), whereas others correspond to proteins that are involved in the transport to the lysosome (e.g. VPS35), mitophagy (e.g. Parkin, PINK1, DJ-1), or other autophagic related functions (e.g. LRRK2) (Cherian and Divya, 2020).

Autophagy is a dynamic process in which dysfunctional cytoplasmic components (organelles and proteins) are rerouted toward the lysosomal environment for degradation. Three types of autophagy have been identified based on the pathway by which the substrates reach the lysosomal compartment: macroautophagy, microautophagy, and chaperone-mediated autophagy (CMA) (Nikoletopoulou and Tavernarakis, 2018).

Multiple steps in these autophagic lysosomal systems (ALS) have been implicated in PD pathogenesis, including dysfunction in autophagosome formation, autophagosome axonal transport, subsequent autophagosome and lysosome fusion, reduction in LAMP2A and hsc70 (key components of CMA pathway), and decreased lysosomal activity of multiple enzymes, leading ultimately to autophagic cargo accumulation (Singh and Muqit, 2020). Furthermore, several studies link the protein α-syn to ALS as α-syn accumulation has been described to impair autophagic function by disrupting hydrolases trafficking from the endoplasmic reticulum (ER) to the lysosome as well as by decreasing GCs activity. Likewise, dysfunction in autophagic pathways impairs the ability to remove toxic aggregates, which increases α-syn levels and the probability of α-syn aggregation and spreading, establishing a reciprocal relationship (Klein and Mazzulli, 2018). However, most of these studies have been centered in the SN cell bodies and many questions remain about the contribution of synaptic autophagy to PD pathogenesis.

Emerging evidence suggests that autophagy has been adapted to the microenvironment of the synapse in order to serve local functions related to synaptic transmission (Nikoletopoulou and Tavernarakis, 2018). Although live-cell imaging studies have indicated that autophagosomes (LC3/Atg8-labeled structures) are formed at synaptic terminals and are transported along axons to the cell body for acidification and degradation due to lysosomal fusion, recent work indicates that proteins uniquely present at the presynaptic terminal also control this process. Indeed, dopaminergic synapses are located far from neuronal cell bodies and they must maintain their

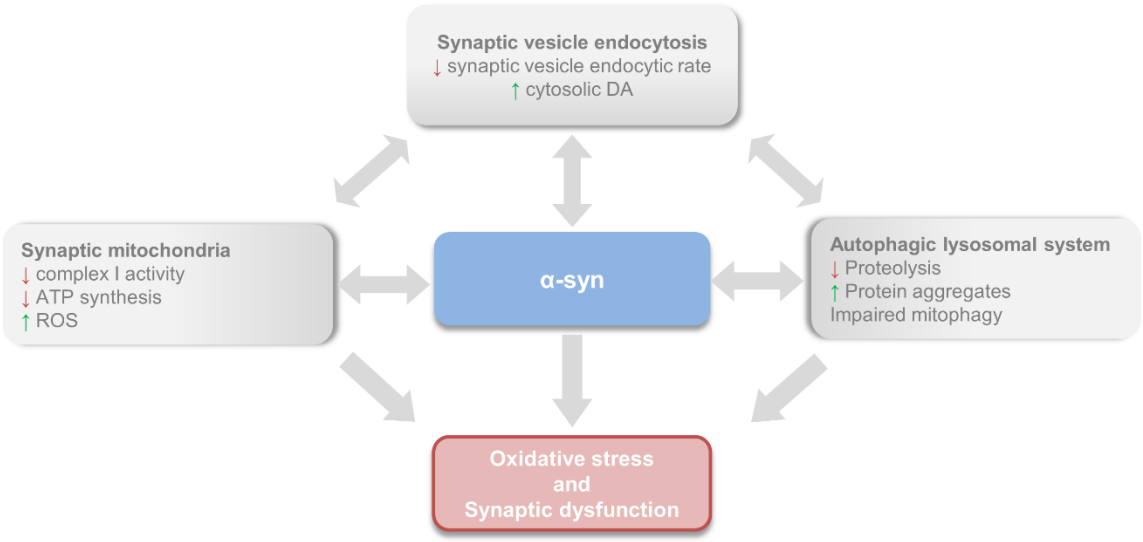

Figure 9: Key synaptic biological processes that might contribute to synaptic dysfunction. The convergence of synaptic vesicle endocytosis, mitochondrial and autophagic lysosomal system dysfunction may exacerbate α-syn accumulation and oxidative stress that ultimately result in synaptic dysfunction in PD.

synaptic protein integrity and homeostasis with specific and localized pathways of autophagy (Soukup et al., 2018). In this sense, several lines of evidence suggest that presynaptic autophagy is tightly regulated and activated under the changing demands of the presynaptic compartment by mechanisms that remain to be fully elucidated (Nikoletopoulou and Tavernarakis, 2018). Additionally, turnover of synaptic proteins, regulations of neurotransmitter release and the elimination of damaged mitochondria and oxidized DA by lysosomes via synaptic autophagy are critical in maintaining dopaminergic synapses (Nguyen et al., 2019; Soukup et al., 2018). Thus, it has been postulated that synaptic, mitochondrial, and autophagic dysfunction may synergize during PD pathogenesis (Figure 9).

5.4 Synaptic dysfunction in PD patients

It has been proposed that the pathogenesis process underlying PD may feature a dying-back mechanism of cell degeneration, in which cell death is a consequence of early impairment of synaptic function and axon degeneration and retrograde progression of the pathology, as it has been described in other neurodegenerative diseases (Tagliaferro and Burke, 2016).

The first evidence that axons were affected in PD came from the study of Braak and coworkers. They demonstrated that α-syn inclusions were not only present in LB inclusions at the neuron soma, but also present in LNs and that the accumulation of α-syn at the axonal

processes preceded that in cell bodies (Braak et al., 1999, 2003). Moreover, previous *post-mortem* studies, showed that nearly 90% of α-syn aggregates were located at synapses in the frontal cortex of other synucleinopathies (Kramer and Schulz-Schaeffer, 2007; Schulz-Schaeffer, 2010; Tanji et al., 2010) and significant synaptic pathology with almost complete loss of dendritic spines was observed at the postsynaptic areas (Kramer and Schulz-Schaeffer, 2007; Zaja-Milatovic et al., 2005). These observations have also been confirmed by positron emission tomography (PET), where PD patients in the early stages of the disease showed extensive axonal damage and loss of nigrostriatal pathway connectivity (Caminiti et al., 2017). Recently, decreased synaptic vesicle 2A (SV2A) distribution was also shown in caudate and putamen of early PD patients using ^{11}C-UCB-J novel radiotracer (Matuskey et al., 2020; Wilson et al., 2020). Additionally, functional magnetic resonance imaging ($_{f}$MRI) studies have identified abnormal functional connectivity in PD patients since its earliest phase (Mishra et al., 2020; Sreenivasan et al., 2019).

In addition, the expression levels of a range of proteins involved in synaptic transmission were found to be altered in *post-mortem* tissue from PD patients. A pathological study showed that in incidental PD brains ($_{i}$PD; the presence of LBs without the clinical development of PD) there are already altered molecular events in the SN related to oxidative damage, including increased lipoxidation and advanced glycation. Furthermore, α-syn and superoxide dismutase 2 (Sod2), which are synaptic and mitochondrial proteins respectively, were identified with lipoxidative damage, suggesting that the pathological process precedes clinical diagnosis by years (Dalfó et al., 2005). In another study, $_{i}$PD brains at Braak stages I and II showed downregulation of Synapsin 2, complexin 2 and synphilin 1 gene expression and upregulation of synapsin 3, synaptophysin, synaptotagmin 2 in the SN (Dijkstra et al., 2015). Redistribution of SNARE proteins SNAP-25 and syntaxin-1 was also observed at striatal tissue from PD patients (Garcia-Reitböck et al., 2010). A more recent study in PD patients showed increased levels of the synaptic proteins SNAP-25 and neurogranin in cerebrospinal fluid (CSF) (Bereczki et al., 2017). Additionally, a proteomic and ELISA study in prefrontal tissue from PD patients with dementia (PDD), reflecting a more advanced PD stage, showed downregulation of various synaptic proteins (SV2C, NRGN, CBLN4, BDNF, GAP43, SNAP47, LRNF2, SYT2) (Bereczki et al., 2018). Together, these studies demonstrate a synaptic impairment at the protein level in different stages of PD.

Last but not least, it is also important to mention a clinical study of our group of investigation from which this project emerged. As described in the 1.3.2 section, some patients with PD present mild cognitive impairment (PD-MCI; 30% approx.) and after years of evolution

of the disease 70-80% of them develop dementia (PDD), usually representing the MCI the initial phase of dementia. In this study, FDG-PET to assess brain glucose metabolism and MRI to assess structural alterations were performed and showed that cortical hypometabolism is the predominant characteristic in PD-MCI patients, which is replaced by atrophy or loss of volume of grey matter in patients with PDD (González-Redondo et al., 2014). These results suggest that hypometabolism precedes and is replaced by atrophy as the cognitive decline progresses, representing two steps of the same process. The hypometabolism *in vivo* would reflect a synaptic dysfunction that if it were maintained over time would lead to a loss of synaptic terminals and ultimately to neuronal degeneration, which would be detected *in vivo* as atrophy. This sequence of events is highly likely to occur not only at the cortical level in advanced stages of PD but also in the degenerative process caused by α-syn deposits in nigrostriatal dopaminergic neurons in the prodromal phase of PD, although this fact has never been studied at any point in the brain. Moreover, using novel and more sensitive approaches such as Neurite Orientation Dispersion and Density Imaging (NODDI) it has been described that microstructural complexity of axons and dendrites is reduced in SN and putamen of advanced PD patients and interestingly, these axonal abnormalities have been identified before atrophy is evident (Kamagata et al., 2017).

To sum up, since numerous reports have shown accumulation of α-syn at synapses and, consequent alterations in synaptic structure and function have been reported in patients and in experimental models of PD, it is likely that synaptic impairment caused by the pathological accumulation of toxic α-syn plays a central role in PD. In addition, these synaptic alterations have been found to precede cell loss, thus, pointing to synapses as the primary region in the onset of pathology in PD. However, the sequence of synaptic events and the identification of the exact point in which aberrant α-syn disrupts the synaptic activity are still elusive.

6. Animal Models of Parkinson´s Disease

Animal models are very useful tools to study the molecular pathogenesis of PD and provide valuable insight into potential new targets for disease intervention. The ideal animal model should be progressive and reproduce the histopathological, biochemical and pathophysiological features associated with PD. However, as it occurs with other neurodegenerative diseases, PD has not been observed spontaneously in animals. Consequently, the main characteristic features of the disease have been imitated in experimental animals through the administration of different neurotoxic agents or drugs that disrupt dopaminergic neurotransmission or cause similar histopathological changes associated with PD (Van Kampen and Robertson, 2017).

The most commonly used animal models for the study of experimental PD are those resulting from exposure to neurotoxins such as 6-hydroxydopamin (6-OHDA), MPTP, rotenone and methamphetamine in rodents and primates. The PD toxin-based models cause an acute and rapid death of dopaminergic neurons and produce a DA loss phenotype without any progressing evolution of the pathology (Bezard et al., 2013). Of note, the administration of these toxins does not result in α-syn pathology. Although these traditional toxin-based models of PD have proved extremely useful in developing treatments for PD signs and in investigating side effects associated with DA replacement therapies, they do not model the molecular pathology of PD and consequently, have not succeeded in deepening into the neurobiological basis of the disease (Koprich et al., 2017).

Because of the prominent role that α-syn plays in the pathology of PD, it represents an appealing basis for animal models development that allows the study of the neurobiology of PD (Benskey et al., 2016). Furthermore, animal models of PD in which expression of α-syn is altered represent an ideal condition to explore subtle alteration of synaptic activity before neuronal degeneration occurs as they offer the possibility to follow the synaptic events at different time points along with the disease progression. To date, the vast majority of work on α-syn animal models has been performed in rodents, although there has also been research performed in larger mammals such as non-human primates, as well as invertebrates (*Drosophila*, *Caenorhabditis elegans* and zebrafish). These animal models can be subdivided in α-syn transgenic models, models of exogenous α-syn by inoculation of fibrils or oligomers and by viral vector-based overexpression (Gómez-Benito et al., 2020; Koprich et al., 2017). The most relevant PD models in the studies of α-syn induced synaptic dysfunction will be described in the following section.

6.1 Transgenic models

Many transgenic mouse lines overexpressing WT or mutant human α-syn (hα-syn) have been generated to try to model *SNCA* missense mutations or multiplications described in PD. The majority of transgenic lines overexpressing mutant α-syn encode either A53T or A30P familial mutation. However, there are also double mutant transgenic lines that express both mutations, and a few express α-syn with modifications such as C-terminal truncation (Koprich et al., 2017). One major difference between existing α-syn transgenic mice is the promoter used to control transgene expression, which includes mouse thymus cell antigen 1 (*Thy1*) promoter, human platelet-derived growth factor subunit B (*PDGF*) promoter, TH promoter and the prion promoter (*Prnp*) (Garcia-Reitböck et al., 2010; Giasson et al., 2002; Masliah, 2000; Nemani et al., 2010; Tozzi et al., 2016; Van Der Putten et al., 2000). BAC models with upstream promoter elements have also been developed, often on a mouse *SNCA*$^{-/-}$ background, to drive expression of human *SNCA* at endogenous levels and to avoid potential confounding interactions with endogenous mouse α-syn (Janezic et al., 2013). The type of promoter used will determine the type of cells where α-syn transgene will be expressed.

In general, the major shortcoming of current α-syn transgenic mice is the lack of neurodegeneration of the nigrostriatal dopaminergic system (Garcia-Reitböck et al., 2010; Giasson et al., 2002; Masliah, 2000; Van Der Putten et al., 2000), although a few transgenic models have shown a decrease in SN_{pc} cell number (on average 30% cell loss) at 18 months or later (Janezic et al., 2013). Neurodegeneration in PD is an age-related process, and the lifespan of mice may be too short for α-syn mediated neurodegeneration to occur. However, any reliable animal model used to study PD pathology should recapitulate this defining feature. On the other hand, the anatomical distribution of α-syn inclusions also varies widely among transgenic models and in many models α-syn pathology takes more than 6 months to develop (Garcia-Reitböck et al., 2010; Janezic et al., 2013; Tozzi et al., 2016). Most transgenic lines show extensive α-syn inclusions throughout the brain (e.g. cortex, hippocampus, cerebellum and brainstem) (Janezic et al., 2013; Subramaniam et al., 2014; Van Der Putten et al., 2000), but in many cases little or no aggregates have been found in the SN_{pc} (Giasson et al., 2002; Masliah, 2000), suggesting that in those cases in which motor impairments are observed, they are not the result of degeneration of the nigrostriatal system, but more likely represent pyramidal or motor neuron degeneration. Thus, the utility of motor phenotypes as outcome measures in transgenic models seems to be limited because of their variability and questionable relevance to dopaminergic dysfunction. However, extranigral expression of α-syn in transgenic animals

provides the potential for studying the effects of synucleinopathy outside the nigrostriatal system and modeling non-motor features of PD (Koprich et al., 2017).

Regarding the studies using transgenic models that provide important insight about synaptic alterations induced by α-syn, experimental data show that accumulation of toxic α-syn species causes a synaptic neurotransmitter deficiency that precedes cell death, pointing to synapses as the region of primary α-syn pathology in the cell (Garcia-Reitböck et al., 2010; Janezic et al., 2013; Nemani et al., 2010). For example, mice overexpressing truncated α-syn (1-120) under TH promoter in catecholaminergic cells present α-syn aggregates at striatal dopaminergic terminals in the absence of nigral dopaminergic neuron loss. Interestingly, the release of DA from nigrostriatal synaptic terminals is progressively impaired (at 12 and 18 months) and is accompanied by a redistribution of SNARE proteins in nigrostriatal terminals (Garcia-Reitböck et al., 2010). In another α-syn transgenic model where human WT α-syn is overexpressed from the BAC construct (BAC-*SNCA*), nigral neurodegeneration is displayed at 18 months, but the deficit in DA release in the striatum was already observed at 3 months of age without changes in total DA content (Janezic et al., 2013). This study suggests that dopaminergic dysfunction is not initially a direct effect of cell death or reduction of DA content, but is rather caused by functional impairment of neurotransmitter release at the synapse. However, in this mouse model no clear α-syn aggregation in either the SN_{pc} or the striatum has been reported. Other study overexpressing WT α-syn by *PrnP* promoter also shows a physiological defect in SV recycling that is accompanied by a reduction in peripheral membrane proteins of SVs such as synapsin. These defects precede detectable neuropathology and an ultrastructural analysis confirmed reduced SV density at the active zone (Nemani et al., 2010). These experiments demonstrate that increased expression of α-syn causes a specific physiological impairment of neurotransmitter release in the absence of overt toxicity. Nevertheless, it remains unclear whether these functional disturbances lead eventually to anatomical degeneration as its temporal pattern has not been often studied. On the other hand, α-syn mediated alteration in striatal synaptic plasticity has also been investigated by studying electrophysiological features of both SPNs and ChIs using a truncated α-syn (1-120) transgenic model under TH promoter. In a presymptomatic stage in 6 months-old animals, before any neuronal degeneration was detected, α-syn overexpression selectively blocks the induction of long-term potentiation (LTP) of striatal ChIs but not of SPNs, producing early memory and motor alterations (Tozzi et al., 2016). Another study overexpressing hα-syn under PDGF promoter showed decreased cortical spine density and abnormalities in spine dynamics in an age-dependent manner from 4 months onwards, but the motor activity and the integrity of the nigrostriatal systems were not studied

(Blumenstock et al., 2017). In a more recent study, electron microscopy was used to image striatal neuropil in both WT mice and a BAC-A53T-*SNCA* transgenic mouse model at 1, 3, 6, and 22 months of age. They demonstrated that spine density gradually decreases, and average spine head volume gradually increases with age in WT mice, suggesting a homeostatic balance between spine head volume and spine density. However, this inverse relationship between spine head volume and spine density was not observed in BAC-A53T-*SNCA* mice, suggesting that α-syn induces an abnormality in the mechanisms that control synapse growth and maturity. However, although the temporal pattern was assessed in this study there is a lack of information about the motor activity and the nigrostriatal pathway integrity (Parajuli et al., 2020).

To sum up, α-syn transgenic mouse models possess strong construct validity, as they are based on human genetic data implicating mutations in overexpression of *SNCA* in PD. These models collectively exhibit key features of PD, including α-syn inclusions, nigrostriatal synaptic dysfunction and non-motor symptoms, but show limited and inconsistent neurodegeneration on the SN_{pc}, questionable motor signs and prolonged time course to develop pathology.

6.2 Models of inoculation of exogenous α-syn preformed fibrils/oligomers or LB containing tissue

Following the description of Braak, the hypothesis that α-syn spreads between interconnected anatomical areas has become an interesting way of modeling PD progression. Several models of α-syn spread that lead to degeneration have been developed, including intracerebral injection with LB containing tissue from *post-mortem* human brains or the injection with synthetic preformed fibrils (PFFs) or oligomers.

Variability with the human brain extract model is a critical problem, as there is no clear means by which different extracts can be benchmarked and thus how a reliable source can be developed to provide consistent quality for a robust animal model (Arotcarena et al., 2020; Recasens et al., 2014). The synthetic PFF or oligomer approach can be standardized and may circumvent this issue, although it is not still clear how robust or variable will be once applied in multiple laboratories (Patterson et al., 2019).

Inoculation of PFFs or oligomers of recombinant α-syn into the striatum in rodents induces a progressive pattern of pathology that resembles many PD features such as the spatial and temporal pattern of neurotoxicity and the formation of α-syn inclusions that resemble LBs and LNs found in diseased brains. As observed in PD, the presence of aggregated α-syn throughout the brain in this model precedes loss of dopaminergic terminals and striatal DA, the subsequent

death of SN_{pc} neurons (30-40% TH+ neuron loss), and corresponding motor impairment (Luk et al., 2012; Patterson et al., 2019; Paumier et al., 2015). α-syn inclusion formation occurs in brain areas distant from the injection site; when injected in the striatum they also appear in the hippocampus, cortex, midbrain and other regions (Luk et al., 2012; Paumier et al., 2015; Volpicelli-Daley et al., 2014), which allows examining the impact of these aggregates on diverse neuronal populations. Thus, the potential to study the effects of α-syn pathology in multiple neurochemical systems and to model non-motor symptoms is an advantage of this model. This model has also been translated into non-human primates, providing a model of α-syn spread in an anatomical system closer to that of humans (Arotcarena et al., 2020; Chu et al., 2019; Recasens et al., 2014).

One of the major drawbacks of the fibril model is the lack of knowledge about the spread of pathologic α-syn and the exact mechanism by which the fibrils induce endogenous α-syn to misfold. Although the progressive accumulation of aggregated α-syn in different brain regions over time may reflect a prion-like spread, the proposed cell-to-cell transfer remains controversial (Benskey et al., 2016). Additionally, it is important to highlight the great variability that exists in these models regarding the injection site (SN_{pc}, striatum, olfactory bulb, ventricles and combined models), the amount and type of PFFs or oligomers injected, and the animal species or strains used, which influence the development of neuropathology. Indeed, oligomers and PFFs present poor stability and a tendency to dissociate, not all the species hold the same toxicity, and the mechanisms of structure-related toxicity are still largely unclear. In addition, the animal species from which the α-syn is derived seems to be critical (Gómez-Benito et al., 2020; Luk et al., 2012).

In this sense, most studies have been centered on the trans-synaptic propagation of α-syn and very few studies have been performed regarding synaptic alterations after the injection of these exogenous pathological α-syn forms. A study showed impaired DA release by *in vivo* amperometry recordings 10 days after the inoculation of hα-syn PFFs into the rat SN in combination with viral vector-mediated overexpression of hα-syn. These animals exhibited a reduction in DA release and reuptake rates in the striatum that was accompanied by progressive degeneration of dopaminergic neurons in the SN, neuritic swelling, and impaired motor behaviour over time (Thakur et al., 2017). Recently, electrophysiology recordings from slices from striatal PFF injected mice revealed dysfunction in synaptic transmission and plasticity. These animals exhibited LTP impairment in both populations of the SPNs by selectively targeting the GluN2A-NMDAR current, with no detrimental effect on LTD (Durante et al., 2019). Another study showed cortical α-syn aggregation and decreased cortical spine density as well as

dystrophic deformation of apical dendritic shafts 5 months after inoculation of PFFs into the dorsal striatum (Blumenstock et al., 2017).

To sum up, although α-syn spread models induce a progressive pattern of pathology that resembles many PD features, they currently represent models of a hypothesis (model of trans-synaptic spread of α-syn) rather than a disease, as they largely rely on the still controversial prion hypothesis. Further investigations and established guidelines for PFF preparation and injection protocols are required to characterize the robustness and reproducibility of this model and circumvent the great variability among different research studies (Koprich et al., 2017; Peelaerts et al., 2015), as they might be very valuable for evaluating therapies targeted at α-syn spread or blocking of seeding.

6.3 Adeno associated viral vector-based α-syn overexpression models

The development of gene delivery techniques using recombinant viral vectors has been very useful to address the need for animal models recapitulating the specific neuropathological processes of various neurodegenerative diseases. In this context, viral vector-mediated overexpression models for PD were developed using recombinant adeno-associated viral vectors (rAAV) encoding either WT or mutant hα-syn inoculated in the SN_{pc} (Bourdenx et al., 2015; Decressac et al., 2012; Klein et al., 2002; Ulusoy et al., 2010) and striatum (Kirik et al., 2002). This vector system uses single-stranded DNA that integrates into the host genome and provides long term expression in the transduced neurons, reaching up to 95% efficiency (Ulusoy et al., 2008, 2010), and thus represent the current most used tool for preclinical studies (Koprich et al., 2017). Indeed, this model is also attractive as it can be applied in a broad range of animal species including rodents and non-human primates (Vermilyea and Emborg, 2015).

The hα-syn (native or mutant) overexpression using rAAV (rAAV-hα-syn) leads to a progressive loss of dopaminergic neurons in the SN_{pc} (25-80% loss of TH+ neurons), and loss of terminals in the striatum (30-60% loss of TH or DAT markers), although the extent of neurodegeneration and time course are variable (Bourdenx et al., 2015; Chung et al., 2009; Decressac et al., 2012; Gorbatyuk et al., 2008; Kirik et al., 2002; Oliveras-Salvá et al., 2013; Phan et al., 2017; Ulusoy et al., 2010). These neurodegenerative changes are associated with the development of motor impairments (Bourdenx et al., 2015; Decressac et al., 2012; Gaugler et al., 2012; Kirik et al., 2002; Koprich et al., 2010; Oliveras-Salvá et al., 2013; Ulusoy et al., 2010) and interestingly, the impact of α-syn overexpression seems to be different between the two major dopaminergic neuron subtypes, leading to prominent cell loss in the A9 cells of the SN, while A10 cells in the adjacent VTA survive, despite similar levels of α-syn expression (Maingay

et al., 2006). Furthermore, overexpression of hα-syn produces the formation of Lewy-like α-syn cytoplasmic inclusions and prominent axonal pathology (Chung et al., 2009; Decressac et al., 2012; Kirik et al., 2002; Koprich et al., 2010; Lundblad et al., 2012; Phan et al., 2017). The axonal changes include swollen and dystrophic morphology of presynaptic terminals, which develop early after vector injection and precede dopaminergic neuron cell loss (Decressac et al., 2012; Gaugler et al., 2012; Koprich et al., 2010; Lundblad et al., 2012; Phan et al., 2017). Of note, the morphology of these dystrophic axons is remarkably similar to those observed in brains from PD patients (Braak et al., 1999; Galvin et al., 1999). Besides, the rAAV-hα-syn model induces also an immune reaction characterized by activation of microglia, increased pro-inflammatory cytokine expression and infiltration of lymphocytes (Chung et al., 2009; Rodríguez-Chinchilla et al., 2020; Sanchez-Guajardo et al., 2010; Theodore et al., 2008), similar to what has been reported in PD patients (Reish and Standaert, 2015).

Several important considerations when using the rAAV-hα-syn model that will influence the comparison among studies are the serotype, the promoter, inclusions of the woodchuck hepatitis post-transcriptional regulatory element (WPRE) and the type of hα-syn overexpressed. There are several serotypes of rAAV vectors that have different propensity to transduce neurons in different brain regions (Ulusoy et al., 2010). The most efficient and extensively studied serotype for use in the SN is the rAAV2, although over the last years new hybrid AAV serotypes which show increased transduction and spread of hα-syn have been implemented in this model (Decressac et al., 2012; Gaugler et al., 2012; Gorbatyuk et al., 2008; Oliveras-Salvá et al., 2013; Ulusoy et al., 2010). Specifically, rAAV2/9 is the most efficient in hα-syn transduction (Bourdenx et al., 2015). Regarding the most common promoters to direct the expression of hα-syn, they include the hybrid cytomegalovirus (CMV), chicken β-actin (CBA), phosphoglycerate kinase (PGK), and human synapsin-I promoters. Synapsin-I promoter provides neuronal-specific transgene expression, while the other types provide a more ubiquitous expression. Furthermore, the inclusion of WPRE into the plasmid improves transgene expression levels (Decressac et al., 2012). On the other hand, the type of hα-syn overexpressed is also critical. Animal studies suggest that the A53T mutation is more toxic and prone to aggregate than either the A30P mutation or the WT form (Lu et al., 2015; Oliveras-Salvá et al., 2013; Van der Perren et al., 2015).

However, the key critical factors defining the successful outcome of rAAV vectors for disease modeling are related to the quality, purity and titer of the vector preparations. Since production, purification and titration methods vary between laboratories, it is often difficult to compare results between studies. The variability observed in the level of transgene expression

and dopaminergic depletion will primarily depend on these critical steps (Ulusoy et al., 2008; Volpicelli-Daley et al., 2016). The purification procedure varies across studies and is crucial for obtaining a high yield of infectious rAAV that could cause non-specific toxic effects or immune reactions (Ulusoy et al., 2008). Determination of the titer or the number of viral genome copies is also critical, as the expression level is primarily determined by the titer. The amount of protein produced after transduction with rAAV may vary, but, typically, there is an approximately 2-4 fold increase in hα-syn levels compared to endogenous protein levels, similar to what might be caused by *SNCA* triplications in PD patients (Gorbatyuk et al., 2008; Volpicelli-Daley et al., 2016).

The progressive time course of the rAAV-hα-syn model has provided interesting data and accessible means of studying dopaminergic synaptic alterations (Table 1). For example, as early as 10 days after injection of rAAV6-WT-hα-syn into the SN_{pc}, there is a significant reduction in DA reuptake rates in the striatum, suggesting impairments in the DAT, which are followed by a reduction in evoked DA release from 3 weeks onwards. However, SN_{pc} TH^+ loss and striatal dopaminergic depletion are not significantly reduced until the 3rd week and motor activity is not reduced until the 5th week post-inoculation (p.i.) (Lundblad et al., 2012). Another study overexpressing WT hα-syn by rAAV2/6 into the SN_{pc} described that the reduced DA release corresponds to a decreased density of dopaminergic vesicles and dopaminergic synaptic contacts in striatal terminals at the ultrastructural level at 10 weeks p.i. and reported a 6 fold increase in autophagosomes. Motor activity was also decreased at this time point, but the nigrostriatal integrity was not assessed (Gaugler et al., 2012). Moreover, other study overexpressing rAAV2-A53T-hα-syn showed that the appearance of dystrophic axonal swellings along the nigrostriatal projection precede neuronal death and is accompanied by altered levels of proteins involved in axonal transport and synaptic transmission, although motor activity was not studied (Chung et al., 2009). Recent electrophysiological studies overexpressing rAAV2/6-WT-hα-syn provide further evidence that α-syn overexpression leads to a failure in the striatal synaptic plasticity. Tozzi and coworkers showed that α-syn selectively blocks the induction of LTP in striatal ChIs, without affecting SPNs, along with neuronal degeneration and decrease in motor activity (Tozzi et al., 2016). The same group has recently shown that during the acquisition phase of motor learning in the rotarod task, mice overexpressing hα-syn do not show the correct shift from LTD to LTP that healthy animals do and demonstrate that this reorganization of cellular plasticity within the dorsolateral striatum is mediated by D_1R and DAT (Giordano et al., 2018). Overall, these studies show that the described synaptic changes occur before the onset of dopaminergic cell death (Chung et al., 2009; Gaugler et al., 2012; Lundblad et al., 2012; Phan et al., 2017) and suggest that synaptic and axonal defects induced by hα-syn overexpression

contribute to the development of PD well before neuron death occurs, which matches with the observed pattern in PD patients (Gómez-Benito et al., 2020).

However, most of these studies have been performed by a unilateral inoculation of rAAV vector (Chung et al., 2009; Gaugler et al., 2012; Lundblad et al., 2012; Phan et al., 2017; Tozzi et al., 2016), which differs from what occurs in PD. Furthermore, it should be considered that a compensatory mechanism from the unaffected side could also take place. On the other hand, although evidence show that synapses are the primary site of pathology in α-synucleinopathies, most studies using the rAAV model have been primarily focused on the cell death and there is a lack of studies focused on the active functional α-syn pathology that interferes with normal synaptic physiology. Studies focused on the temporal pattern of synaptic abnormalities that take place during the onset and progression of the dopaminergic degeneration would give valuable insights into the precise synaptic mechanisms that take place on the prodromal phase of the disease and disease progression and would allow us to implement new pharmacological approaches.

Summarized, targeted overexpression of hα-syn in midbrain dopaminergic neurons using rAAV vectors reproduces many of the characteristic features of PD as it is accompanied by abnormal accumulation of hα-syn leading to aggregation, cellular, biochemical and axonal pathologies, neuroinflammation, dopaminergic system degeneration and consequent motor impairment that develop progressively over time. Thus, this model represents the current most used tool for preclinical studies as it offers a robust tool for the study of the neurobiological basis of the disease and its progression as well as for the preclinical evaluation of new therapies that could help to slow or halt its development.

Reference	Species	rAAV vector serotype and promoter	Titer (gp/mL)	Site of injection	Time post-inoculation	Motor activity	SN_{pc} TH^+ neuron loss	Str dopaminergic depletion (TH/DAT)	Striatal DA/DOPAC content	Striatal synaptic alterations	Synaptic Pathology
Chung et al., 2009	Rat	AAV2-A53T-hα-syn Synapsin I	1.8 x 10^{12}	SN_{pc} unilateral	4 weeks	-	ns	ns	ns/↑	**Protein expression:** ↑ Rabhilin3A, KIF3A, ↑ Myosin VA, Actin;↓ KIF17, Dynein	Swollen axons
					8 weeks		ns	ns	ns/↑	↑ Dynein, Dynamin, Dynactin, Neurofil 160, actin; ↓ Rabphilin3A, Syntaxin, KIF (1A,1B,2A and 3A), Miosin Va, α-and γ-tubulin	Swollen axons
Lundblad et al., 2012 and Decressac et al., 2012	Rat	AAV6-WT-hα-syn, Synapsin I +WPRE	3.1 x 10^8	SN_{pc} unilateral	10 days	ns	ns	ns	ns/ns	**DA release:** ns Peak amplitude, ↓ Linear rise rate, ↓↓ DA reuptake, ns Total AUC	-
					3 weeks	ns	42%	31%/24%	ns/ns	↓↓ Peak amplitude, ↓↓↓ Linear rise rate, ↓↓↓ DA reuptake, ↓↓ Total AUC	Swollen axons
					5 weeks	↓	68%	30%/45%	↓/ns	↓↓ Peak amplitude, ↓↓↓ Linear rise rate, ↓↓↓ DA reuptake, ↓↓ Total AUC	Swollen axons
					8 weeks	↓	80%	58%/57%	↓/↓	↓↓↓ Peak amplitude, ↓↓↓ Linear rise rate, ↓↓↓ DA reuptake, ↓↓↓ Total AUC	Swollen axons
					16 weeks	↓	74%	60/60%	↓/↓	↓↓↓ Peak amplitude, ↓↓↓ Linear rise rate ↓↓↓ DA reuptake, ↓↓↓ Total AUC	Swollen axons
Gaugler et al., 2012	Rat	AAV2/6-WT-hα-syn PGK +WPRE	4.1 x 10^{13}	SN_{pc} unilateral	8 weeks	↓	-	-	↓/ns	50% ↓ evoked DA release	-
					10 weeks		-	-	-	**Electron Microscopy:** 40% ↓ synaptic vesicle density,34%↓ dopaminergic synapses, 6x ↑ autophagosomes	
					4 months (16 weeks)		25%	29%	-	-	
Tozzi et al., 2016	Rat	AAV2/6-WT-hα-syn Synapsin I +WPRE	3.1 x 10^8	SN_{pc} unilateral	4 months (16 weeks)	↓	50%	-	↓/-	**Electrophysiology:** ns SPN LTD and LTP, ns SPN LTP,↓ ChIs LTP	-
Bido et al., 2017	Rat	AAV2/9-A53T-hα-syn CMV +WPRE	6.9x10^{13}	SN_{pc} bilateral	8 weeks	↓	50%	50%	↓/ns	**Mitochondrial respiration in synaptosomes:** ↓ OCR	-
Giordano et al., 2018	Rat	AAV2/6-WT-hα-syn Synapsin I +WPRE	7.7 x 10^{14}	$SN_{pc;}$ each AAV on one hemisphere	8 weeks	ns but, ↓motor learning	ns	40%/60%	ns/ns	**Electrophysiology:** ns SPN LTD and LTP	-

HYPOTHESIS AND AIMS

We hypothesize that the onset of the neurodegenerative process of the dopaminergic system in PD is related to a failure of the synaptic function due to the accumulation of presynaptic α-syn aggregates, which would progress to structural changes and neuronal death, and occur before the development of motor disturbances. Hence, functional changes and ultrastructural changes would be two steps of the same process and early therapeutic interventions in the first stage (synaptic failure) could prevent or delay the development of the dopaminergic system neurodegeneration, avoiding the progression of PD.

The main objective of this doctoral thesis is to elucidate the temporal sequence of functional and structural changes related to α-syn overexpression and dopaminergic degeneration in a rat model of progressive parkinsonism induced by viral vector-mediated overexpression of A53T mutated hα-syn in the SN_{pc}.

The following specific objectives were established:

- To study the temporal sequence of the motor behaviour associated with the overexpression of hα-syn.
- To evaluate the temporal sequence of the hα-syn overexpression and its relation with the dopaminergic degeneration in the SN_{pc} and striatal axonal terminals.
- To study the temporal sequence of the synaptic functionality in isolated striatal synapses by bioenergetic and proteomic approaches.
- To determine the temporal sequence of synaptic ultrastructure in the striatal axonal terminals by electron microscopy.
- To evaluate changes in the density and morphology of dendritic spines of the postsynaptic dendritic tree of striatal SPNs by high-resolution confocal microscopy.

MATERIAL AND METHODS

The most relevant antibodies and buffers used in the different experiments of this doctoral thesis are detailed in the annex section**.**

1. Development of the animal model of parkinsonism

1.1 Animals

Adult male Sprague-Dawley rats (300 g) were obtained from the animal facilities of Charles River Laboratories. Animals were housed in pairs in standard conditions of temperature and humidity (70% humidity, 22ºC), kept on a regular 12 h light/dark cycle and allowed food and tap water *ad libitum.* All the experimental procedures were approved by the ethics committee for animal research of Biodonostia Health Research Institute (CEEA16/11; San Sebastian, Spain) and CIMA-Universidad de Navarra (107-17; Pamplona, Spain) and were carried out in strict accordance with the guidelines of the Spanish Government (RD53/2013) and the European Union Council Directive (2010/63/EU) on the protection of animals used for scientific purposes. All efforts were cautiously carried out to avoid and/or alleviate animal suffering.

1.2 Viral vectors

Recombinant adeno associated viral vectors with rAAV2/9 serotype were custom ordered from the core facility of production of adeno associated vectors of the University of Bordeaux (Bordeaux, France). Each vector was driven by a cytomegalovirus (CMV) promoter and transgene expression was enhanced using a woodchuck hepatitis virus post-transcriptional regulatory element (WPRE).

1.3 Experimental design

The study consisted of two experimental groups:

- **hα-syn group**: inoculated with the viral vector rAAV2/9-CMV/hα-synA53T, that overexpresses the human α-syn (hα-syn) protein with A53T mutation (viral titer: 8 x 10^{12} genomic particles/ml).

- **EVV group**: inoculated with the viral vector rAAV2/9-CMV/EVV, which are empty capsids of the adeno-associated viral vector with no overexpression of transgene (EVV) and representing the control group (viral titer: 2 x 10^{13} genomic particles/ml).

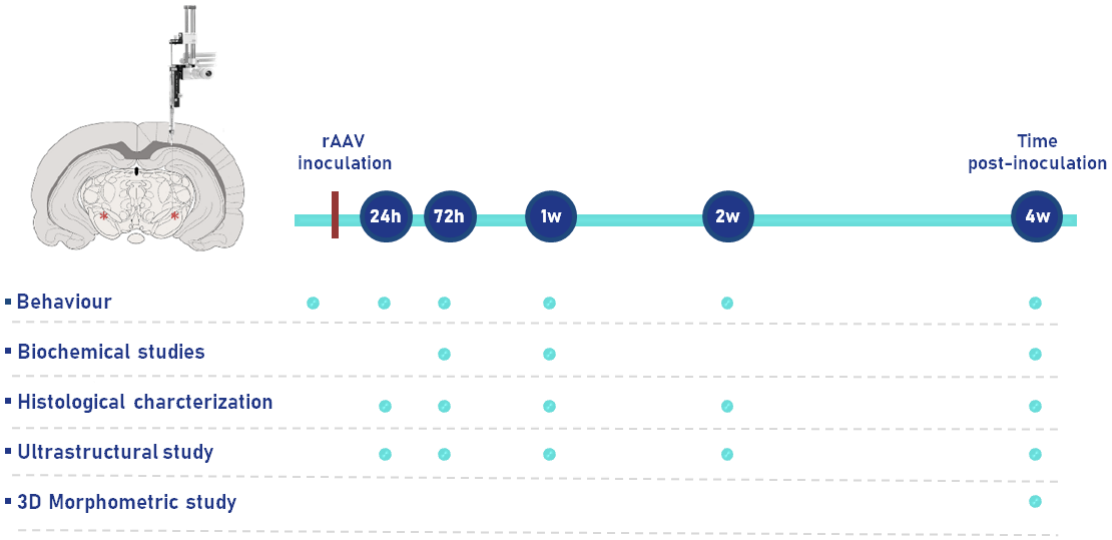

Figure 10: Experimental design. Representation of the viral vector inoculation site (red asterisks, bilaterally in the SN_{pc}) and experimental design for the different studies with the final evaluation time points after the inoculation of the rAAVs.

We conducted a cross-sectional study involving two experimental groups (hα-syn and EVV) with multiple independent subgroups of rats evaluated at different post-inoculation (p.i.) time points according to the final evaluation time point: 24 hours (h), 72 h, 1 week (w), 2 w and 4 w. The time points selected for each study are explained in the following section.

For motor evaluation, histological characterization and the ultrastructural study animals were sacrificed at 24 h, 72 h, 1, 2 and 4 weeks post-inoculation. For biochemical studies 72 h, 1 and 4 weeks p.i. time points were chosen based on results of the previous studies and the following reasons: 72 h represents the beginning of hα-syn overexpression in the SN_{pc}, 1 week represents the onset of hα-syn overexpression in the striatum and 4 weeks represents the point of significant neurodegeneration of dopaminergic neurons and dopaminergic terminals. The three-dimension morphometric study of dendritic spines was conducted at 4 w p.i., as several significant ultrastructural alterations in the dopaminergic terminals as well as significant dopaminergic neurodegeneration were observed at this time point in the previous experiments. A representation of the different studies is summarized in the figure 10.

1.4 Stereotaxic Surgery

Animals were anesthetized with isoflurane in oxygen-enriched air (4% induction and 2-2.5% maintenance) and placed on a stereotaxic frame (Stoelting Instruments). The head was fixed with the ear bars and with the incisor bar positioned -3.3 mm below the interaural line. A sagittal incision was made in the skin and the periosteum was carefully separated to locate the cranial sutures. The coordinates where the rAAV was inoculated were calculated from Bregma (the anatomical point on the skull at which the coronal suture is intersected perpendicularly by the sagittal suture) as the origin for anteroposterior (AP) and mediolateral (ML) axis, and related to dura as the origin for dorsoventral (DV) axis. Two small holes were drilled in the animal's skull with a dental drill. The rAAVs were bilaterally inoculated in two points in each SN_{pc} (1 µL per point) using a Hamilton syringe (10 µL, Neuros #1701RN, Hamilton Company) connected to an infusion pump (Harvard Apparatus) at a rate of 0.2 µl/min (4 µl of total volume/animal). The coordinates for the injections were the following: 1) AP: -4.9, ML: +/-2.2, DV: -7.7 mm; 2) AP: -5.4, L: +/-2.0, DV: -7.7 mm according to the Atlas of Paxinos and Watson (Jiménez-Urbieta et al., 2019; Paxinos et al., 1985). The needle was left in place for an additional 1 min to facilitate correct inoculation of the viral vector, and it was slowly retracted from the brain. Finally, the skin was sutured and the evolution of the postoperative was controlled to avoid any complication.

2. Behavioural studies

All behavioural tests were performed before the inoculation of the rAAV (basal) and before the sacrifice of the rats (24 h, 72 h, 1, 2 and 4 w p.i.). Before any behavioural test animals were handled by the experimenter for five days for familiarization with the handling procedure and test environment and to avoid handing-induced anxiety**.**

2.1 Adjusting stepping test

For *in vivo* monitoring of the effects of progressive dopaminergic depletion on the motor activity, the adjusting stepping test was used. Animals were held by the experimenter with one hand fixing the hind limbs and slightly raising the hind part above the surface. With the other hand, the experimenter fixed one of the upper limbs and the animals were slowly moved sideways over a table 0.9 m in approximately 5 s in both directions. The test was repeated twice for each animal each session and the average values of the number of adjusting steps in both directions (adduction and abduction) with each forepaw were considered for the analysis. The

decrease in the number of steps performed by the animal is considered an adequate measure of bradykinesia (Olsson et al., 1995).

2.2 Open field test

Spontaneous locomotor activity and anxiety-like behaviour were assessed with the open field test. Animals were given one habituation session to explore the open arena (1 m length x 1 m width x 60 cm height) for 15 min with dim light. The same day the open field (OF) test was performed, and animals were allowed to explore the arena for 15 min and the activity was video recorded. Using the software Ethovision X13 (Noldus Information Technology), the following parameters were analyzed: total distance traveled (cm), total velocity (cm/s), % of the time moving as well as % of time spent in the center as a measure of anxiety-like behaviour.

3. Biochemical studies

3.1 Brain tissue collection

For bioenergetic studies (n = 3/group and time point) and proteomics (n = 5/group and time point), animals were deeply anesthetized with a mixture of oxygen and isoflurane (5%) and sacrificed at the corresponding end time points p.i. (72 h, 1 week and 4 weeks). Brains were rapidly removed, and the striatum of both hemispheres was carefully extracted. One of the striatum was maintained on ice in order to maintain fresh tissue for the bioenergetics assays that were performed subsequently, and the other striatum was immediately frozen on dry ice and stored at -80ºC until processing.

3.2 Isolation of synaptosomes

The set-up for the biochemical isolation of striatal synaptosomes was carried out at the Biophysics Unit (UPV/EHU, CSIC; Leioa, Spain) due to a short-term stay of the Ph.D. student in the laboratory of the molecular basis of cognitive function with the collaboration of the group led by Dr. Shira Knafo and under the supervision of Dr. Alberto Ouro.

Biochemical isolation of striatal synaptosomes was carried out as described previously with slight modifications (Jurado et al., 2010). The striatum from all groups of rats were weighed and homogenized in a Dounce glass homogenizer (Thermo Fisher Scientific) with buffer A (10% wt/vol) followed by 12 up and down strokes with a syringe with a 26 GA needle. This homogenate was spun down at 1.400 g for 10 min at 4°C. The supernatant was kept and the

pellet was resuspended in buffer A and spun again at 710 g for 10 min at 4°C. Both supernatants were mixed and spun down at 11.600 g for 12 min at 4°C. The pellet (synaptosomal fraction) was resuspended in buffer A and overlaid on buffer B. After centrifugation at 20.000 g for 1 hour at 4°C, the interphase was collected (crude synaptosomal fraction).

3.3 Protein quantification

The protein content of individual synaptosomes samples was quantified using Pierce™ BCA protein assay kit (Thermo Fisher Scientific). This colorimetric assay is based on the reduction of Cu^{2+} to Cu^{1+} by protein in an alkaline medium with the highly sensitive and selective colorimetric detection of the cuprous cation (Cu^{1+}) by bicinchoninic acid (BCA), which leads to a colorimetric change from green to purple. Synaptosomes samples were mix with BCA reagent (BCA reagent was first mixed (A:B) at 50:1 and afterward with synaptosome sample (Sample:BCA) at 2.5:100) and were incubated (Raypa Incubator) for 30 min at 37°C. The absorbance was read at 570 nm in a photometer (Multiskan Ascent Microplate Reader, Thermo Fisher Scientific) and the obtained values were compared to a standard curve made using bovine serum albumin (BSA). All the measurements were made in duplicates and the mean value of both replicates was calculated.

3.4 Western Blot

Isolated striatal synaptosomal fractions (see 3.2 section) were sonicated with 2 pulses of 5 seconds using an output power of 3 in an ultrasonic probe. Protein concentrations of synaptosomal samples were determined by BCA assay as described in the 3.3 section and samples were mix with loading buffer 4x and lysis buffer. Samples were denatured at 100ºC for 10 min. After that, 7 µg of total protein extracts of synaptosomal samples were subjected to SDS-PAGE on 4-15% polyacrylamide Mini-PROTEAN® TGX Stain-Free™ Protein Gels (BioRad) using running buffer and a voltage of 100 V for 20 minutes (to allow the package of the proteins) and 120 V for the rest of the electrophoresis phase. A prestained standard molecular weight ruler was included (Panreac) in order to check the migration and transference of the proteins, as well as to facilitate the detection of the molecular weight of the protein targets. Subsequently, proteins in the gel were transferred to PVDF blotting membranes (0.45 µm pore size, Bio-Rad) using a Trans-Blot Turbo Transfer System (BioRad) through an electric current of 400 mA for 7 minutes. Then, the transferred membrane was cut and the membrane piece corresponding to hα-syn molecular weight was incubated in PBS containing 4% paraformaldehyde (Electron Microscopy Sciences) for 30 min. After incubation, the membrane

was washed in TBS-T for 10 min 3 times. For the detection of β-actin in the superior membrane piece, the fixative treatment was omitted. The membrane was incubated in blocking solution for 30 min. The membrane was further incubated in TBS-T containing 2.5% skim milk and primary antibody (Table 18) overnight at 4°C. Membranes were subsequently washed in TBS-T for 10 min 3 times and were incubated with HRP-conjugated secondary antibody (Table 19) diluted in blocking solution for 1 hour at RT. Following washes in TBS-T and an additional wash in TBS, antibody labeling was visualized with an enhanced chemiluminescent substrate (ECL Luminata Forte Western HRP Substrate, Millipore). The luminescence of the reaction was detected in the ChemiDoc MP Imaging system (Bio-Rad). β-actin was used as the sample loading control.

3.5 Mitochondrial respiration and glycolysis: Seahorse bioenergetics assay

The oxygen-consumption-rates (OCR) and extracellular-acidification rates (ECAR) were measured in freshly purified synaptosomes using Seahorse XF96 extracellular flux analyzer (Agilent) as described previously with some modifications (Choi et al., 2009).

One day prior to the assay day, 96 wells XF96 microplates (Agilent) were coated with polyethyleneimine (PEI; 1:15.000 dilution in H_2O from 50% PEI solution, Sigma) overnight at room temperature (RT) followed by incubation with Geltrex (1:100 diluted in buffer A, Thermo Fisher Scientific) for 1 hour at 37°C to optimize attachment. Following synaptosomal isolation (described in 3.2), synaptosomes were centrifuged at 15.000 g for 15 min at 4°C to remove the sucrose medium and were diluted into the same volume of ionic medium. Synaptosomes (8 µg per well) were loaded into the PEI/Geltrex-coated microplate and centrifuged at 3.400 g for 1 h at 4°C (Beckman Coulter Allegra X-12R centrifuge). The ionic medium was replaced with 175 µl of incubation medium. The microplate was incubated in a non-CO_2 incubator (Incudigit) for 10-15 min at 37°C and then loaded into the XF96 extracellular analyzer following the manufacturer's instructions. Mitochondrial respiration as indicated by oxygen OCR and glycolysis as indicated by ECAR were monitored simultaneously in real-time throughout the assay. Different parameters of mitochondrial respiration (Figure 11 and Table 2) were obtained after the sequential injections of modulators of the mitochondrial electron transport chain (ETC): oligomycin (5 µM), carbonyl cyanide-4-(trifluoromethoxy) phenylhydrazone (FCCP; 4 µM), and rotenone/antimycin A (2 µM each). Oligomycin inhibits ATP synthase (complex V) and is injected first in the assay following basal measurements. It decreases electron flow through the ETC, resulting in a reduction in mitochondrial respiration or OCR. FCCP is the second injection following Oligomycin and represents an uncoupling agent that collapses the proton gradient and

disrupts the mitochondrial membrane potential. As a result, electron flow through the ETC is uninhibited, and oxygen consumption by complex IV reaches the maximum. The third injection is a mixture of rotenone, a complex I inhibitor, and antimycin A, a complex III inhibitor. This combination shuts down mitochondrial respiration and enables the calculation of non-mitochondrial respiration driven by processes outside the mitochondria.

OCR and ECAR data represent the mean rates of each measurement cycle, which consisted of 30 s mixing time, 30 s waiting time, followed by 3 min of data acquisition. Basal respiration was measured before the first injection (3 cycles) and 3 data points were obtained following each injection (12 data points in total). After the assay the plate was stained with crystal violet (Sigma) for data normalization and data was analyzed using Wave Desktop 2.6 software (Agilent). The following mitochondrial respiration parameters were obtained from the OCR data, which were calculated following the equations described in table 2:

- **Basal respiration**: Oxygen consumption used to meet cellular ATP demand resulting from mitochondrial proton leak. Shows energetic demand of the cell under baseline conditions.

- **ATP Production**: The decrease in oxygen consumption rate upon injection of the ATP synthase inhibitor oligomycin represents the portion of basal respiration that was being used to drive ATP production. Shows ATP produced by the mitochondria that contribute to meeting the energetic needs of the cell.

- **H^+ (Proton) leak**: Remaining basal respiration not coupled to ATP production. Proton leak can be a sign of mitochondrial damage or can be used as a mechanism to regulate mitochondrial ATP production.

- **Maximal respiration**: The maximal oxygen consumption rate attained by adding the uncoupler FCCP. FCCP mimics a physiological “energy demand” by stimulating the respiratory chain to operate at maximum capacity, which causes rapid oxidation of substrates (sugars, fats, and amino acids) to meet this metabolic challenge. Shows the maximum rate of respiration that the cell can achieve.

- **Spare respiratory capacity**: This measurement indicates the capability of the cell to respond to an energetic demand as well as how closely the cell is respiring to its theoretical maximum. The cell's ability to respond to demand can be an indicator of cell fitness or flexibility.

- **Coupling efficiency (%):** Proportion of respiratory activity that is used to make ATP.
- **Non-mitochondrial respiration**: Oxygen consumption that persists due to a subset of cellular enzymes that continue to consume oxygen after the addition of rotenone and antimycin A. This is important to get an accurate measure of mitochondrial respiration.

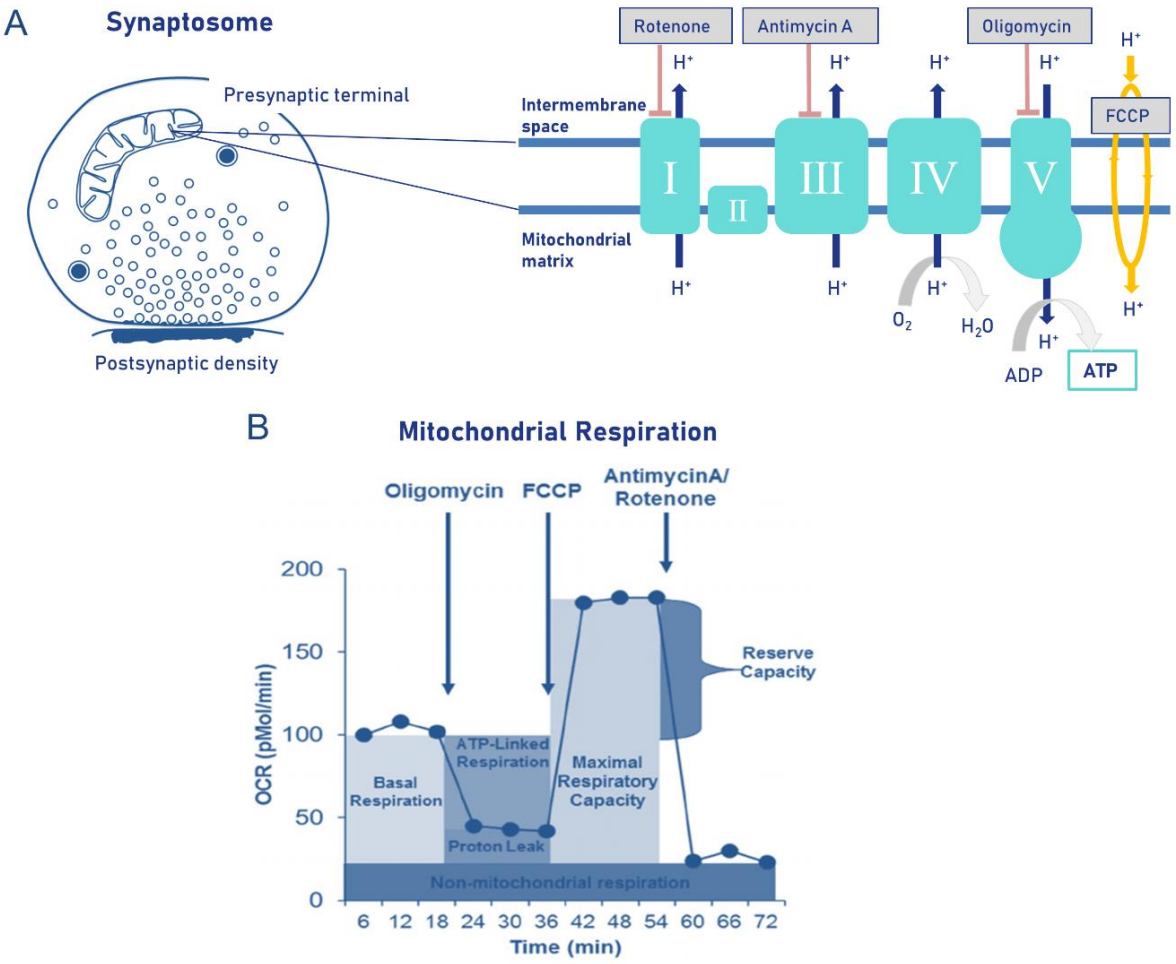

Figure 11: A) Left: Schematic representation of a synaptosome composed of the presynaptic terminal and the adjacent PSD. The presynaptic fraction of synaptosomes contains mitochondria and synaptic vesicles and maintains their metabolic activity. **Right**: Mitochondria are composed of different complexes (I-V) that form the electron transport chain (ETC). The targets of action for all the mitochondrial respiration modulators used in the assay are shown: oligomycin (complex V inhibitor), FCCP (uncoupling agent that collapses the proton gradient), rotenone (complex I inhibitor) and antimycin A (complex III inhibitor). **B)** The Seahorse XF Mitostress test is a well-recognized assay for measuring mitochondrial function. The assay reports multiple key parameters represented in the graphical representation of the mitochondrial respiration profile after the serial injections of the ETC modulators. The equations for obtaining mitochondrial respiration parameters from this assay are described in table 2.

Table 2: Mitochondrial Respiration parameters obtained from OCR data after sequential injection of modulators of the ETC

Parameter	Equation
Basal Respiration	(Last OCR measurement before Oligomycin injection) – (Non-Mitochondrial Respiration)
ATP Production	(Last OCR measurement before Oligomycin injection) – (Minimum OCR measurement after Oligomycin injection)
H^+ (Proton) Leak	(Minimum OCR measurement after Oligomycin injection) – (Non-Mitochondrial Respiration)
Maximal Respiration	(Maximum OCR measurement after FCCP injection) – (Non-Mitochondrial Respiration)
Spare Respiratory Capacity	(Maximal Respiration) – (Basal Respiration)
Coupling Efficiency (%)	(ATP Production)/ (Basal Respiration) x 100
Non-mitochondrial Respiration	Minimum OCR measurement after Rotenone/antimycin A injection

ECAR data allowed us to study the role of glycolysis under basal and stressed (following oligomycin and FCCP injections) conditions by the indirect measurement of medium acidification that is produced during glucose oxidation. Basal and stressed ECAR were calculated following the equations described in table 3.

Table 3: Parameters obtained from ECAR data after sequential injection of modulators of the ETC

Parameter Value	Equation
Basal ECAR	Last ECAR measurement before Oligomycin injection
Stressed ECAR	Maximum ECAR measurement after oligomycin and FCCP injection

3.6 Quantitative proteomics by SWATH-MS

The proteomic study of striatal synaptosomes was carried out in the clinical neuroproteomics laboratory at IIS Navarrabiomed Health Research Institute (Pamplona, Spain) with the collaboration of the group led by Dr. Joaquín Fernandez and Dr. Enrique Santamaría.

Sample preparation and protein digestion

Synaptosomal fractions were homogenized in lysis buffer containing 7 M urea, 2 M thiourea, and 50 mM DTT. The homogenates were spun down at 100.000 × g for 1 h at 15 °C and protein concentration was measured by Bradford assay (Bio-rad). A pool of all samples was used as input for generating the sequential window acquisition of all theoretical mass spectra–mass spectrometry (SWATH-MS) assay library. To increment the proteome coverage, an in-gel digestion was applied. Protein extracts (30 µg) were diluted in Laemmli sample buffer and loaded into a 0.75 mm thick polyacrylamide gel with a 4% stacking gel casted over a 12.5% resolving gel. The total gel was stained with Coomassie Brilliant Blue and 12 equal slides from the pooled sample were excised from the gel and transferred into 1.5 mL Eppendorf tubes. Protein enzymatic cleavage was carried out with trypsin (Promega; 1:20, w/w) at 37 °C for 16 h as previously described (Shevchenko et al., 2007). Purification and concentration of peptides were performed using C18 Zip Tip Solid Phase Extraction (Millipore). The peptides recovered from in-gel digestion processing were reconstituted into a final concentration of 0.5 µg/µl of 2% ACN, 0.5% FA, 97.5% MilliQ-water prior to mass spectrometric analysis.

LC-MS/MS analysis for spectral library generation

MS/MS datasets for spectral library generation were acquired on a TripleTOF 5600+ mass spectrometer (Sciex) interfaced to an Eksigent nanoLC ultra 2D pump system (Sciex) fitted with a 75 µm ID column (Thermo Scientific 0.075 × 250 mm, particle size 3 µm and pore size 100 Å). Before separation, the peptides were concentrated on a C18 precolumn (Thermo Scientific 0.1 × 50 mm, particle size 5 µm and pore size 100 Å). Mobile phases were 100% water 0.1% formic acid (FA) (buffer A) and 100% Acetonitrile 0.1% FA (buffer B). The column gradient was developed in a gradient from 2% B to 40% B in 120 min. The column was equilibrated in 95% B for 10 min and 2% B for 10 min. During all process, the precolumn was in line with the column and flow was maintained all along the gradient at 300 nl/min. The output of the separation column was directly coupled to the nano-electrospray source. MS1 spectra were collected in the range of 350-1250 m/z for 250 ms. The 35 most intense precursors with charge states of 2 to 5 that exceeded 150 counts per second were selected for fragmentation using rolling collision

energy. MS2 spectra were collected in the range of 230–1500 m/z for 100 ms. The precursor ions were dynamically excluded from reselection for 15 s.

Database search and results processing of assay library

MS/MS data acquisition was performed using AnalystTF 1.7 (Sciex) and spectra files were processed through ProteinPilot v5.0 search engine (Sciex) using ParagonTM Algorithm (v.4.0.0.0) (Shilov et al., 2007) for database search. To avoid using the same spectral evidence in more than one protein, the identified proteins were grouped based on MS/MS spectra by the Progroup™ Algorithm, regardless of the peptide sequence assigned. False discovery rate (FDR) was performed using a non-linear fitting method (Tang et al., 2008) and displayed results were those reporting a 1% Global FDR or better.

SWATH-MS

Individual protein extracts (20 µg) from all experimental groups (6 groups; 5 independent synaptosomal fractions per group) were subjected to in-gel digestion, peptide purification and reconstitution before mass spectrometric analysis as previously described. For SWATH-MS-based experiments, the TripleTOF 5600+ instrument was configured as described by Gillet and coworkers (Gillet et al., 2012). Using an isolation width of 16 Da (15 Da of optimal ion transmission efficiency and 1 Da for the window overlap), a set of 37 overlapping windows was constructed covering the mass range 450–1000 Da. In this way, 2 µl of each sample was loaded onto a trap column (Thermo Scientific 0.1 × 50 mm, particle size 5 µm and pore size 100 Å) and desalted with 0.1% TFA at 2 µl/min for 10 min. The peptides were loaded onto an analytical column (Thermo Scientific 0.075 × 250 mm, particle size 3 µm and pore size 100 Å) equilibrated in 2% acetonitrile 0.1% FA. Peptide elution was carried out with a linear gradient of 2 to 40% B in 120 min (mobile phases A: 100% water 0.1% formic acid (FA) and B: 100% Acetonitrile 0.1% FA) at a flow rate of 300 nl/min. Eluted peptides were infused in the mass-spectrometer. The Triple TOF was operated in swath mode, in which a 0.050 s TOF MS scan from 350 to 1250 m/z was performed, followed by 0.080 s product ion scans from 230 to 1800 m/z on the 37 defined windows (3.05 s/cycle). The collision energy was set to optimum energy for a 2 + ion at the center of each SWATH block with a 15 eV collision energy spread.

Label-free quantitative data analysis

The resulting ProteinPilot group file from library generation was loaded into PeakView® (v2.1, Sciex) and peaks from SWATH runs were extracted with a peptide confidence threshold of 99% confidence (Unused Score ≥ 1.3) and FDR lower than 1%. For this, the MS/MS spectra of

the assigned peptides were extracted by ProteinPilot, and only the proteins that fulfilled the following criteria were validated: (1) peptide mass tolerance lower than 10 ppm, (2) 99% of confidence level in peptide identification, and (3) complete b/y ions series found in the MS/MS spectrum. Only proteins quantified with at least two unique peptides were considered.

Bioinformatic analysis

The identification of significantly enriched structural complexes and biological processes from the deregulated proteins in synaptosomal fractions was performed using Metascape (Zhou et al., 2019). For the generation of the different heatmaps, after the identification of all statistically enriched terms (structural complex: GO/KEEG terms; biological process: GO/KEGG terms, canonical pathways, hallmark gene sets), cumulative hypergeometric p values and enrichment factors were calculated and used for filtering. The remaining significant terms were then hierarchically clustered into a tree based on Kappa-statistical similarities among their gene memberships. Then, a 0.3 kappa score was applied as the threshold to cast the tree into term clusters. The term with the best p-value within each cluster was selected as its representative term and displayed in a dendrogram. The heat map cells are colored by their p values and grey cells indicate the lack of enrichment for that term in the corresponding list. The interactomes of human and rat α-syn were obtained from the curated Biological General Repository for Interaction Datasets (BioGRID: https://thebiogrid.org; (Oughtred et al., 2019). The synaptic ontology analysis was performed using the SynGo platform (https://syngoportal.org; (Koopmans et al., 2019). The "brain expressed" background set was selected, containing 18,035 unique genes in total, of which 1104 overlap with SynGO annotated genes. For each ontology term, a one-sided Fisher exact test was performed to compare differential datasets and the "brain expressed" background set. The result is shown in the "*p* value" column. To find enriched terms within the entire SynGO ontology, a multiple testing correction using false discovery rate (FDR) was applied (*q* value column).

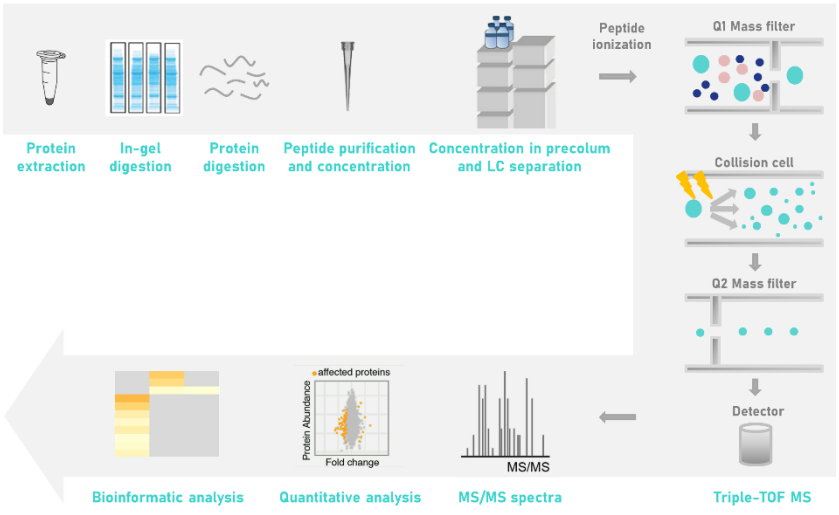

Figure 12. Proteomic study workflow

4. Histological characterization

4.1 Brain tissue collection

For immunohistological studies for the histological characterization (n = 4/group and time point), animals were deeply anesthetized with a mixture of oxygen and isoflurane (5%) and sacrificed at the corresponding p.i. end-time points (24 h, 72 h, 1, 2 and 4 weeks p.i.). Animals were perfused transcardially with 0.1 M phosphate-buffered saline (PBS; pH 7.4) followed by 4% paraformaldehyde (PFA) and 0.2% glutaraldehyde diluted in 0.1 M phosphate buffer (PB; pH 7.4). Brains were quickly removed and post-fixed in the same fixative solution for 24 h and then transferred to a cryoprotective solution containing 30% sucrose in PBS solution (pH 7.4) and subsequently freeze-thawed in isopentane to enhance the penetration of immunoreagents. Brains were serially sectioned using a vibratome (VT1000S, Leica Microsystems) into 50 µm-thick coronal slides that were stored in a preservative solution containing 0.03% sodium azide in PBS (pH 7.4) at 4°C until their use.

4.2 Immunohistochemistry

Immunohistochemical staining was performed on coronal free-floating sections to assess the integrity of the nigrostriatal pathway by tyrosine hydroxylase (TH) and dopamine transporter (DAT) as well as to assess the overexpression of hα-syn. Every sixth section throughout the entire SN_{pc} and striatum were selected for immunostaining. Three different protocols were optimized for the analyses of each protein and described in the following section.

Sections encompassing SN_{pc} and striatum were rinsed in PBS and endogenous peroxidase was quenched in 3% H_2O_2 in PBS for 10 min at RT. Sections were washed in PBS and preincubated with their corresponding blocking solution to inhibit unspecific staining and allow for tissue permeabilization, according to the different protocols:

(I) **TH**: 4% normal horse serum (NHS) and 0.2% Triton X-100 in PBS (PBS-T) incubated for 30 min RT.

(II) **DAT:** 10% normal rabbit serum (NRS) and 0.4% PBS-T incubated for 1 h at RT.

(III) **hα-syn:** 10% NHS and 0.2% PBS-T incubated for 1 h at RT.

Afterward, sections were incubated overnight with their corresponding primary antibody:

(I) mouse anti-TH in 1% NHS in PBS incubated at RT

(II) goat anti-DAT in 4% NRS in 0.2% PBS-T incubated at RT

(III) mouse anti-hα-syn in 10% NHS in 0.2% PBS-T incubated at 4°C

The following day, after washing in PBS, sections were incubated with their corresponding biotinylated secondary antibody:

(I) anti-mouse in PBS for 1 h and 30 min at RT

(II) anti-goat in 4% NRS in 0.2% PBS-T for 1 h at RT

(III) anti-mouse in 0.2% PBS-T for 1 h at RT

Afterward, all sections were washed and processed with the avidin-biotin complex diluted in PBS (ABC; 1:200 diluted in PBS) for 1 h and 30 min at RT. Finally, immunostaining was developed following a reaction with 0.02% 3,3-diaminobenzidine (DAB) and 0.001% H_2O_2 solution diluted in PBS for 4 min. All stained sections were mounted on glass superfrost slides (Thermo Fischer Scientific), dehydrated in ascending alcohol concentrations for 5 min (70%, 95%, 100%), cleared in xylene for 10 min and coverslipped with Eukitt® mounting medium.

All incubations were performed in agitation for enhancing and homogeneous penetration of immunoreagents. More details of the nature, origin and dilution of the primary and secondary antibodies are available in table 16 and table 17 of the annex section. In each experiment, negative controls with the tissue incubated without the primary antibody but including the secondary antibody were performed.

4.3 Optical microscopy and quantitative analysis

4.3.1 Stereological quantification of TH^+ neurons in the SN_{pc}

TH+ neurons in SN_{pc} were determined by the unbiased stereological method using an Olympus Bx61 motorized microscope (Olympus) equipped with a DP71 digital camera (Olympus) connected to an XYZ stepper (H101BX, PRIOR) and driven by CAST Visiopharm software (Visiopharm). The optical fractionator method (West, 1999) was used to estimate the total number of TH^+ cells in the SN_{pc} of each animal, as previously described (Jiménez-Urbieta et al., 2019; Rodríguez-Chinchilla et al., 2020). To sum up, this method is designed to provide estimates of the total number of neurons from thick sections sampled randomly with a systematic randomly sampled set of unbiased optical dissectors covering the entire nucleus. Thick sections provide the opportunity to observe cells in their full 3D extent and thus, allow for easy and robust cell classification based on morphological criteria. The optimal sampling parameters were determined previously in a pilot study (Jiménez-Urbieta et al., 2019) including a few animals to determine the number of sections to be analyzed and the number of optical dissectors within the sampled sections. Based on the tissue thickness and distribution of TH^+ labeled neurons the

optimal size of the optical dissectors employed was 4538.03 µm^2 with an x-y-step length of 213 µm and the dissector height was set to 20 µm (Drøjdahl et al., 2010). The estimation criteria to obtain an efficient stereological design was minimum counting of 150-200 neurons to ensure covering 10% of the total of the SN_{pc} for each hemisphere and animal according to the Gundersen method (Gundersen and Jensen, 1987; West, 1999).

A total number of 7 sections per animal covering the entire rostrocaudal extent of the SN_{pc} nucleus (between -4.30 mm y -6.72 mm from Bregma according to stereotaxic atlas) (Paxinos et al., 1985) were quantified. The SN_{pc} of each section was delineated using a 4x scanning objective (Olympus) employing external structures used as reference (Paxinos et al., 1985). Once the boundaries of the SN_{pc} were delimited, cell counting of TH^+ cells was performed using a 100x oil immersion objective (Olympus). A positive cell was defined as a nucleus covered and surrounded by the corresponding TH immunostaining and the size and shape criteria of the somas were kept uniform throughout the study. Only the somas that were located inside the counting frame or those that touched the inclusion lines were included in the quantification. All somas that were out of the grid or on the bottom and left edges were discarded.

Estimation of the total number (N) of TH^+ cells in the SN_{pc} was calculated indirectly using the following equation:

$$N = \Sigma Q \times \frac{t}{h} \times \frac{1}{asf} \times \frac{1}{ssf}$$

Where ΣQ is the total number of counted particles, t is the average thickness of each section, h is the height of the optical dissector, *asf* is the sampling fraction of the area and *ssf* is the sampling fraction of the sections. Estimated populations for the SN_{pc} of each hemisphere were averaged across all animals for each group and time point (Gundersen and Jensen, 1987; West, 1999).

4.3.2 Relative optical density quantification

<u>hα-syn immunoreactivity in the SN_{pc}</u>

In order to quantify the representative surface expression of hα-syn in the SN_{pc}, 3 representative sections of the SN_{pc} per animal (approx. –5.30 mm, –5.60 mm and –6.00 mm from Bregma according to stereotaxic atlas) (Paxinos et al., 1985) were analyzed. Images of all sections were acquired using a Zeiss Axioimager M1 microscope (Zeiss) with 5x objective (Zeiss) using autowhite option and the same acquisition parameters for all sections. Images were

converted to 8-bit greyscale images and the SN_{pc} was delimitated according to the stereotaxic atlas (Paxinos et al., 1985). Relative optical density (ROD) of grey levels of hα-syn immunoreactivity were obtained using ImageJ software (NIH) according to the following formula (Tatulli et al., 2018; Vermilyea et al., 2019).

$$ROD = log\left(\frac{basal\ gray\ level}{signal\ gray\ level}\right)$$

The mean ROD values were averaged across all animals for each group and time point.

TH, DAT and hα-syn immunoreactivity in the striatum

The extent of expression of TH, DAT and hα-syn markers was determined by ROD quantification. For each marker, three striatal sections per animal (approx. +1.60 mm, +1.00 mm and -0.26 mm from Bregma according to stereotaxic atlas) (Paxinos et al., 1985) were analyzed. Images of all sections were acquired using a Zeiss Axioimager M1 microscope (Zeiss) with a 2.5x scanning objective (Zeiss) using the same acquisition parameters for all sections. ROD values of immunoreactivity for whole striatum (Caudate-Putamen; CPu) were obtained using ImageJ software (NIH) by calculating the average grey value of 8-bit grayscale images in the delineated CPu. The unspecific staining was subtracted calculating the ROD of a small square placed in the *corpus callosum* of each section. The ROD values of each CPu were averaged across all animals for each group and time point (Rodríguez-Chinchilla et al., 2020).

4.4 Immunofluorescence

Immunofluorescence staining was performed on coronal free-floating sections of the striatum in order to assess the nature of electroclear vesicles observed within dopaminergic fibers in the electron microscopy study (see section 5.3.1). Two different protocols were optimized for the analyses of several proteins involved in autophagic and endocytic pathways.

(I) Triple immunofluorescence for TH, LC3B and Lamp1

Triple immunofluorescence for TH, microtubule-associated proteins 1A/1B light chain 3B (LC3B) and anti-lysosomal-associated membrane protein (Lamp1) was performed as previously described with slight modifications (Du et al., 2018). Firstly, striatal sections were permeabilized with 0.3% PBS-T for 10 min at RT. After blocking with 10% NGS for 1 h, sections were incubated overnight with rabbit anti-TH, mouse anti-LC3B, and rat anti-Lamp1 antibodies in PBS at 4 °C. The following day, sections were washed three times in PBS and were incubated with their

corresponding secondary antibodies anti-mouse, anti-rabbit and anti-rat conjugated to Alexa Fluor 633, 488 and 546 fluorochromes, respectively, and diluted in PBS (1:500) for 1 h at RT protected from light. Cell nuclei were counterstained with 4,6-diamidino-2-phenylindole (DAPI; 1:10.000; Sigma) diluted in PBS for 10 min and after the washes with PBS sections were mounted on superfrost slides (Thermo Fisher Scientific) with Vectashield mounting medium (Vector Laboratories) and coverslipped.

(II) Triple immunofluorescence for TH, Rab5 and Rab7

Triple immunofluorescence for TH, Rab5 and Rab7 was performed as previously described with slight modifications (Rao et al., 2011). First, striatal sections were blocked in 4% normal donkey serum (NDS) and 4% BSA and permeabilized in 0.3% PBS-T for 1 h at RT. Next, sections were incubated with the primary antibodies, mouse anti-TH, goat anti-Rab5 rabbit anti-Rab7 diluted in 0.3% PBS-T with 4% NDS for 48 h at 4°C. The following day, sections were washed in PBS and were incubated with their corresponding secondary antibodies anti-goat, anti-rabbit and anti-mouse conjugated to Alexa Fluor 488, 567 and 647 fluorochromes, respectively, and diluted in PBS for 1 h and 30 min at RT protected from light. Cell nuclei were counterstained with DAPI diluted in PBS for 10 min and after the washes in PBS, sections were mounted on superfrost slides (Thermo Fisher Scientific) and coverslipped with Vectashield mounting medium (Vector Laboratories).

All incubations were performed in agitation for enhancing and homogeneous penetration of immunoreagents. More details of the nature, origin and dilution of the primary and secondary antibodies are available in table 16 and 17 of the annex section. In each experiment, negative controls with the tissue incubated without the primary antibody but including the secondary antibody were performed.

4.5 Confocal microscopy

The slides processed by immunofluorescence were visualized by a Zeiss LSM 800 confocal laser microscope (Carl Zeiss) with a Plan-Apochromat 63x/1.4 numerical aperture oil-immersion objective (Carl Zeiss). Fluorescence was visualized by combining the following laser set: λ = 350-488-568-633 nm. Image acquisition parameters were optimized for each marker and were maintained constant for all the images. Images of the dorsal striatum (approx. +0.2 mm from Bregma according to stereotaxic atlas) were acquired using ZEN Imaging Software (Carl Zeiss). The image size was 608 x 371 pixels with a field of view of 82.53 x 50.36 µm.

5. Ultrastructural study

5.1 Brain tissue collection

Brains were collected as described for immunohistological studies (described in 4.1) (n = 6 in EVV group; n = 4 in hα-syn group per time point).

5.2 Tissue processing and Electron Microscopy

The tissue processing and image acquisition of the electron microscopy study were carried out in the laboratory of the physiopathology of parkinsonian syndromes at the "*Institut des maladies neurodégénératives*" of the University of Bordeaux (Bordeaux, France) with the collaboration of the group led by Dr. Erwan Bezard.

To study synaptic ultrastructural changes of the striatum, striatal coronal sections were processed for pre-embedding immunoperoxidase labeling as described before with some modifications (Charron et al., 2011)(Figure 13). Firstly, sections were processed with the previously described TH immunohistochemistry staining protocol (see 4.2.I). After immunodetection, the sections were washed twice in 0.1 M PB and were post-fixed in 0.5% osmium tetroxide diluted in 0.1 M PB for 15 min. After two washes in 0.1 M PB, sections were dehydrated in an ascending series of ethanol dilutions that also included 70% ethanol with 1% uranyl acetate (70%, 70% with 1% uranyl acetate, 96% and 100% ethanol) for 10 min each. The sections were then incubated in ethoxypropanol for 15 min and were embedded in epoxy resin (Durcupan™ ACM) at RT for 2 h prior to polymerization at 60 °C for 48 h. Once the sections and resin were dry, 0.1 µm semi-thin sections were obtained in a Reichert Ultracut S ultramicrotome

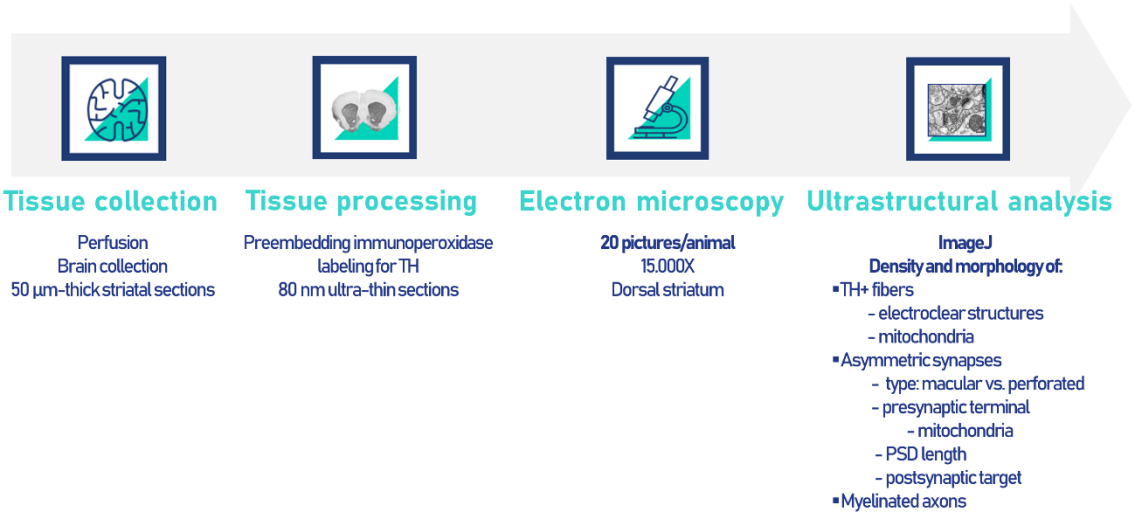

Figure 13: Ultrastructural study workflow with fundamental details.

(Reichert technologies). Afterward, three to five ultra-thin sections of 80 nm from the superficial planes were cut with the ultramicrotome, isolated in nickel grids. Finally, sections were contrasted with 2.5% lead citrate for 20 min and were examined with a transmission electron microscope (TEM; Hitachi H-7650 microscope) equipped with a SC1000 Orius CCD camera (Gatan). Digital images were obtained randomly from the dorsal striatum (approx. +0.2 mm from Bregma according to stereotaxic atlas)(Paxinos et al., 1985) at a final magnification of 15.000x using the Metamorph software (Molecular Devices). Images were obtained avoiding the blood vessels, occasional grouped areas of myelination, and the astroglial swelling to ensure that predominantly neurons and synapses were analyzed. Image resolution in the *xy* plane was 3.4 nm/pixel and image size was 3284 x 2600 pixels. The area per field of view was 104.35 μm^2.

5.3 Electron microscopy image analysis

Twenty images per animal from the dorsal striatum obtained by TEM were analyzed using ImageJ software (NIH) to assess different ultrastructural parameters. All the values calculated were averaged across all animals for each group and time point.

5.3.1 Ultrastructural parameters of TH^+ fibers

TH^+ fibers were defined as DAB immunostained electrodense structures. All the TH^+ fibers found were manually traced and their density, area, perimeter and area/perimeter ratio were measured. A total number of 9.965 TH^+ fibers were analyzed.

Additionally, density, size measurements (area and perimeter) and shape descriptors of all the mitochondria found inside TH^+ fibers were measured by manually tracing clearly identifiable mitochondria. A total number of 1.631 mitochondria were analyzed. Morphological shape measurements included the following parameters: aspect ratio (AR), computed as [(major axis)/(minor axis)] and reflects the length-to-width ratio; circularity [4π·(surface area/perimeter)] and roundness [4·(surface area)/(π·major axis)], which are two-dimensional indexes of sphericity with values of 1 indicating perfect spheroids; and Feret diameter, which represents the longest distance (µm) of a selected mitochondrion (Picard et al., 2013). Furthermore, quantification of mitochondrial ultrastructural defects was analyzed based on its ultrastructural appearance and classified into one of the following categories: intact mitochondria, with normal appearing cristae; damaged mitochondria, with either swollen or irregular cristae or with crystalline intermembrane inclusions; and degenerating mitochondria, which consisted in a mitochondrion inside an autophagic vesicle (mitophagy) or a mitochondrion

fused with an electroclear structure (Sisková et al., 2010). Lastly, density and size measurements of electroclear internal structures found inside TH^+ fibers were measured by manually tracing their boundaries. Electroclear structures were defined as a discernible electron-lucent lumen that contrasted with the electrodense DAB immunostaining and resembled autophagic structures as previously described (Jung et al., 2019; Martinet et al., 2014).

5.3.2 Ultrastructural parameters of asymmetric synapses

Asymmetric synapses (AS) were defined by a presynaptic terminal containing spherical synaptic vesicles adjacent to an electron-dense PSD and only clearly identifiable AS were quantified. A total number of 7.802 AS were analyzed. AS were classified into two categories according to the shape of their PSD, as previously described (Hara et al., 2012). Macular synapses, when contained a continuous PSD, and perforated synapses, when contained two or more physically discontinuous PSDs. The density and PSD length from both types of AS were measured. Additionally, based on the postsynaptic targets, synapses were further classified as axospinous synapses (synapses contacting on dendritic spines) and axodendritic synapses (synapses contacting on dendritic shafts) (Domínguez-álvaro et al., 2018). Finally, size and morphological parameters (area, perimeter and area/perimeter ratio) of presynaptic terminals forming AS and the mitochondria inside these terminals were also measured. A total number of 2.914 clearly identifiable presynaptic terminals forming AS were analyzed.

5.3.2 Ultrastructural parameters of cross-sectioned myelinated axons

Cross-sectioned myelinated axons were defined by an electroclear circular shape axoplasma surrounded by an electrodense myelin sheat and their density and morphology were quantified. Morphological measurements included axon area, diameter, eccentricity and G-ratio. G-ratio was calculated by dividing the axonal diameter by the total fiber diameter. Both diameters were calculated by using the Feret diameter measurements. The G-ratio is a fundamental property of white matter relating to the functional and structural index of optimal axonal myelination (Chomiak and Hu, 2009). Eccentricity was calculated with the following formula: $e = \frac{c}{a} = \sqrt{1 - \left(\frac{b}{a}\right)^2}$, were *b* is the value corresponding to the mayor axis and *a* the one corresponding to the minor axis. The mean eccentricity is a measurement of how much a section deviates from being circular. The eccentricity of a circle is zero and the eccentricity of an ellipse is greater than zero but less than one (Abdollahzadeh et al., 2019). For each group at least 70 randomly selected axons with compact morphology were analyzed.

6. 3D morphometric study of dendritic spines

6.1 Brain tissue collection

For high-resolution morphometric and the corresponding immunohistological studies (n = 7/group), experimental groups (EVV or hα-syn) at 4 weeks p.i. time point were used. Animals were deeply anesthetized with a mixture of oxygen and isoflurane (5%) and perfused transcardially with 1% PFA in 0.1 M PB (pH 7.4) for 1 min followed by 4% PFA in 0.1 M PB (pH 7.4) for 11 min (40 ml/min flow rate). Brains were quickly removed and post-fixed in 4% PFA in 0.1 M PB (pH 7.4) solution with agitation for 2 h at 4°C. Finally, brains were transferred to a preservative solution containing 0.1% sodium azide in PBS (pH 7.4) and were stored at 4°C until their use. The striatum was serially sectioned on a vibratome (VT1000S, Leica Microsystems) into a systematic series of one 300 µm-thick coronal slice followed by three 50 µm-thick slices. Specifically, the posterior 300 µm-thick sections of the striatum (approx. + 0.2- + 0.7 mm from Bregma) (Paxinos et al., 1985) were used for single-cell intracellular injections and the 50 µm-thick sections were used for immunohistochemical studies in order to confirm the lesion. The whole SN_{pc} was serially sectioned into 50 µm-thick sections for further immunohistochemical studies.

6.2 Single-cell intracellular microinjections

Single-cell microinjections and the dendritic spine imaging were carried out at the New York State Psychiatric Institute at Columbia University (New York, USA) due to a 6 months research stay of the Ph.D. student in the laboratory of the developmental origins of resilience led by Dr. Dani Dumitriu.

Intracellular injections of striatal SPNs with Alexa Fluor 568 hydrazide were performed according to previously published methods (Dumitriu et al., 2011; Motley et al., 2018). 300 µm-thick sections were counterstained with DAPI to permit visualization of the soma using epifluorescence under a UV filter in a fluorescent microscope (Nikon 230083). Sections were mounted on nitrocellulose filter paper and immersed in 0.1 M PBS. Using DAPI as a staining guide, SPNs were identified and impaled with sharp micropipettes and filled with Alexa Fluor 568 hydrazide (Thermo Fischer Scientific) using 1–20 nA direct current for 3–5 min until the dye had filled distal processes. Ten neurons (5 from each hemisphere) per section were microinjected, spaced sufficiently apart so that dendritic arbors did not overlap. One to two sections were used per animal, representing a random sampling of SPNs throughout the dorsal

striatum. Finally, sections were mounted on glass slides with VectaShield mounting medium (Vector Laboratories) and covered with number 1.5 cover glasses (Corning).

6.3 High-resolution confocal microscopy

High-resolution confocal microscopy was used for dendritic spine imaging. An upright Leica TCS SP8 confocal microscope (Leica Microsystems) equipped with a resonance scanner was used. Firstly, a confocal tile image of the section was taken at 10x magnification to create a neuron map (Figure 15A). All microinjected neurons per animal were included for the quantitative spine analysis. The selected neurons presented dendritic segments that were completely filled as evidenced by their well-defined endings. A confocal *z* stack image of each neuron was taken at 20x magnification, which was used for an unbiased but systematic selection of segments to be imaged at high resolution. These neuron map images were intentionally low resolution such that segments, but not spines, were visible, so as not to bias the experimenter in the choice of segments to be imaged at high magnification. Concentric rings were drawn around the soma at 50 µm and 100 µm from the center. Secondary or tertiary dendritic segments were sampled if they crossed between 50 and 100 µm from the soma (Figure 15B). Additionally, only dendritic segments that were parallel with the section were imaged, and bifurcations, large fluctuations in the dendritic diameter and the first and last 10% of dendritic segments were avoided. Thirty dendritic segments per animal were sampled, with no more than three segments taken from the same neuron (Figure 15C). Confocal *z* stack images of each segment were taken at 63x magnification with a 63x 1.4 numerical aperture oil-immersion objective (Leica Microsystems). Confocal *z* stacks of 100–300 images were acquired with an *x*, *y* resolution of 0.04 µm and a *z* step of 0.04 µm. All *z* stacks included at least 1 µm above the most superficial spine and 1 µm below the deepest spine to ensure that all spines were completely imaged.

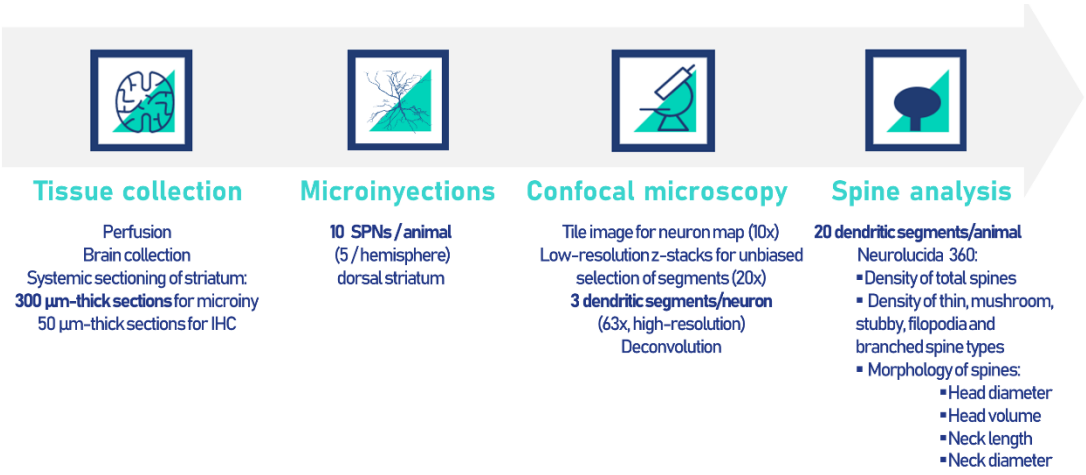

Figure 14. 3D morphometric study workflow with fundamental details.

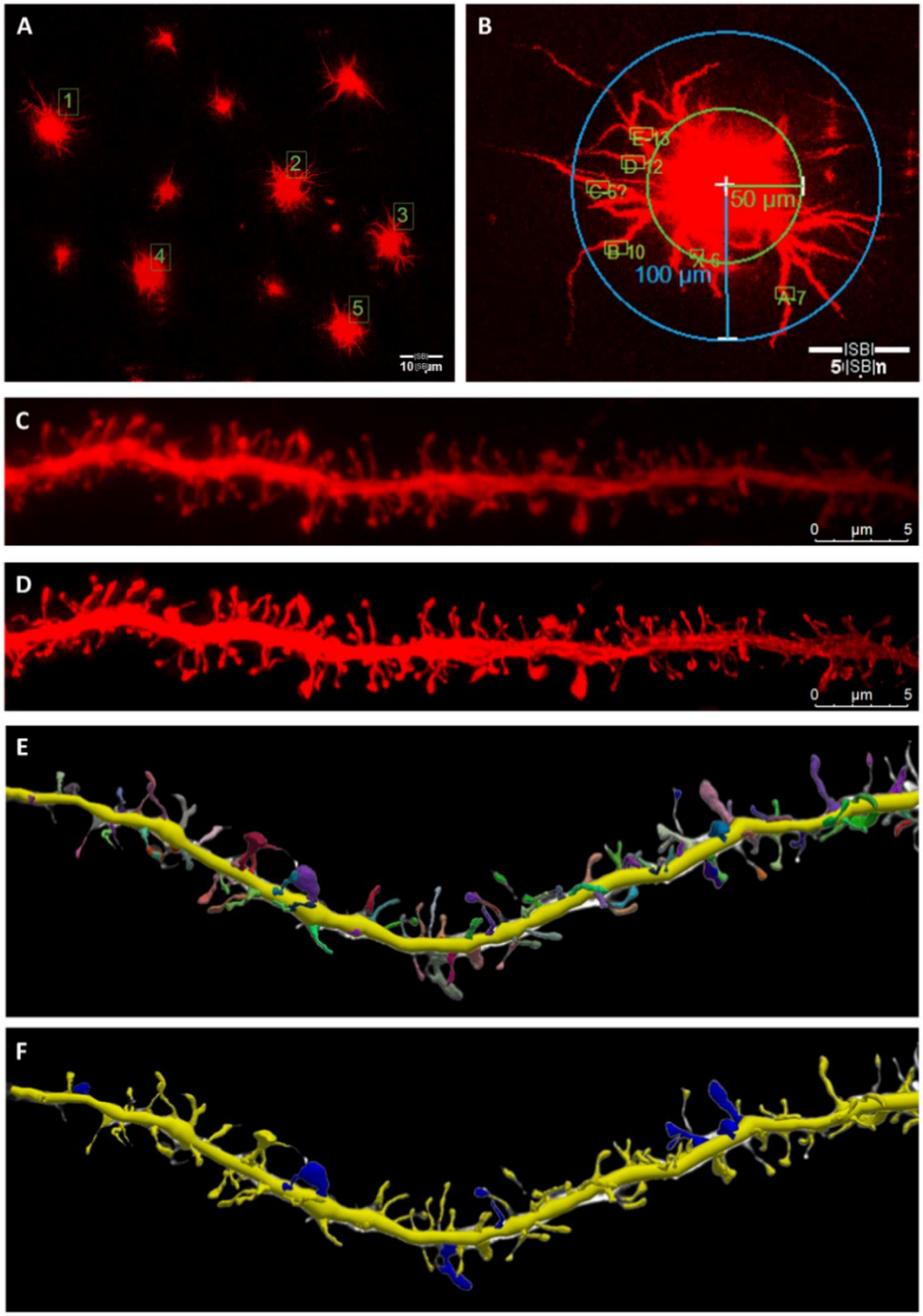

Figure 15: Representative photomicrographs of microinjected SPNs. (**A**) 5 properly microinjected neurons/hemisphere were selected at 10X magnification. (**B**) In order to be unbiased low-resolution images were obtained at 20X magnification and concentric circles were drawn at 50 and 100 µm from the soma. Dendritic segments that were between both circles were selected for high-resolution imaging (3 dendritic segments/neuron). (**C-F**) Representative high-resolution dendritic segments at 63X magnification (**C**) before and (**D**) after deconvolution and (**E-F**) when analyzed at Neurolucida 360 software. (**E**) Neurolucida 360 semi-automatically detects dendritic spines. (**F**) It further classifies spines into the three major morphometric types: thin (yellow), mushroom (blue), stubby and filopodia (not present in the picture).

Alexa Fluor 568 was excited using a 561 nm wavelength with an emission filter of 568–712 nm, a pinhole size of 0.5 airy units, a digital zoom of 3.75, a gain of 10%, an averaging of 8, and a pixel dwell time of 12 ns. The final resolution of the *z* stacks was 1232 x 200 pixels. The length of each segment imaged was determined by the parameters of *x* resolution (1232 pixels), the magnification (63x), and the digital zoom (3.75x), resulting in a FOV that was 49.21 µm in length. The exact length of each segment included was between 49 and 60 µm, depending on the curvature of the segment in the field of view. To achieve the best signal possible, the laser power was set to maximize the dynamic range such that, for a given segment, there were only a few pixels of maximum signal intensity on one spine and only a few pixels of minimum signal intensity in the FOV. Laser power ranged from 0.1 to 3.0. Photobleaching was not detected with these laser powers. Images were deconvolved with Lightning software (Leica Microsystems) to correct the optical distortion inherent in all light microscopic imaging systems and thus, improve contrast and resolution for more accurate measurements (Dumitriu et al., 2011) (Figure 15D).

6.4 Dendritic spine analysis

Images were analyzed using Neurolucida 360 software (MBF Bioscience) for automatic 3D detection and analysis of dendritic spines. Spines were automatically detected, and the experimenter blinded to the condition manually corrected the errors in order to verify that all spines had been appropriately identified (Figure 15E, F). All spine measurements (total number of 26.642 spines) were performed in 3D from the *z* stacks obtained from each segment and described in 6.3. The morphometric parameters analyzed for each spine included: spine density (the number of spines on a given segment divided by the segment length), spine head volume and diameter and neck length and diameter. Neurolucida 360 further classified spines into the four major morphometric types: thin, mushroom, stubby and filopodia (Figure 16), according to criteria defined in previous studies (Dumitriu et al., 2011; Motley et al., 2018; Rodriguez et al., 2008).

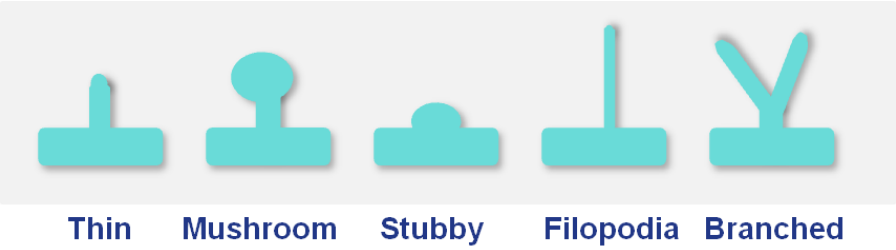

Figure 16. Schematic representation of dendritic spine types: thin, mushroom, stubby, filopodia and branched.

Spines were automatically classified as thin when the head diameter was less than 0.35 µm and the length-to-head ratio was 2.5, stubby when the length-to-head ratio was 1.1, mushroom when the head diameter was higher than 0.35 µm and filopodia when their length was higher than 3 µm. After automatic classification of spines, the errors, if present, were manually corrected by the experimenter and alternate complex types (e.g., branched) were also assigned. Branched spines (occasionally found) were classified by multiple spine heads attached to a single spine neck. Average from dendritic segments analyzed in each cell were obtained using MATLAB script (Mathworks). Afterward, data were grouped per animal and corresponding group (EEV or hα-syn).

7. Statistical analysis

All statistical analyses were performed using GraphPad Prism 5.0 software (GraphPad Sofware Inc.). Data distribution for normality was assessed using the Kolmogorov-Smirnov (K–S) test and variance equality by Levene's test. For behavioural tests and data comparison within the same animals over time Wilcoxon test or Friedman test were used. For pair-wise comparisons between means of hα-syn and EVV groups, unpaired t-test or Mann–Whitney test was performed, when data were parametric or non-parametric, respectively. For multiple comparisons between means of hα-syn and EVV groups One-way ANOVA followed by Bonferroni´s *post-hoc* test or Kruskal-Wallis test followed by Dunn´s *post-hoc* test were used, when data were parametric or non-parametric, respectively. For multiple comparisons between means of different time points within hα-syn group, Kruskal-Wallis test followed by Dunn´s *post-hoc* test was used, as data were non-parametric. Group data are represented in graphs as mean ± SEM and statistically significant differences were set at $p < 0.05$.

RESULTS

This doctoral thesis has been carried out by different experiments to address the objectives, as the results of the experiments were known. In the experiments conducted in this doctoral thesis, the time points for evaluation are different. This was chosen based on the result of the previous studies and is described for each study in the following section.

1. Motor and histological evaluation of the dopaminergic degeneration

1.1 Experimental design

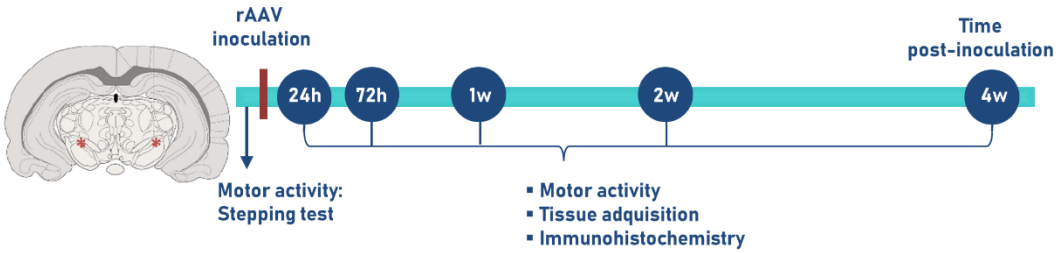

Figure 17: Experimental design for motor and histological evaluation. Animals were inoculated with either rAAV-hα-syn or rAAV-EVV bilaterally in the SN_{pc} and they were perfused at their corresponding final time point (24 h, 72 h, 1, 2 and 4 weeks p.i.) after performing the stepping test. Brains were removed and coronal slices were acquired for immunohistochemical studies.

To study the temporal sequence and motor behaviour associated with the overexpression of hα-syn and the dopaminergic degeneration in the SN_{pc} and striatal axonal terminals, and the relation among them, animals were inoculated with rAAV-hα-syn and were sacrificed at different time points post-inoculation (p.i.): 24 h, 72 h, 1, 2 and 4 weeks. For the control group, animals were inoculated with rAAV-EVV and only one time point (4 weeks p.i.) was studied to reduce the number of used animals (Figure 17).

1.2 Evaluation of motor activity

To evaluate forelimb bradykinesia the stepping test was performed in the hα-syn group before surgery (basal) and 24 h, 72 h, 1, 2, 3 and 4 weeks p.i. No differences in the number of adjusting steps were found relative to their basal measurement or over time within subgroups (Figure 18).

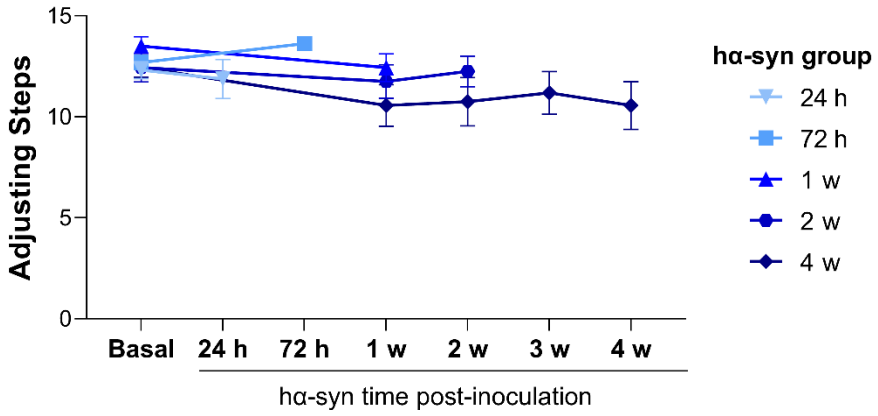

Figure 18. Evaluation of the motor activity in the hα-syn group. Values represent the average number of adjusting steps of both forelimbs and are presented as the mean ± SEM. Friedman or Wilcoxon test within each subgroup. n = 4 for each time point evaluated.

1.3 Evaluation of the dopaminergic degeneration

1.3.1 hα-syn overexpression in the SN_{pc} and the striatum

In the SN_{pc}, inoculation of rAAV-hα-syn resulted in a robust and persistent expression of hα-syn since 72 h p.i. onwards that expanded progressively and changed to a more diffuse pattern in later time points (Figure 19A, B, D). Of note, hα-syn was expressed in nigral cell bodies (Figure 19D). Hα-syn expression reached a significant increment at 1 week p.i. ($p < 0.01$ vs. 24 h p.i.), 2 weeks p.i. ($p < 0.01$ vs. 24 h p.i. and $p < 0.05$ vs. 72 h p.i.) and 4 weeks p.i. ($p < 0.01$ vs. 24 h p.i. and $p < 0.05$ vs. 72 h p.i.) (Figure 19B).

In the striatum, hα-syn expression was detected since 1st week p.i. ($p < 0.05$ vs. 24 h and $p < 0.01$ vs. 72 h p.i.) reaching its highest level at 2 weeks p.i. ($p < 0.01$ vs. 24 h and 72 h p.i.) and slightly decreasing at 4 weeks p.i. but maintaining significant levels ($p < 0.05$ vs. 72 h) (Figure 19A, C, E). Striatal fibers expressing hα-syn appeared pathological with dystrophic terminal swellings and thickening of fibers that resemble Lewy-like neurites at 4 weeks p.i. (Figure 19E).

No hα-syn expression was observed in either the SN_{pc} or the striatum in the EVV control group (Figure 19A).

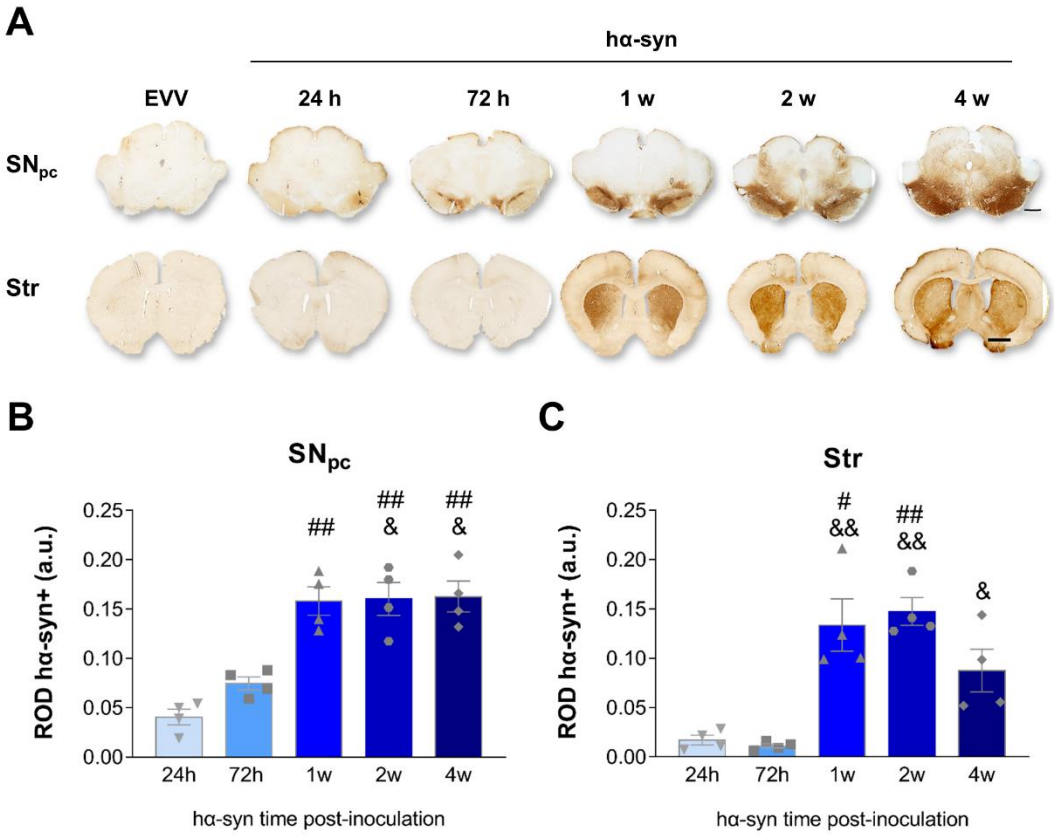

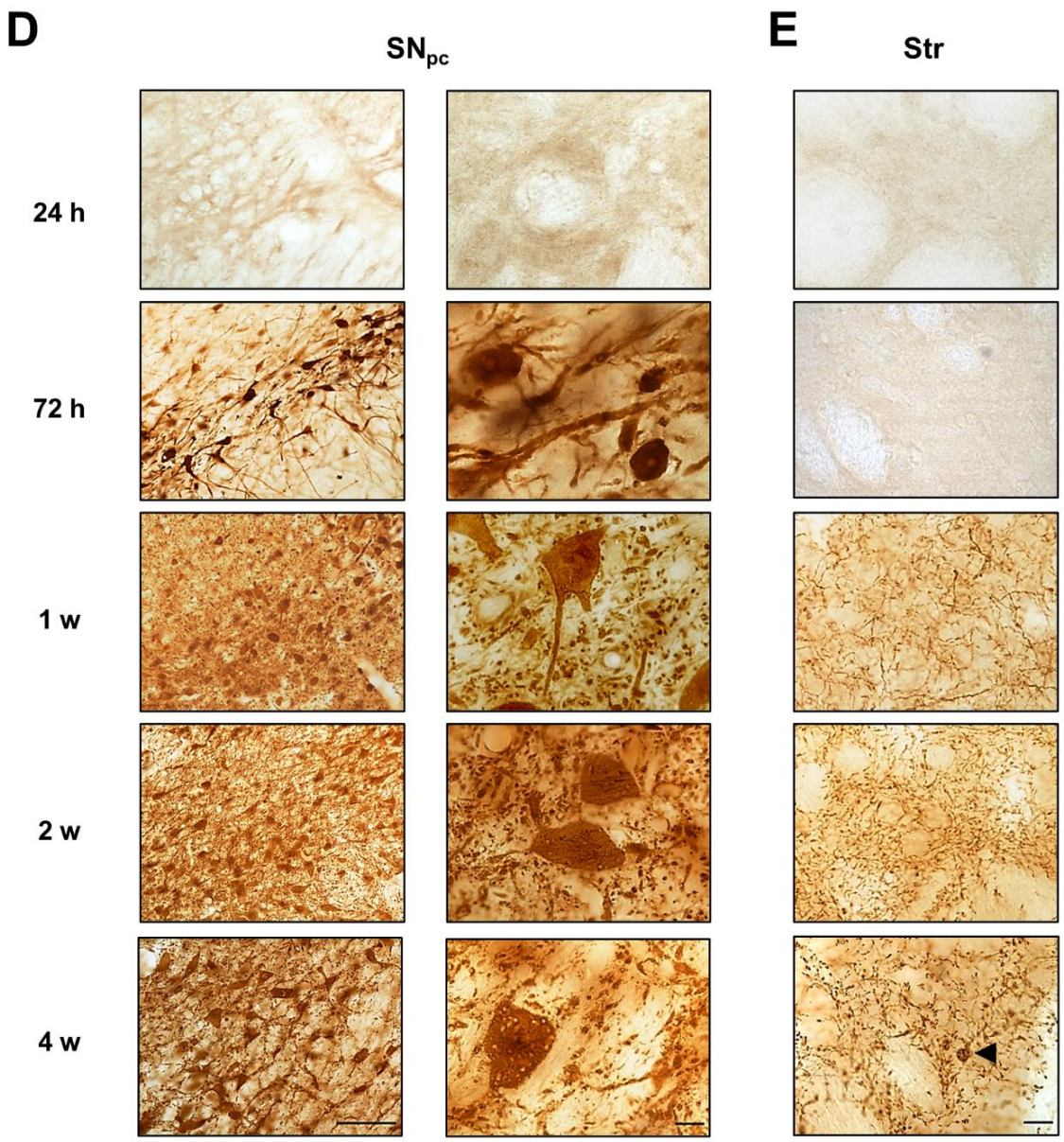

Figure 19: hα-syn overexpression in the nigrostriatal pathway. (**A**) Representative photomicrographs for hα-syn staining in coronal sections of the SN_{pc} and the striatum from EVV group and hα-syn group at 24 h, 72 h, 1, 2 and 4 weeks (w) p.i. Scale bar, 2 mm. (**B**) Relative optical density (ROD) analysis of hα-syn expression in the SN_{pc} and (**C**) striatum from the hα-syn group at the corresponding time points p.i. Values are presented as the mean ± SEM. Kruskal-Wallis followed by Dunn´s *post-hoc* test: # $p < 0.05$, ## $p < 0.01$ vs. 24 h p.i.; & $p < 0.05$, && $p < 0.01$ vs. 72 h p.i. (**D**) Representative SN_{pc} higher magnification photomicrographs for hα-syn staining. Scale bars, 100 µm and 10 µm, respectively. (**E**) Representative striatal high magnification photomicrographs for hα-syn staining. Pathological hα-syn$^+$ terminal swellings (black arrowhead) and thickening of fibers were observed at 4 weeks p.i. Scale bar, 10 µm. n = 4 for each time point evaluated.

1.3.2 Quantification of the dopaminergic neuronal loss in the SN_{pc}

In the hα-syn group, significant reduction in the number of nigral TH^+ dopaminergic neurons was observed at 4 weeks p.i. (31% reduction, $p < 0.05$ vs. EVV group and vs. 24 h and 1 w p.i.; $p < 0.01$ vs. 72 h p.i. (Figure 20).

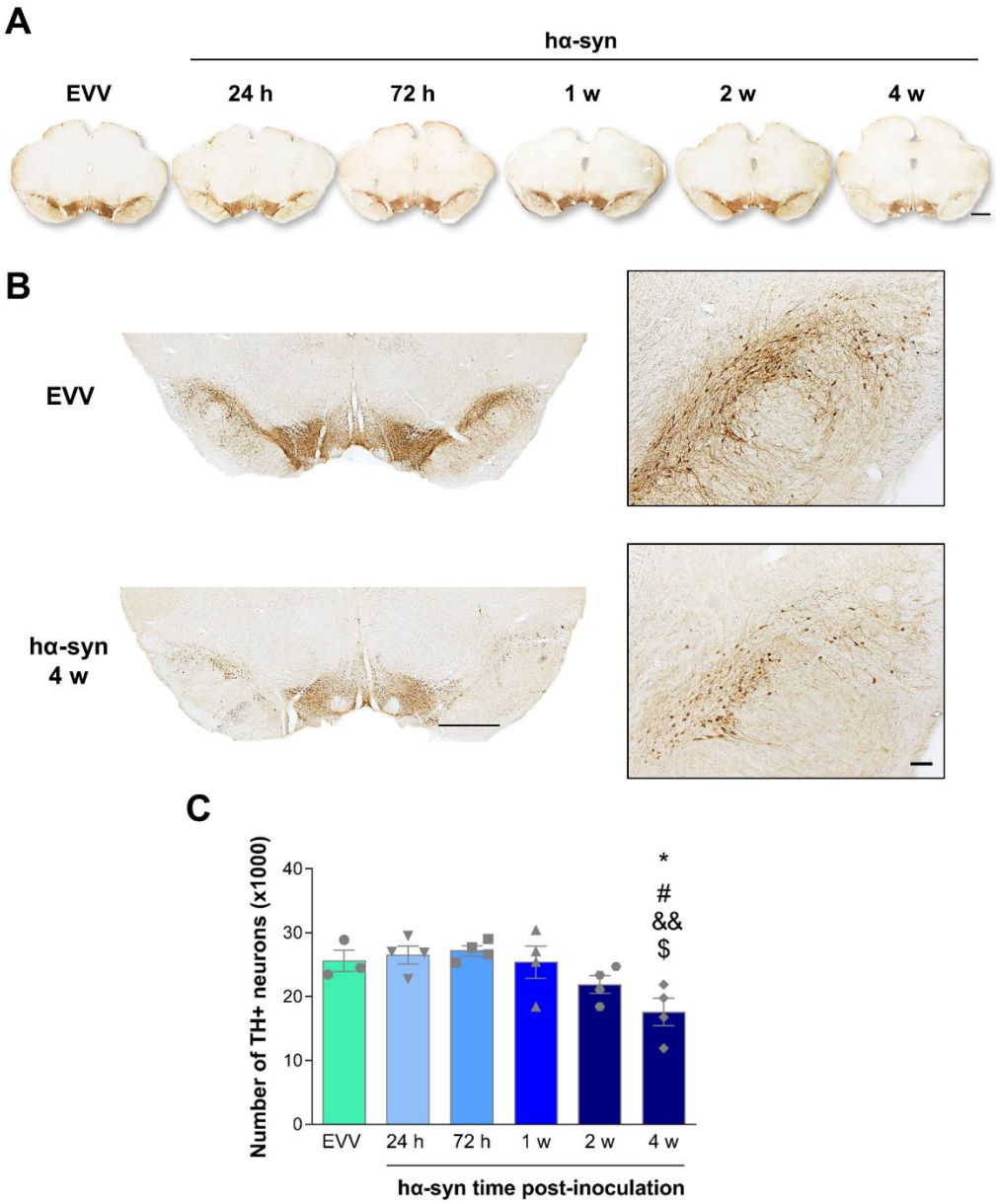

Figure 20: **TH expression in the SN_{pc}**. (**A**) Representative SN_{pc} photomicrographs for TH staining in coronal sections from EVV group and hα-syn group corresponding to 24 h, 72 h, 1, 2 and 4 weeks p.i. Scale bar, 1 mm. (**B**) Representative high magnification photomicrographs of TH staining in the SN_{pc} comparing EVV and hα-syn groups at 4 w p.i. Scale bars, 1 mm and 100 µm, respectively. (**C**) Stereological quantification in the SN_{pc} for TH^+ neurons of EVV and hα-syn groups. Values are presented as the mean ± SEM. Kruskal-Wallis followed by Dunn´s *post-hoc* test: * $p < 0.05$ vs. EVV group; # $p < 0.05$ vs. 24 h p.i.; && $p < 0.01$ vs. 72 h p.i.; $ $p < 0.05$ vs. 1 w p.i. n = 4 for each time point evaluated, except for EVV (n = 3) due to SN_{pc} tissue technical damage.

1.3.3 Quantification of the expression of TH$^+$ and DAT$^+$ dopaminergic fibers in the striatum

Intranigral inoculation of rAAV-hα-syn resulted in a progressive reduction of striatal dopaminergic fibers (Figure 21A, B), evidenced by a significant reduction of TH expression at 2 weeks p.i. (25% reduction; $p < 0.05$ vs. EVV group and 24 h p.i.) and 4 weeks p.i. (48% reduction, $p < 0.01$ vs. EVV group and 24 h p.i.; $p < 0.05$ vs. 72 h p.i and 1 w p.i.) (Figure 21C). A progressive reduction in striatal DAT expression was also observed at 2 w p.i. (22% reduction, $p < 0.05$ vs. EVV group and 24 h p.i.) and 4 w p.i. (55% reduction, $p < 0.05$ vs. EVV group and 1 w p.i., $p < 0.001$ vs. 24 h p.i. and 72 h p.i; Figure 21B, D).

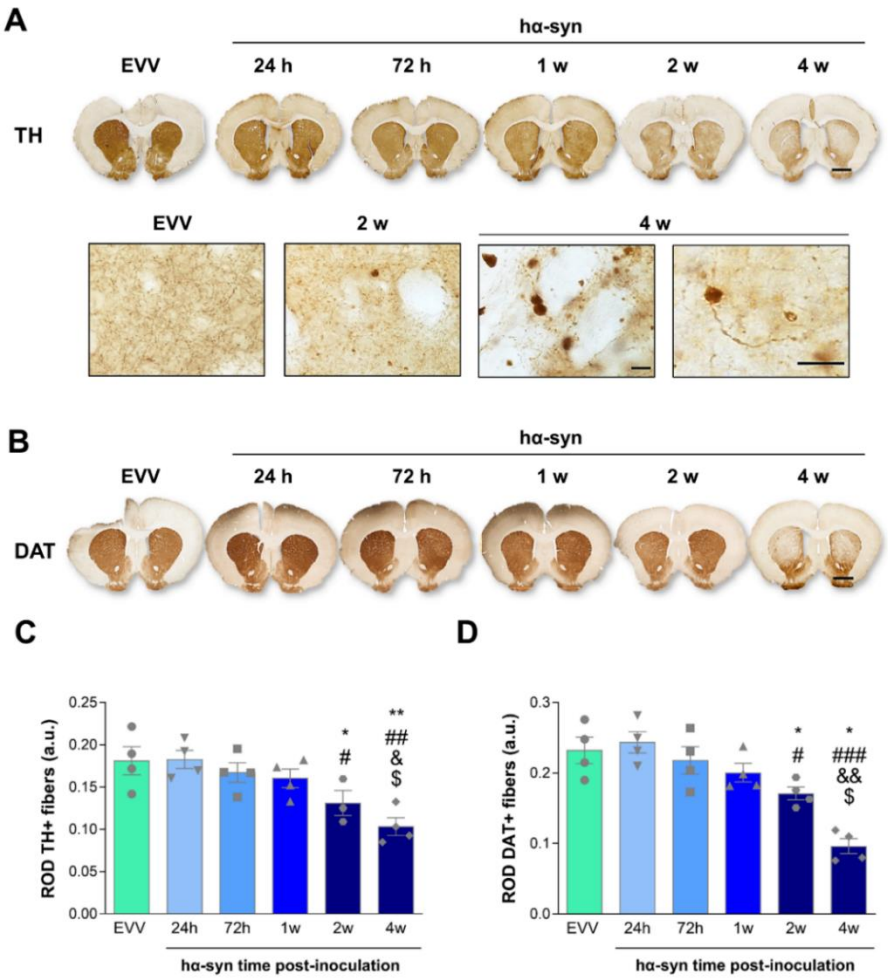

Figure 21: TH and DAT expression in the striatum. (**A**) Representative striatal photomicrographs for TH staining and (**B**) DAT staining in coronal sections from EVV and hα-syn groups at 24 h, 72 h, 1, 2 and 4 weeks p.i., scale bar 2 mm. Higher magnification photomicrographs of TH staining are shown in the lower part of A. Scale bars, 10 µm. (**C**) Relative optical density (ROD) values of TH and (**D**) DAT expression in the EVV and hα-syn groups. All values are presented as mean ± SEM. Kruskal-Wallis followed by Dunn´s *post-hoc* test: * $p < 0.05$ and ** $p < 0.01$ vs. EVV group; # $p < 0.05$, ##· $p < 0.01$ and ### $p < 0.001$ vs. 24 h; & $p < 0.05$ and && $p < 0.01$ vs. 72 h; $ $p < 0.05$ vs. 1 w p.i. n = 4 for each time point evaluated.

2. Bioenergetic and proteomic profiling of striatal synaptosomes

2.1 Experimental design

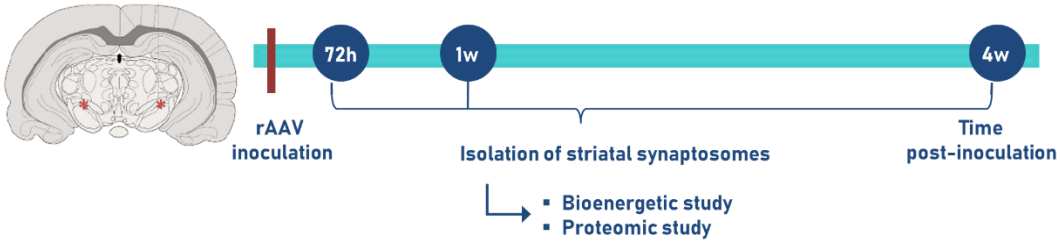

Figure 22: Experimental design of the functional studies. Animals were inoculated with either rAAV-hα-syn or rAAV-EVV bilaterally in the SN_{pc} and they were sacrificed at their corresponding final time point (72 h, 1 week and 4 weeks p.i.). Striatal tissue was dissected from the brain and after isolation of synaptosomes, bioenergetic and proteomic studies were performed.

In order to study the temporal sequence of the synaptic functionality in isolated striatal synapses, bioenergetic and proteomic studies were conducted. For this purpose, animals were inoculated with either rAAV-hα-syn or rAAV-EVV and the studies were undertaken at three representative p.i. time points of hα-syn overexpression in both groups: 72 h, 1 week and 4 weeks (Figure 22).

The choice of these p.i. time points was because of the following reasons: 72 h represents the beginning of hα-syn overexpression in the SN_{pc}, 1 week represents the onset of hα-syn overexpression in the striatum and 4 weeks represents the point of significant neurodegeneration of dopaminergic neurons and dopaminergic terminals.

2.2 Confirmation of hα-syn overexpression

The expression of the hα-syn protein in the striatal tissue of animals was confirmed by western blot. In the hα-syn group, progressively increased expression of hα-syn was observed from 1 week onwards (Figure 23). No expression of hα-syn was observed in the EVV group at any time point.

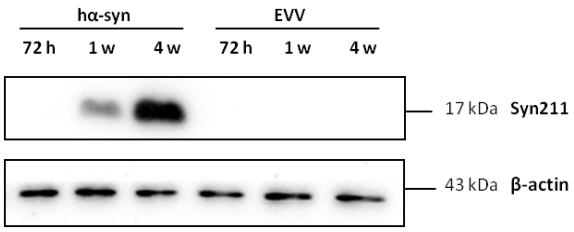

Figure 23: Expression of hα-syn. Representative western blot showing that hα-syn protein is being overexpressed in the striatum of the hα-syn group at 1 week and 4 weeks p.i. β-actin was used as loading control.

2.3 Mitochondrial respiration of striatal synaptosomes

To determine whether hα-syn overexpression can physiologically influence synaptic terminal respiration, we measured the oxygen consumption rate (OCR) of isolated striatal synaptosomes from EVV and hα-syn groups in independent studies at 72 h, 1 week and 4 weeks p.i. by the Seahorse XFe96 Extracellular Flux Analyzer.

At 72 h p.i., no differences were detected in the OCR bioenergetic profile (Figure 24A) or the detailed analysis of OCR derived bioenergetic parameters in any of the groups (Figure 24D-I).

Interestingly, at 1 week p.i., the hα-syn group showed significantly decreased levels in the OCR bioenergetic profile compared to the EVV group (Figure 24B). A detailed analysis of bioenergetic parameters has shown that the hα-syn group showed significantly decreased basal respiration ($p < 0.01$ vs. 1 w p.i. EVV group; Figure 24D) as well as decreased proton leak ($p < 0.05$ vs. 1 w p.i. EVV group; Figure 24E) compared to their EVV group. No differences were observed in the rest of the bioenergetic parameters analyzed between both groups.

At 4 weeks, the hα-syn group also showed a significantly reduced OCR bioenergetic profile (Figure 24C). Focusing on derived bioenergetic parameters we also found a significant decrease in basal respiration ($p < 0.05$ vs. 4 w p.i. EVV group; Figure 24D) and proton leak ($p < 0.05$ vs. 4 w p.i. EVV group; Figure 24E). Remarkably, significant decreased maximal respiration ($p < 0.05$

vs. 4 w p.i. EVV group; Figure 24G) and spare respiratory capacity ($p < 0.05$ vs. 4 w p.i. EVV group; Figure 24H) was also observed in the hα-syn group compared to their corresponding EVV group.

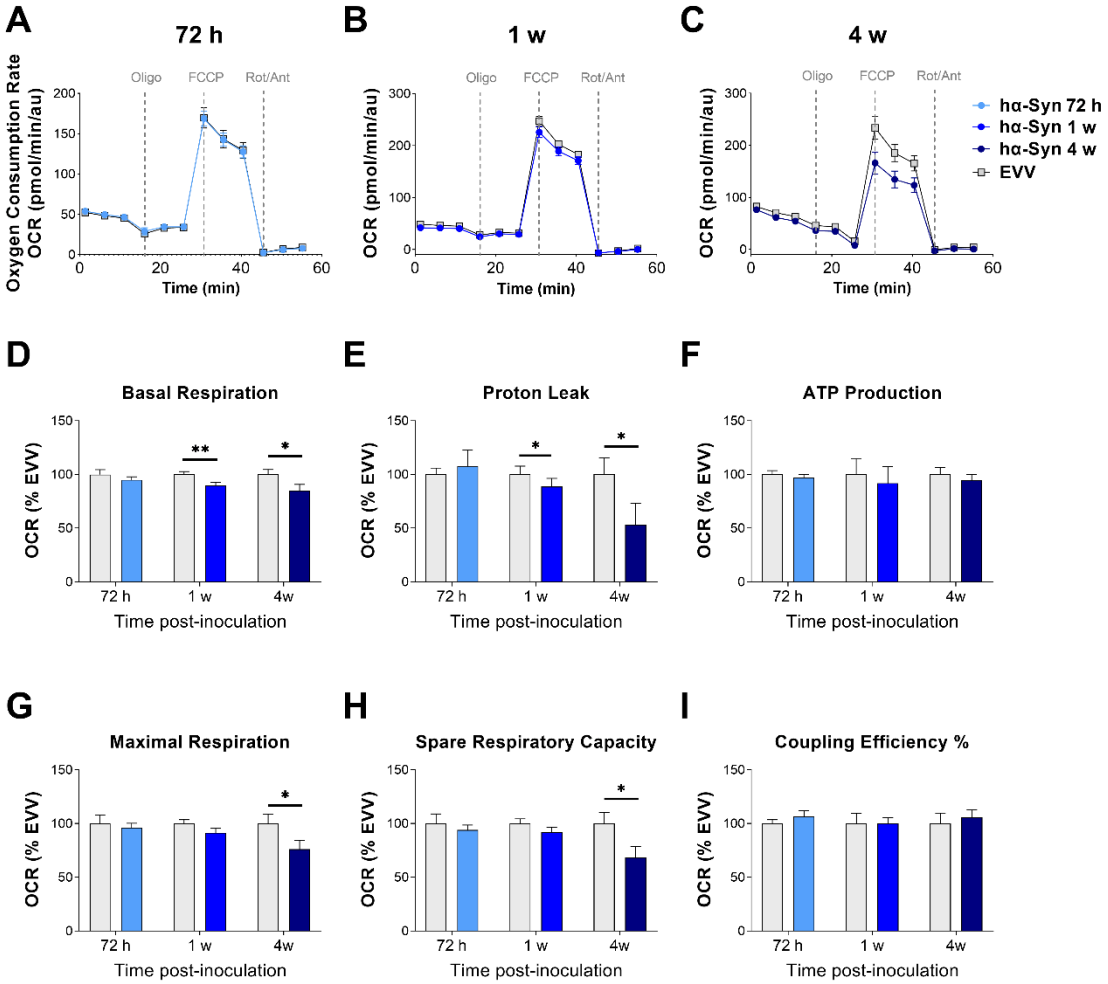

Figure 24. Mitochondrial bioenergetics of striatal synaptosomes. A-C, Normalized oxygen consumption rates (OCR; pmol/min/au) in synaptosomes from EVV and hα-syn groups at (**A**) 72 h p.i., (**B**) 1 w p.i. and (**C**) 4 w p.i. after sequential injections of oligomycin, FCCP and rotenone/antimycin. **D-I**, Normalized bioenergetic parameters derived from results in A, B and C, representing (**D**) basal respiration, (**E**) proton leak, (**F**) ATP production, (**G**) maximal respiration, (**H**) spare respiratory capacity and (**I**) coupling efficiency (%). Three independent experiments (one per each time point: 72 h, 1w and 4 w p.i.). n= 3 animals per group and time point and n= 8-12 wells per animal. Data are presented as mean ± SEM. Mann-Whitney test: *$p < 0.05$ vs. respective EVV group; **$p < 0.01$ vs. respective EVV group. au, arbitrary units.

2.4 Anaerobic glycolysis of striatal synaptosomes

We examined the extracellular acidification rate (ECAR) profile, an indirect index of cellular glucose oxidation in both groups and time points. Changes in basal conditions (basal ECAR) and in response to oligomycin and FCCP, which are mitochondrial aerobic respiration inhibitors, (stressed ECAR) were evaluated.

Notably, the ECAR bioenergetic profile revealed that basal ECAR is maintained in both groups at all time points evaluated (Figure 25A-D). By contrast, under stressed conditions (after oligomycin and FCCP stimulus) the hα-syn group showed maintained levels of ECAR at 72 h and 1 w p.i. but significantly decreased ECAR at 4 compared to the EVV group (Figure 25E).

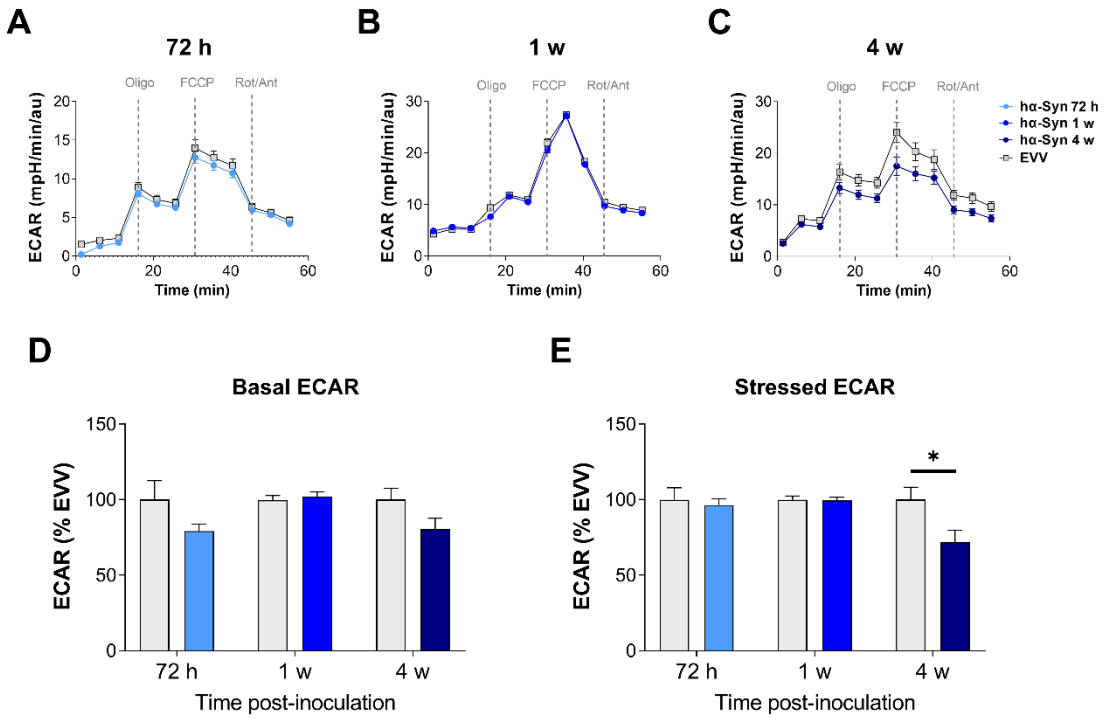

Figure 25: Extracellular acidification rates (ECAR) of striatal synaptosomes. ECAR (mpH/min/au) in striatal synaptosomes from EVV and hα-syn groups at (**A**) 72 h p.i., (**B**) 1 w p.i. and (**C**) 4 w p.i. time points after sequential injections of oligomycin, FCCP and rotenone/antimycin, determined in parallel with OCR. Glycolytic ratios derived from results in A, B and C, representing glycolytic capacity under (**D**) basal and (**E**) stressed (oligomycin + FCCP) conditions. Three independent experiments (one per each time point: 72 h, 1w and 4 w p.i.). n= 3 animals per group and time point and n= 8-12 wells per animal. Data are presented as mean ± SEM. Mann-Whitney test: *p < 0.05 vs. respective EVV group. au, arbitrary units.

2.5 Proteomics of striatal synaptosomes

In total, 2298 individual proteins were identified by SWATH-MS proteomics in isolated synaptosomes from the striatum. The differential analysis revealed 65 statistically significantly deregulated proteins in the hα-syn group along the different time points evaluated and compared to their corresponding EVV group. Within these significant proteins, 31 were detected as up-regulated while the other 36 were detected as significantly down-regulated (Table 4). Of note, among these deregulated proteins 18 belonged to 72 h p.i., 15 proteins to 1 week p.i. and 34 proteins to 4 w p.i. time point (Figure 26A, Table 4).

According to the clustering analysis with the significantly deregulated proteins in each time point, just one upregulated protein, ubiquitin carboxyl-terminal hydrolase 15 (Usp15), was overlapped across 1 week and 4 weeks p.i. time points (Figure 26A).

The comparison of all the significantly deregulated proteins in the hα-syn group with rat and human α-syn interactomes showed no overlap between rat α-syn interactome while, in contrast, 2 proteins overlapped with hα-syn interactome: Cryab and Ywhaq proteins. These proteins were significantly downregulated at 4 weeks p.i. and have been described to be interactors of hα-syn experimentally (Figure 26B).

The differentially expressed proteins were distributed into corresponding structural complexes to facilitate the understanding of selective or shared biological pathways at each time point. Focusing on the synaptic structural complex, no association was obtained at 72h p.i. The majority of deregulated proteins at 1 week p.i. were associated with mitochondria and cell cytoplasm, while at 4 weeks p.i. they were related to ribosomes, postsynaptic density and focal adhesion (Figure 26C). The deregulated proteome was further distributed into several biological processes. At 72 h p.i. the main part of the proteins was associated with the organic hydroxyl compound metabolic process. At 1 week p.i. proteins were related with autophagy, organophosphate biosynthetic process and cell part morphogenesis. Finally, 4 weeks p.i. proteins were associated with endocytosis, aging, histone modification, negative regulation of hydrolase activity, cellular response to abiotic stimulus, monosaccharide metabolic process, negative regulation of transport and translation (Figure 26D). Moreover, 15 proteins from the total deregulated synaptosome proteome were mapped to SynGO annotated genes. A deep synaptic ontology analysis (Table 5) revealed that protein derangements occur at the presynaptic and postsynaptic levels, being partially involved in protein translation and synaptic signaling and organization.

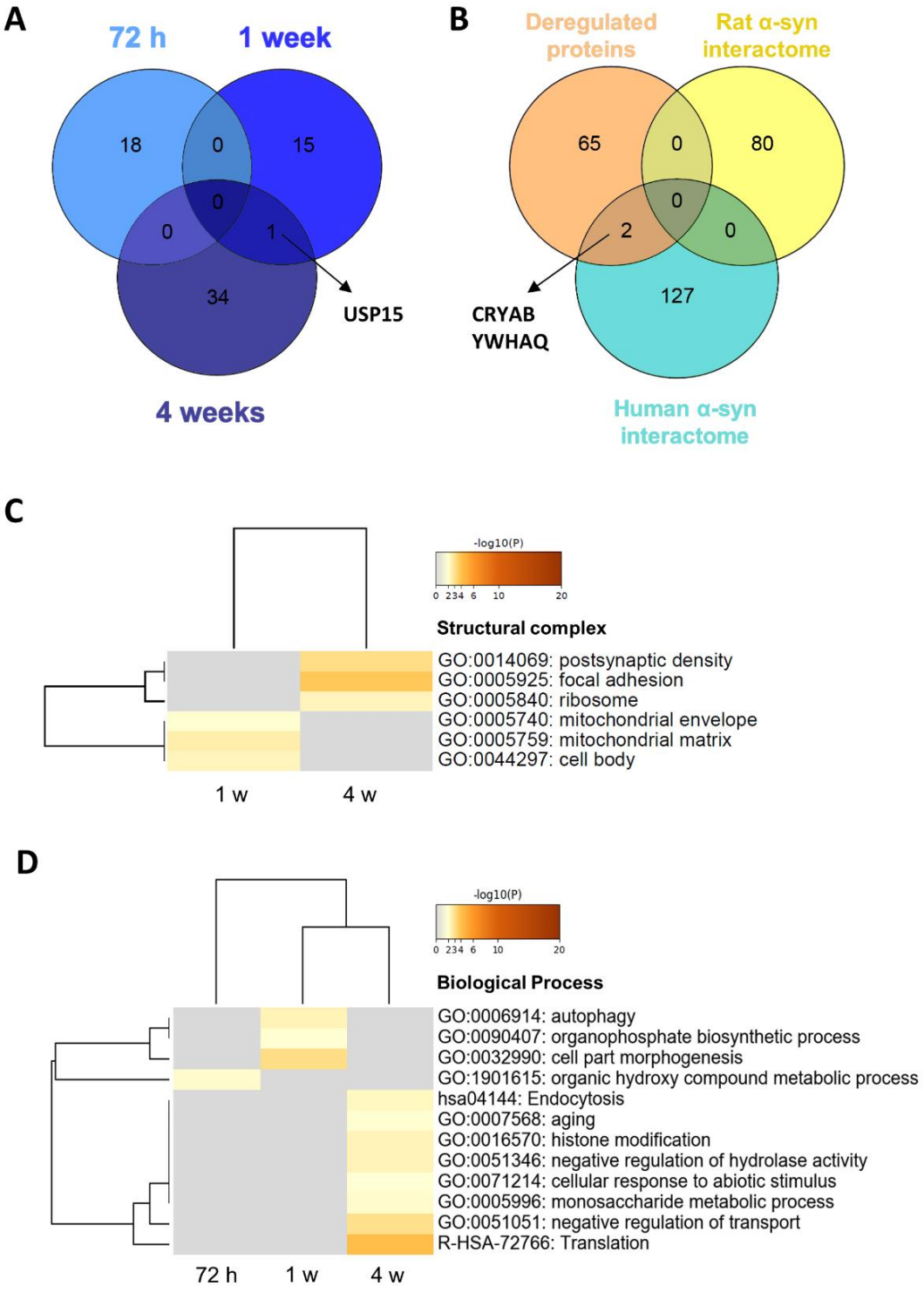

Figure 26. (**A**) Cluster overlap of deregulated proteins at striatal synaptosomes in the different time points p.i. (72 h, 1 week and 4 weeks) of the hα-syn group (**B**) Cluster overlap between deregulated proteins in the hα-syn group and α-syn interactomes from both rat and human. (**C-D**) Heatmap showing the top enrichment terms (GO), across the time points p.i. using a color scale to represent statistical significance. The gray color indicates a lack of significance. (**C**) Enriched structural complexes across 1 w and 4 weeks p.i. time points of the hα-syn group. No enriched structural complex was observed at 72 h p.i. (**D**) Enriched biological pathway and gene ontology clusters across time points p.i. of the hα-syn group. n= 5 per group and time point.

Table 4: Significant deregulated proteins in hα-syn group striatal synaptosomes.

Description	Gene Name	Uniprot	Peptide Count	Ratio	p Value
72 h					
Down-regulated proteins					
Dolichol-phosphate mannosyltransferase subunit 1	Dpm1	D4A8N1	2	0,5153	0,0226
Engulfment and cell motility 1	Elmo1	G8CYZ7	2	0,5335	0,0090
ADP-ribosylation factor-like GTPase 8A	Arl8a	D3ZPP2	2	0,5645	0,0254
RCG25591, isoform CRA_a	Stt3b	B2RYD7	2	0,6409	0,0005
Lysophosphatidylcholine acyltransferase 4	Lpcat4	D3ZR52	5	0,6434	0,0038
60S ribosomal protein L15	Rpl15	P61314	4	0,6520	0,0094
Cysteinyl-tRNA synthetase	Cars	G3V9K0	4	0,6554	0,0143
Tumor protein D54	Tpd52l2	Q6PCT3	4	0,6965	0,0285
Ubiquilin 2	Ubqln2	D4AA63	4	0,7012	0,0012
Polypyrimidine tract-binding protein 2	Ptbp2	Q66H20	2	0,7063	0,0029
Stromal interaction molecule 1	Stim1	A0A0G2K5C8	3	0,7163	0,0171
Alpha-mannosidase 2C1	Man2c1	Q5M9I2	7	0,7535	0,0396
Up-regulated proteins					
Phytanoyl-CoA hydroxylase-interacting protein-like	Phyhipl	Q6AYN4	6	1,3875	0,0356
Phosphofurin acidic cluster sorting protein 1	Pacs1	F1LPG3	10	1,4131	0,0315
Protein kinase AMP-activated non-catalytic subunit gamma 2	Prkag2	A0A140UHX4	2	1,5921	0,0100
Small G protein-signaling modulator 1	Sgsm1	D3ZAS2	2	1,9722	0,0140
MAP kinase-activating death domain protein	Madd	A0A0G2KA27	7	2,3184	0,0078
Transthyretin	Ttr	P02767	3	2,8239	0,0194

Description	Gene Name	Uniprot	Peptide Count	Ratio	p Value
1 week					
Down-regulated proteins					
Acyl-CoA dehydrogenase family, member 8	Acad8	M0RDK9	2	0,5381	0,0473
Transportin 3	Tnpo3	D4AAM0	2	0,6327	0,0171
Polyribonucleotide nucleotidyltransferase 1	Pnpt1	G3V6G7	2	0,6530	0,0440
Rho guanine nucleotide exchange factor 7	Arhgef7	A0A0G2QC21	4	0,7137	0,0436
Vacuolar protein sorting-associated protein 16 homolog	Vps16	Q642A9	3	0,7149	0,0335
RAB24, member RAS oncogene family	Rab24	A0A096MKB0	3	0,7161	0,0308
Guanylate cyclase soluble subunit alpha-1	Gucy1a1	P19686	7	0,7191	0,0414
FAD synthase	Flad1	D4A4P4	3	0,7229	0,0028
Leucine zipper putative tumor suppressor 1	Lzts1	Q8CFC9	2	0,7432	0,0288
Up-regulated proteins					
Apoptosis-inducing factor, mitochondria-associated 3	Aifm3	D3ZF03	6	1,3116	0,0232
Evolutionarily conserved signaling intermediate in Toll pathway	Ecsit	Q5XIC2	2	1,3211	0,0425
VPS39 subunit of HOPS complex	Vps39	E9PT04	4	1,4222	0,0145
Ubiquitin carboxyl-terminal hydrolase	Usp15	A0A0A0MY07	2	1,5970	0,0219
GDNF family receptor alpha-2	Gfra2	O35977	2	1,6091	0,0336
Receptor-type tyrosine-protein phosphatase epsilon	Ptpre	B2GV87	2	2,3642	0,0021
Ethanolamine-phosphate cytidylyltransferase	Pcyt2	O88637	2	2,4023	0,0308
4 weeks					
Down-regulated proteins					
Oxidative stress-responsive kinase 1	Oxsr1	D3ZUC9	2	0,3131	0,0298
IST1 homolog	Ist1	Q568Z6	2	0,3902	0,0162
Cytochrome b5	Cyb5a	P00173	3	0,6194	0,0215
NEDD8-activating enzyme E1 regulatory subunit	Nae1	F1M7W7	4	0,6229	0,0497
Hydroxysteroid dehydrogenase-like protein 2	Hsdl2	Q4V8F9	6	0,6376	0,0013
Voltage-dependent R-type calcium channel subunit alpha	Cacna1e	F1LMS1	2	0,6460	0,0474

Description	Gene Name	Uniprot	Peptide Count	Ratio	p Value
Alpha-crystallin B chain	Cryab	P23928	2	0,6496	0,0231
Malonyl-CoA decarboxylase, mitochondrial	Mlycd	Q920F5	4	0,6732	0,0242
Dead end homolog 1	Hars	Q4QQV4	3	0,6996	0,0244
Anion exchange protein	Slc4a3	G3V8P8	6	0,7041	0,0061
Eukaryotic translation elongation factor 1 epsilon 1	Eef1e1	B2RYN3	2	0,7085	0,0225
14-3-3 protein theta	Ywhaq	P68255	11	0,7325	0,0070
RuvB-like helicase	Ruvbl2	G3V8T5	2	0,7333	0,0413
Catenin alpha 1 isoform CRA_b	Ctnna1	Q5U302	10	0,7341	0,0180
Ubiquitin-like-conjugating enzyme ATG3	Atg3	Q6AZ50	3	0,7485	0,0378
Up-regulated proteins					
60S ribosomal protein L7	Rpl7	B0K031	7	1,3351	0,0283
Ribonuclease inhibitor	Rnh1	E2RUH2	10	1,3571	0,0213
Retinoid-inducible serine carboxypeptidase	Scpep1	Q920A6	2	1,3696	0,0220
60S ribosomal protein L6	Rpl6-ps1	F1LQS3	5	1,3790	0,0407
IQ motif and Sec7 domain ArfGEF 2	Iqsec2	A0A0G2JZX5	9	1,3809	0,0324
Mitochondrial ribosomal protein S24	Mrps24	A9UMV2	2	1,4151	0,0353
60S ribosomal protein L24	Rpl24	A0A0H2UH99	4	1,4250	0,0411
Mitochondrial carnitine/acylcarnitine carrier protein	Slc25a20	P97521	6	1,4584	0,0061
Ubiquitin carboxyl-terminal hydrolase	Usp15	A0A0A0MY07	2	1,4977	0,0391
Adhesion G protein-coupled receptor B1	Adgrb1	C0HL12	4	1,5214	0,0253
Vesicle-trafficking protein SEC22b	Sec22b	Q4KM74	7	1,5500	0,0016
Cyclin M1	Cnnm1	D4A1C0	2	1,6207	0,0114
ADP-ribosylation factor-like protein 2	Arl2	O08697	2	1,6340	0,0271
Amyloid-like protein 2	Aplp2	M0RDX2	2	1,6732	0,0280
Rab GTPase-binding effector protein 1	Rabep1	G3V9J7	3	1,6860	0,0199
Sodium/bile acid cotransporter 4	Slc10a4	F1LQG5	3	1,6865	0,0407
Nitric oxide synthase	Nos1	F1LQL1	2	1,7050	0,0091

RCG48334, isoform CRA_e (RNA-binding motif protein 14)	Rbm14	M0R9Q1	2	1,8935	0,0394
Glycerol-3-phosphate phosphatase	Pgp	D3ZDK7	2	1,9772	0,0398
Lactamase, beta	Lactb	D3ZFJ6	6	2,5059	0,0370

Table 5: Synaptic ontologies across deregulated proteome in hα-syn group.

Ontology term	Protein count	Corresponding time point of proteins	p-value	q-value
Cellular component				
synapse	13	2 (72 h), 2 (1 w), 9 (4 w)	3.77e-5	2.26e-4
presynapse	8	2 (1 w), 6 (4 w)	3.32e-4	9.95e-4
postsynapse	8	1 (72 h), 1 (1 w), 6 (4 w)	1.29e-3	1.93e-3
presynaptic ribosome	3	1 (72 h), 2 (4 w)	1.01e-3	1.93e-3
postsynaptic ribosome	3	1 (72 h), 2 (4 w)	2.30e-3	2.76e-3
postsynaptic density	4	1 (1 w), 3 (4 w)	0.0120	0.0120
Biological Process				
process in the synapse	12	2 (72 h), 3 (1 w), 7 (4 w)	2.41e-5	1.20e-4
protein translation at presynapse	3	1 (72 h), 2 (4 w)	9.62e-4	2.07e-3
protein translation at postsynapse	3	1 (72 h), 2 (4 w)	1.24e-3	2.07e-3
synaptic signaling	3	1, (1 w), 2 (4 w)	0.0233	0.0291
synapse organization	3	2 (1 w), 1 (4 w)	0.0829	0.0829
synaptic vesicle cycle	2	2 (4 w)	NaN	NaN
Process in postsynapse	2	2 (4 w)	NaN	NaN
Postsynaptic actin cytoskeleton organization	2	1 (1 w), 1 (4 w)	NaN	NaN

The protein count column shows the number of proteins that are annotated in SynGO against each term.

2.5.1 Mitochondrial content of striatal synaptosomes

To ensure that mitochondrial content was similar in EVV and hα-syn groups, and to confirm that alterations on mitochondrial respiration prompted by hα-syn overexpression at striatal synaptosomes were not being induced by a reduction in mitochondrial amount, we examined the expression level of fundamental mitochondrial proteins detected by quantitative proteomics. No changes were observed in the quantified levels of protein subunits of the translocase of the mitochondrial outer membrane (TOM), NADH dehydrogenase complex (complex I), cytochrome c oxidase (complex IV) and ATP synthase (complex V) in the hα-syn group at any of the studied time points compared to their respective EVV group.

Furthermore, we determined if striatal synaptosomes from the hα-syn group displayed alterations in mitochondrial dynamics, which are necessary to maintain the functionality and the location of mitochondria to meet the cell's energy needs. Thus, we examined the expression levels of mitochondrial fusion and fission related proteins. The expression levels of mitochondrial fusion proteins, mitofusin 2 (Mfn2) and optic strophy 1 (Opa1) and the recruitment of mitochondrial fission protein, dynamin 1 (Dnm1), were not altered in the hα-syn group at any of the studied time points in comparison to their respective EVV group.

Additionally, it is important to note that the expression of fundamental proteins for clearance of damaged mitochondria via mitophagy, such as PINK1, Parkin, p62, LC3, Bnip3L/Nix, Bcl-2 and FUNDC1 have not been detected by this proteomic approach due to technical limitations.

3. Ultrastructural alterations in the dorsal striatal synapses

3.1 Experimental Design

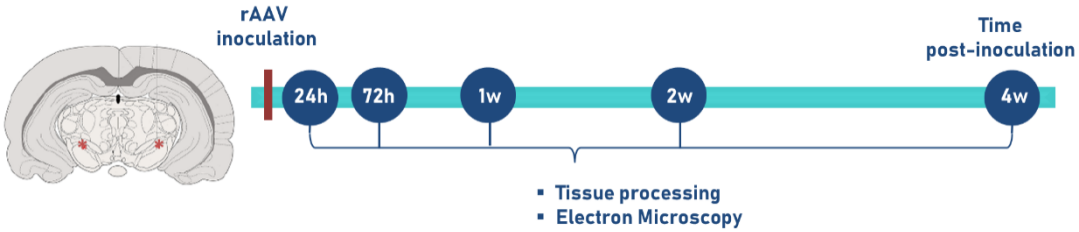

Figure 27: Experimental design of the ultrastructural study of the striatal synapses. Animals were inoculated with either rAAV-hα-syn or rAAV-EVV bilaterally in the SN_{pc} and they were perfused at their corresponding final time point (24 h, 72 h, 1, 2 and 4 weeks p.i.). Brains were removed and coronal slices were acquired for an electron microscopy study.

To study the temporal sequence of synaptic ultrastructure in the synapses of the dorsal striatum, the same animals as for the motor and histological evaluation were used. Thus, animals were inoculated with rAAV-hα-syn and were sacrificed at different p.i. time points: 24 h, 72 h, 1, 2 and 4 weeks. For the control group, animals were inoculated with rAAV-EVV and only 4 w p.i. time point was studied to decrease the number of used animals (Figure 27).

3.2 Ultrastructural alterations in TH^+ dopaminergic fibers

3.2.1 Density and morphology of TH^+ dopaminergic fibers

Ultrastructural examination of dorsal striatal tissue confirmed signs of distal neurodegeneration and axon pathology at dopaminergic fibers induced by hα-syn overexpression (Figure 28B, D) not observed in the EVV group (Figure 28A). Inoculation of hα-syn resulted in a progressive reduction of TH^+ fibers at 2 weeks p.i. ($p < 0.05$ vs. 72 h p.i.) and 4 weeks p.i. (81 % reduction, $p < 0.01$ vs. EVV group, 72h and 1 w p.i.; $p < 0.05$ vs. 24 h p.i) (Figure 28C, Table 6).

Regarding the morphology of TH^+ fibers, a significant increment in their size was observed at 4 weeks p.i ($p < 0.05$ vs. EVV group and 2 w p.i.; $p < 0.01$ vs. 72 h and 1 w p.i.; Figure 28E) along with an increment in their area/perimeter ratio ($p < 0.05$ vs. EVV group, 24 h, 72 h and 2 w p.i.; $p < 0.01$ vs. 1 w p.i.; Figure 28G, Table 6) at this time point.

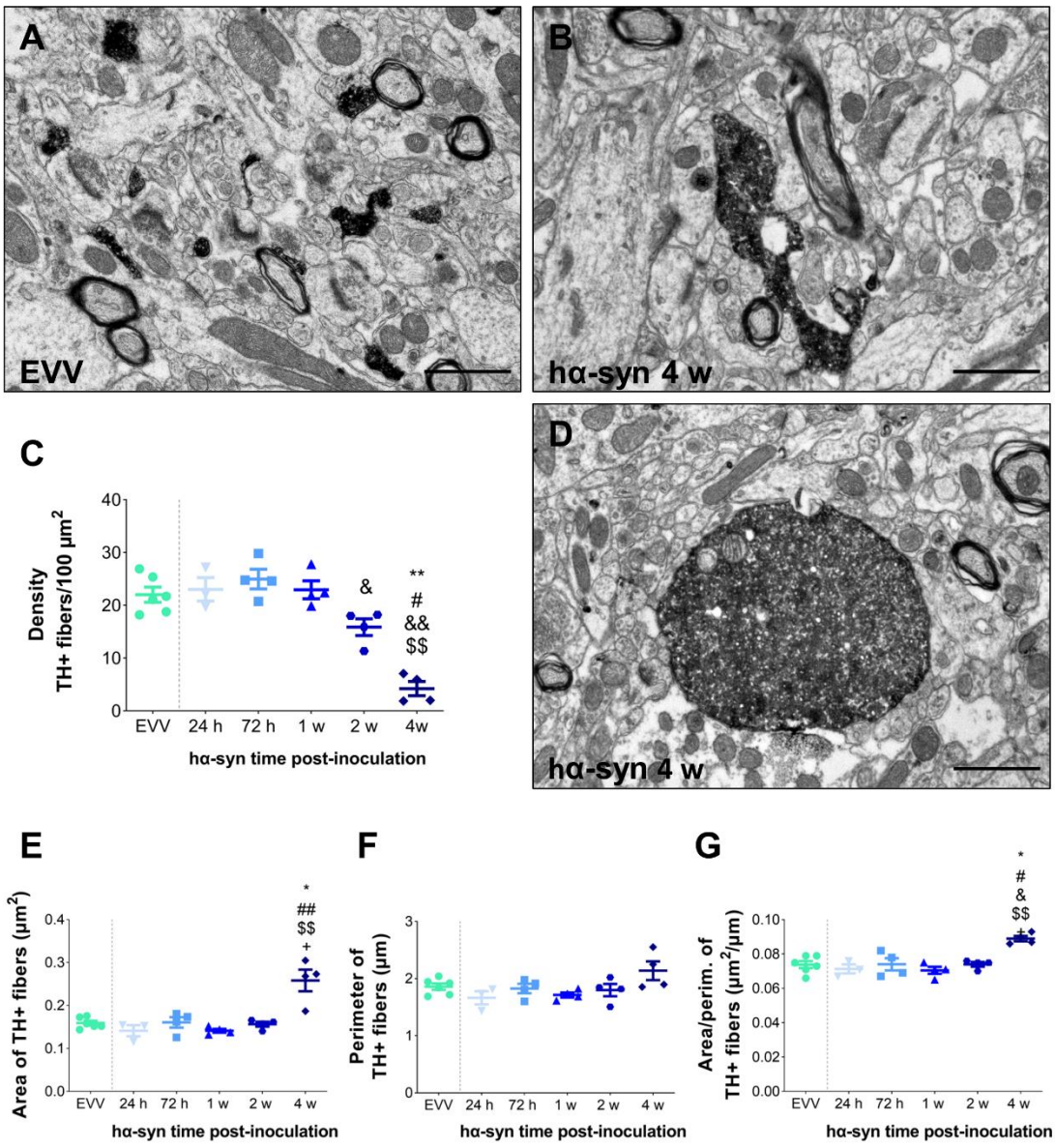

Figure 28: Ultrastructure of TH⁺ dopaminergic fibers. A-B, Representative electron microscopy photomicrographs of stained TH⁺ fibers (black) in the dorsal striatum from (**A**) EVV group and (**B, D**) hα-syn group at 4 w time point. Scale bars, 1 µm. (**C**) Density of TH⁺ fibers from EVV and hα-syn groups. **E-F**, Quantification of morphological parameters from TH⁺ fibers from EVV and hα-syn groups: (**E**) area (µm²), (**F**) perimeter (µm), (**G**) area/perimeter ratio (µm²/µm). All values are presented as mean ± SEM. Kruskal-Wallis followed by Dunn´s *post-hoc* test: * $p < 0.05$ and ** $p < 0.01$ vs. EVV group; # $p < 0.05$ and ## $p < 0.01$ vs. 24 h; & $p < 0.05$ and && $p < 0.01$ vs. 72 h; $$ $p < 0.01$ vs. 1 w p.i.; + $p < 0.05$ vs. 2 w p.i. n = 6 (EVV), n = 4 (in hα-syn, for each time point evaluated).

Table 6: Detailed data of density and morphological parameters of TH⁺ fibers from EVV and hα-syn groups.

	TH⁺ fibers					
Parameter	**EVV**	**24 h**	**72 h**	**1 w**	**2 w**	**4 w**
Density TH⁺ fibers per 100 µm²	22.024 ± 1.431	23.030 ± 2.203	24.987 ± 1.856	22.950 ± 1.688	15.871 ± 1.593 *	4.228 ± 1.342 **
Morphology Nb of analyzed terminals	2758	1442	2084	1916	1412	353
Area (µm²)						
Mean ± SEM	0.159 ± 0.005	0.141 ± 0.012	0.160 ± 0.012	0.141 ± 0.004	0.156 ± 0.005	0.258 ± 0.025 *
Range	0.144 - 0.176	0.166 - 0.155	0.126 - 0.181	0.132 - 1.152	0.140 - 0.166	0.187 - 0.305
Perimeter (µm)						
Mean ± SEM	1.858 ± 0.055	1.664 ± 0.114	1.826 ± 0.082	1.712 ± 0.044	1.797 ± 0.107	2.137 ± 0.164
Range	1.689 - 2.040	1.493 - 1.815	1.01 - 1.978	1.611 -1.822	1.506 - 2.022	1.853 - 2.552
Area/perim. (µm²/µm)						
Mean ± SEM	0.073 ± 0.002	0.071 ± 0.002	0.074 ± 0.003	0.070 ± 0.002	0.073 ± 0.001	0.089 ± 0.001 *
Range	0.066 - 0.079	0.067 - 0.076	0.067 - 0.082	0.065 - 0.075	0.070 - 0.076	0.086 - 0.093

* $p < 0.05$ and ** $p < 0.01$ vs. EVV group.

3.2.2 Density and morphology of electroclear structures inside TH⁺ dopaminergic fibers and characterization of its nature

Electroclear structures within TH⁺ fibers were characterized as a discernible electron-lucent lumen that contrasted with the electrodense DAB immunostaining and can contain different cellular structures inside. These electroclear structures resembled autophagic vesicles (Figure 29A-E).

Overexpression of hα-syn in dopaminergic fibers resulted in a significant increment in the number of electroclear structures within TH⁺ fibers. We found approximately 2 times and 4 times as many electroclear structures in hα-syn group at 2 weeks p.i ($p < 0.05$ vs. EVV group) and 4 weeks p.i. ($p < 0.01$ vs. EVV group; $p < 0.01$ vs. 24 h p.i.; $p < 0.05$ vs. 72 h p.i.; $p < 0.01$ vs. 1 w p.i.), respectively (Figure 29F).

No differences were observed in the morphological parameters (area, perimeter and area/perimeter ratio) of electroclear structures in the EVV group and hα-syn group at any time point (Figure 29G-I, Table 7).

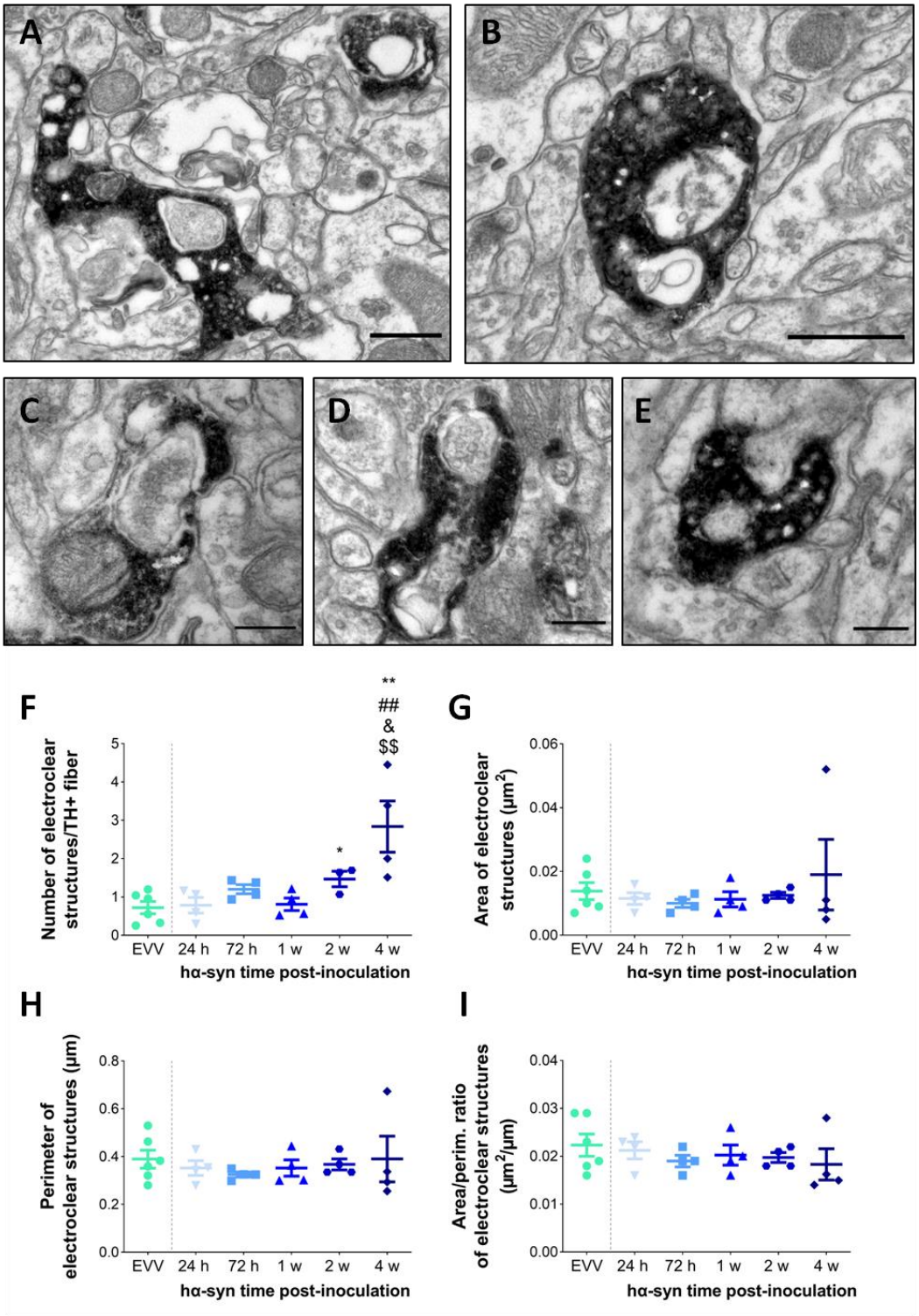

Figure 29: Electroclear structures within TH⁺ dopaminergic fibers. (A-E) Representative electron microscopy photomicrographs of electroclear structures found inside TH⁺ fibers. Scale bar, 200 nm. (**F**) Number of electroclear structures per TH⁺ fiber from EVV and hα-syn groups (**G-I**) Quantification of their morphological parameters from EVV group and hα-syn groups: (**G**) area (µm²), (**H**) perimeter (µm), (**I**) area/perimeter ratio (µm²/µm). All values are presented as mean ± SEM. Kruskal-Wallis followed by Dunn´s *post-hoc* test: * $p < 0.05$ and ** $p < 0.01$ vs. EVV group; ## $p < 0.01$ vs. 24 h; & $p < 0.05$ vs. 72 h; $$ $p < 0.01$ vs. 1 w p.i. n = 6 (EVV), n = 4 for each time point.

Table 7: Detailed data of density and morphological parameters of electroclear structures inside TH⁺ fibers from EVV and hα-syn groups.

	Electroclear structures inside TH⁺ fibers					
Parameter	**EVV**	**24 h**	**72 h**	**1 w**	**2 w**	**4 w**
Struc./TH⁺ f.	0.724 ± 0.065	0.785 ± 0.101	1.203 ± 0.059	0.823 ± 0.072	1.233 ± 0.138 *	2.837 ± 0.334 **
Area (µm²)						
Mean ± SEM	0.013 ± 0.002	0.011 ± 0.001	0.011 ± 0.001	0.010 ± 0.002	0.012 ± 0.001	0.019 ± 0.011
Range	0.007 - 0.024	0.007 - 0.016	0.007 - 0.013	0.007 - 0.018	0.011 - 0.015	0.005 - 0.052
Perimeter (µm)						
Mean ± SEM	0.389 ± 0.037	0.352 ± 0.030	0.325 ± 0.010	0.352 ± 0.033	0.367 ± 0.022	0.390 ± 0.095
Range	0.280 - 0.530	0.280 - 0.431	0.299 - 0.350	0.300 - 0.444	0.335 - 0.432	0.256 - 0.673
Area/perim. (µm²/µm)						
Mean ± SEM	0.022 ± 0.002	0.021 ± 0.001	0.019 ± 0.001	0.020 ± 0.002	0.019 ± 0.001	0.018 ± 0.003
Range	0.016 - 0.029	0.016 - 0.024	0.016 - 0.022	0.016 - 0.026	0.018 - 0.022	0.014 - 0.028

* $p < 0.05$ and ** $p < 0.01$ vs. EVV group.

In order to characterize the nature of these electroclear structures, we studied the expression of key endocytic (Rab5 and Rab7) and autophagic (LC3B and Lamp1) proteins inside TH⁺ fibers at 4 weeks p.i. time point. A positive accumulation for LC3 and Rab5 (green channel) proteins was colocalized (yellow marks) with dopaminergic swollen fibers (red channel) compared to the EVV group (Figure 30A-H). By contrast, Rab7 and Lamp1 expression (orange channel) was not overlapped on TH⁺ fibers compared to the EVV group. Interestingly, positive expression of these markers was mainly observed surrounding the nucleus stained by DAPI (blue channel), suggesting that Lamp1 and Rab7 are more related to mechanisms produced in striatal cell bodies (Figure 30A-H).

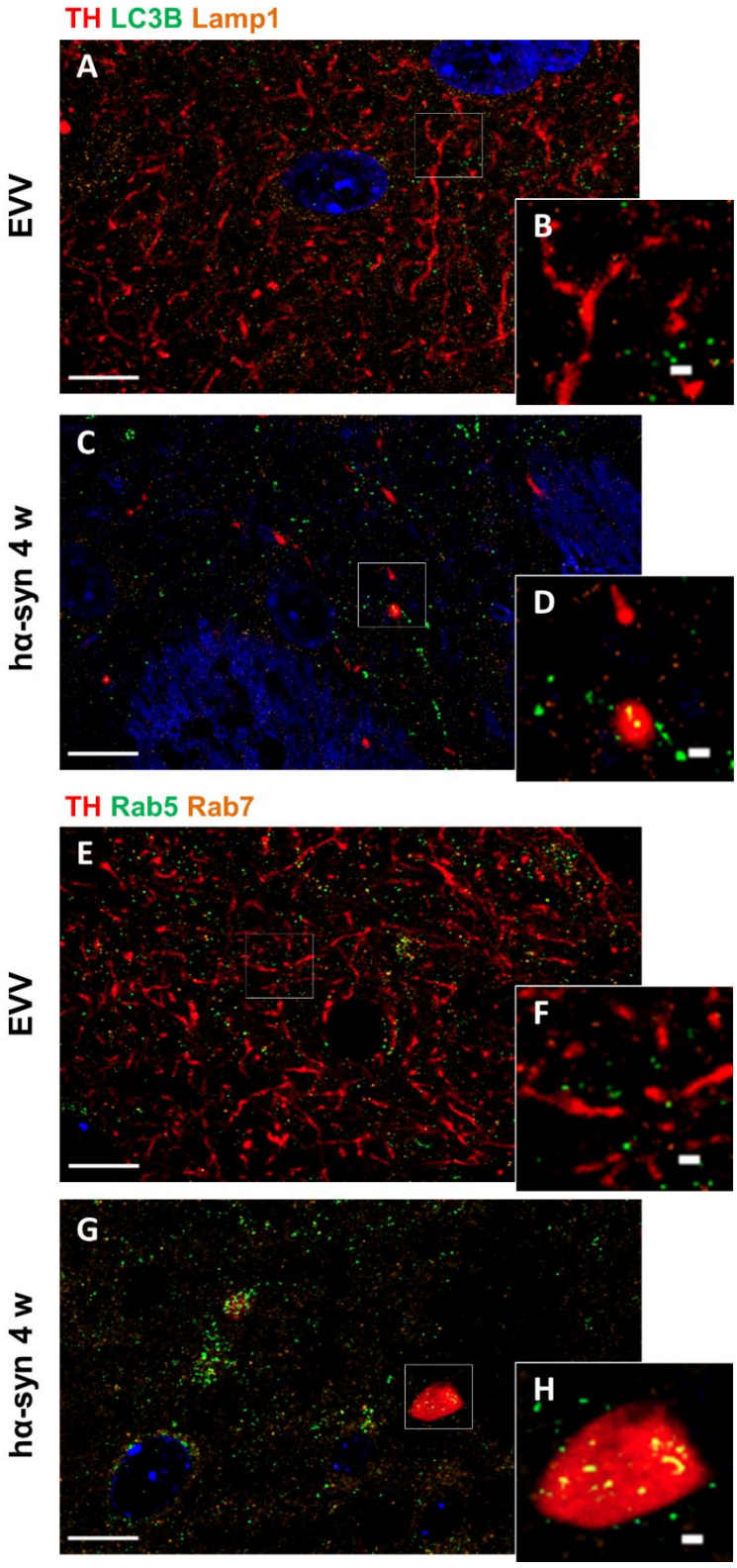

Figure 30: Expression of autophagic and endocytic proteins within TH⁺ dopaminergic fibers. Representative triple immunofluorescence photomicrographs (**A-D**) for TH, LC3B and Lamp1 expression and (**E-H**) TH, Rab5, Rab7 expression from EVV group and hα-syn group at 4 w time point p.i. Scale bars, 10 µm. (**B, D, F, H**) Higher magnification photomicrographs of details framed in the photos; scale bars 1 µm. DAPI, blue channel.

3.2.3 Density and morphology of mitochondria of the TH⁺ dopaminergic fibers

3.2.3.1 Total mitochondria

In the hα-syn group, no significant changes in the number of total mitochondria within the TH⁺ dopaminergic fibers from the dorsal striatum were observed at any time point compared with the EVV group or between time points (Figure 31B).

In addition, no significant changes were observed in the analysis of major mitochondrial shape descriptors such as total mitochondrial morphological parameters (area, perimeter, area/perimeter ratio, circularity, roundness, aspect ratio and Feret diameter) at any time point compared with the EVV group or between time points (Figure 34). Morphologically, we observed that in the TH⁺ dopaminergic fibers, mitochondria are mostly small and tubular in shape (mean roundness < 0.7; Figure 34) containing mostly longitudinally oriented and densely packed cristae (Figure 31A).

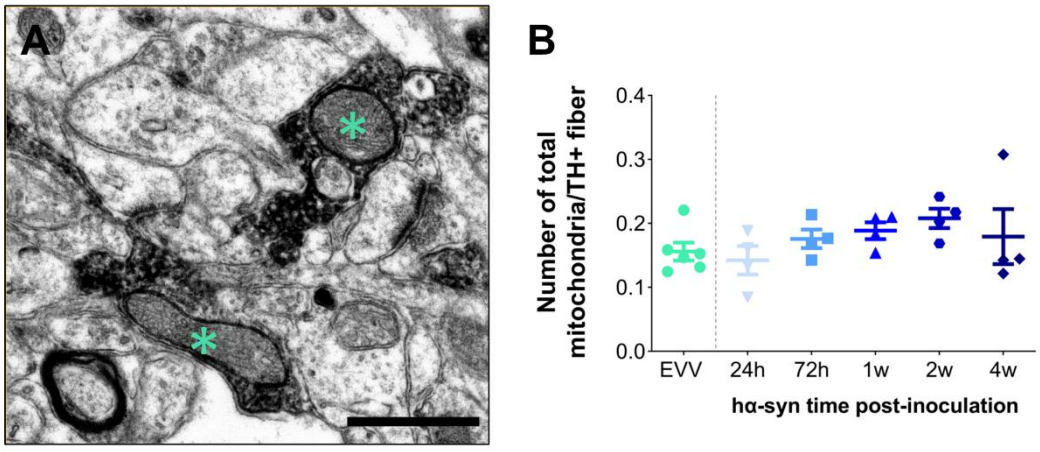

Figure 31: Mitochondria within TH⁺ dopaminergic fibers. (A) Representative electron microscopy photomicrograph of mitochondria (green asterisks) found inside TH⁺ fibers (black staining). Scale bar, 0.5 µm. (**B**) The number of mitochondria per TH⁺ fiber in EVV group and hα-syn group at different time points. All values are presented as mean ± SEM. No statistical differences (Kruskal-Wallis test). n = 6 (EVV), n = 4 for each time point.

Frequency distributions for the studied morphological parameters of total mitochondria were very similar. Interestingly, several morphological parameters of total mitochondria (area, perimeter, aspect ratio and feret diameter) were highly (> 1.0) skewed in the EVV and in the hα-syn time points (Figure 32; Table 8).

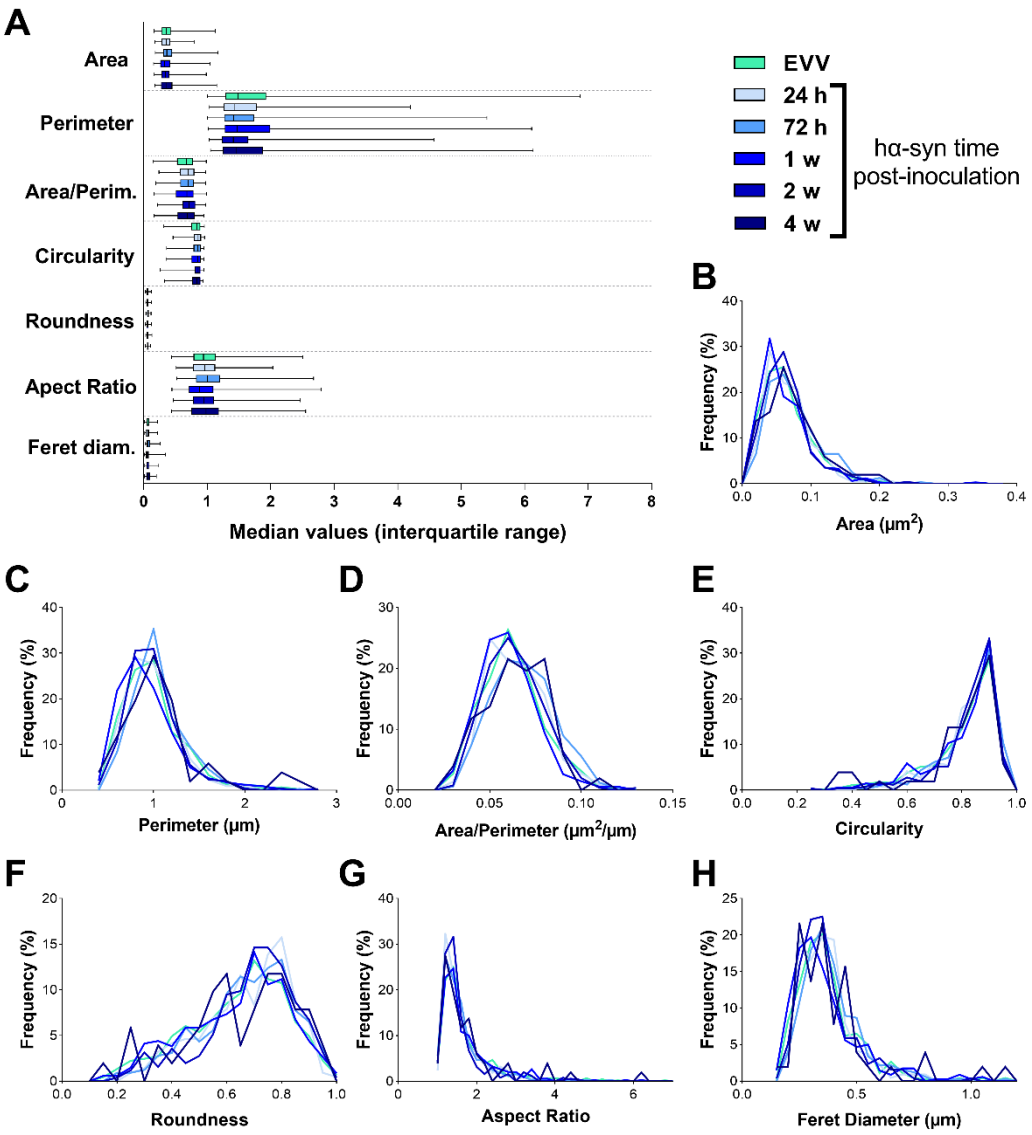

Figure 32: Analysis of morphological parameter distribution of mitochondria within TH⁺ fibers. (**A**) Box plot graph representing mitochondrial morphological parameters from EVV and hα-syn group time points. Bars represent the range of values that contain 50% of all mitochondria (interquartile range) for each parameter. (**B–H**) Frequency distribution histograms (% total mitochondria) for each morphological parameter: (**B**) area, (**C**) perimeter, (**D**) area/perimeter ratio, (**E**) circularity, (**F**) roundness, (**G**) aspect ratio and (**H**) Feret diameter. N of mitochondria per group: n= 447 (EVV), n= 217 (24 h), n = 323 (72 h), n = 340 (1 w), n= 253 (2 w), n= 51 (4 w).

Table 8: Skewness of the distribution of morphological parameters of mitochondria of TH⁺ fibers from EVV and hα-syn groups.

	Skewness					
Parameter	**EVV**	**24 h**	**72 h**	**1 w**	**2 w**	**4 w**
Area (µm²)	1.269	1.490	1.134	2.176	1.452	1.069
Perimeter (µm)	1.409	0.977	1.329	1.574	1.349	1.761
Area/Perimeter (µm²/(µm)	0.538	0.621	0.334	0.663	0.558	0.022
Circularity (0-1)	-1.422	-1.340	-1.605	-1.367	-2.089	-1.893
Roundness (0-1)	0.512	-0.575	-0.572	-0.435	-0.789	-0,624
Aspect Ratio	2.676	1.960	2.609	2.314	2.569	2.785
Feret diameter (µm)	1.894	1.266	1.762	1.778	1.521	2.302

***** Skewness is a measure of asymmetry in distributions. A value of 0 = normally or randomly distributed population; a value > 0 = more smaller values than expected; and a value < 0 = more larger values than expected. n= 447 (EVV), n= 217 (24 h), n = 323 (72 h), n = 340 (1 w), n= 253 (2 w), n= 51 (4 w) mitochondria.

3.2.3.2 Mitochondrial subtypes

Mitochondria within TH⁺ dopaminergic fibers were further classified into three subtypes (intact, damaged and degenerating mitochondria; Figure 33A-C) and their density and morphology were evaluated.

The density of intact mitochondria reached a significant reduction in the hα-syn group at 4 w p.i. ($p < 0.05$ vs. EVV group and 1 w and 2 w p.i.; $p < 0.01$ vs. 72 h p.i.; Figure 33D). Concomitantly, a significant increase in the density of damaged mitochondria ($p < 0.05$ vs. EVV group and 24 h p.i.; $p < 0.01$ vs. 72 h p.i.; Figure 33E) and a significant decrease in the density of degenerating mitochondria ($p < 0.05$ vs. EVV group, 24 h, 72 h and 1 w p.i.; Figure 33F) were observed.

The analysis of the morphological parameters of intact mitochondria in the hα-syn group indicated that there were no significant differences compared to the EVV group, but found significant changes in the means of aspect ratio and roundness along with time points (Figure 34). Intact mitochondria acquire a more tubular shape at 4 weeks p.i., as observed by an increase in the length-to-width ratio ($p < 0.01$ vs. 24 h p.i. and $p < 0.05$ vs. 2 w p.i.) and a decrease in their roundness ($p < 0.01$ vs. 24 h p.i. and $p < 0.05$ vs. 2w p.i.; $p = 0.070$ vs. EVV group). No significant changes were observed in the damaged mitochondria in the hα-syn group in any morphological parameter compared to the EVV group or between time points (Figure 34).

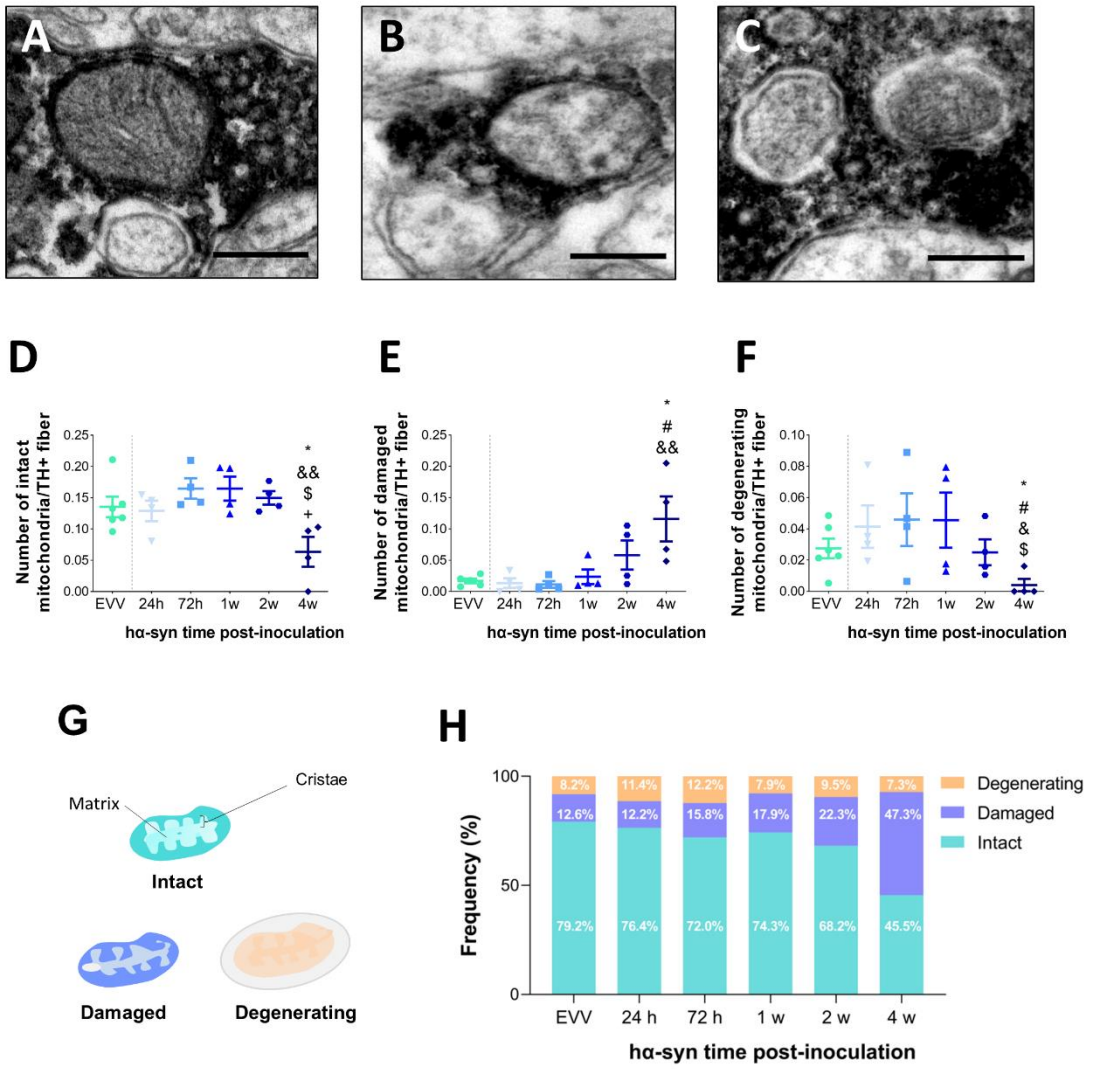

Figure 33: Mitochondrial subtypes in TH⁺ dopaminergic fibers. A-C, Representative electron microscopy photomicrographs of (**A**) intact mitochondria, (**B**) damaged mitochondria and (**C**) degenerating mitochondria in TH⁺ fibers from the dorsal striatum in the hα-syn group. Scale bars, 200 nm. (**D**) Number of intact mitochondria, (**E**) damaged mitochondria and (**F**) degenerating mitochondria per TH⁺ fiber in EVV and hα-syn groups at 24 h, 72 h, 1, 2 and 4 weeks p.i. All values are presented as mean ± SEM. Kruskal-Wallis followed by Dunn´s *post-hoc* test: * $p < 0.05$ vs. EVV group; # $p < 0.05$ vs. 24 h; & $p < 0.05$ vs. 72 h; && $p < 0.01$ vs. 72 h; $ $p < 0.05$ vs. 1 w p.i; + $p < 0.05$ vs. 2 w p.i. (**G**) Schematic representation of intact, damaged and degenerating mitochondria. (**H**) The proportion of intact, damaged and degenerating mitochondria in TH⁺ fibers in EVV and hα-syn groups. n = 6 (EVV), n = 4 in each time point evaluated.

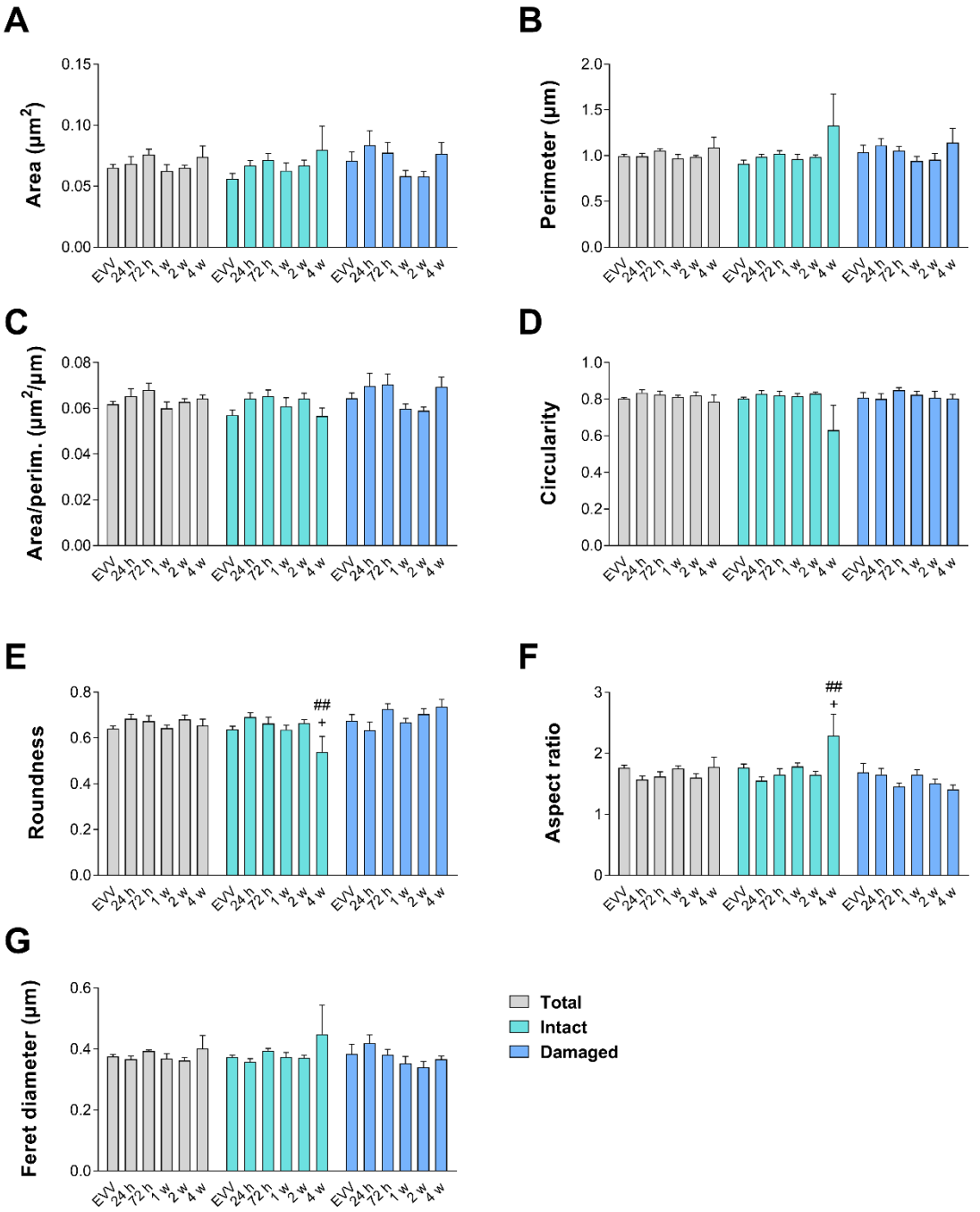

Figure 34: Analysis of average morphological parameters of the total, intact and damaged mitochondria inside TH⁺ fibers from EVV and hα-syn groups. (**A**) Area, (**B**) perimeter, (**C**) area/perimeter, (**D**) circularity, (**E**) roundness, (**F**) aspect ratio and (**G**) Feret diameter of the total, intact and damaged mitochondria from EVV and hα-syn group at 24 h, 72 h, 1, 2 and 4 weeks p.i. All values are presented as mean ± SEM. Kruskal-Wallis followed by Dunn´s *post-hoc* test for each type of mitochondria: ## $p < 0.01$ vs. 24 h; + $p < 0.05$ vs. 2 w p.i. n = 6 (EVV), n = 4 for each time point evaluated.

3.3 Ultrastructural alterations in asymmetric synapses

Dopaminergic terminals converge with glutamatergic terminals at the dendritic spines of striatal SPNs and an integrated crosslink between DA and glutamate plays an essential role in driving SPNs firing for a physiological motor behaviour (as described in section 2.1.5 of the introduction). Under the electron microscope, glutamatergic synapses, which are excitatory in function, are characterized by forming asymmetric synapses (AS). Thus, apart from studying the striatal dopaminergic component, the density and morphology of the different compartments (presynaptic terminal, PSD and postsynaptic target) of ASs within the dorsal striatum were also studied. For this purpose, three representative p.i. time points of hα-syn overexpression were selected: 72 h, 1 week and 4 weeks.

3.3.1 Density of asymmetric synapses and its subtypes: macular and perforated

No significant alterations in the density of ASs were found in the striatum of the hα-syn group compared with the EVV group or between time points (Figure 35D).

However, when classifying ASs of the hα-syn group into macular or perforated synapses (see section 5.3.2 of Materials and Methods), we observed an increase in the number of perforated synapses, considered structural intermediates in synaptic plasticity. The density of perforated AS reached a significant increment of 75 % at 1 week p.i. ($p < 0.05$ vs. EVV group) and 53 % at 4 weeks p.i. ($p < 0.05$ vs. EVV group) (Figure 35F). Between hα-syn time points, an increment of 98 % in the density of perforated AS was found at 1 week p.i. ($p < 0.05$ vs. 72 h p.i.).

No significant alterations in the density of macular ASs were found in the hα-syn group compared with the EVV group or between time points. (Figure 35E).

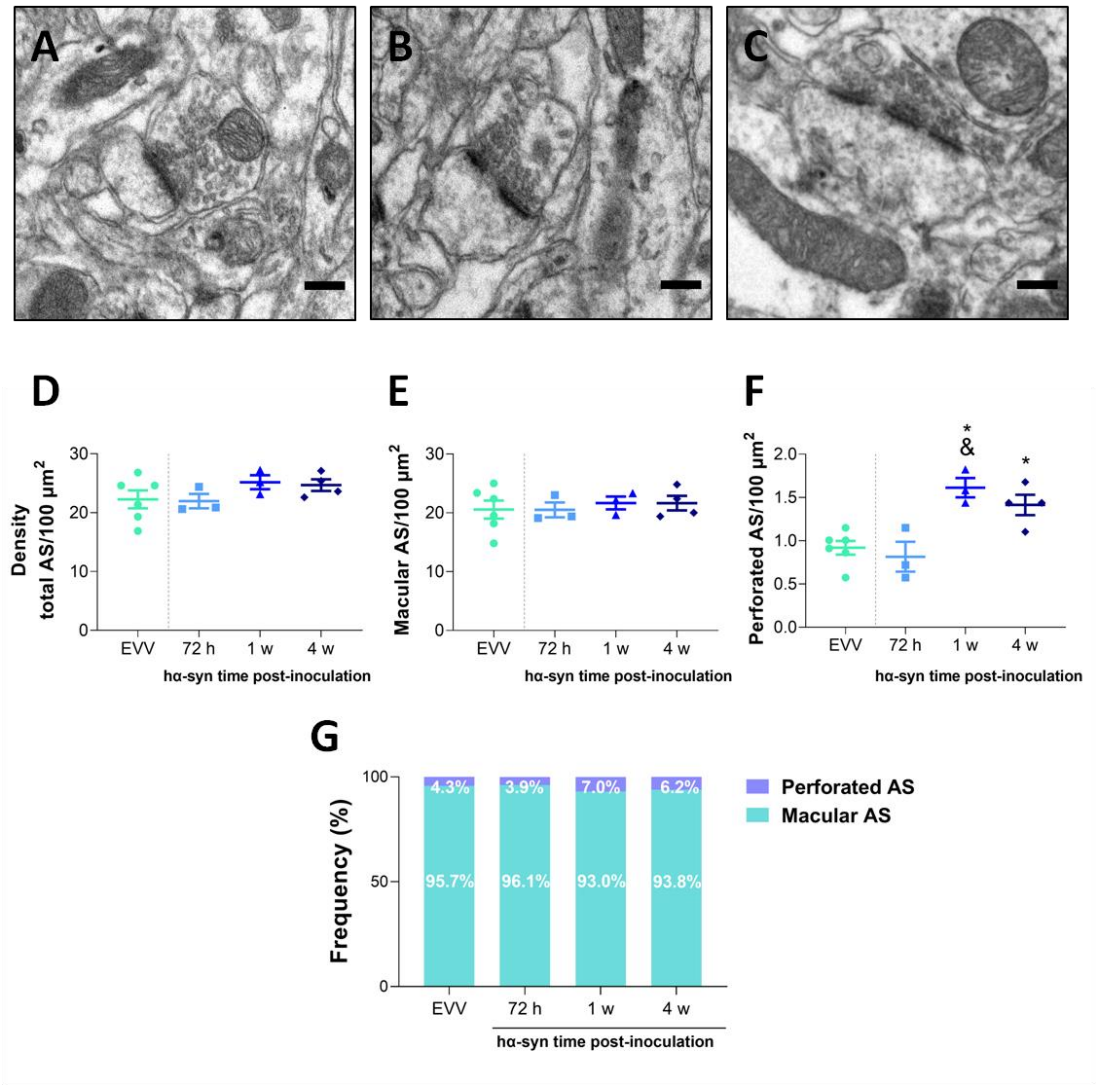

Figure 35: Density of asymmetric synapses. (**A**) Representative electron microscopy photomicrographs from the dorsal striatum of macular AS and (**B**) perforated AS with a single perforation and (**C**) with a double perforation. Scale bars, 200 nm. (**D**) The density of total ASs, (**E**) macular ASs and (**F**) perforated ASs per 100 µm² from EVV and hα-syn groups. All values are presented as mean ± SEM. Kruskal-Wallis followed by Dunn´s *post-hoc* test: * $p < 0.05$ and vs. EVV group; & $p < 0.05$ vs. 72 h p.i. (**G**) The proportion of perforated and macular AS (% total AS).

Table 9. Proportion of the different asymmetric synapses in EVV and hα-syn groups.

Group	Type of asymmetric synapse		
	Macular AS	Perforated AS	Total AS
EVV	95,72 % (2572)	4,28 % (115)	100 % (2687)
72 h	96,12 % (1263)	3,88 % (51)	100 % (1314)
1 w	93,07 % (1357)	6,93 % (101)	100 % (1458)
4 w	93,86 % (1806)	6,13 % (118)	100 % (1924)

* Data are expressed as percentages with the absolute number of synapses studied given in parentheses.

3.3.2 Presynaptic terminals forming asymmetric synapses (excitatory terminals)

3.3.2.1 Morphology

In the hα-syn group, no statistical differences were observed regarding the morphology (area, perimeter, area/perimeter ratio) of excitatory presynaptic terminals in the different time points in the hα-syn group compared with the EVV group or between time points (Figure 36; Table 10).

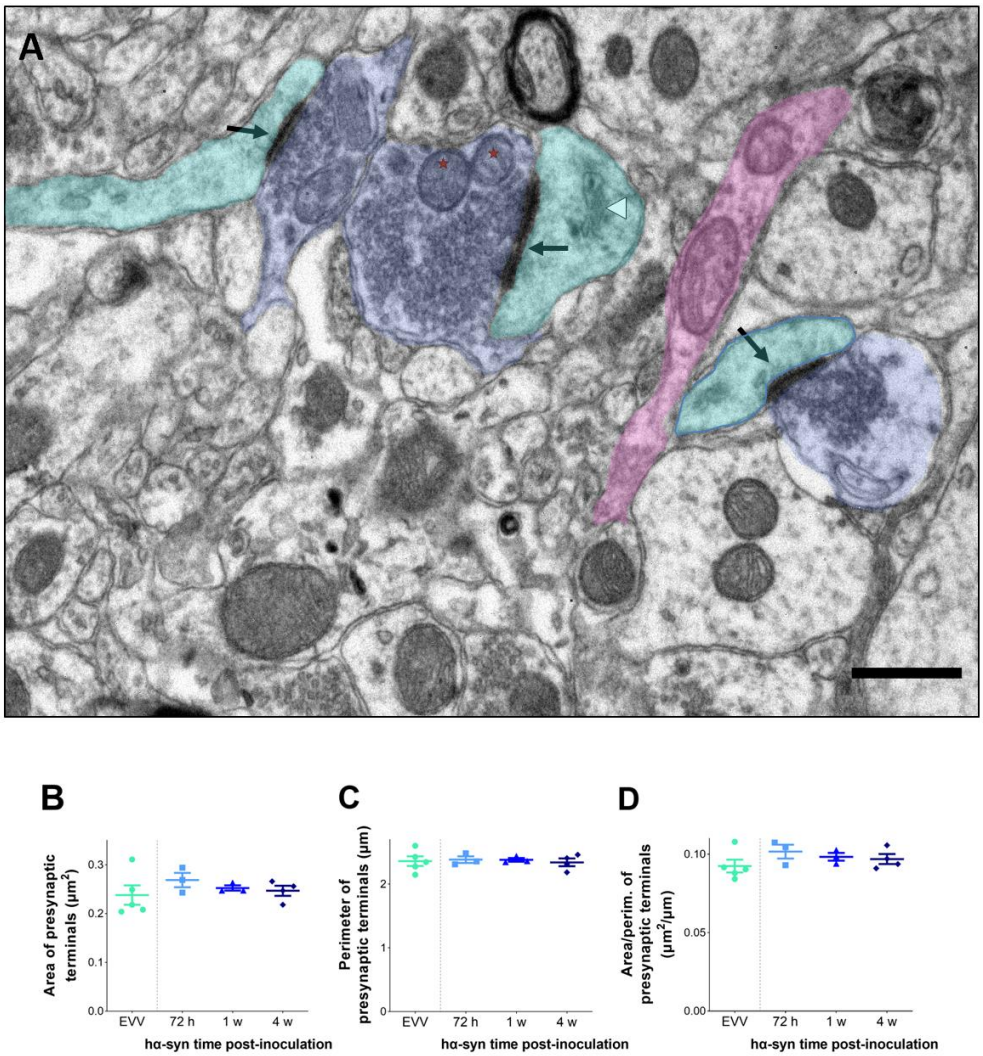

Figure 36: Excitatory presynaptic terminals. (**A**) Representative electron microscopy photomicrograph showing the different components of an AS: the presynaptic terminal (blue) with small and round synaptic vesicles and mitochondria (red stars) inside; the electrodense PSD (black arrows); the postsynaptic dendritic spine (turquoise), with the spiny apparatus (white arrowhead) inside, and the dendritic shaft (purple). Scale bar, 0.5 µm. **B-D**, Quantification of morphological parameters from excitatory presynaptic terminals of EVV and hα-syn groups: (**B**) area (μm^2), (**C**) perimeter (µm), (**D**) area/perimeter ratio (μm^2/ µm). All values are presented as mean ± SEM. No statistical differences (Kruskal-Wallis). n = 6 (EVV); n = 3 (72 h); n = 3 (1 w); n = 4 (4 w) animals.

Table 10: Detailed morphological data regarding area (µm²), perimeter (µm), and area/perimeter ratio (µm²/µm) of excitatory presynaptic terminals from EVV and hα-syn groups.

	Excitatory presynaptic terminal					
Group	Area (µm²)		Perimeter (µm)		Area/perimeter (µm²/µm)	
	Mean ± SEM	Range	Mean ± SEM	Range	Mean ± SEM	Range
EVV	0.238 ± 0.019	0.204-0.311	2.360 ± 0.075	2.147-2.600	0.092 ± 0.004	0.842-0.107
72 h	0.268 ± 0.014	0.243-0.294	2.384 ± 0.051	2.311-2.483	0.101 ± 0.004	0.093-0.107
1 w	0.252 ± 0.005	0.247-0.263	2.380 ± 0.028	2.344-2.437	0.098 ± 0.002	0.093-0.102
4 w	0.246 ± 0.010	0.218-0.266	2.341 ± 0.060	2.183-2.460	0.096 ± 0.003	0.091-0.105

3.3.2.2 Mitochondria

In the hα-syn group, an increment in the number of mitochondria within excitatory presynaptic terminals was observed at 4 weeks p.i. ($p < 0.05$ vs. EVV group; Figure 37A) but no significant changes were observed between time points in the hα-syn group (Figure 37A).

In addition, no alterations were observed in the proportion of intact, damaged and degenerating mitochondria in hα-syn time points compared to the EVV group or between time points (Figure 37B). There were no alterations in the distribution (Figure 38) of any morphological parameter of mitochondria within excitatory presynaptic terminals of the hα-syn group time points.

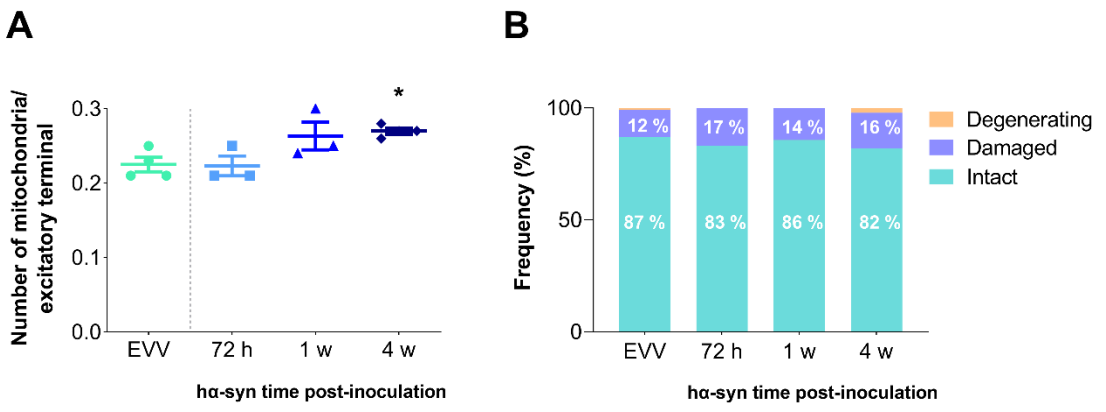

Figure 37: Mitochondria in excitatory presynaptic terminals. (**A**) Number of mitochondria per excitatory presynaptic terminal in EVV and hα-syn groups. All values are presented as mean ± SEM. Kruskal-Wallis followed by Dunn´s *post-hoc* test: * $p < 0.05$ vs. EVV group. (**B**) Proportion of intact, damaged and degenerating mitochondria (% total mitochondria) in EVV and hα-syn groups.

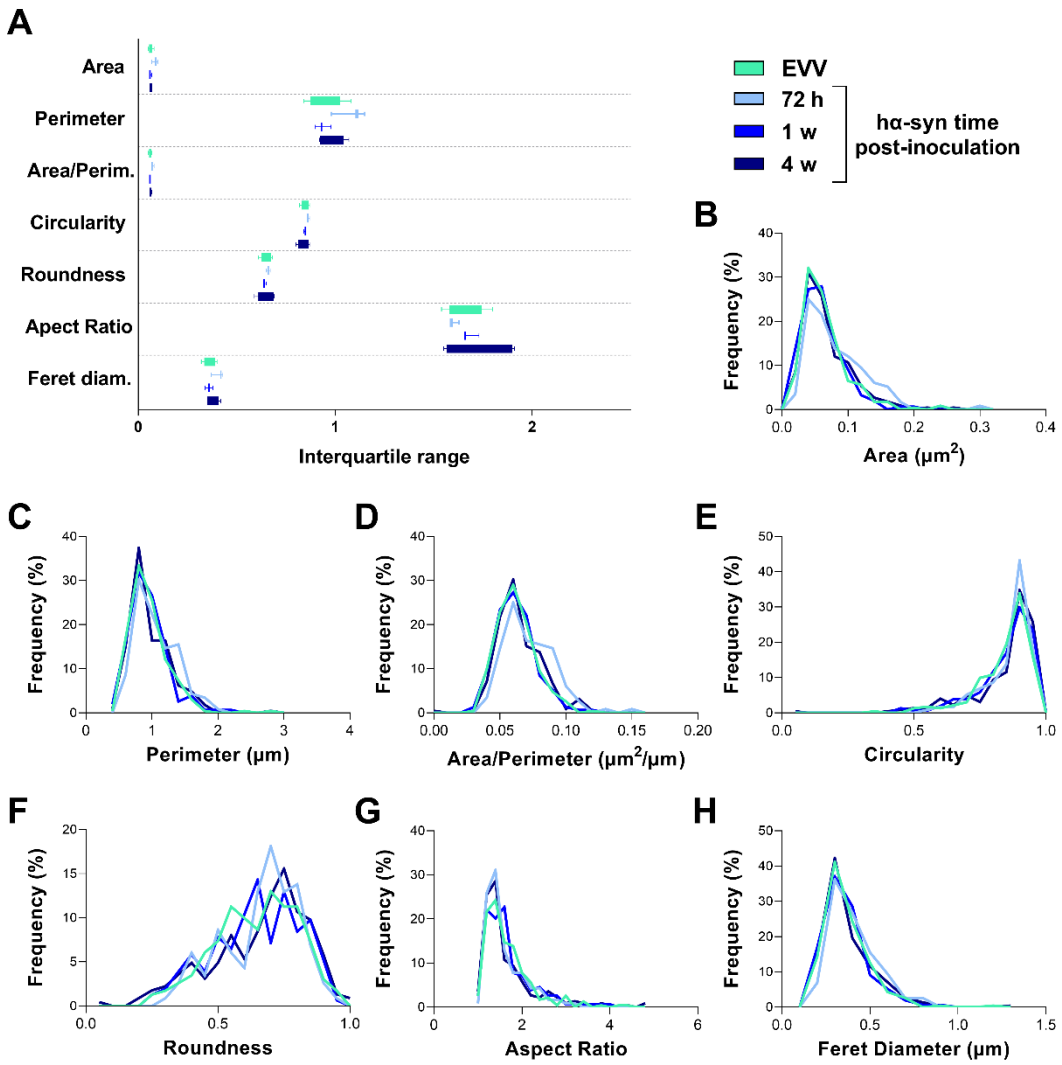

Figure 38: Analysis of the distribution of morphological parameters of mitochondria within excitatory presynaptic terminals. (**A**) Box plot graph representing mitochondrial morphological parameters from EVV and hα-syn groups. Bars represent the range of values that contain 50% of all mitochondria (interquartile range) for each parameter. (**B–H**) Frequency distribution histograms (% total mitochondria) for each morphological parameter: (**B**) area, (**C**) perimeter, (**D**) area/perimeter ratio, (**E**) circularity, (**F**) roundness, (**G**) aspect ratio, (**H**) Feret diameter. No statistical differences in the means (Kruskal-Wallis). n= 231 (EVV), n= 116 (72 h); n= 154 (1 w); n= 225 (4 w) mitochondria.

3.3.3 Postsynaptic density length of asymmetric synapses

The length of the postsynaptic density (PSD) that forms AS was also quantified (Figure 39; Table 11). In the hα-syn group, we did not find an alteration in the length of the PSD of either total AS or when classifying the PSD into macular or perforated compared with the EVV group or between time points (Figure 39).

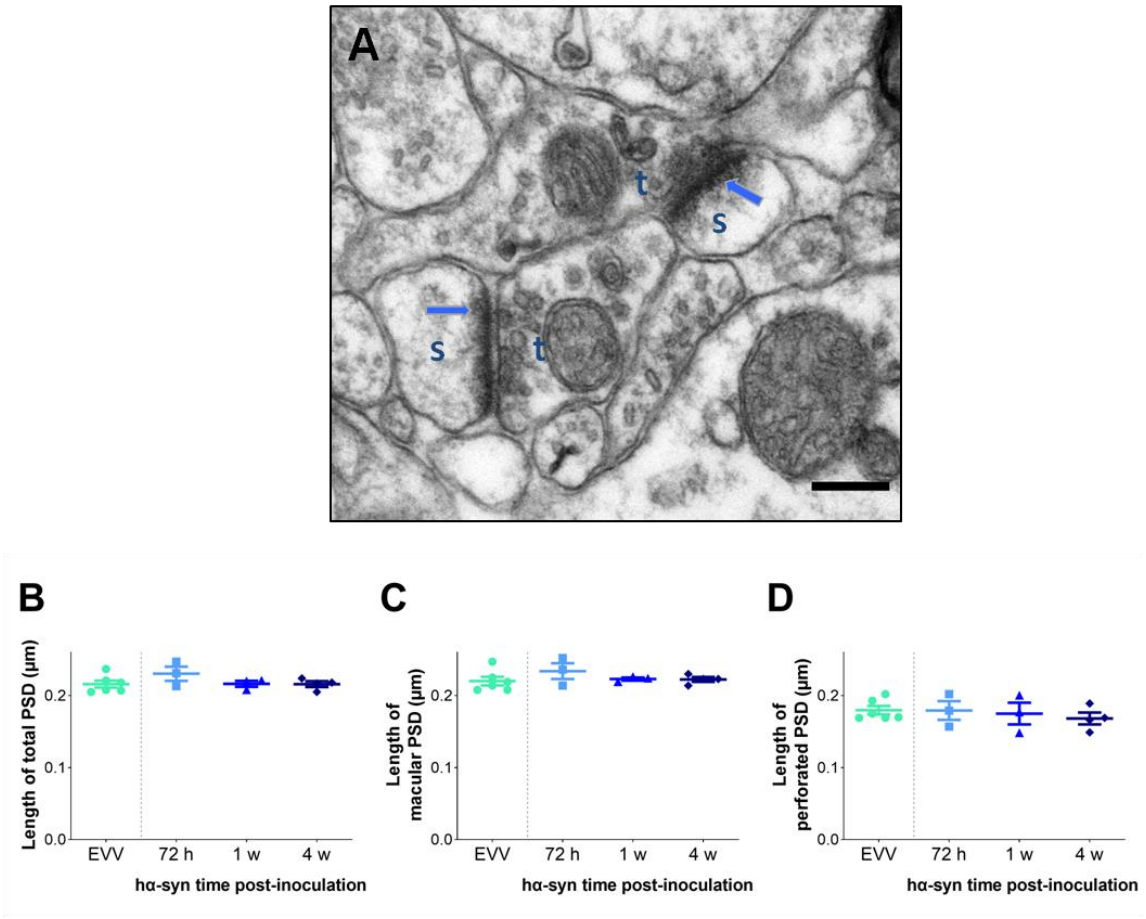

Figure 39: Postsynaptic density length of asymmetric synapses. (**A**) Electron microscopy photomicrograph showing the PSD (blue arrows) of an AS. (**B**) Average length of total PSD, (**C**) macular PSD and (**D**) perforated PSD of asymmetric synapses from EVV group and hα-syn group at 72 h, 1 week and 4 weeks p.i. All values are presented as mean ± SEM. No statistical differences in the means (Kruskal-Wallis). n = 6 (EVV), n = 3 (72 h), n = 3 (1 w), n = 4 (4 w) animals. Abbreviations: s, spine; t, synaptic terminal.

Table 11: Data regarding postsynaptic density length of asymmetric synapses.

		PSD Length (µm)		
Group		**Macular AS**	**Perforated AS**	**Total AS**
EVV	Mean ± SEM	0.2202 ± 0.0059	0.1797 ± 0.0058	0.2160 ± 0.0049
	Range	0.208 - 0.247	0.169 - 0.202	0.205 - 0.237
72 h	Mean ± SEM	0.2340 ± 0.0110	0.1793 ± 0.0129	0.2303 ± 0.0098
	Range	0.214 - 0.252	0.157 -0.202	0.213 - 0.247
1 w	Mean ± SEM	0.2230 ± 0.0020	0.1750 ± 0.0150	0.2163 ± 0.0041
	Range	0.219 - 0.226	0.148 - 0.200	0.208 - 0.221
4 w	Mean ± SEM	0.2225 ± 0.0032	0.1683 ± 0.0082	0.2160 ± 0.0039
	Range	0.214 - 0.230	0.149 - 0.189	0.205 - 0.224

3.3.4 Postsynaptic target proportion: dendritic spines vs. dendritic shaft

Two main postsynaptic targets were considered: dendritic spines (axospinous synapses, Figure 40A, turquoise arrows) and dendritic shafts (axodendritic synapses, Figure 40A, blue arrows). A reduction in the proportion of axospinous synapses and an increase in the proportion of axodendritic synapses were found in the striatum of the hα-syn group at 72 h ($p < 0.01$ vs. EVV) and 4 weeks p.i. ($p < 0.05$ vs. EVV) compared with the EVV group. No differences were found between time points (Figure 40B; Table 12).

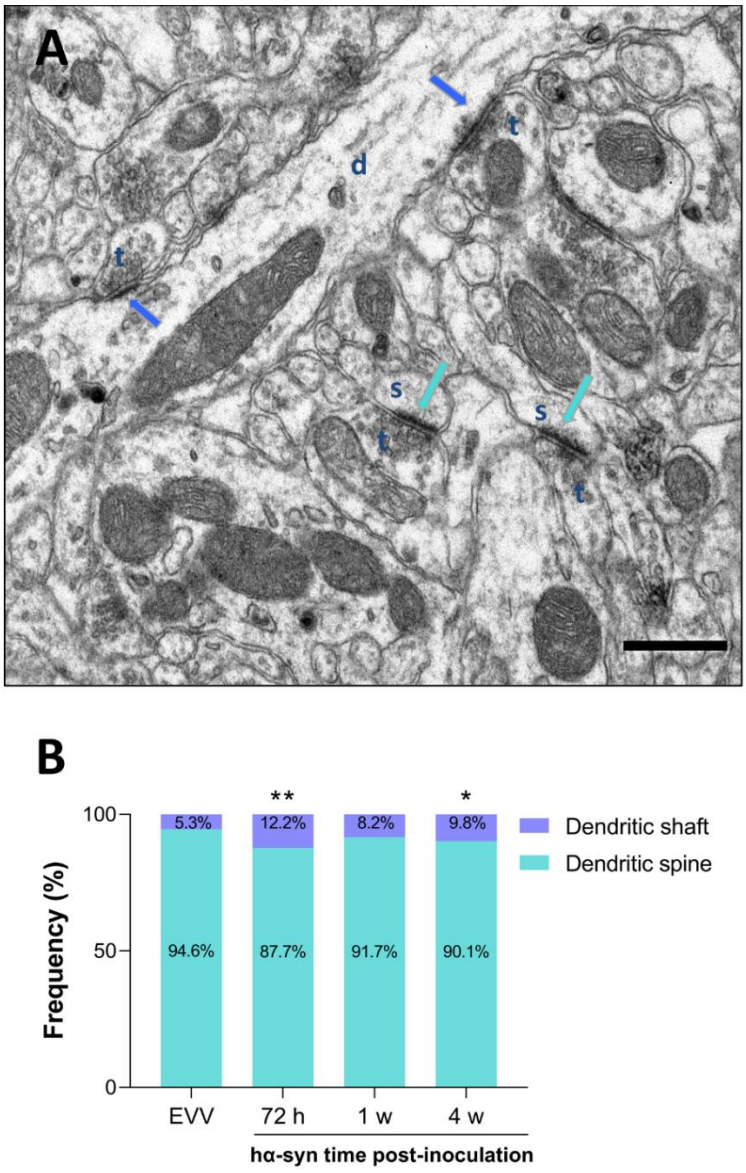

Figure 40. Postsynaptic targets of AS. (**A**) Electron microscopy photomicrograph showing AS on dendritic spines (turquoise arrows) and dendritic shafts (blue arrows). (**C**) Proportion of AS on dendritic spines and dendritic shafts. Scale bar, 0.5 µm. Kruskal-Wallis followed by Dunn´s *post-hoc* test for both types of targets: * $p < 0.05$ and ** $p < 0.01$ vs. EVV group. Abbreviations: d, dendritic shaft; s, dendritic spine; t, synaptic terminal.

Table 12: Proportion of postsynaptic targets of AS

	Type of postsynaptic target		
Group	**Dendritic spine**	**Dendritic shaft**	**Totals**
EVV	94.63 % (1304)	5.37 % (74)	100 % (1378)
72 h	87.76 % (595) **	12.24 % (83) **	100 % (678)
1 w	91.72 % (709)	8.28 % (64)	100 % (733)
4 w	90.18 % (928) *	9.82 % (101) *	100 % (1029)

* $p < 0.05$ and ** $p < 0.01$ vs. EVV group. Data are expressed as percentages with the absolute number of synapses studied given in parentheses.

3.4 Cross-sectioned myelinated axons

The dorsal striatum receives two main types of axonal inputs: glutamatergic and dopaminergic (as described in section 2.1.2 of the introduction). In this study, dopaminergic fibers were immunostained (TH^+; black staining) and it is known that dopaminergic axons are unmyelinated or thinly myelination (Sulzer and Surmeier, 2013), thus considering that the remaining non-immunostained and myelinated axons represent mainly glutamatergic axons. Under the electron microscope, cross-sectioned myelinated axons can be easily detected by their characteristic electrodense myelin sheet (Figure 41A, B). Thus, glutamatergic afferent projections to the dorsal striatum were also evaluated as a measure of compensatory glutamatergic mechanisms by the study of the density and morphology of cross-sectioned myelinated axons within the dorsal striatum. For this purpose, three representative p.i. time points of hα-syn overexpression were selected: 72 h, 1 week and 4 weeks.

In the hα-syn group, a tendency for an increase in the axon density was observed in the dorsal striatum at 4 weeks p.i. compared to the EVV group ($p = 0.07$ vs. EVV group; Figure 41C; Table 13). However, no alterations were found in their morphology (axon diameter, axon area, G-ratio and eccentricity) compared with the EVV group or between time points (Figure 41D-E; Table 13).

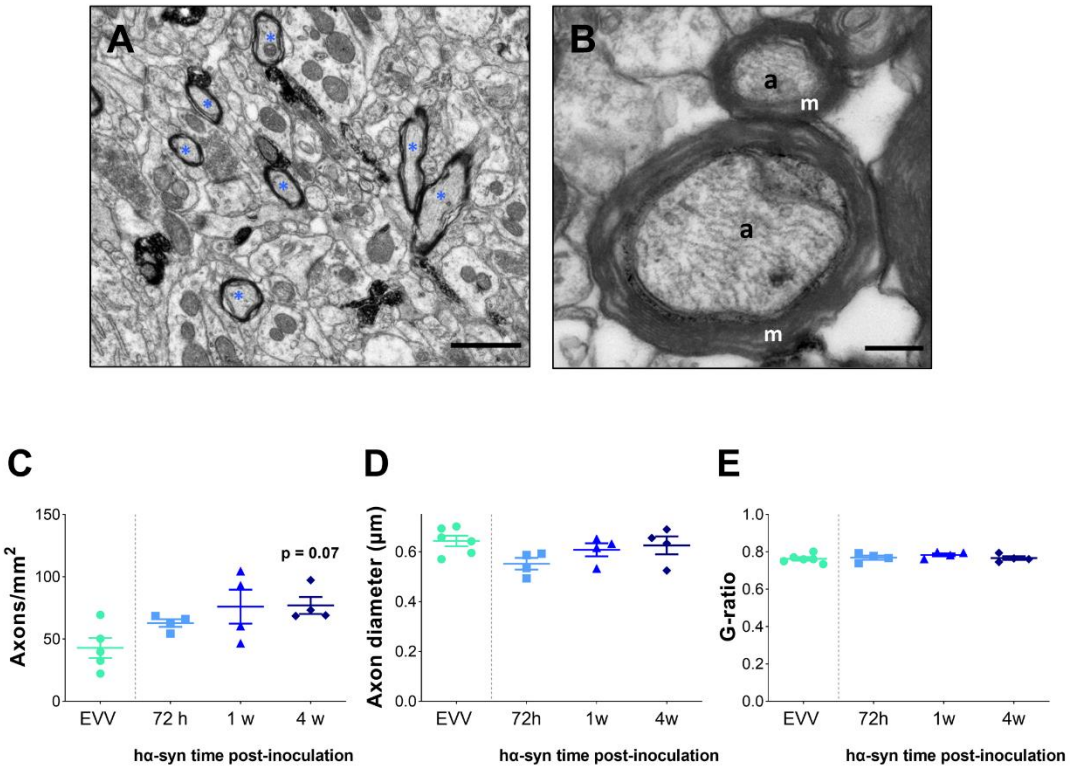

Figure 41. Density and ultrastructure of cross-sectioned myelinated axons in the dorsal striatum. (**A**) Representative electron micrograph from the dorsal striatum containing myelinated axons (blue asterisks). Scale bar, 1 µm. (**B**) High magnification electron micrograph showing axons (a) and the surrounding myelin sheat (m). Scale bar, 200 nm. (**C**) Axon density (number of axons per mm²) in the dorsal striatum of EVV group and hα-syn group at 72 h, 1 week and 4 weeks p.i. (**D**) Axon diameter (µm) and (**E**) G-ratio of myelinated axons from EVV group and hα-syn group at 72 h, 1 week and 4 weeks p.i. All values are presented as mean ± SEM. Kruskal-Wallis followed by Dunn´s *post-hoc* test: * p < 0.05 vs. EVV group. n = 6 (EVV), n = 4 (72 h), n = 4 (1 w), n = 4 (4 w) animals.

Table 13. Density and morphometric data of myelinated axons in dorsal striatum from EVV and hα-syn groups.

		Myelinated Axons			
Parameter		**EVV**	**72 h**	**1 w**	**4 w**
Density (axons/mm²)	Mean ± SEM	47.85 ± 8.23	62.84 ± 3.08	76.07 ± 13.58	77.03 ± 6.83
	Range	22.33 - 72.60	54.43 - 68.52	46.48 - 104.5	68.52 - 97.27
Axon diameter (µm)	Mean ± SEM	0.644 ± 0.021	0.552 ± 0.023	0.608 ± 0.026	0.626 ± 0.035
	Range	0.571 - 0.702	0.494 - 0.593	0.533 - 0.652	0.525 - 0.690
Axon area (µm²)	Mean ± SEM	0.188 ± 0.012	0.159 ± 0.014	0.168 ± 0.010	0.169 ± 0.011
	Range	0.151 - 0.236	0.121 - 0.187	0.144 - 0.193	0.136 - 0.188
G-ratio	Mean ± SEM	0.763 ± 0.009	0.769 ± 0.011	0.784 ± 0.008	0.766 ± 0.010
	Range	0.734 - 0.801	0.739 - 0.792	0.761 - 0.798	0.745 - 0.794
Eccentricity	Mean ± SEM	0.750 ± 0.022	0.707 ± 0.025	0.752 ± 0.019	0.772 ± 0.025
	Range	0.688 - 0.836	0.631 - 0.736	0.710 - 0.799	0.733 - 0.844

4. Three-dimension dendritic spine analysis of spiny projection neurons from dorsal striatum

4.1 Experimental design

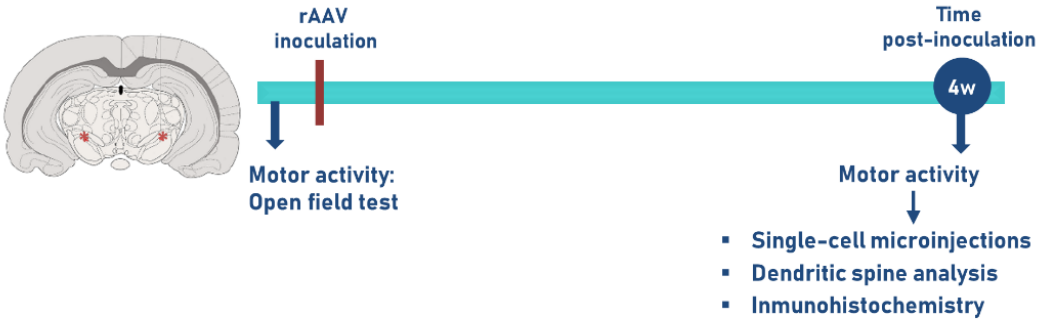

Figure 42: Experimental design of the dendritic spine analysis of spiny projection neurons. Animals were inoculated with either rAAV-hα-syn or rAAV-EVV bilaterally in the SN_{pc}. Motor activity was assessed before surgery (basal) and at 4 weeks p.i. Subsequently, animals were sacrificed and perfused. Brains were removed and coronal slices from dorsal striatum were acquired for microinjection of spiny projection neurons (SPNs) and a 3D dendritic spine analysis was performed. Finally, the degeneration of the dopaminergic system was evaluated by immunohistochemistry.

To study the postsynaptic compartment of the striatal synapses where dopaminergic and glutamatergic terminals converge, a detailed dendritic spine analysis has been carried out. For this part of the doctoral thesis, only the last p.i. time point (4 w p.i.) has been studied, as several significant ultrastructural alterations in the dopaminergic terminals, as well as a significant dopaminergic neurodegeneration, were observed in this time point in the previous experiments. Thus, for this purpose, animals were inoculated with rAAV-hα-syn or rAAV-EVV and were sacrificed at 4 weeks p.i. (Figure 42).

4.2 Evaluation of the motor activity: Open field test

In order to verify that animals did not present motor alterations at 4 weeks p.i. another behavioural test was performed, that additionally analyzed anxiety-like behaviour.

No differences in any of the locomotion variables (distance, velocity, % of time spent in the center and % of time spent moving) were found in the EVV and hα-syn groups relative to their basal or between groups (Figure 43).

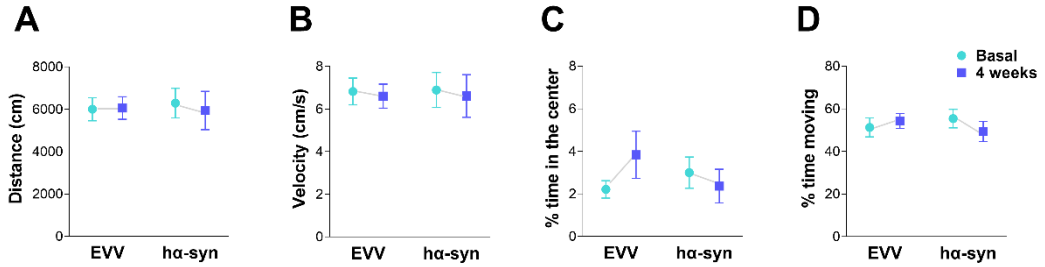

Figure 43. Evaluation of the motor activity. The open field test was performed before surgery (basal) and at 4 weeks p.i. in EVV and hα-syn groups. Different locomotion parameters were analyzed: (**A**) distance (cm), (**B**) velocity (cm/s), (**C**) % time spent in the center and (**D**) % time spent moving. All values are shown as the mean ± SEM. No statistical differences (Two-way ANOVA).

4.3 Dendritic spine density

The hα-syn group showed a significant loss of total dendritic spines in SPNs from the dorsal striatum at 4 weeks p.i. compared to the EVV group ($p < 0.01$ vs. EVV group; Figure 44C; Table 14).

This overall hα-syn overexpression related loss was driven entirely by a loss of thin spines ($p < 0.01$ vs. EVV group; Figure 44D). No statistical differences were observed between groups in the density of mushroom, stubby, filopodia or branched subtypes (Figure 44D, E). Due to the low abundance of branched and filopodia, they were not considered for the following morphological studies.

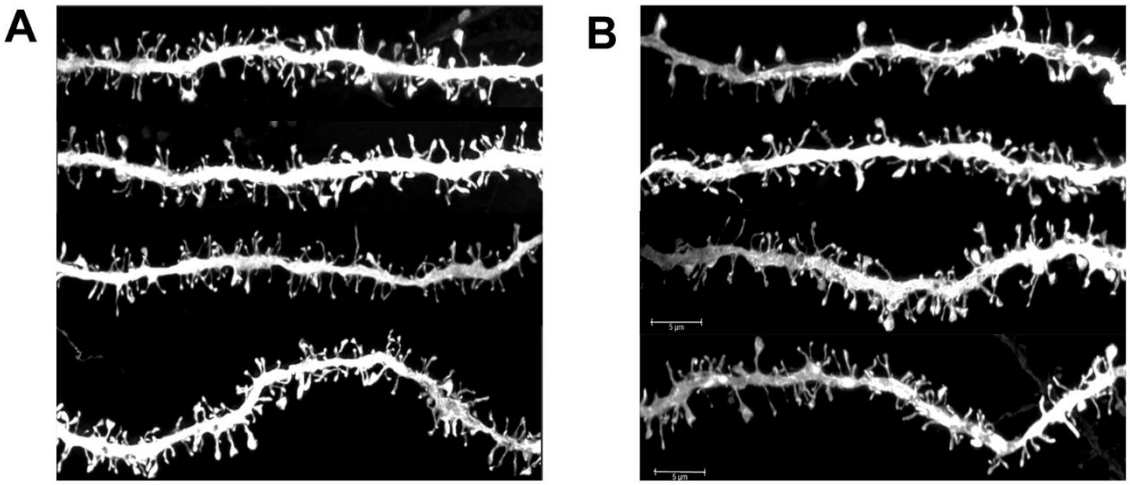

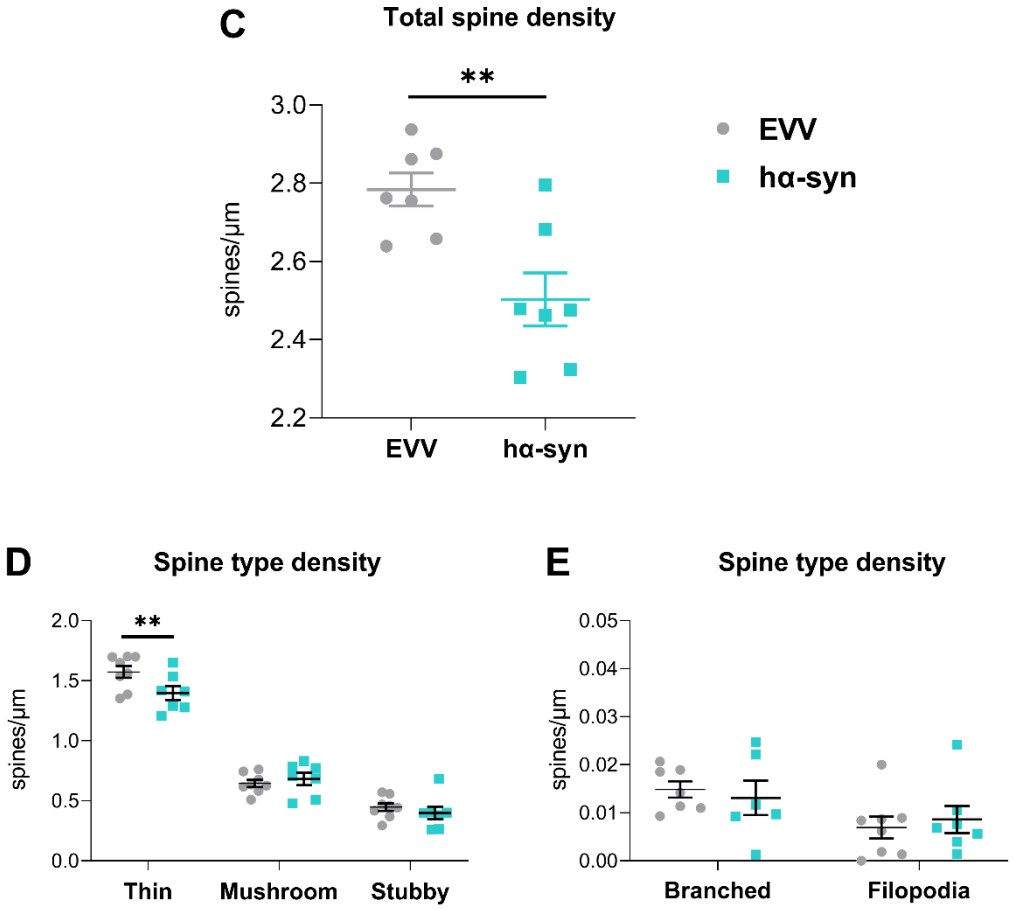

Figure 44: Dendritic spine density of SPNs from dorsal striatum at 4 weeks p.i. (**A-B**) Representative dendritic segments from (**A**) the EVV group and (**B**) the hα-syn group at 4 w p.i. Scale bars, 5 µm. (**C**) Total dendritic spine density of EVV and hα-syn groups. (**D**) Spine density of thin, mushroom and stubby spine subtypes and (**E**) branched and filopodia spine subtypes of EVV and hα-syn groups. Values are presented as mean ± SEM. Unpaired t-test: ** $p < 0.01$ vs. EVV group.

4.4 Dendritic spine morphology

Different morphological parameters of individual spines were examined to assess hα-syn overexpression related changes in spine size.

In the hα-syn group, results showed larger spine head volumes compared with the EVV group ($p < 0.01$ vs. EVV group; Figure 45A; Table 14). This overall grater spine head size was due to an increase in thin ($p < 0.01$ vs. EVV group) and mushroom ($p < 0.05$ vs. EVV group) spine head volumes (Figure 45A; Table 14).

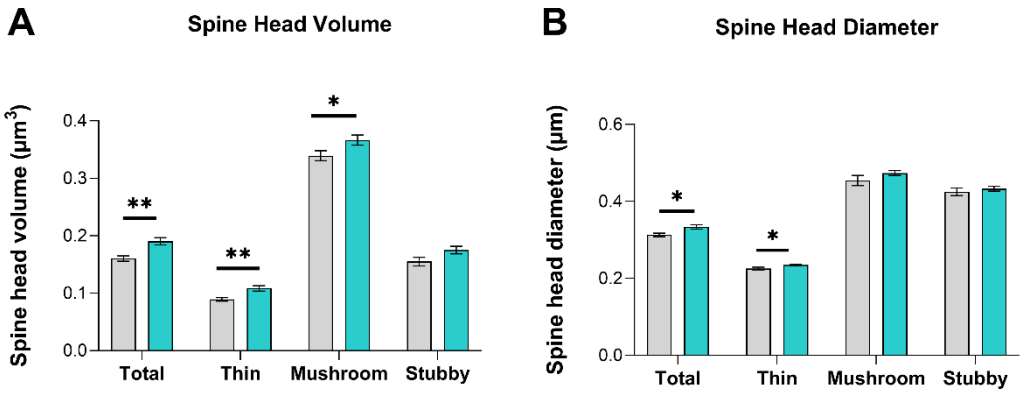

Figure 45: Dendritic spine head volume and diameter of SPNs from dorsal striatum at 4 weeks p.i. (**A**) Spine head volume and (**B**) spine head diameter of total spines and spine subtypes (thin, mushroom and stubby) from EVV and hα-syn groups. Values are presented as mean ± SEM. Unpaired t-test: * $p < 0.05$; ** $p < 0.01$ vs. EVV group.

As expected, the hα-syn group had also a larger spine head diameter compared with the EVV group ($p < 0.05$ vs. EVV group; Figure 45B). However, this overall grater spine head diameter was just related to an increase in thin spine head diameter ($p < 0.05$ vs. EVV group; Figure 45B; Table 14).

No statistical differences were observed in spine neck length and neck diameter between groups when comparing the overall spines or when classifying the different spine subtypes (Table 14).

4.5 Confirmation of hα-syn overexpression

The expression of the hα-syn protein in the SN_{pc} of the hα-syn group was confirmed by immunohistochemistry at 4 weeks p.i. No expression of hα-syn was observed in the EVV group (Figure 46).

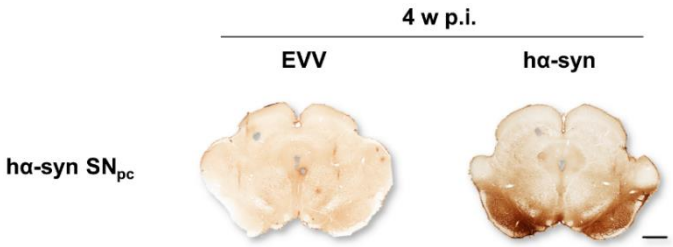

Figure 46: Expression of hα-syn. Representative photomicrographs showing hα-syn overexpression in the SN_{pc} of the hα-syn group at 4 weeks p.i.

4.6 Evaluation of the dopaminergic degeneration in the SN_{pc} and striatum

In the hα-syn group, there was a significant reduction in the number of TH^+ dopaminergic neurons in the SN_{pc} at 4 weeks p.i. compared to the respective EVV group (20%; $p < 0.05$ vs. EVV group; Figure 47A).

A reduction of striatal TH expression was observed at 4 weeks p.i. compared to the EVV group (38% reduction, $p < 0.01$ vs. EVV group; Figure 47B), as well as DAT expression, which was also significantly decreased at 4 weeks p.i. compared to the EVV group (22% reduction, $p < 0.05$ vs. EVV group; Figure 47C).

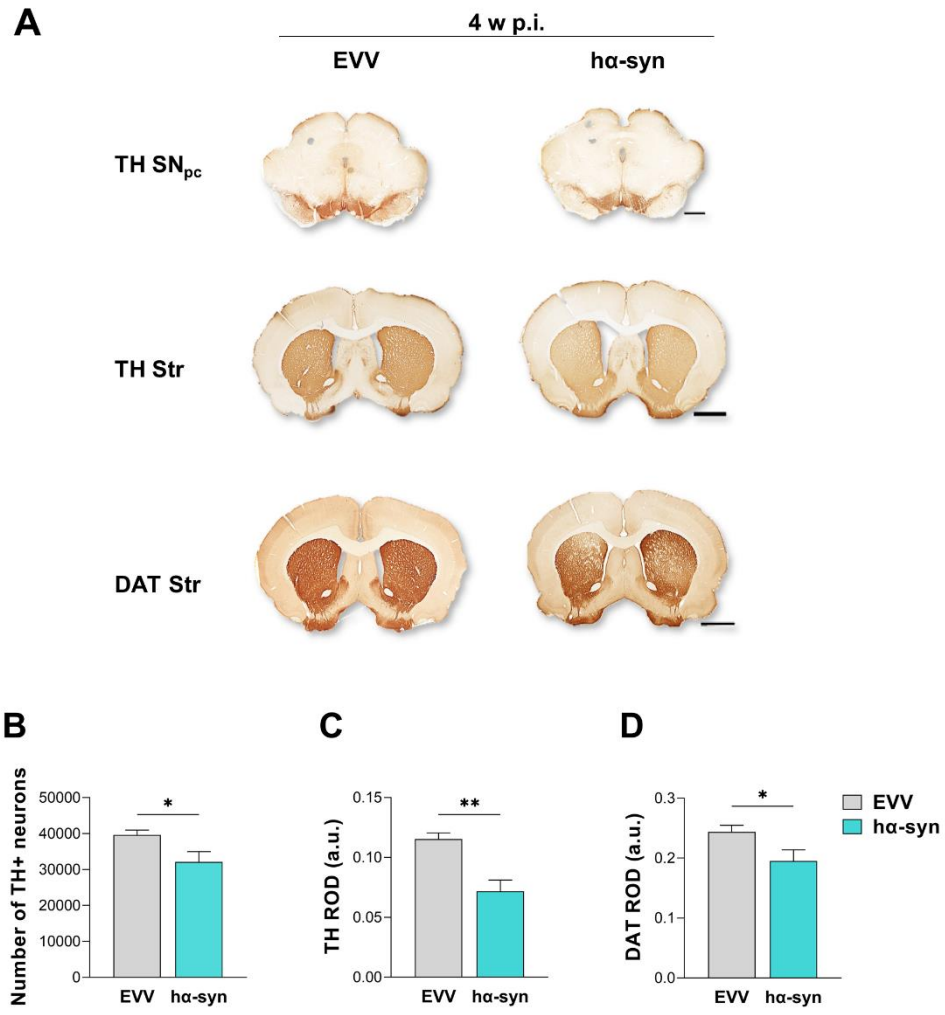

Figure 47: **Dopaminergic denervation in the SN_{pc} and striatum at 4 weeks p.i.** (**A**) Representative photomicrographs showing TH and DAT immunostaining in SN_{pc} and striatum from EVV and hα-syn groups. (**B**) Stereological quantification of the number of TH^+ neurons in the SN_{pc} from EVV and hα-syn groups (**C**) ROD values of TH and (**D**) DAT expression in the striatum from EVV and hα-syn groups. Values are presented as mean ± SEM. Unpaired t-test: * $p < 0.05$ and ** $p < 0.01$ vs. EVV group.

Table 14: Data from density and morphological parameters of dorsal striatal dendritic spines of SPNs from EVV and hα-syn groups at 4 weeks p.i.

	EVV		hα-syn	
Parameter	mean ± SEM	Range	mean ± SEM	Range
Spine density (spines/µm)				
Total	2.784 ± 0.042	2.639 - 2.937	2.503 ± 0.067**	2.303 - 2.795
Thin	1.573 ± 0.049	1.353 - 1.701	1.398 ± 0.058**	1.205 - 1.649
Mushroom	0.644 ± 0.029	0.509 - 0.761	0.680 ± 0.051	0.477 - 0.831
Stubby	0.447 ± 0.032	0.293 - 0.570	0.397 ± 0.052	0.260 - 0.680
Branched	0.014 ± 0.001	0.009 - 0.020	0.013 ± 0.003	0.001 - 0.024
Filopodia	0.006 ± 0.002	0 - 0.020	0.008 ± 0.002	0.001 - 0.022
Spine head volume (µm³)				
Total	0.160 ± 0.004	0.146 - 0.186	0.190 ± 0.006**	0.171 - 0.216
Thin	0.089 ± 0.003	0.080 - 0.106	0.108 ± 0.004**	0.093 - 0.128
Mushroom	0.339 ± 0.008	0.304 - 0.362	0.366 ± 0.008*	0.327 - 0.402
Stubby	0.155 ± 0.007	0.135 - 0.182	0.175 ± 0.006	0.156 - 0.198
Spine head diameter (µm)				
Total	0.313 ± 0.004	0.302 - 0.336	0.333 ± 0.005*	0.310 - 0.354
Thin	0.225 ± 0.003	0.218 - 0.247	0.235 ± 0.001*	0.228 - 0.241
Mushroom	0.454 ± 0.013	0.425 - 0.526	0.474 ± 0.006	0.454 - 0.505
Stubby	0.425 ± 0.009	0.396 - 0.479	0.433 ± 0.006	0.412 - 0.458
Spine neck length (µm)				
Total	1.347 ± 0.029	1.276 - 1.492	1.386 ± 0.021	1.283 - 1.435
Thin	1.382 ± 0.025	1.318 - 1.511	1.419 ± 0.014	1.368 - 1.472
Mushroom	1.673 ± 0.035	1.579 - 1.859	1.687 ± 0.018	1.621 - 1.763
Stubby	0.668 ± 0.123	0.622 - 0.714	0.701 ± 0.011	0.664 - 0.759
Spine neck diameter (µm)				
Total	0.162 ± 0.005	0.139 - 0.189	0.175 ± 0.010	0.151 - 0.228
Thin	0.077 ± 0.002	0.065 - 0.083	0.085 ± 0.005	0.067 - 0.100
Mushroom	0.165 ± 0.003	0.151 - 0.179	0.175 ± 0.007	0.149 - 0.200
Stubby	0.474 ± 0.011	0.444 - 0.541	0.479 ± 0.007	0.448 - 0.515

* $p < 0.05$ and ** $p < 0.01$ vs. EVV group.

Table 15: Summary of the main results obtained in this study in the hα-syn group. Significant increases are shown in green and significant decreases in red. Abbreviations: na, not available.

		hα-syn p.i. time-point				
		24 h	**72 h**	**1 w**	**2 w**	**4 w**
rAAV-A53T-hα-syn model						
hα-syn SN_{pc}		-	↑ ns	↑↑	↑↑	↑↑
hα-syn Str		-	-	↑↑	↑↑↑	↑
TH/DAT^+ Str		-	-	-	↓	↓↓
TH^+ SN_{pc}		-	-	-	-	↓
Functional alterations of striatal synaptosomes						
Mitochondrial respiration		na	-	↓	na	↓↓
Stressed ECAR		na	-	-	na	↓
Protein deregulation		na	↑	↑	na	↑↑
Main deregulated biological processes and related structures		na	Metabolism	Mitochondria Metabolism Autophagy Morphogenesis	na	Postsynaptic density Focal adhesion Endocytosis Transport Translation and ribosomes
Structural alterations of striatal terminals						
Dopaminergic fibers	Density	-	-	-	↓	↓↓↓
	Morphology	-	-	-	-	↑↑
	Mitochondrial defects	-	-	-	-	↑↑
	Electroclear vesicles	-	-	-	↑	↑
Glutamatergic synapses	% Perforated AS	na	-	↑↑	na	↑
	Presynaptic mitochondria	na	-	-	na	↑
	Length PSD	na	-	-	na	-
	% Axospinus synapse	na	↓	-	na	↓
Dendritic spines	Density	na	na	na	na	↓
	Head volume	na	na	na	na	↑

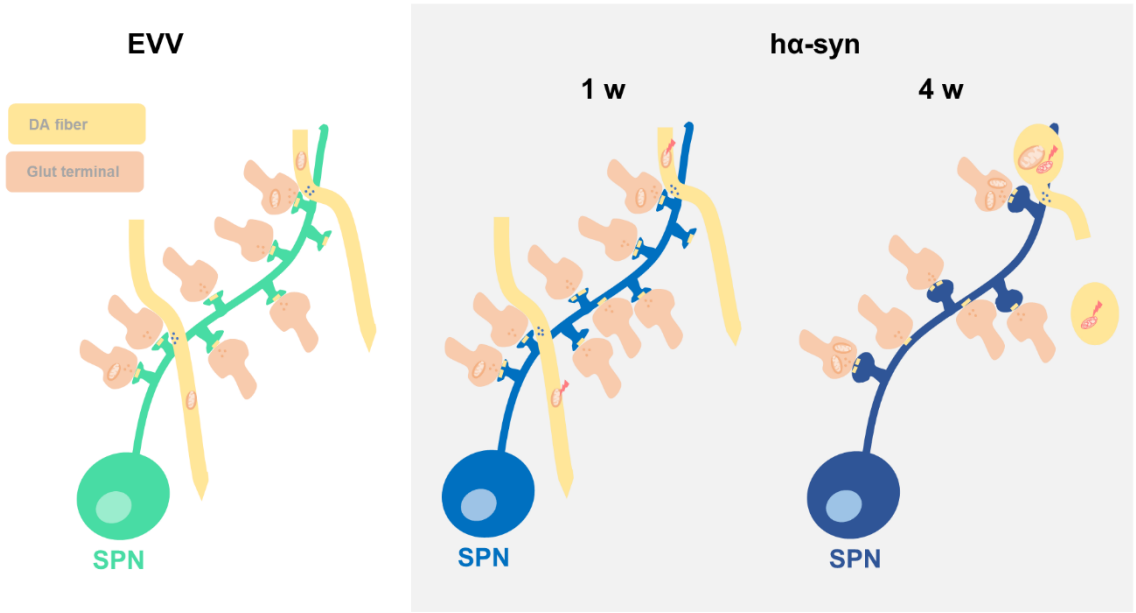

Figure 48: Schematic representation of the synaptic alterations described in representative groups of this study. In the hα-syn group, at 1 w p.i. synaptic mitochondria were functionally altered, and several deregulated mitochondrial proteins were observed, as well as an increase in perforated synapses compared to the EVV group. At 4 w p.i. a severe reduction in synaptic mitochondrial respiration was observed in the hα-syn group compared to the EVV group. Additionally, a reduction in dopaminergic fibers was observed with an increase in the size of remaining fibers and mitochondrial ultrastructural defects inside. Regarding excitatory asymmetric synapses, an increase in perforated synapses, in the number of mitochondria within presynaptic terminals and in the proportion of axodendritic synapses was observed in the hα-syn group at 4 w p.i. compared to the EVV group. Lastly, a reduction in dendritic spine density with an increase in their sizes was observed in this group.

DISCUSSION

This doctoral thesis has focused on elucidating the temporal relationship between the presence of hα-syn in the striatal terminals and the early synaptic changes at a functional and structural level induced by hα-syn overexpression with the A53T mutation in SN_{pc}. We have analyzed the pre- and postsynaptic compartments.

1. Temporal sequence of the overexpression of hα-syn and its relation with motor behaviour and dopaminergic degeneration

To date, few studies have analyzed synaptic abnormalities that take place at the beginning and progression of the neurodegenerative process in animal models of PD. Most studies on synapse have been performed using traditional neurotoxin-based models that induce an acute and massive loss of dopaminergic terminals that limits their validity to study the prodromal phases of PD and the onset of the neurodegenerative progress (Graves and Surmeier, 2019; Ingham et al., 1989; Suarez et al., 2016; Villalba et al., 2015; Villalba and Smith, 2018). Other studies have been undertaken in transgenic models of ubiquitous overexpression of native or mutated α-syn. However, in these models the dopaminergic neurodegeneration was absent or was not studied, motor alterations were questionable, and there was a lack of α-syn inclusions in the nigrostriatal system in most cases (Blumenstock et al., 2017; Garcia-Reitböck et al., 2010; Janezic et al., 2013; Nemani et al., 2010; Parajuli et al., 2020).

The rAAV-hα-syn either with WT or mutated (A53T or A30P) are well-established models and the best choice to investigate synaptic alterations taking place at the onset of parkinsonism. These models produce a progressive dopaminergic degeneration (Bourdenx et al., 2015; Decressac et al., 2012; Lindgren et al., 2012; Ulusoy et al., 2010) reproduce the parkinsonian phenotype and the formation of hα-syn aggregates in dopaminergic cell bodies and neurites (Bourdenx et al., 2015; Chung et al., 2009; Gorbatyuk et al., 2008; Jiménez-Urbieta et al., 2019; Kirik et al., 2002; Rodríguez-Chinchilla et al., 2020). However, most of the studies have been focused on a mid-stage of the dopaminergic neurodegeneration (>50% cell loss), mimicking the disease at the moment of PD diagnosis but not evaluating the previous stages where motor signs have not manifested yet and the dopaminergic system pathology is starting. Furthermore these studies are based on unilateral dopaminergic lesion, which can be not appropriate due to the functional compensation by the unaffected side of the brain (Jedrzejewska et al., 1990) as the presence of 5–10% crossed nigrostriatal pathways that project to the contralateral striatum have been reported in adult rats (Gerfen et al., 1982). Lastly, these studies have been mainly centered on the alterations that take place in the cell bodies of the SN_{pc}, paying less attention

to the pathophysiological alterations occurring in the synaptic terminals (see Table 1 in the introduction).

For these reasons and differentially from previous studies on synapse, our study shows that bilateral inoculation of rAAV-A53T-hα-syn causes a progressive hα-syn expression in SN_{pc} and striatum that is significant from 1st week onward. In parallel, a mild and progressive bilateral loss of dopaminergic neurons is observed in the SN_{pc} being significant at the 4th week p.i. (31% cell loss) and in the striatum with a progressive loss of TH^+ and DAT^+ fibers from the 2nd week onwards (25% and 22%; 48% and 55% at 4 weeks p.i., respectively). Interestingly, this dopaminergic loss is not associated with impairment in motor activity, measured by the stepping and the open field test. This result is consistent with a previous study from our research group with the same animal model, where the progressive motor impairment was significant from 7th week p.i. onwards (Jiménez-Urbieta et al., 2019).

These data support that this model resembles the earliest stage of PD, where subjects do not show motor alterations yet, although the neurodegenerative process has already been initiated and cell loss is minimal (Burke and O'Malley, 2013). Additionally, the mild but time-dependent neurodegeneration and the associated hα-syn pathology in the regions that are specifically affected in PD such as the striatum and the SN_{pc}, validate this model for the study of the main objectives of this doctoral thesis. Thus, our data indicate that the rAAV-hα-syn model used in this doctoral thesis, can provide insights into the study of synaptic changes before and when dopaminergic degeneration is starting but antedating motor signs. This temporal window constitutes a unique opportunity to study the earliest deficits leading to progressive neuronal death, which have never been previously assessed.

2. The temporal sequence of synaptic functionality and its relation with overexpression of hα-syn before the dopaminergic degeneration

Synaptosomal preparations are ideally suited for the metabolic and proteome assessment of brain tissue from experimental animals as they contain all the synaptic and metabolic machinery, including presynaptic terminal mitochondria and proteins involved in synaptic function. Thus, this doctoral thesis work describes for the first time the temporal pattern of mitochondrial bioenergetics and glycolysis, as well as changes in proteostasis, concerning their progressive interaction with hα-syn accumulation in striatal synaptosomes. Individual proteins

from the deregulated protein list with potential links to PD or neurodegeneration were selected by extensive literature search, and those with high relevance are detailed below.

2.1 The overexpression of hα-syn in the SN_{pc} is leading to alterations in proteostatis and homeostatic changes in the striatal synapses at 72h p.i.

These are the earliest changes observed by hα-syn overexpression in the SN_{pc}. Pathological accumulation of hα-syn in dopaminergic cell somas of the SN_{pc} at 72 h p.i. influenced the physiological status of the striatal synaptic terminals by protein deregulation affecting mainly cell metabolism, even in the absence of hα-syn in the striatal terminals. Interestingly, although metabolic misbalance seems to be starting, an intact bioenergetic function was observed, giving clues about the first pathways acting downstream of hα-syn overexpression that may trigger the deregulation of other proteins as well as functional and structural alterations in later time points. In this sense, a reduction in the proportion of axospinous synapses and the downregulation of proteins involved in spine formation such as Elmo1 (Kim et al., 2011) is observed in this time point. These results are consistent with previous observations referring to the fact that α-syn overexpression induces abnormalities in spine dynamics (Blumenstock et al., 2017).

More in-depth, at 72 h p.i., there is a significant impairment in several proteins (Dmp1, Stt3b, Prkag2, and Ttr) that participate in chemical reactions and pathways involving organic hydroxyl compound. Among these proteins, Dpm1 and Stt3b, are two downregulated proteins involved in protein modification pathways, specifically in protein glycosylation. Glycosylation defects can significantly influence the function of neurotransmitter receptors and transporters (Scott and Panin, 2014). Interestingly, aberrant glycosylation has been related to a decrease in DAT membrane expression, as well as an imbalance between the functional vs. dysfunctional (or less efficient) receptor populations. These alterations result in an accumulation of DA in the synaptic cleft, thus contributing to an increase in ROS formation that leads to an oxidative stress condition (Videira and Castro-Caldas, 2018). This oxidative stress condition is also supported by the fact that Ttr (transthyretin) is the most upregulated protein at 72 h and a positive correlation between oxidative stress and Ttr expression has been reported (Sharma et al., 2019; Wong et al., 2019). Furthermore, increased levels of Ttr may help to clear hα-syn aggregates, as it has been described with β-amyloid deposits in AD (Nilsson et al., 2018). Upregulation of Prkag2, the γ2 regulatory subunit of AMP-activated protein kinase, which acts as a sensor of cellular energy status and is activated during metabolic stress, not only supports the mentioned stress condition

but also suggests that hα-syn overexpression is triggering an energetic deficit since the earliest stages, which becomes accentuated in the following time points. Of note, it has been proposed as a biomarker for early PD (Sun et al., 2014). Lpcat4 is another significantly reduced metabolic enzyme involved in remodeling lysophospholipids, that catalyzes the conversion of lysophosphatidylcholine (LPC) to phosphatidycholine (PC), which participate in signal transduction and control synaptic neurotransmission and plasticity (García-Morales et al., 2015). Therefore, the decrease in Lpcat4 migth contribute to possible alteration in key signaling functions in synaptic transmission that lead to a pathological state. On the other hand, Arl8a and Sgsm1 are two proteins that interact with the endocytic system and autophagy-related proteins and their deregulation at 72 h might lead to a disruption in both systems, as we observed in later time points. Loss of Arl8 results in the accumulation of synaptic vesicles contributing to impaired neurotransmission (Vukoja et al., 2018). Lastly, Madd kinase plays an important regulatory role in apoptosis (Miyoshi and Takai, 2004), thus, the observed upregulation of this protein could indicate the onset of a signaling cascade that may lead to cell death in later time points.

2.2. Mitochondrial respiratory defects occur at 1 week p.i. without changes in mitochondrial content or structure

The presence of hα-syn in the striatal terminals is observed from 1st week p.i. onwards. Concomitantly, function of synaptic mitochondria start to be slightly altered as indicated by the reduced basal respiration and proton leak. Remarkably this precedes the onset of dopaminergic degeneration. These findings are consistent with results observed in early PD and RBD patients (who have a greatly increased risk of developing PD and may represent a prodromal stage of PD) that showed functional bioenergetic deficits in blood cells, suggesting that mitochondrial dysfunction may contribute to PD pathology in the prodromal and early stages of PD (Smith et al., 2018). Of note, and in contrast to alterations in proteostasis, no mitochondrial changes were produced at 72 h p.i. although hα-syn is already being overexpressed in the dopaminergic cell soma. Therefore, these results support that functional bioenergetic changes in the striatal synapses are linked to the accumulation of hα-syn at the presynaptic level or related to the proteostatic changes taking place at 72 h p.i. In more detail, basal respiration, which is used to meet the endogenous ATP demand and drive proton leak, seems to be influenced by a reduction in proton leak. Neurons are exposed to high fluxes of Ca^{2+}, which utilize the proton gradient and so increase the rate of oxygen consumption independent of ATP demand. Thus, the apparent decrease in proton leak observed in our study could be related to several factors including a

decrease in Ca^{2+} buffering and proton conductance, or representing a compensatory mechanism to increase mitochondrial efficiency for ATP production, as it has been previously described in response to rotenone and MPP^+ neurotoxins (Giordano et al., 2012). However, to unequivocally identify whether altered proton conductance is driving the changes seen in respiration, measurements of mitochondrial membrane potential must be conducted, although these measurements in synaptosomes are technically challenging (Choi et al., 2009; Gerencser et al., 2012).

Importantly, this occurs without a reduction of fundamental mitochondrial proteins that are used to study mitochondrial content such as TOM and cytochrome c. Moreover, the amount of overall mitochondria in the striatal TH^+ fibers and the glutamatergic presynaptic terminals, as well as mitochondrial subtypes and their morphology showed no apparent structural alterations at this time-point. These findings confirm that bioenergetic alterations occurring by hα-syn overexpression were due to a uniquely functional deficit in respiration and not by changes in mitochondrial content or structure.

Of note, there is an emergence of other deregulated proteins related to the mitochondrial compartment (Acad8, Pnpt1, Aifm3, Ecsit), consistent with the onset of a reduction in mitochondrial respiration at this time point. Likewise, these data provide substantial experimental support for the hypothesis that α-syn has important physical and/or functional interactions with mitochondria (Nakamura, 2013). Among these mitochondrial related proteins, Escit, a signaling integrator that ascertains cell homeostasis, is of special interest. It is involved in the stability of the mitochondrial ETC complexes and response to signals of oxidative stress or mitochondrial damage, and induces the activation of protective molecular mechanisms such as mitophagy (Soler-López et al., 2012). Hence, the observed mitochondrial dysfunction and hα-syn accumulation at this time point could induce the upregulation of Escit to activate response mechanisms to repair the mitochondrial damage.

On the other hand, the mitochondrial clearance system might be disrupted. We have found that Usp15 is the only protein deregulated at both 1 and 4 week time points. The Usp15 protein is a deubiquitinating enzyme that catalyzes the removal of ubiquitin from substrates and has been described to oppose Parkin-mediated mitophagy (Cornelissen et al., 2014). The upregulation of Usp15 suggests a possible inhibition of mitophagy, which in fact, concurs with the onset of the mitochondrial respiratory defects, which might cause later mitochondrial

ultrastructural changes. Finally, Aifm3 is an apoptosis-inducing factor that in cellular stress paradigms is released from the mitochondria to the nucleus inducing DNA fragmentation. The upregulation of this mitochondrial protein might be a factor contributing to the dopaminergic fiber degeneration in the following time points.

2.3. Proteostatic alterations at 1 week p.i. involve cell part morphogenesis, autophagy, and metabolism

The presence of hα-syn in the striatal terminals is also leading to an emergence of deregulated proteins related to several biological processes. Among cell part morphogenesis related proteins (Gfra2, Arhgef7, Lzts1, Pnpt1, Ptpre) Gfra2 is of special interest. It is a receptor for neurturin, which belongs to the GDNF neurotrophic factor family that regulate the survival and function of neurons by the activation of the RET tyrosine kinase receptor. A recent study showed that activation of RET signaling protected dopaminergic neurons from α-syn accumulation (Chmielarz et al., 2020). For this reason, we could speculate that Gfra2 upregulation could be an indicator of the increased RET signaling induced by hα-syn overexpression to hamper its accumulation.

There is also an appearance of autophagy-related protein deregulation (lzts1, Vps39, Vps16 and Rab24). The upregulation of Vps39 protein, which is involved in the maturation process of late-endosomes to bind lysosomes, suggests impairment in the development of autophagic intermediates, leading to ultrastructural alterations at later time points. Moreover, this upregulation at 1 week p.i. is linked with the downregulation of Arl8 found at 72 h. Arl8 is necessary to bind lysosomes to Rab7, present in late-endosomes, through Vps39 protein, suggesting that the observed increased expression of Vps39 at 1 week p.i. could be a consequence of decreased Arl8 at 72h p.i., leading consequently to a failure in the endosomal maturation cycle (Balderhaar and Ungermann, 2013). These results strengthen a sequence of early proteostatic changes in the autophagic/endocytic system, which could be triggering the following pathophysiological events. Interestingly, it is widely established that autophagy responds to a lack of nutrients, so a potential autophagic disruption could be a consequence of defects in cell metabolism. Apart from the onset of bioenergetic defects, we observed deregulated proteins involved in metabolic processes such as the organophosphate biosynthetic processes (Gucy1a1, Pcyt2, and Flad1). As metabolic maintenance is of utmost importance for

correct synaptic homeostasis, our findings could indicate that this process could be compromised very early due to hα-syn accumulation.

3. The temporal sequence of synaptic functionality and its relation with dopaminergic degeneration

3.1 Respiratory deficiency at striatal synapses is compromised concomitantly to significant dopaminergic degeneration at 4 weeks p.i.

The extended hα-syn accumulation in the striatal terminals leads to an increase in compromised synaptic mitochondria at 4 weeks p.i., as observed by the maintenance of reduced basal respiration and proton leak, and the reduction in maximal rate of mitochondrial respiration as well as a 31% reduction of spare respiratory capacity. The decrease in maximal respiration and spare respiratory capacity indicate that striatal synaptosomes are not able to achieve the maximum rate of respiration under prolonged hα-syn accumulation. These results are consistent with previous studies using human induced pluripotent stem cells (iPSC) from PD patients carrying A53T mutation or triplication of *SNCA* gen, showing that α-syn accumulation was associated with a reduction in basal respiration, maximal respiration, and spare respiratory capacity (Ryan et al., 2013; Zambon et al., 2019). Additionally, under conditions of oxidative stress or exposure to neurotoxins such as rotenone and 6-OHDA, the spare respiratory capacity is depleted in cell cultures (Dranka et al., 2013; Giordano et al., 2012), and its reduction has been considered as a major factor that defines the survival of the neuron (Choi et al., 2009; Divakaruni et al., 2014). More specifically, the reduction in spare respiratory capacity observed in our study at 4 weeks p.i. put forward that synaptic mitochondria are functionally damaged, which probably contribute to the synaptic dysfunction and survival of those synapses, and consequently to cell death. Indeed, these mitochondrial bioenergetic defects coincide with a significant dopaminergic cell death in the $SN_{pc,}$ as well as with the maximal denervation of dopaminergic fibers in the striatum which precedes the appearance of motor deficits have not manifested, emphasizing that this functional failure precedes the appearance of motor signs. These results are in keeping with the role of α-syn causing mitochondrial dysfunction in other animal studies. Previous data in a transgenic mouse model overexpressing WT α-syn showed a 25% reduction in maximal respiration after FCCP injection and an impairment in complex V in the striatum at 6 months of age (Subramaniam et al., 2014). However, in this work mitochondria were not exclusively isolated from the synaptic fraction, and the evaluation of motor behaviour and dopaminergic degeneration was not performed. Only one previous study using the same animal

model as in this doctoral thesis, showed a decrease in maximal rate of mitochondrial respiration at 8 weeks p.i. that resulted in approx. a 60% reduced spare respiratory capacity (Bido et al., 2017). However, these findings were observed when the motor function was significantly decreased and the dopaminergic loss in SN_{pc} and striatum was 50%, thus representing the dopaminergic neurodegeneration of PD patients at early or mid-stage of the motor manifestations.

3.2 Alterations in metabolic flexibility arise when the dopaminergic loss becomes significant at 4 weeks p.i.

On the other hand, synaptic neurotransmission has both a high mitochondrial and glycolytic requirement. Therefore, simultaneous measurements of ECAR profile provide us an indirect index of glycolysis in striatal synaptosomes. Synaptosomes display a robust Pasteur effect, enhancing glycolysis in response to an inhibition of mitochondrial ATP synthesis (Kauppinen and Nicholls, 1986). In this sense, our work shows that the rate of acidification increased after the addition of oligomycin and the following addition of FCCP resulted in a further increase in rate, consistent with an activation of glycolysis as compensation for the energy demand crisis occasioned by stressed mitochondria. Moreover, hα-syn overexpression revealed a decrease in ECAR after a stress challenge (oligomycin and FFCP addition) at 4 weeks p.i. but not in previous time points or basal conditions. This deficit put forward that other metabolic pathways such as glycolysis, which compensate for the induced energy stress, may also be compromised when mitochondria are impaired. There are no previous studies regarding ECAR about hα-syn overexpression, so our results add new insight into the presence of not only a respiratory deficiency but also potential alterations in overall metabolic flexibility. These findings are consistent with our proteomic data at 4 weeks p.i. showing a clear dysregulation of proteins related to monosaccharide metabolism and synaptic vesicle endocytosis. Glycolysis is necessary to sustain the synaptic vesicle cycle, particularly under conditions of energy stress in which mitochondrial function at the synapse is compromised (Jang et al., 2016). Our data clearly shows a defective energetic capacity of striatal synaptosomes to adapt to stressful situations, unveiling their poor metabolic flexibility under prolonged hα-syn overexpression, as stipulated by recent studies in fibroblasts from PD patients (Juárez-Flores et al., 2020).

3.3 Prolonged hα-syn accumulation increments alterations in proteostasis network and synaptic dyshomeostasis at 4 weeks p.i.

At 4 weeks p.i. there is an emergence of 35 deregulated proteins that are linked to ribosomes, the postsynaptic density, and focal adhesion, consistent with the enrichment of deregulated proteins related to protein translation, synaptic vesicle cycle, processes in postsynapse and postsynaptic organization. In this line, the regulation of local synaptic protein translation drives homeostasis and plasticity at synapses and thus, the observed unbalance in this process (Hars1, Rpl7, Rpl24, Eef1e1, Mprs24, Rabep1, Atg3, Iwhaq, Iqsec2 Mlycd, Ruvbl2) may be another indicator of synaptic dysfunction (Hafner et al., 2019). Besides, the deregulation of proteins related to endocytosis (Rabep1, Ist1, Iqsec2) and transport (Cryab, Mos1, Oxsr1, Ywhaq, Atg3, Cacna1e, Cyb5a, Slc10a4) are also of great interest since they can explain, at least in part, the observed ultrastructural alterations. Among endocytic process-related proteins, Rabep1 and Ist1 are of special interest. Rabep1 was significantly upregulated in this study, which is a vital regulator and molecular switch for Rab5 function. Rab5 is widely known to regulate the processes of docking and fusion of early-endosomal membranes as well as their motility. It should be noted that overexpression of Rabep1 triggers the accumulation of large endocytic vesicles, upsetting this pathway (Yang et al., 2015). Ist1 interacts with endosomal sorting complexes required for transport (ESCRT) and interestingly, its inhibition has been recently described to repress autophagic flux (Feng et al., 2020). Atg3 is another downregulated protein, known to play a key role in the regulation of autophagy by promoting the progression of autophagosome formation. Of note, reduction in autophagy by the deletion of Atg3 increases α-syn at the synapse and within Lewy bodies (Friedman et al., 2012). Moreover, Sec22b is of particular importance to autophagy as it interacts with SNAREs to mediate the fusion of the secretory autophagosome and plasma membrane (Credle et al., 2015). Thus, the observed downregulation of Ist1 and Atg3 proteins and upregulation of Rabep1 and Sec22b at 4 weeks p.i. may represent additional indicators of disruption of endocytosis machinery, endosome trafficking, and autophagy.

By last, Cacna1e, a voltage-dependent R-type calcium channel, has been found downregulated in our study at 4 weeks p.i. In this line, sustained Ca^{2+} entry into multiple dopaminergic synaptic terminals may lead to a stress condition that could be responsible for their selective vulnerability, rather than simply a late-stage consequence (Nguyen et al., 2019; Zaichick et al., 2017). This hypothesis is consistent with the centrality of the ER and mitochondria

(key organelles in Ca^{2+} homeostasis) as several proteins related to mitochondria and ER have been found in our study. Thus, alterations in Ca^{2+} entry could be contributing to both abnormal mitochondrial respiration and ultrastructure defects observed at 4 weeks p.i., exacerbating neurotoxic events towards the death of dopaminergic terminals observed at the same time point.

By comparing the human α-syn interactome with our deregulated proteome, we found that Cryab (α-crystallin B) significantly downregulated at 4 weeks p.i., which has been described to interact with hα-syn. Interestingly, Cryab is a small heat shock protein, ubiquitously present throughout the body, that prevents aggregation of denatured proteins, and changes in its levels have been reported in several neurological disorders (Dabir et al., 2004; Zabel et al., 2002). In our study, the decrease in Cryab protein levels could indicate a failure in the proteostatic systems that prevent protein aggregation of hα-syn and consequent neurotoxicity, as it coincides with the appearance of $\alpha\text{-syn}^{+}$ Lewy-like structures in the striatum and the onset of degeneration of dopaminergic cell bodies.

Besides, downregulated Ywhaq or 14-3-3θ protein, which has chaperone function and regulates protein trafficking, also interact with hα-syn. Interestingly, it reduces α-syn toxicity and propagation, and its inhibition accelerates the transfer and aggregation of α-syn, as well as enhances toxicity and neuronal death in several animal models of PD (Ding et al., 2015; Wang et al., 2018). Reduced expression of 14-3-3θ has also been observed in a transgenic α-syn model (Yacoubian et al., 2010). Thus, we speculate that the decrease in 14-3-3θ is directly related to hα-syn accumulation and that it may be a critical mechanism by which α-syn propagation and toxicity occur in PD.

4. The temporal sequence of ultrastructure and its relation with overexpression of hα-syn and the dopaminergic degeneration

4.1. Dopaminergic fibers show ultrastructural alterations and potential endocytic and autophagic system alterations at 4 weeks p.i.

A progressive loss of dopaminergic axon terminals from the 2^{nd} week onwards was confirmed under the electron microscope in the hα-syn group where dopaminergic axon terminals increased their area and area/perimeter ratio at 4 weeks p.i. These results indicate that the remaining dopaminergic fibers acquire a pathological conformation with an observable swollen and bulging morphology. These alterations are in keeping with previous studies as

swollen TH^+ fibers have also been described in the striatal terminals of *post-mortem* brains of advanced PD (Halliday et al., 1990; Huot et al., 2006) and animal models of PD (Pickel et al., 1992; Song et al., 2004). Moreover, a progressive increase in the number of electroclear structures within dopaminergic fibers is observed from 2nd week onwards. Although the nature of these structures was difficult to determine under the electron microscope, a colocalization study revealed an increase in $LC3^+$ and $Rab5^+$ staining in swollen dopaminergic fibers at 4 weeks p.i., suggesting that the observed electroclear structures could correspond to autophagic or endocytic system vesicles. Likewise, the proteomic study also supported these results, as several deregulated proteins of the hα-syn group are related to autophagy and endocytosis processes at 72 h, 1, and 4 weeks p.i. (Vps39, Arl8a, Sgsm1, Atg3, Vps16, Ist1, Rabep1 among others). In animal models of parkinsonism, a growing body of studies point that defective hα-syn accumulation resulted in decreased autophagy, starting a cascade leading to synaptic defects (Chandra et al., 2004). Additionally, it has been described that increased autophagy can remove toxic α-syn aggregates within neuronal bodies in *vitro* and *in vivo* (Campbell et al., 2018). Therefore, evidence suggests that synaptic dysfunction may be driven, in part, by a reduction in autophagy at the synapse in PD. In the present study, the overexpression of ha-syn induced the deregulation of proteins involved in endosome trafficking and autophagic flux, which we speculate may result in impairment in the maturation of autophagic intermediates and subsequent fusion with lysosomes, which may lead to an accumulation of endosomes and aberrant hα-syn. This hypothesis is in keeping with the observed increase in Rab5 staining (early-endosomes) and the lack of Rab7 staining (late-endosomes) in TH^+ fibers at 4 weeks p.i, as well as with the significant increase in electroclear structures within degenerating dopaminergic terminals since 2nd week onwards, potentially reflecting an accumulation of autophagic vesicles. The confirmation and better understanding of these events are crucial to harnessing the potential therapeutic benefits of autophagy to implement specific strategies directed to restore the function of key autophagic proteins or intermediates. However, as with many other fields in science, our ability to answer key questions of the autophagic and endocytic processes depends on the development of better experimental tools, that would allow us to regulate these processes in a temporally and spatially restricted manner, thereby allowing us to investigate them at the level of specific synapses. Furthermore, the development of sensors that can accurately measure autophagic flux *in vivo* or real-time is critical.

4.2. Striatal dopaminergic axon terminals show mitochondrial ultrastructural abnormalities and an increase in damaged mitochondria at 4 weeks p.i.

We investigated whether the dysfunction in mitochondrial respiration reported within striatal synaptosomes was related to mitochondrial ultrastructural abnormalities in striatal dopaminergic axon terminals. Our study did not find alterations in the density or morphology of overall mitochondria at any of the studied time points p.i. This suggests that dopaminergic axons may attempt to maintain mitochondrial populations within remaining axons as a compensatory mechanism to facilitate continued neural transmission in the presence of dopaminergic neurodegeneration. However, as hα-syn p.i. time increased, we encountered increasing numbers of mitochondria containing various morphological defects. Mitochondria showed disordered and sparse cristae with the presence of electroclear internal structures in the matrix, which were considered damaged mitochondria. The quantitative study of different subtypes of mitochondria showed an increment in damaged mitochondria and a decrease in intact mitochondria at 4 weeks p.i. which suggests that mechanisms responsible for maintaining a healthy pool of mitochondria are progressively being affected. Interestingly, we observed an increment in length-to-width ratio and a decrease in the roundness of intact mitochondria at 4 weeks p.i., which may be an attempt of remaining intact mitochondria to compensate somehow for the loss of neighboring axons and support the maintenance of neural transmission as this type of morphology is more functional (Picard et al., 2013). On the other hand, the widespread of pathological process itself, could be inducing this increase in damaged mitochondria at this time point.

Mitochondrial defects within the cell bodies of SN neurons are prominent in both PD patients and animal models, but there is a lack of information about mitochondria from dopaminergic axon terminals (Chen et al., 2015; Stichel et al., 2007). The first ultrastructural description of mitochondrial morphological abnormalities due to hα-syn overexpression in the nigrostriatal system was reported in a double mutant transgenic mouse model of PD (hα-syn mutation and Parkin deletion) with neither histopathological abnormalities nor overt motor disabilities (Stichel et al., 2007). Similarly to our findings, they showed that the number of damaged mitochondria was significantly increased in a detailed ultrastructural analysis and that it was not accompanied by alterations in the number or the size of overall mitochondria. However, no synaptic terminals were studied, and the observed changes were restricted to the SN in an age-dependent manner without alterations in the striatal cell somas. A more recent

study using a transgenic mouse model overexpressing A53T-hα-syn also reported mitochondrial abnormalities in the SN including an increase of mitochondrial inclusions that colocalized with macroautophagy markers (LC3 and p62), reduction of averaged mitochondrial length (an indicator of mitochondrial fragmentation) and ultrastructural abnormalities including swollen matrix and disappearance of outer membranes, which were developed previous to the dopaminergic neuron loss. Interestingly, they clearly identified hα-syn within mitochondria of these transgenic mice using double immunogold EM (Chen et al., 2015). As far as we know, no studies have been performed in PD *post-mortem* brains regarding synaptic mitochondrial ultrastructure of dopaminergic fibers.

Additionally, mitochondrial dynamics is a fundamental biological mechanism essential to maintaining mitochondrial health by processes that restore or eliminate dysfunctional mitochondria (Westermann et al., 2010). Thus, one possibility for the increase in damaged mitochondria could be a deregulation of fusion and fission mechanisms, whose balance is required to maintain a healthy pool of mitochondria and also determine mitochondrial morphology. The skewed distributions of (> 1) mitochondrial sizes and several morphological parameters shown in our study suggest the presence of physiological mechanisms to actively preserve small mitochondrial sizes and specific morphology at synapses, which are not disrupted due to hα-syn overexpression (Picard et al., 2013). Also, the proteomic study confirmed that there were no alterations in fusion and fission related fundamental proteins (Opa1, Mfn2, Dlp1) in striatal synaptosomes at any time point, indicating that the ability of synaptic mitochondria to undergo fission and fusion processes is not altered due to hα-syn overexpression. In contrast to our results, several groups have reported that round and fragmented mitochondria increase upon overexpression of either WT or mutant forms of α-syn, both *in vitro* as well as *in vivo* studies, and suggest a possible pathological role of α-syn in reducing mitochondrial fusion process (Bido et al., 2017; Chen et al., 2015; Kamp et al., 2010; Nakamura et al., 2011). These discrepancies could be related to the fact that these studies were performed in TH^+ cell bodies of the SN, which could differ from what occurs in the mitochondria from axon terminals. Also, those studies were performed using confocal microscopy, and it should be argued that approaches employing fluorescent molecules are limited by the natural resolution limits of 200 nm of light microscopy, which do not enable accurate quantification of mitochondrial morphology.

Other possibility is that the increase in damaged mitochondria within dopaminergic fibers might be due to a defect in degradation, potentially due to defective mitophagy. Our analysis revealed a decrease in the density of degenerating mitochondria at 4 weeks p.i. and the proteomic study further confirmed deregulation of mitochondrial proteins (Acad8, Pnpt1, Aifm3, Ecsit) and proteins related to autophagy (lzts1, Vps39, Vps16, Rab24…) and mitophagy processes (Usp15) during the progression of hα-syn overexpression. Regarding previous studies, few have assessed mitophagy *in vivo* because its study remains challenging in human and animal brains. Evidence from cellular models and A53T-α-syn transgenic mice suggest that overexpression of α-syn may inappropriately induce mitophagy, thus leading to an accumulation of dysfunctional mitochondria (Chen et al., 2015; Chinta et al., 2010; Choubey et al., 2011). In contrast to our study, those studies described that α-syn accumulation induced an increase in the mitophagy process, and they were studied in midbrain dopaminergic neurons. Moreover, the observed increase in electroclear vesicles in our study could also be related to an increase in the mitophagy process, but it is not possible to know the specific content of these organelles because they are partially degraded. Thus, it is important to argue that further work will be needed to detail the impairment in the mitochondrial clearance process. In this sense, novel and more specific methods to detect mitochondria-targeted for degradation are required.

4.3. Compensatory mechanisms in synaptic plasticity of the glutamatergic synapse at 1 and 4 weeks p.i.

The degeneration of the nigrostriatal dopaminergic pathway leads to significant morphological and functional changes in the striatal neuronal circuitry, including modifications of the corticostriatal glutamatergic synaptic architecture with consequent alteration of striatal synaptic plasticity in advanced stages of neurodegeneration in animal models and PD patients (Kashani et al., 2007; Villalba et al., 2015). Accordingly, characterizing the role played by glutamatergic synapses before and in the initiation of the neurodegenerative process of the dopaminergic system is essential for a full comprehension of PD pathogenesis. However, to date, these changes have not been assessed due to the lack of animal models that show a progressive neurodegenerative process. In a novel way, the ultrastructural analysis of the striatal excitatory synapses of this study revealed that hα-syn induces homeostatic changes in glutamatergic synapses before the onset of the neurodegenerative process. This has been characterized by an increase in the density of perforated synapses from 1 week p.i. onwards, without alterations in the overall or macular synapse density. It has been described that an increase in the number of

perforated synapses represents the structural basis for the expression of synaptic plasticity, as they are considered structural intermediates in this process (Nieto-Sampedro et al., 1982). Perforated synapses are considered to represent higher efficacy of synaptic transmission than macular synapses (Geinisman et al., 1988). The perforations may function to increase the perimeter surface of the PSDs, increasing the amount of transmitter released during each impulse, and thus, leading to an enhancement of the efficiency of neurotransmission. Thus, this change in glutamatergic synapses might be increasing their synaptic efficacy in an attempt to compensate for the loss of dopaminergic signaling induced by hα-syn overexpression, even in the absence of overt neurodegeneration. Indeed, although we have not studied the dopaminergic transmission in our model, impaired dopaminergic neurotransmission caused by overexpression of hα-syn has been described as an early synaptic event that precedes neuronal degeneration and cell loss (Lundblad et al., 2012). Increases in perforated synapse numbers have also been observed in rats under various experimental conditions, including 6-OHDA (Avila-Costa et al., 2005; Calverley and Jones, 1990).

At 4 weeks p.i., coinciding with the onset of dopaminergic degeneration, apart from an increase in the number of perforated synapses, an increase in mitochondria within glutamatergic terminals has also been observed without apparent ultrastructural defects, as well as a reduction in the proportion of axospinous synapses. This observed increase in the number of mitochondria, could potentially sustain the observed mechanisms of synaptic plasticity or neurotransmission that compensate for the degeneration of dopaminergic fibers. Although our findings do not show an increase in the density of glutamatergic terminals, we observed an increasing tendency for a higher glutamatergic axon density at 4 weeks p.i., which might become more evident with the progression of the disease, and could represent another indicator of compensatory glutamatergic plasticity that respond to the dopaminergic denervation. Recently, these compensatory mechanisms have been attributed to α-syn effects to enhance axon outgrowth (Schechter et al., 2020).

Some authors postulate that this brain plasticity could be deleterious for the spines, as glutamatergic synapses are excitatory, and in the presence of reduced modulatory effects of DA neurotransmission, the neuron could die through excitotoxic mechanisms (Anaya-Martínez et al., 2014). The increased number of perforated synapses observed at 1 week is higher than at 4 weeks p.i., suggesting that glutamatergic synapses may have exceeded a threshold and could not compensate for the lack of dopaminergic fibers, finally contributing to neuronal death. Thus,

we postulate that the increase in perforated synapses represents an early synaptic plasticity mechanism as a compensatory attempt to maintain synaptic efficacy and support continued communication with striatal SPNs during the prodromal period. However, this compensation sustained over time, might also trigger a form of maladaptive synaptic plasticity due to continued glutamatergic excitotoxicity, which may induce functional alterations in synaptic integration, processing, and transmission in SPNs and consequently, dysregulation of the overall basal ganglia circuitry. This would lead to a cascade of pathophysiological events that may favour the neurodegenerative process and may trigger the onset of motor signs.

4.4 Dendritic spine loss together with early plastic events in the remaining dendritic spines at 4 weeks p.i.

The described compensatory mechanisms are also supported by the observed increase in the size of the head of dendritic spines that could be related to the decrease in dendritic spine density at 4 weeks p.i. It is well established that striatal SPNs undergo complex structural changes in the density, morphology, and ultrastructural features of their dendritic spines in PD patients and neurotoxin-induced animal modes. The first evidence for striatal spine loss in PD came from *post-mortem* analysis of Golgi-impregnated striatal neurons in PD patients, which showed significant atrophy of the dendritic tree and loss of spines on individual SPNs of the striatum (McNeill et al., 1988). These findings were later confirmed and extended by numerous studies using *post-mortem* tissue from patients and neurotoxin-based animal models, which have demonstrated different degrees of spine pruning and plastic changes in striatal SPNs (Ingham et al., 1989; Suarez et al., 2016; Villalba et al., 2015; Villalba and Smith, 2010; Zaja-Milatovic et al., 2005). However, most studies about striatal spine loss in PD come from advanced PD patients or animal models of parkinsonism with severe nigrostriatal dopaminergic denervation, and thus, it is not known if dendritic spine modifications occur since the onset of nigrostriatal dopaminergic degeneration or are associated with more advanced stages, as well as what is its relation to the presence of parkinsonian motor signs.

In the current study, we have addressed this issue in the rAAV-hα-syn rat model of progressive parkinsonism, and have found a significant 11% spine loss on striatal SPNs when there is a 25% loss of dopaminergic neurons in the SN and 36% of striatal denervation and before the onset of parkinsonian motor signs. Furthermore, we have observed that the decrease is specific to thin spines, which predominate in SPNs and are considered an immature type of spines, suggesting a decrease in spine turnover. These results are in line with a previous study

that showed that loss of spines in hα-syn transgenic mice was driven by a reduced fraction of newly gained spines, while the fraction of stable spines was increased (Blumenstock et al., 2017). Moreover, the observed loss of thin spines is accompanied by an increase in volume in thin and mushroom spines. This could reflect a compensatory mechanism, as decreased spine turnover would require that new inputs potentiate already existing spines, possibly leading to increased spine head size (Yang et al., 2008). The synaptic ontologies analysis of the deregulated proteome further supports these results, confirming the alteration of proteins involved in this biological process in the postsynapse and postsynaptic actin cytoskeleton organization at 4 weeks p.i. Based on these findings, we conclude that striatal spine loss and increase in spine head volumes are early plastic events that are tightly associated with the onset of the dopaminergic neurodegeneration and precede parkinsonian motor signs. However, the functional significance of these synaptic alterations remains to be elucidated. On one hand, it could be considered as a compensatory response that helps maintain normal striatal activity potentiating already existing spines despite progressive striatal dopaminergic degeneration and spine loss, during the motor asymptomatic prodromal stage of PD. Alternatively, it could be considered the beginning of a pathological process that progressively alters striatal glutamatergic transmission, SPNs activity and the activity of basal ganglia circuitry. Lastly, both interpretations can be in play at the same time. Future studies that relate striatal electrophysiological recordings and dendritic spine analyses at different stages of dopaminergic neurodegeneration should help further address these issues. Additionally, the previous time points (1 and 2 weeks) will also be analyzed, that due to practical issues, have not been possible to include in this doctoral thesis.

In summary, combined evidence from the present work in striatal terminals clearly shows that functional alterations are primary events in the pathological process induced by overexpression of hα-syn, which are followed by structural alterations in later time points, suggesting that synaptic dysfunction and ultrastructural alterations are two interrelated events of the same process. Furthermore, what this study demonstrates is that overexpression of hα-syn can lead to synaptic mitochondrial damage *in vivo,* as observed by reduced respiration and increase in deregulated proteins related to this structure, and that mitochondrial function and metabolism are altered early before the initiation of mitochondrial ultrastructural defects and the neurodegenerative process. Major biological processes altered in these early steps are related to autophagic flux and alterations in the endocytic vesicle cycle although more studies are needed to elucidate the specific mechanisms underlying these processes. These functional alterations are followed by ultrastructural alterations within dopaminergic fibers and neuronal

death. In addition, compensatory plastic changes within glutamatergic synapses are observed, even before the dopaminergic alteartions, which initially could help in the normal function of the motor circuit preventing the expression of motor abnormalities. However, when maintained would progressively increase striatal glutamatergic transmission and neuronal death by excitotoxicity, along with abnormal activity of basal ganglia circuitry, ultimately resulting in parkinsonian motor signs and foster neuronal death. Importantly, the progressive synaptopathy observed is not associated with the development of parkinsonian motor signs, mimicking the pre-motor stage and thus, with the potential to develop early synapse-targeted therapies.

CONCLUSIONS

1. Bilateral inoculation of AAV-hα-sin-A53T into the SN_{pc} causes a progressive hα-syn expression firstly in the SN_{pc} and later in the striatum causing mild dopaminergic loss initiated at striatal terminals, before the manifestation of motor impairment.

2. The first alteration encountered at striatal level before functional changes, is deregulation of proteins affecting metabolism and neurotransmitter release. This occurs in the absence of hα-syn in the striatal terminals just by the influence of overexpression of hα-syn in the SN_{pc}.

3. Striatal functional alterations appear concomitant with the presence of hα-syn in the synaptic terminals. They consist of mitochondrial respiratory defects and altered proteostasis in autophagic and metabolic processes.

4. The maintained functional changes in the striatal synapses lead to a defective energetic capacity of synapses, accounting not only for respiratory deficiency but probably also for alterations in overall metabolic flexibility, taking place when the dopaminergic loss becomes significant.

5. Sustained striatal synaptic dysfunction evolves towards ultrastructural alterations in dopaminergic striatal fibers that acquire a pathological conformation with swollen and bulging morphology.

6. Once started the dopaminergic neurodegeneration, dopaminergic axons maintain mitochondrial populations as a possible compensatory mechanism to facilitate continued neural transmission.

7. Defective autophagy and endocytic pathways occurring since the 2^{nd} week were confirmed by the increase in electroclear structures positive to $LC3^{+}$ and $Rab5^{+}$ markers within the swollen dopaminergic fibers at the 4^{th} week. This indicates that this failure could be exacerbating the disease pathology by the accumulation of autophagic/endocytic cargo in the dopaminergic synapses.

8. The early presence of hα-syn in the dopaminergic terminals induces homeostatic changes in glutamatergic synapses, which can be interpreted as an attempt to compensate for the loss of dopaminergic signaling, even in the absence of overt neurodegeneration.

9. Alterations in the postsynaptic compartment observed by a loss of thin spines in striatal SPNs, as well as changes in proteins involved in the postsynapse, occur concomitantly to significant dopaminergic degeneration.

10. Dendritic spine loss is accompanied by plastic events including an increase in the head volume of thin and mushroom spines that occur before the development of parkinsonian motor signs. These findings could represent a possible compensatory mechanism to enhance the function of existing spines, balancing the observed decrease in spine turnover and probably maintaining normal function during the onset of dopaminergic degeneration.

11. This doctoral thesis presents a good model to study prodromal PD, demonstrating the hypothesis of this work by showing that the synapse is the first neuronal compartment altered by α-syn overexpression, with functional alterations preceding structural changes, and before parkinsonism. This model will open new studies for the development of disease-modifying therapies directed to key synaptic proteins to regain synaptic function in this prodromal phase.

REFERENCES

Aarsland, D., Creese, B., Politis, M., Chaudhuri, K.R., Ffytche, D.H., Weintraub, D., Ballard, C., 2017. Cognitive decline in Parkinson disease. Nat. Rev. Neurol. 13, 217–231. https://doi.org/10.1038/nrneurol.2017.27

Aarsland, D., Marsh, L., Schrag, A., 2009. Neuropsychiatric symptoms in Parkinson's disease. Mov. Disord. 24, 2175–2186. https://doi.org/10.1002/mds.22589

Abdollahzadeh, A., Belevich, I., Jokitalo, E., Tohka, J., Sierra, A., 2019. Automated 3D Axonal Morphometry of White Matter. Sci. Rep. 9, 6084. https://doi.org/10.1038/s41598-019-42648-2

Abeliovich, A., Gitler, A.D., 2016. Defects in trafficking bridge Parkinson's disease pathology and genetics. Nature. https://doi.org/10.1038/nature20414

Abeliovich, A., Schmitz, Y., Fariñas, I., Choi-Lundberg, D., Ho, W.-H., Castillo, P.E., Shinsky, N., Verdugo, J.M.G., Armanini, M., Ryan, A., Hynes, M., Phillips, H., Sulzer, D., Rosenthal, A., 2000. Mice Lacking α-Synuclein Display Functional Deficits in the Nigrostriatal Dopamine System. Neuron 25, 239–252. https://doi.org/10.1016/S0896-6273(00)80886-7

Albin, R.L., Young, A.B., Penney, J.B., 1989. The functional anatomy of basal ganglia disorders. Trends Neurosci. 12, 366–375. https://doi.org/10.1016/0166-2236(89)90074-X

Anaya-Martínez, V., Gutierrez-Valdez, A.L., Ordoñez-Librado, J.L., Montiel-Flores, E., Sánchez-Betancourt, J., Sánchez Vázquez del Mercado, C., Reynoso-Erazo, L., Tron-Alvarez, R., Avila-Costa, M.R., 2014. The presence of perforated synapses in the striatum after dopamine depletion, is this a sign of maladaptive brain plasticity? Microscopy 63, 427–435. https://doi.org/10.1093/jmicro/dfu032

Arotcarena, M.L., Dovero, S., Prigent, A., Bourdenx, M., Camus, S., Porras, G., Thiolat, M.L., Tasselli, M., Aubert, P., Kruse, N., Mollenhauer, B., Damas, I.T., Estrada, C., Garcia-Carrillo, N., Vaikath, N.N., El-Agnaf, O.M.A., Herrero, M.T., Vila, M., Obeso, J.A., Derkinderen, P., Dehay, B., Bezard, E., 2020. Bidirectional gut-to-brain and brain-to-gut propagation of synucleinopathy in non-human primates. Brain 143, 1462–1475. https://doi.org/10.1093/brain/awaa096

Assous, M., Kaminer, J., Shah, F., Garg, A., Koós, T., Tepper, J.M., 2017. Differential processing of thalamic information via distinct striatal interneuron circuits. Nat. Commun. 8, 15860. https://doi.org/10.1038/ncomms15860

Avila-Costa, M.R., Colín-Barenque, L., Aley-Medina, P., Gutíerrez Valdez, A.L., Ordoñes Librado, J.L., Flores Martinez, E., Fortoul, T.I., 2005. Bilateral increase of perforated synapses after unilateral dopamine depletion. Int. J. Neurosci. https://doi.org/10.1080/00207450490512669

Balderhaar, H.J. k., Ungermann, C., 2013. CORVET and HOPS tethering complexes - coordinators of endosome and lysosome fusion. J. Cell Sci. 126, 1307–1316. https://doi.org/10.1242/jcs.107805

Baliki, M.N., Mansour, A., Baria, A.T., Huang, L., Berger, S.E., Fields, H.L., Apkarian, A.V., 2013. Parceling Human Accumbens into Putative Core and Shell Dissociates Encoding of Values for Reward and Pain. J. Neurosci. 33, 16383–16393. https://doi.org/10.1523/JNEUROSCI.1731-13.2013

Barbour, R., Kling, K., Anderson, J.P., Banducci, K., Cole, T., Diep, L., Fox, M., Goldstein, J.M., Soriano, F., Seubert, P., Chilcote, T.J., 2008. Red blood cells are the major source of alpha-synuclein in blood. Neurodegener. Dis. https://doi.org/10.1159/000112832

Barone, P., Antonini, A., Colosimo, C., Marconi, R., Morgante, L., Avarello, T.P., Bottacchi, E., Cannas, A., Ceravolo, G., Ceravolo, R., Cicarelli, G., Gaglio, R.M., Giglia, R.M., Iemolo, F., Manfredi, M., Meco, G., Nicoletti, A., Pederzoli, M., Petrone, A., Pisani, A., Pontieri, F.E., Quatrale, R., Ramat, S., Scala, R., Volpe, G., Zappulla, S., Bentivoglio, A.R., Stocchi, F., Trianni, G., Dotto, P. Del, 2009. The PRIAMO study: A multicenter assessment of nonmotor symptoms and their impact on quality of life in Parkinson's disease. Mov. Disord. 24, 1641–1649. https://doi.org/10.1002/mds.22643

Bellou, V., Belbasis, L., Tzoulaki, I., Evangelou, E., Ioannidis, J.P.A., 2016. Environmental risk factors and Parkinson's disease: An umbrella review of meta-analyses. Parkinsonism Relat. Disord. 23, 1–9. https://doi.org/10.1016/j.parkreldis.2015.12.008

Benito-León, J., Bermejo-Pareja, F., Morales-González, J.M., Porta-Etessam, J., Trincado, R., Vega, S., Louis, E.D., 2004. Incidence of Parkinson disease and parkinsonism in three elderly populations of central Spain. Neurology 62,

734–741. https://doi.org/10.1212/01.WNL.0000113727.73153.68

Benskey, M.J., Perez, R.G., Manfredsson, F.P., 2016. The contribution of alpha synuclein to neuronal survival and function – Implications for Parkinson's disease. J. Neurochem. 137, 331–359. https://doi.org/10.1111/jnc.13570

Berardelli, A., Rothwell, J.C., Thompson, P.D., Hallett, M., 2001. Pathophysiology of bradykinesia in parkinson's disease. Brain 124, 2131–2146. https://doi.org/10.1093/brain/124.11.2131

Bereczki, E., Bogstedt, A., Höglund, K., Tsitsi, P., Brodin, L., Ballard, C., Svenningsson, P., Aarsland, D., 2017. Synaptic proteins in CSF relate to Parkinson's disease stage markers. npj Park. Dis. 3, 1–4. https://doi.org/10.1038/s41531-017-0008-2

Bereczki, E., Branca, R.M., Francis, P.T., Pereira, J.B., Baek, J.H., Hortobágyi, T., Winblad, B., Ballard, C., Lehtiö, J., Aarsland, D., 2018. Synaptic markers of cognitive decline in neurodegenerative diseases: A proteomic approach. Brain 141, 582–595. https://doi.org/10.1093/brain/awx352

Berg, D., Postuma, R.B., Adler, C.H., Bloem, B.R., Chan, P., Dubois, B., Gasser, T., Goetz, C.G., Halliday, G., Joseph, L., Lang, A.E., Liepelt-Scarfone, I., Litvan, I., Marek, K., Obeso, J., Oertel, W., Olanow, C.W., Poewe, W., Stern, M., Deuschl, G., 2015. MDS research criteria for prodromal Parkinson's disease. Mov. Disord. 30, 1600–1611. https://doi.org/10.1002/mds.26431

Bernheimer, H., Birkmayer, W., Hornykiewicz, O., Jellinger, K., Seitelberger, F., 1973. Brain dopamine and the syndromes of Parkinson and Huntington Clinical, morphological and neurochemical correlations. J. Neurol. Sci. 20, 415–455. https://doi.org/10.1016/0022-510X(73)90175-5

Bezard, E., Yue, Z., Kirik, D., Spillantini, M.G., 2013. Animal models of Parkinson's disease: Limits and relevance to neuroprotection studies. Mov. Disord. 28, 61–70. https://doi.org/10.1002/mds.25108

Bido, S., Soria, F.N., Fan, R.Z., Bezard, E., Tieu, K., 2017. Mitochondrial division inhibitor-1 is neuroprotective in the A53T-α-synuclein rat model of Parkinson's disease. Sci. Rep. 7, 1–13. https://doi.org/10.1038/s41598-017-07181-0

Binotti, B., Jahn, R., Chua, J., 2016. Functions of Rab Proteins at Presynaptic Sites. Cells 5, 7. https://doi.org/10.3390/cells5010007

Björklund, A., Dunnett, S.B., 2007. Dopamine neuron systems in the brain: an update. Trends Neurosci. 30, 194–202. https://doi.org/10.1016/j.tins.2007.03.006

Blesa, J., Trigo-Damas, I., Quiroga-Varela, A., Jackson-Lewis, V.R., 2015. Oxidative stress and Parkinson's disease. Front. Neuroanat. 9, 1–9. https://doi.org/10.3389/fnana.2015.00091

Blumenstock, S., Rodrigues, E.F., Peters, F., Blazquez-Llorca, L., Schmidt, F., Giese, A., Herms, J., 2017. Seeding and transgenic overexpression of alpha-synuclein triggers dendritic spine pathology in the neocortex. EMBO Mol. Med. 9, 716–731. https://doi.org/10.15252/emmm.201607305

Borczyk, M., Śliwińska, M.A., Caly, A., Bernas, T., Radwanska, K., 2019. Neuronal plasticity affects correlation between the size of dendritic spine and its postsynaptic density. Sci. Rep. 9, 1–12. https://doi.org/10.1038/s41598-018-38412-7

Bourdenx, M., Dovero, S., Engeln, M., Bido, S., Bastide, M.F., Dutheil, N., Vollenweider, I., Baud, L., Piron, C., Grouthier, V., Boraud, T., Porras, G., Li, Q., Baekelandt, V., Scheller, D., Michel, A., Fernagut, P.-O., Georges, F., Courtine, G., Bezard, E., Dehay, B., 2015. Lack of additive role of ageing in nigrostriatal neurodegeneration triggered by α-synuclein overexpression. Acta Neuropathol. Commun. 3, 46. https://doi.org/10.1186/s40478-015-0222-2

Braak, H., Sandmann-Keil, D., Gai, W., Braak, E., 1999. Extensive axonal Lewy neurites in Parkinson's disease: a novel pathological feature revealed by α-synuclein immunocytochemistry. Neurosci. Lett. 265, 67–69. https://doi.org/10.1016/S0304-3940(99)00208-6

Braak, H., Tredici, K. Del, Rüb, U., de Vos, R.A.., Jansen Steur, E.N.H., Braak, E., 2003. Staging of brain pathology related to sporadic Parkinson's disease. Neurobiol. Aging 24, 197–211. https://doi.org/10.1016/S0197-4580(02)00065-9

Bridi, J.C., Hirth, F., 2018. Mechanisms of α-Synuclein induced synaptopathy in parkinson's disease. Front. Neurosci. 12, 1–18. https://doi.org/10.3389/fnins.2018.00080

Burke, D.A., Rotstein, H.G., Alvarez, V.A., 2017. Striatal Local Circuitry: A New Framework for Lateral Inhibition. Neuron 96, 267–284. https://doi.org/10.1016/j.neuron.2017.09.019

Burke, R.E., O'Malley, K., 2013. Axon degeneration in Parkinson's disease. Exp. Neurol. 246, 72–83. https://doi.org/10.1016/j.expneurol.2012.01.011

Burré, J., 2015. The Synaptic Function of α-Synuclein. J. Parkinsons. Dis. 5, 699–713. https://doi.org/10.3233/JPD-150642

Burré, J., Sharma, M., Südhof, T.C., 2014. α-Synuclein assembles into higher-order multimers upon membrane binding to promote SNARE complex formation. Proc. Natl. Acad. Sci. 111, E4274–E4283. https://doi.org/10.1073/pnas.1416598111

Burre, J., Sharma, M., Tsetsenis, T., Buchman, V., Etherton, M.R., Sudhof, T.C., 2010. -Synuclein Promotes SNARE-Complex Assembly in Vivo and in Vitro. Science (80-.). 329, 1663–1667. https://doi.org/10.1126/science.1195227

Busch, D.J., Oliphint, P.A., Walsh, R.B., Banks, S.M.L., Woods, W.S., George, J.M., Morgan, J.R., 2014. Acute increase of α-synuclein inhibits synaptic vesicle recycling evoked during intense stimulation. Mol. Biol. Cell 25, 3926–3941. https://doi.org/10.1091/mbc.e14-02-0708

Butler, B., Saha, K., Rana, T., Becker, J.P., Sambo, D., Davari, P., Goodwin, J.S., Khoshbouei, H., 2015. Dopamine Transporter Activity Is Modulated by α-Synuclein. J. Biol. Chem. 290, 29542–29554. https://doi.org/10.1074/jbc.M115.691592

Calo, L., Wegrzynowicz, M., Santivañez-Perez, J., Grazia Spillantini, M., 2016. Synaptic failure and α-synuclein. Mov. Disord. 31, 169–177. https://doi.org/10.1002/mds.26479

Calverley, R.K.S., Jones, D.G., 1990. Contributions of dendritic spines and perforated synapses to synaptic plasticity. Brain Res. Rev. 15, 215–249. https://doi.org/10.1016/0165-0173(90)90002-6

Caminiti, S.P., Presotto, L., Baroncini, D., Garibotto, V., Moresco, R.M., Gianolli, L., Volonté, M.A., Antonini, A., Perani, D., 2017. Axonal damage and loss of connectivity in nigrostriatal and mesolimbic dopamine pathways in early Parkinson's disease. NeuroImage Clin. 14, 734–740. https://doi.org/10.1016/j.nicl.2017.03.011

Campbell, P., Morris, H., Schapira, A., 2018. Chaperone-mediated autophagy as a therapeutic target for Parkinson disease. Expert Opin. Ther. Targets 22, 823–832. https://doi.org/10.1080/14728222.2018.1517156

Cerri, S., Mus, L., Blandini, F., 2019. Parkinson's Disease in Women and Men: What's the Difference? J. Parkinsons. Dis. 9, 501–515. https://doi.org/10.3233/JPD-191683

Chahine, L.M., Amara, A.W., Videnovic, A., 2017. A systematic review of the literature on disorders of sleep and wakefulness in Parkinson's disease from 2005 to 2015. Sleep Med. Rev. 35, 33–50. https://doi.org/10.1016/j.smrv.2016.08.001

Chandra, S., Fornai, F., Kwon, H., Yazdani, U., Atasoy, D., Liu, X., Hammer, R.E., Battaglia, G., German, D.C., Castillo, P.E., Su, T.C., 2004. Double-knockout mice for alpha- and beta-synuclein: Effect on synaptic functions. PNAS.

Charron, G., Doudnikoff, E., Laux, A., Berthet, A., Porras, G., Canron, M.-H., Barroso-Chinea, P., Li, Q., Qin, C., Nosten-Bertrand, M., Giros, B., Delalande, F., Van Dorsselaer, A., Vital, A., Goumon, Y., Bezard, E., 2011. Endogenous morphine-like compound immunoreactivity increases in parkinsonism. Brain 134, 2321–2338. https://doi.org/10.1093/brain/awr166

Chartier-Harlin, M.-C., Kachergus, J., Roumier, C., Mouroux, V., Douay, X., Lincoln, S., Levecque, C., Larvor, L., Andrieux, J., Hulihan, M., Waucquier, N., Defebvre, L., Amouyel, P., Farrer, M., Destée, A., 2004. α-synuclein locus duplication as a cause of familial Parkinson's disease. Lancet 364, 1167–1169. https://doi.org/10.1016/S0140-6736(04)17103-1

Chen, L., Feany, M.B., 2005. α-Synuclein phosphorylation controls neurotoxicity and inclusion formation in a

Drosophila model of Parkinson disease. Nat. Neurosci. 8, 657–663. https://doi.org/10.1038/nn1443

Chen, L., Periquet, M., Wang, X., Negro, A., McLean, P.J., Hyman, B.T., Feany, M.B., 2009. Tyrosine and serine phosphorylation of α-synuclein have opposing effects on neurotoxicity and soluble oligomer formation. J. Clin. Invest. https://doi.org/10.1172/JCI39088

Chen, L., Xie, Z., Turkson, S., Zhuang, X., 2015. A53T Human -Synuclein Overexpression in Transgenic Mice Induces Pervasive Mitochondria Macroautophagy Defects Preceding Dopamine Neuron Degeneration. J. Neurosci. 35, 890–905. https://doi.org/10.1523/JNEUROSCI.0089-14.2015

Cheng, H.C., Ulane, C.M., Burke, R.E., 2010. Clinical progression in Parkinson disease and the neurobiology of axons. Ann. Neurol. 67, 715–725. https://doi.org/10.1002/ana.21995

Cherian, A., Divya, K.P., 2020. Genetics of Parkinson's disease. Acta Neurol. Belg. 120, 1297–1305. https://doi.org/10.1007/s13760-020-01473-5

Chesnokova, A.Y., Ekimova, I. V., Pastukhov, Y.F., 2019. Parkinson's Disease and Aging. Adv. Gerontol. 9, 164–173. https://doi.org/10.1134/S2079057019020085

Chinta, S.J., Mallajosyula, J.K., Rane, A., Andersen, J.K., 2010. Mitochondrial alpha-synuclein accumulation impairs complex I function in dopaminergic neurons and results in increased mitophagy in vivo. Neurosci. Lett. 486, 235–239. https://doi.org/10.1016/j.neulet.2010.09.061

Chmielarz, P., Er, Ş., Konovalova, J., Bandres, L., Hlushchuk, I., Albert, K., Panhelainen, A., Luk, K., Airavaara, M., Domanskyi, A., 2020. GDNF/RET Signaling Pathway Activation Eliminates Lewy Body Pathology in Midbrain Dopamine Neurons. Mov. Disord. 1, 1–12. https://doi.org/10.1002/mds.28258

Choi, S.W., Gerencser, A.A., Nicholls, D.G., 2009. Bioenergetic analysis of isolated cerebrocortical nerve terminals on a microgram scale: spare respiratory capacity and stochastic mitochondrial failure. J. Neurochem. 109, 1179–1191. https://doi.org/10.1111/j.1471-4159.2009.06055.x

Chomiak, T., Hu, B., 2009. What Is the Optimal Value of the g-Ratio for Myelinated Fibers in the Rat CNS? A Theoretical Approach. PLoS One 4, e7754. https://doi.org/10.1371/journal.pone.0007754

Choubey, V., Safiulina, D., Vaarmann, A., Cagalinec, M., Wareski, P., Kuum, M., Zharkovsky, A., Kaasik, A., 2011. Mutant A53T α-Synuclein induces neuronal death by increasing mitochondrial autophagy. J. Biol. Chem. 286, 10814–10824. https://doi.org/10.1074/jbc.M110.132514

Chu, Y., Kordower, J.H., 2007. Age-associated increases of α-synuclein in monkeys and humans are associated with nigrostriatal dopamine depletion: Is this the target for Parkinson's disease? Neurobiol. Dis. 25, 134–149. https://doi.org/10.1016/j.nbd.2006.08.021

Chu, Y., Muller, S., Tavares, A., Barret, O., Alagille, D., Seibyl, J., Tamagnan, G., Marek, K., Luk, K.C., Trojanowski, J.Q., Lee, V.M.Y., Kordower, J.H., 2019. Intrastriatal alpha-synuclein fibrils in monkeys: spreading, imaging and neuropathological changes. Brain 142, 3565–3579. https://doi.org/10.1093/brain/awz296

Chung, C.Y., Koprich, J.B., Siddiqi, H., Isacson, O., 2009. Dynamic changes in presynaptic and axonal transport proteins combined with striatal neuroinflammation precede dopaminergic neuronal loss in a rat model of AAV α-synucleinopathy. J. Neurosci. 29, 3365–3373. https://doi.org/10.1523/JNEUROSCI.5427-08.2009

Cole, N.B., DiEuliis, D., Leo, P., Mitchell, D.C., Nussbaum, R.L., 2008. Mitochondrial translocation of α-synuclein is promoted by intracellular acidification. Exp. Cell Res. 314, 2076–2089. https://doi.org/10.1016/j.yexcr.2008.03.012

Conte, A., Khan, N., Defazio, G., Rothwell, J.C., Berardelli, A., 2013. Pathophysiology of somatosensory abnormalities in Parkinson disease. Nat. Rev. Neurol. 9, 687–697. https://doi.org/10.1038/nrneurol.2013.224

Cornelissen, T., Haddad, D., Wauters, F., Van Humbeeck, C., Mandemakers, W., Koentjoro, B., Sue, C., Gevaert, K., De Strooper, B., Verstreken, P., Vandenberghe, W., 2014. The deubiquitinase USP15 antagonizes Parkin-mediated mitochondrial ubiquitination and mitophagy. Hum. Mol. Genet. 23, 5227–5242. https://doi.org/10.1093/hmg/ddu244

Credle, J.J., Forcelli, P.A., Delannoy, M., Oaks, A.W., Permaul, E., Berry, D.L., Duka, V., Wills, J., Sidhu, A., 2015. α-Synuclein-mediated inhibition of ATF6 processing into COPII vesicles disrupts UPR signaling in Parkinson's disease. Neurobiol. Dis. 76, 112–125. https://doi.org/10.1016/j.nbd.2015.02.005

Cutillo, G., Simon, D.K., Eleuteri, S., 2020. VPS35 and the mitochondria: Connecting the dots in Parkinson's disease pathophysiology. Neurobiol. Dis. 145, 105056. https://doi.org/10.1016/j.nbd.2020.105056

Dabir, D. V., Trojanowski, J.Q., Richter-Landsberg, C., Lee, V.M.Y., Forman, M.S., 2004. Expression of the Small Heat-Shock Protein αB-Crystallin in Tauopathies with Glial Pathology. Am. J. Pathol. 164, 155–166. https://doi.org/10.1016/S0002-9440(10)63106-9

Dalfó, E., Portero-Otín, M., Ayala, V., Martínez, A., Pamplona, R., Ferrer, I., 2005. Evidence of oxidative stress in the neocortex in incidental Lewy body disease. J. Neuropathol. Exp. Neurol. 64, 816–830. https://doi.org/10.1097/01.jnen.0000179050.54522.5a

de Bie, R.M.A., Clarke, C.E., Espay, A.J., Fox, S.H., Lang, A.E., 2020. Initiation of pharmacological therapy in Parkinson's disease: when, why, and how. Lancet Neurol. 19, 452–461. https://doi.org/10.1016/S1474-4422(20)30036-3

Decressac, M., Mattsson, B., Lundblad, M., Weikop, P., Björklund, A., 2012. Progressive neurodegenerative and behavioural changes induced by AAV-mediated overexpression of α-synuclein in midbrain dopamine neurons. Neurobiol. Dis. 45, 939–953. https://doi.org/10.1016/j.nbd.2011.12.013

Dehay, B., Bourdenx, M., Gorry, P., Przedborski, S., Vila, M., Hunot, S., Singleton, A., Olanow, C.W., Merchant, K.M., Bezard, E., Petsko, G.A., Meissner, W.G., 2015. Targeting α-synuclein for treatment of Parkinson's disease: mechanistic and therapeutic considerations. Lancet Neurol. 14, 855–866. https://doi.org/10.1016/S1474-4422(15)00006-X

Del Rey, N.L.G., Quiroga-Varela, A., Garbayo, E., Carballo-Carbajal, I., Fernández-Santiago, R., Monje, M.H.G., Trigo-Damas, I., Blanco-Prieto, M.J., Blesa, J., 2018. Advances in parkinson's disease: 200 years later. Front. Neuroanat. 12, 1–14. https://doi.org/10.3389/fnana.2018.00113

Delgado-Alvarado, M., Gago, B., Navalpotro-Gomez, I., Jiménez-Urbieta, H., Rodriguez-Oroz, M.C., 2016. Biomarkers for dementia and mild cognitive impairment in Parkinson's disease. Mov. Disord. 31, 861–881. https://doi.org/10.1002/mds.26662

DeMaagd, G., Philip, A., 2015. Parkinson's Disease and Its Management: Part 1: Disease Entity, Risk Factors, Pathophysiology, Clinical Presentation, and Diagnosis. P T 40, 504–32. https://doi.org/10.1016/j.nicl.2019.101946

Desplats, P., Lee, H.-J., Bae, E.-J., Patrick, C., Rockenstein, E., Crews, L., Spencer, B., Masliah, E., Lee, S.-J., 2009. Inclusion formation and neuronal cell death through neuron-to-neuron transmission of -synuclein. Proc. Natl. Acad. Sci. 106, 13010–13015. https://doi.org/10.1073/pnas.0903691106

Devi, L., Raghavendran, V., Prabhu, B.M., Avadhani, N.G., Anandatheerthavarada, H.K., 2008. Mitochondrial import and accumulation of α-synuclein impair complex I in human dopaminergic neuronal cultures and Parkinson disease brain. J. Biol. Chem. 283, 9089–9100. https://doi.org/10.1074/jbc.M710012200

Dickson, D.W., Braak, H., Duda, J.E., Duyckaerts, C., Gasser, T., Halliday, G.M., Hardy, J., Leverenz, J.B., Del Tredici, K., Wszolek, Z.K., Litvan, I., 2009. Neuropathological assessment of Parkinson's disease: refining the diagnostic criteria. Lancet Neurol. 8, 1150–1157. https://doi.org/10.1016/S1474-4422(09)70238-8

Dijkstra, A.A., Ingrassia, A., De Menezes, R.X., Van Kesteren, R.E., Rozemuller, A.J.M., Heutink, P., Van De Berg, W.D.J., 2015. Evidence for immune response, axonal dysfunction and reduced endocytosis in the substantia nigra in early stage Parkinson's disease. PLoS One 10, 1–21. https://doi.org/10.1371/journal.pone.0128651

Ding, H., Underwood, R., Lavalley, N., Yacoubian, T.A., 2015. 14-3-3 inhibition promotes dopaminergic neuron loss and 14-3-3θ overexpression promotes recovery in the MPTP mouse model of Parkinson's disease. Neuroscience 307, 73–82. https://doi.org/10.1016/j.neuroscience.2015.08.042

Divakaruni, A.S., Paradyse, A., Ferrick, D.A., Murphy, A.N., Jastroch, M., 2014. Analysis and Interpretation of Microplate-Based Oxygen Consumption and pH Data, in: Methods in Enzymology. Elsevier Inc., pp. 309–354. https://doi.org/10.1016/B978-0-12-801415-8.00016-3

Domínguez-álvaro, M., Montero-Crespo, M., Blazquez-Llorca, L., Insausti, R., DeFelipe, J., Alonso-Nanclares, L., 2018. Three-dimensional analysis of synapses in the transentorhinal cortex of Alzheimer's disease patients. Acta Neuropathol. Commun. https://doi.org/10.1186/s40478-018-0520-6

Dorsey, E.R., Constantinescu, R., Thompson, J.P., Biglan, K.M., Holloway, R.G., Kieburtz, K., Marshall, F.J., Ravina, B.M., Schifitto, G., Siderowf, A., Tanner, C.M., 2007. Projected number of people with Parkinson disease in the most populous nations, 2005 through 2030. Neurology 68, 384–6. https://doi.org/10.1212/01.wnl.0000247740.47667.03

Doty, R.L., 2012. Olfactory dysfunction in Parkinson disease. Nat. Rev. Neurol. 8, 329–339. https://doi.org/10.1038/nrneurol.2012.80

Dranka, B.P., Benavides, G.A., Diers, A.R., Giordano, S., Blake, R., Reily, C., Zou, L., Chatham, J.C., Hill, B.G., Landar, A., Darley-usmar, V.M., 2013. By Metabolic Profiling 51, 1621–1635. https://doi.org/10.1016/j.freeradbiomed.2011.08.005.Assessing

Drøjdahl, N., Nielsen, H.H., Gardi, J.E., Wree, A., Peterson, A.C., Nyengaard, J.R., Eyer, J., Finsen, B., 2010. Axonal plasticity elicits long-term changes in oligodendroglia and myelinated fibers. Glia 58, 29–42. https://doi.org/10.1002/glia.20897

Du, T.-T., Chen, Y.-C., Lu, Y.-Q., Meng, F.-G., Yang, H., Zhang, J.-G., 2018. Subthalamic nucleus deep brain stimulation protects neurons by activating autophagy via PP2A inactivation in a rat model of Parkinson's disease. Exp. Neurol. 306, 232–242. https://doi.org/10.1016/j.expneurol.2018.05.017

Dumitriu, D., Rodriguez, A., Morrison, J.H., 2011. High-throughput, detailed, cell-specific neuroanatomy of dendritic spines using microinjection and confocal microscopy. Nat. Protoc. 6, 1391–1411. https://doi.org/10.1038/nprot.2011.389

Durante, V., de Iure, A., Loffredo, V., Vaikath, N., De Risi, M., Paciotti, S., Quiroga-Varela, A., Chiasserini, D., Mellone, M., Mazzocchetti, P., Calabrese, V., Campanelli, F., Mechelli, A., Di Filippo, M., Ghiglieri, V., Picconi, B., El-Agnaf, O.M., De Leonibus, E., Gardoni, F., Tozzi, A., Calabresi, P., 2019. Alpha-synuclein targets GluN2A NMDA receptor subunit causing striatal synaptic dysfunction and visuospatial memory alteration. Brain 142, 1365–1385. https://doi.org/10.1093/brain/awz065

Eleuteri, S., Albanese, A., 2019. VPS35-Based Approach: A Potential Innovative Treatment in Parkinson's Disease. Front. Neurol. 10, 1–11. https://doi.org/10.3389/fneur.2019.01272

Feng, Q., Luo, Y., Zhang, X.-N., Yang, X.-F., Hong, X.-Y., Sun, D.-S., Li, X.-C., Hu, Y., Li, X.-G., Zhang, J.-F., Li, X., Yang, Y., Wang, Q., Liu, G.-P., Wang, J.-Z., 2020. MAPT/Tau accumulation represses autophagy flux by disrupting IST1-regulated ESCRT-III complex formation: a vicious cycle in Alzheimer neurodegeneration. Autophagy 16, 641–658. https://doi.org/10.1080/15548627.2019.1633862

Ffytche, D.H., Creese, B., Politis, M., Chaudhuri, K.R., Weintraub, D., Ballard, C., Aarsland, D., 2017. The psychosis spectrum in Parkinson disease. Nat. Rev. Neurol. 13, 81–95. https://doi.org/10.1038/nrneurol.2016.200

Fieblinger, T., Graves, S.M., Sebel, L.E., Alcacer, C., Plotkin, J.L., Gertler, T.S., Chan, C.S., Heiman, M., Greengard, P., Cenci, M.A., Surmeier, D.J., 2014. Cell type-specific plasticity of striatal projection neurons in parkinsonism and L-DOPA-induced dyskinesia. Nat. Commun. 5, 5316. https://doi.org/10.1038/ncomms6316

Fløngs, I.H., Fernandez-Vizarra, E., Lykouri, M., Brakedal, B., Skeie, G.O., Miletic, H., Lilleng, P.K., Alves, G., Tysnes, O.B., Haugarvoll, K., Dölle, C., Zeviani, M., Tzoulis, C., 2018. Neuronal complex I deficiency occurs throughout the Parkinson's disease brain, but is not associated with neurodegeneration or mitochondrial DNA damage. Acta Neuropathol. 135, 409–425. https://doi.org/10.1007/s00401-017-1794-7

Foster, M., Sherrington, C.S., 1897. A Textbook of Physiology, Part Three: The Central Nervous System, Seventh Edition. MacMillan Co Ltd.

Friedman, L.G., Lachenmayer, M.L., Wang, J., He, L., Poulose, S.M., Komatsu, M., Holstein, G.R., Yue, Z., 2012. Disrupted Autophagy Leads to Dopaminergic Axon and Dendrite Degeneration and Promotes Presynaptic Accumulation of -Synuclein and LRRK2 in the Brain. J. Neurosci. 32, 7585–7593. https://doi.org/10.1523/JNEUROSCI.5809-11.2012

Fussi, N., Höllerhage, M., Chakroun, T., Nykänen, N.-P., Rösler, T.W., Koeglsperger, T., Wurst, W., Behrends, C., Höglinger, G.U., 2018. Exosomal secretion of α-synuclein as protective mechanism after upstream blockage of macroautophagy. Cell Death Dis. 9, 757. https://doi.org/10.1038/s41419-018-0816-2

Galvin, J.E., Uryu, K., Lee, V.M., Trojanowski, J.Q., 1999. Axon pathology in Parkinson's disease and Lewy body dementia hippocampus contains alpha-, beta-, and gamma-synuclein. Proc. Natl. Acad. Sci. U. S. A.

García-Morales, V., Montero, F., González-Forero, D., Rodríguez-Bey, G., Gómez-Pérez, L., Medialdea-Wandossell, M.J., Domínguez-Vías, G., García-Verdugo, J.M., Moreno-López, B., 2015. Membrane-Derived Phospholipids Control Synaptic Neurotransmission and Plasticity. PLOS Biol. 13, e1002153. https://doi.org/10.1371/journal.pbio.1002153

Garcia-Reitböck, P., Anichtchik, O., Bellucci, A., Iovino, M., Ballini, C., Fineberg, E., Ghetti, B., Della Corte, L., Spano, P., Tofaris, G.K., Goedert, M., Spillantini, M.G., 2010. SNARE protein redistribution and synaptic failure in a transgenic mouse model of Parkinson's disease. Brain 133, 2032–2044. https://doi.org/10.1093/brain/awq132

Gaugler, M.N., Genc, O., Bobela, W., Mohanna, S., Ardah, M.T., El-Agnaf, O.M., Cantoni, M., Bensadoun, J.C., Schneggenburger, R., Knott, G.W., Aebischer, P., Schneider, B.L., 2012. Nigrostriatal overabundance of α-synuclein leads to decreased vesicle density and deficits in dopamine release that correlate with reduced motor activity. Acta Neuropathol. 123, 653–669. https://doi.org/10.1007/s00401-012-0963-y

Geinisman, Y., Morrell, F., DeToledo-Morrell, L., 1988. Remodeling of synaptic architecture during hippocampal "kindling". Proc. Natl. Acad. Sci. 85, 3260–3264. https://doi.org/10.1073/pnas.85.9.3260

George, J.M., 2002. The synucleins. Genome Biol. https://doi.org/10.1186/gb-2001-3-1-reviews3002

Gerencser, A.A., Chinopoulos, C., Birket, M.J., Jastroch, M., Vitelli, C., Nicholls, D.G., Brand, M.D., 2012. Quantitative measurement of mitochondrial membrane potential in cultured cells: calcium-induced de- and hyperpolarization of neuronal mitochondria. J. Physiol. 590, 2845–2871. https://doi.org/10.1113/jphysiol.2012.228387

Gerfen, C.R., 2000. Molecular effects of dopamine on striatal-projection pathways. Trends Neurosci. 23, S64–S70. https://doi.org/10.1016/S1471-1931(00)00019-7

Gerfen, C.R., Engber, T.M., Mahan, L.C., Susel, Z., Chase, T.N., Monsma, F.J., Sibley, D.R., 1990. D1 and D2 dopamine receptor-regulated gene expression of striatonigral and striatopallidal neurons. Science (80-.). https://doi.org/10.1126/science.2147780

Gerfen, C.R., Staines, W.A., Fibiger, H.C., Arbuthnott, G.W., 1982. Crossed connections of the substantia nigra in the rat. J. Comp. Neurol. 207, 283–303. https://doi.org/10.1002/cne.902070308

Gerfen, C.R., Surmeier, D.J., 2011. Modulation of Striatal Projection Systems by Dopamine. Annu. Rev. Neurosci. 34, 441–466. https://doi.org/10.1146/annurev-neuro-061010-113641

Ghiglieri, V., Calabrese, V., Calabresi, P., 2018. Alpha-Synuclein: From Early Synaptic Dysfunction to Neurodegeneration. Front. Neurol. 9. https://doi.org/10.3389/fneur.2018.00295

Giasson, B.I., Duda, J.E., Quinn, S.M., Zhang, B., Trojanowski, J.Q., Lee, V.M.Y., 2002. Neuronal α-Synucleinopathy with Severe Movement Disorder in Mice Expressing A53T Human α-Synuclein. Neuron 34, 521–533. https://doi.org/10.1016/S0896-6273(02)00682-7

Gillet, L.C., Navarro, P., Tate, S., Röst, H., Selevsek, N., Reiter, L., Bonner, R., Aebersold, R., 2012. Targeted data extraction of the MS/MS spectra generated by data-independent acquisition: A new concept for consistent and accurate proteome analysis. Mol. Cell. Proteomics 11, 1–17. https://doi.org/10.1074/mcp.O111.016717

Giordano, N., Iemolo, A., Mancini, M., Cacace, F., De Risi, M., Latagliata, E.C., Ghiglieri, V., Bellenchi, G.C., Puglisi-Allegra, S., Calabresi, P., Picconi, B., De Leonibus, E., 2018. Motor learning and metaplasticity in striatal neurons: relevance for Parkinson's disease. Brain 141, 505–520. https://doi.org/10.1093/brain/awx351

Giordano, S., Lee, J., Darley-Usmar, V.M., Zhang, J., 2012. Distinct Effects of Rotenone, 1-methyl-4-phenylpyridinium and 6-hydroxydopamine on Cellular Bioenergetics and Cell Death. PLoS One 7, e44610. https://doi.org/10.1371/journal.pone.0044610

Goedert, M., Compston, A., 2018. Parkinson's disease - The story of an eponym. Nat. Rev. Neurol. 14, 57–63. https://doi.org/10.1038/nrneurol.2017.165

Goldman, J.G., Postuma, R., 2014. Premotor and nonmotor features of Parkinson's disease. Curr. Opin. Neurol. 27, 434–441. https://doi.org/10.1097/WCO.0000000000000112

Gómez-Benito, M., Granado, N., García-Sanz, P., Michel, A., Dumoulin, M., Moratalla, R., 2020. Modeling Parkinson's Disease With the Alpha-Synuclein Protein. Front. Pharmacol. 11, 1–15. https://doi.org/10.3389/fphar.2020.00356

Gonzales, K.K., Smith, Y., 2015. Cholinergic interneurons in the dorsal and ventral striatum: Anatomical and functional considerations in normal and diseased conditions. Ann. N. Y. Acad. Sci. 1349, 1–45. https://doi.org/10.1111/nyas.12762

González-Redondo, R., García-García, D., Clavero, P., Gasca-Salas, C., García-Eulate, R., Zubieta, J.L., Arbizu, J., Obeso, J.A., Rodríguez-Oroz, M.C., 2014. Grey matter hypometabolism and atrophy in Parkinson's disease with cognitive impairment: a two-step process. Brain 137, 2356–2367. https://doi.org/10.1093/brain/awu159

Gorbatyuk, O.S., Li, S., Sullivan, L.F., Chen, W., Kondrikova, G., Manfredsson, F.P., Mandel, R.J., Muzyczka, N., 2008. The phosphorylation state of Ser-129 in human -synuclein determines neurodegeneration in a rat model of Parkinson disease. Proc. Natl. Acad. Sci. 105, 763–768. https://doi.org/10.1073/pnas.0711053105

Grahn, J.A., Parkinson, J.A., Owen, A.M., 2009. The role of the basal ganglia in learning and memory: Neuropsychological studies. Behav. Brain Res. 199, 53–60. https://doi.org/10.1016/j.bbr.2008.11.020

Graves, S.M., Surmeier, D.J., 2019. Delayed spine pruning of direct pathway spiny projection neurons in a mouse model of parkinson's disease. Front. Cell. Neurosci. 13, 1–6. https://doi.org/10.3389/fncel.2019.00032

Gray, E.G., 1959. Axo-somatic and axo-dendritic synapses of the cerebral cortex: an electron microscope study. J. Anat. 93, 420–33.

Graybiel, A.M., 1990. Neurotransmitters and neuromodulators in the basal ganglia. Trends Neurosci. 13, 244–254. https://doi.org/10.1016/0166-2236(90)90104-I

Greten-Harrison, B., Polydoro, M., Morimoto-Tomita, M., Diao, L., Williams, A.M., Nie, E.H., Makani, S., Tian, N., Castillo, P.E., Buchman, V.L., Chandra, S.S., 2010. αβγ-Synuclein triple knockout mice revealage-dependent neuronal dysfunction. Proc. Natl. Acad. Sci. U. S. A. 107, 19573–19578. https://doi.org/10.1073/pnas.1005005107

Gross, O.P., von Gersdorff, H., 2016. Recycling at synapses. Elife 5. https://doi.org/10.7554/eLife.17692

Gundersen, H.J.G., Jensen, E.B., 1987. The efficiency of systematic sampling in stereology and its prediction*. J. Microsc. 147, 229–263. https://doi.org/10.1111/j.1365-2818.1987.tb02837.x

Guo, J.T., Chen, A.Q., Kong, Q., Zhu, H., Ma, C.M., Qin, C., 2008. Inhibition of Vesicular Monoamine Transporter-2 Activity in α-Synuclein Stably Transfected SH-SY5Y Cells. Cell. Mol. Neurobiol. 28, 35–47. https://doi.org/10.1007/s10571-007-9227-0

Guo, Q., Wang, D., He, X., Feng, Q., Lin, R., Xu, F., Fu, L., Luo, M., 2015. Whole-Brain Mapping of Inputs to Projection Neurons and Cholinergic Interneurons in the Dorsal Striatum. PLoS One 10, e0123381. https://doi.org/10.1371/journal.pone.0123381

Gustafsson, G., Lööv, C., Persson, E., Lázaro, D.F., Takeda, S., Bergström, J., Erlandsson, A., Sehlin, D., Balaj, L., György, B., Hallbeck, M., Outeiro, T.F., Breakefield, X.O., Hyman, B.T., Ingelsson, M., 2018. Secretion and Uptake of α-Synuclein Via Extracellular Vesicles in Cultured Cells. Cell. Mol. Neurobiol. 38, 1539–1550. https://doi.org/10.1007/s10571-018-0622-5

Haelterman, N.A., Yoon, W.H., Sandoval, H., Jaiswal, M., Shulman, J.M., Bellen, H.J., 2014. A Mitocentric View of Parkinson's Disease. Annu. Rev. Neurosci. 37, 137–159. https://doi.org/10.1146/annurev-neuro-071013-014317

Hafner, A.-S., Donlin-Asp, P.G., Leitch, B., Herzog, E., Schuman, E.M., 2019. Local protein synthesis is a ubiquitous

feature of neuronal pre- and postsynaptic compartments. Science (80-.). 364, eaau3644. https://doi.org/10.1126/science.aau3644

Halliday, G.M., Li, Y.W., Blumbergs, P.C., Joh, T.H., Cotton, R.G.H., Howe, P.R.C., Blessing, W.W., Geffen, L.B., 1990. Neuropathology of immunohistochemically identified brainstem neurons in Parkinson's disease. Ann. Neurol. 27, 373–385. https://doi.org/10.1002/ana.410270405

Hara, Y., Park, C.S., Janssen, W.G.M., Roberts, M.T., Morrison, J.H., Rapp, P.R., 2012. Synaptic correlates of memory and menopause in the hippocampal dentate gyrus in rhesus monkeys. Neurobiol. Aging 33, 421.e17-421.e28. https://doi.org/10.1016/j.neurobiolaging.2010.09.014

Harris, K.M., Weinberg, R.J., 2012. Ultrastructure of Synapses in the Mammalian Brain. Cold Spring Harb. Perspect. Biol. 4, a005587–a005587. https://doi.org/10.1101/cshperspect.a005587

Hegarty, S. V., Sullivan, A.M., O'Keeffe, G.W., 2013. Midbrain dopaminergic neurons: A review of the molecular circuitry that regulates their development. Dev. Biol. 379, 123–138. https://doi.org/10.1016/j.ydbio.2013.04.014

Hely, M.A., Morris, J.G.L., Reid, W.G.J., Trafficante, R., 2005. Sydney Multicenter Study of Parkinson's disease: Non-L-dopa-responsive problems dominate at 15 years. Mov. Disord. 20, 190–199. https://doi.org/10.1002/mds.20324

Herms, J., Dorostkar, M.M., 2016. Dendritic Spine Pathology in Neurodegenerative Diseases. Annu. Rev. Pathol. Mech. Dis. 11, 221–250. https://doi.org/10.1146/annurev-pathol-012615-044216

Holtmaat, A., Caroni, P., 2016. Functional and structural underpinnings of neuronal assembly formation in learning. Nat. Neurosci. 19, 1553–1562. https://doi.org/10.1038/nn.4418

Huang, C.-L., Chao, C.-C., Lee, Y.-C., Lu, M.-K., Cheng, J.-J., Yang, Y.-C., Wang, V.-C., Chang, W.-C., Huang, N.-K., 2016. Paraquat Induces Cell Death Through Impairing Mitochondrial Membrane Permeability. Mol. Neurobiol. 53, 2169–2188. https://doi.org/10.1007/s12035-015-9198-y

Huot, P., Levesque, M., Parent, A., 2006. The fate of striatal dopaminergic neurons in Parkinson's disease and Huntington's chorea. Brain 130, 222–232. https://doi.org/10.1093/brain/awl332

Ingham, C.A., Hood, S.H., Arbuthnott, G.W., 1989. Spine density on neostriatal neurones changes with 6-hydroxydopamine lesions and with age. Brain Res. 503, 334–338. https://doi.org/10.1016/0006-8993(89)91686-7

Irizarry, M.C., Growdon, W., Gomez-isla, T., Newell, K., George, J.M., Clayton, D.F., Hyman, B.T., 1998. Nigral and Cortical Lewy Bodies and Dystrophic Nigral Neurites in Parkinson's Disease and Cortical Lewy Body Disease Contain α-synuclein Immunoreactivity. J. Neuropathol. Exp. Neurol. 57, 334–337. https://doi.org/10.1097/00005072-199804000-00005

Isomura, Y., Takekawa, T., Harukuni, R., Handa, T., Aizawa, H., Takada, M., Fukai, T., 2013. Reward-Modulated Motor Information in Identified Striatum Neurons. J. Neurosci. 33, 10209–10220. https://doi.org/10.1523/JNEUROSCI.0381-13.2013

Janezic, S., Threlfell, S., Dodson, P.D., Dowie, M.J., Taylor, T.N., Potgieter, D., Parkkinen, L., Senior, S.L., Anwar, S., Ryan, B., Deltheil, T., Kosillo, P., Cioroch, M., Wagner, K., Ansorge, O., Bannerman, D.M., Bolam, J.P., Magill, P.J., Cragg, S.J., Wade-Martins, R., 2013. Deficits in dopaminergic transmission precede neuron loss and dysfunction in a new Parkinson model. Proc. Natl. Acad. Sci. 110, E4016–E4025. https://doi.org/10.1073/pnas.1309143110

Jang, S.R., Nelson, J.C., Bend, E.G., Rodríguez-Laureano, L., Tueros, F.G., Cartagenova, L., Underwood, K., Jorgensen, E.M., Colón-Ramos, D.A., 2016. Glycolytic Enzymes Localize to Synapses under Energy Stress to Support Synaptic Function. Neuron 90, 278–291. https://doi.org/10.1016/j.neuron.2016.03.011

Jankovic, J., 2008. Parkinson's disease: Clinical features and diagnosis. J. Neurol. Neurosurg. Psychiatry 79, 368–376. https://doi.org/10.1136/jnnp.2007.131045

Jedrzejewska, A., Wierzba-Bobrowicz, T., Olejniczak, P., Poszwińska, Z., Dymecki, J., 1990. Ultrastructure and

immunocytochemistry of left and right nigrostriatal system after lesion of right side of substantia nigra of rat. Adv. Neurol.

Jellinger, K.A., 2009. Formation and development of Lewy pathology: a critical update. J. Neurol. 256, 270–279. https://doi.org/10.1007/s00415-009-5243-y

Jensen, M.B., Bhatia, V.K., Jao, C.C., Rasmussen, J.E., Pedersen, S.L., Jensen, K.J., Langen, R., Stamou, D., 2011. Membrane Curvature Sensing by Amphipathic Helices. J. Biol. Chem. 286, 42603–42614. https://doi.org/10.1074/jbc.M111.271130

Jiménez-Urbieta, H., Gago, B., Quiroga-Varela, A., Rodríguez-Chinchilla, T., Merino-Galán, L., Oregi, A., Belloso-Iguerategui, A., Delgado-Alvarado, M., Navalpotro-Gómez, I., Marin, C., Fernagut, P.O., Rodríguez-Oroz, M.C., 2019. Pramipexole-induced impulsivity in mildparkinsonian rats: a model of impulse control disorders in Parkinson's disease. Neurobiol. Aging 75, 126–135. https://doi.org/10.1016/j.neurobiolaging.2018.11.021

Joel, D., Weiner, I., 2000. The connections of the dopaminergic system with the striatum in rats and primates: An analysis with respect to the functional and compartmental organization of the striatum. Neuroscience 96, 451–474. https://doi.org/10.1016/S0306-4522(99)00575-8

Jones, E.G., 1999. Golgi, Cajal and the Neuron Doctrine. J. Hist. Neurosci. 8, 170–178. https://doi.org/10.1076/jhin.8.2.170.1838

Juárez-Flores, D.L., Ezquerra, M., Gonzàlez-Casacuberta, Ï., Ormazabal, A., Morén, C., Tolosa, E., Fucho, R., Guitart-Mampel, M., Casado, M., Valldeoriola, F., de la Torre-Lara, J., Muñoz, E., Tobías, E., Compta, Y., García-García, F.J., García-Ruiz, C., Fernandez-Checa, J.C., Martí, M.J., Grau, J.M., Cardellach, F., Artuch, R., Fernández-Santiago, R., Garrabou, G., 2020. Disrupted Mitochondrial and Metabolic Plasticity Underlie Comorbidity between Age-Related and Degenerative Disorders as Parkinson Disease and Type 2 Diabetes Mellitus. Antioxidants 9, 1063. https://doi.org/10.3390/antiox9111063

Jung, M., Choi, H., Mun, J.Y., 2019. The autophagy research in electron microscopy. Appl. Microsc. 49, 1–7. https://doi.org/10.1186/s42649-019-0012-6

Jurado, S., Benoist, M., Lario, A., Knafo, S., Petrok, C.N., Esteban, J.A., 2010. PTEN is recruited to the postsynaptic terminal for NMDA receptor-dependent long-term depression. EMBO J. 29, 2827–40. https://doi.org/10.1038/emboj.2010.160

Kalia, L. V., Lang, A.E., 2015. Parkinson's disease. Lancet 386, 896–912. https://doi.org/10.1016/S0140-6736(14)61393-3

Kamagata, K., Zalesky, A., Hatano, T., Ueda, R., Di Biase, M.A., Okuzumi, A., Shimoji, K., Hori, M., Caeyenberghs, K., Pantelis, C., Hattori, N., Aoki, S., 2017. Gray matter abnormalities in idiopathic Parkinson's disease: Evaluation by diffusional kurtosis imaging and neurite orientation dispersion and density imaging. Hum. Brain Mapp. 38, 3704–3722. https://doi.org/10.1002/hbm.23628

Kamp, F., Exner, N., Lutz, A.K., Wender, N., Hegermann, J., Brunner, B., Nuscher, B., Bartels, T., Giese, A., Beyer, K., Eimer, S., Winklhofer, K.F., Haass, C., 2010. Inhibition of mitochondrial fusion by α-synuclein is rescued by PINK1, Parkin and DJ-1. EMBO J. 29, 3571–3589. https://doi.org/10.1038/emboj.2010.223

Kashani, A., Betancur, C., Giros, B., Hirsch, E., Mestikawy, S. El, 2007. Altered expression of vesicular glutamate transporters VGLUT1 and VGLUT2 in Parkinson disease. Neurobiol. Aging 28, 568–578. https://doi.org/10.1016/j.neurobiolaging.2006.02.010

Kasten, M., Hartmann, C., Hampf, J., Schaake, S., Westenberger, A., Vollstedt, E.J., Balck, A., Domingo, A., Vulinovic, F., Dulovic, M., Zorn, I., Madoev, H., Zehnle, H., Lembeck, C.M., Schawe, L., Reginold, J., Huang, J., König, I.R., Bertram, L., Marras, C., Lohmann, K., Lill, C.M., Klein, C., 2018. Genotype-Phenotype Relations for the Parkinson's Disease Genes Parkin, PINK1, DJ1: MDSGene Systematic Review. Mov. Disord. 33, 730–741. https://doi.org/10.1002/mds.27352

Kauppinen, R.A., Nicholls, D.G., 1986. Synaptosomal bioenergetics. The role of glycolysis, pyruvate oxidation and responses to hypoglycaemia. Eur. J. Biochem. 158, 159–165. https://doi.org/10.1111/j.1432-1033.1986.tb09733.x

Kaushik, S., Cuervo, A.M., 2015. Proteostasis and aging. Nat. Med. 21, 1406–1415. https://doi.org/10.1038/nm.4001

Keeney, P.M., Xie, J., Capaldi, R.A., Bennett, J.P., 2006. Parkinson's disease brain mitochondrial complex I has oxidatively damaged subunits and is functionally impaired and misassembled. J. Neurosci. 26, 5256–5264. https://doi.org/10.1523/JNEUROSCI.0984-06.2006

Khoo, T.K., Yarnall, A.J., Duncan, G.W., Coleman, S., O'Brien, J.T., Brooks, D.J., Barker, R.A., Burn, D.J., 2013. The spectrum of nonmotor symptoms in early Parkinson disease. Neurology 80, 276–281. https://doi.org/10.1212/WNL.0b013e31827deb74

Kim, J.Y., Oh, M.H., Bernard, L.P., Macara, I.G., Zhang, H., 2011. The RhoG/ELMO1/Dock180 signaling module is required for spine morphogenesis in hippocampal neurons. J. Biol. Chem. 286, 37615–37624. https://doi.org/10.1074/jbc.M111.268029

Kim, S., Kwon, S.-H., Kam, T.-I., Panicker, N., Karuppagounder, S.S., Lee, S., Lee, J.H., Kim, W.R., Kook, M., Foss, C.A., Shen, C., Lee, H., Kulkarni, S., Pasricha, P.J., Lee, G., Pomper, M.G., Dawson, V.L., Dawson, T.M., Ko, H.S., 2019. Transneuronal Propagation of Pathologic α-Synuclein from the Gut to the Brain Models Parkinson's Disease. Neuron 103, 627-641.e7. https://doi.org/10.1016/j.neuron.2019.05.035

Kirik, D., Rosenblad, C., Burger, C., Lundberg, C., Johansen, T.E., Muzyczka, N., Mandel, R.J., Björklund, A., 2002. Parkinson-Like Neurodegeneration Induced by Targeted Overexpression of α-Synuclein in the Nigrostriatal System. J. Neurosci. 22, 2780–2791. https://doi.org/10.1523/JNEUROSCI.22-07-02780.2002

Klein, A.D., Mazzulli, J.R., 2018. Is Parkinson's disease a lysosomal disorder? Brain 141, 2255–2262. https://doi.org/10.1093/brain/awy147

Klein, R.L., King, M.A., Hamby, M.E., Meyer, E.M., 2002. Dopaminergic Cell Loss Induced by Human A30P α -Synuclein Gene Transfer to the Rat Substantia Nigra. Hum. Gene Ther. 13, 605–612. https://doi.org/10.1089/10430340252837206

Koopmans, F., van Nierop, P., Andres-Alonso, M., Byrnes, A., Cijsouw, T., Coba, M.P., Cornelisse, L.N., Farrell, R.J., Goldschmidt, H.L., Howrigan, D.P., Hussain, N.K., Imig, C., de Jong, A.P.H., Jung, H., Kohansalnodehi, M., Kramarz, B., Lipstein, N., Lovering, R.C., MacGillavry, H., Mariano, V., Mi, H., Ninov, M., Osumi-Sutherland, D., Pielot, R., Smalla, K.-H., Tang, H., Tashman, K., Toonen, R.F.G., Verpelli, C., Reig-Viader, R., Watanabe, K., van Weering, J., Achsel, T., Ashrafi, G., Asi, N., Brown, T.C., De Camilli, P., Feuermann, M., Foulger, R.E., Gaudet, P., Joglekar, A., Kanellopoulos, A., Malenka, R., Nicoll, R.A., Pulido, C., de Juan-Sanz, J., Sheng, M., Südhof, T.C., Tilgner, H.U., Bagni, C., Bayés, À., Biederer, T., Brose, N., Chua, J.J.E., Dieterich, D.C., Gundelfinger, E.D., Hoogenraad, C., Huganir, R.L., Jahn, R., Kaeser, P.S., Kim, E., Kreutz, M.R., McPherson, P.S., Neale, B.M., O'Connor, V., Posthuma, D., Ryan, T.A., Sala, C., Feng, G., Hyman, S.E., Thomas, P.D., Smit, A.B., Verhage, M., 2019. SynGO: An Evidence-Based, Expert-Curated Knowledge Base for the Synapse. Neuron 103, 217-234.e4. https://doi.org/10.1016/j.neuron.2019.05.002

Koprich, J.B., Johnston, T.H., Reyes, M.G., Sun, X., Brotchie, J.M., 2010. Expression of human A53T alpha-synuclein in the rat substantia nigra using a novel AAV1/2 vector produces a rapidly evolving pathology with protein aggregation, dystrophic neurite architecture and nigrostriatal degeneration with potential to model the pat. Mol. Neurodegener. 5, 43. https://doi.org/10.1186/1750-1326-5-43

Koprich, J.B., Kalia, L. V., Brotchie, J.M., 2017. Animal models of α-synucleinopathy for Parkinson disease drug development. Nat. Rev. Neurosci. 18, 515–529. https://doi.org/10.1038/nrn.2017.75

Kordower, J.H., Chu, Y., Hauser, R.A., Olanow, C.W., Freeman, T.B., 2008. Transplanted dopaminergic neurons develop PD pathologic changes: A second case report. Mov. Disord. 23, 2303–2306. https://doi.org/10.1002/mds.22369

Kramer, M.L., Schulz-Schaeffer, W.J., 2007. Presynaptic -Synuclein Aggregates, Not Lewy Bodies, Cause Neurodegeneration in Dementia with Lewy Bodies. J. Neurosci. 27, 1405–1410. https://doi.org/10.1523/JNEUROSCI.4564-06.2007

Kravitz, A. V., Freeze, B.S., Parker, P.R.L., Kay, K., Thwin, M.T., Deisseroth, K., Kreitzer, A.C., 2010. Regulation of parkinsonian motor behaviours by optogenetic control of basal ganglia circuitry. Nature 466, 622–626. https://doi.org/10.1038/nature09159

Lashuel, H.A., Overk, C.R., Oueslati, A., Masliah, E., 2013. The many faces of α-synuclein: From structure and toxicity to therapeutic target. Nat. Rev. Neurosci. 14, 38–48. https://doi.org/10.1038/nrn3406

Lavedan, C., 1998. The Synuclein Family. Genome Res. 8, 871–880. https://doi.org/10.1101/gr.8.9.871

Lee, A., Gilbert, R.M., 2016. Epidemiology of Parkinson Disease. Neurol. Clin. 34, 955–965. https://doi.org/10.1016/j.ncl.2016.06.012

Lee, H.-J., Suk, J.-E., Bae, E.-J., Lee, J.-H., Paik, S.R., Lee, S.-J., 2008. Assembly-dependent endocytosis and clearance of extracellular a-synuclein. Int. J. Biochem. Cell Biol. 40, 1835–1849. https://doi.org/10.1016/j.biocel.2008.01.017

Lepeta, K., Lourenco, M. V., Schweitzer, B.C., Martino Adami, P. V., Banerjee, P., Catuara-Solarz, S., de La Fuente Revenga, M., Guillem, A.M., Haidar, M., Ijomone, O.M., Nadorp, B., Qi, L., Perera, N.D., Refsgaard, L.K., Reid, K.M., Sabbar, M., Sahoo, A., Schaefer, N., Sheean, R.K., Suska, A., Verma, R., Vicidomini, C., Wright, D., Zhang, X.-D., Seidenbecher, C., 2016. Synaptopathies: synaptic dysfunction in neurological disorders - A review from students to students. J. Neurochem. 138, 785–805. https://doi.org/10.1111/jnc.13713

Li, J.-Y., Englund, E., Holton, J.L., Soulet, D., Hagell, P., Lees, A.J., Lashley, T., Quinn, N.P., Rehncrona, S., Björklund, A., Widner, H., Revesz, T., Lindvall, O., Brundin, P., 2008. Lewy bodies in grafted neurons in subjects with Parkinson's disease suggest host-to-graft disease propagation. Nat. Med. 14, 501–503. https://doi.org/10.1038/nm1746

Lindgren, H.S., Lelos, M.J., Dunnett, S.B., 2012. Do alpha-synuclein vector injections provide a better model of Parkinson's disease than the classic 6-hydroxydopamine model? Exp. Neurol. 237, 36–42. https://doi.org/10.1016/j.expneurol.2012.05.022

Lu, J., Sun, F., Ma, H., Qing, H., Deng, Y., 2015. Comparison between α-synuclein wild-type and A53T mutation in a progressive Parkinson's disease model. Biochem. Biophys. Res. Commun. 464, 988–993. https://doi.org/10.1016/j.bbrc.2015.07.007

Luk, K.C., Kehm, V., Carroll, J., Zhang, B., O'Brien, P., Trojanowski, J.Q., Lee, V.M.-Y., 2012. Pathological -Synuclein Transmission Initiates Parkinson-like Neurodegeneration in Nontransgenic Mice. Science (80-.). 338, 949–953. https://doi.org/10.1126/science.1227157

Lundblad, M., Decressac, M., Mattsson, B., Björklund, A., 2012. Impaired neurotransmission caused by overexpression of α-synuclein in nigral dopamine neurons. Proc. Natl. Acad. Sci. U. S. A. 109, 3213–3219. https://doi.org/10.1073/pnas.1200575109

Maingay, M., Romero-Ramos, M., Carta, M., Kirik, D., 2006. Ventral tegmental area dopamine neurons are resistant to human mutant alpha-synuclein overexpression. Neurobiol. Dis. 23, 522–532. https://doi.org/10.1016/j.nbd.2006.04.007

Martin, L.J., Pan, Y., Price, A.C., Sterling, W., Copeland, N.G., Jenkins, N.A., Price, D.L., Lee, M.K., 2006. Parkinson's disease α-synuclein transgenic mice develop neuronal mitochondrial degeneration and cell death. J. Neurosci. 26, 41–50. https://doi.org/10.1523/JNEUROSCI.4308-05.2006

Martinet, W., Timmermans, J.-P., De Meyer, G.R.Y., 2014. Methods to Assess Autophagy In Situ—Transmission Electron Microscopy Versus Immunohistochemistry, in: Methods in Enzymology. Elsevier Inc., pp. 89–114. https://doi.org/10.1016/B978-0-12-801329-8.00005-2

Martínez-Fernández, R., Rodríguez-Rojas, R., del Álamo, M., Hernández-Fernández, F., Pineda-Pardo, J.A., Dileone, M., Alonso-Frech, F., Foffani, G., Obeso, I., Gasca-Salas, C., de Luis-Pastor, E., Vela, L., Obeso, J.A., 2018. Focused ultrasound subthalamotomy in patients with asymmetric Parkinson's disease: a pilot study. Lancet Neurol. 17, 54–63. https://doi.org/10.1016/S1474-4422(17)30403-9

Masliah, E., 2000. Dopaminergic Loss and Inclusion Body Formation in -Synuclein Mice: Implications for Neurodegenerative Disorders. Science (80-.). 287, 1265–1269. https://doi.org/10.1126/science.287.5456.1265

Matuskey, D., Tinaz, S., Wilcox, K.C., Naganawa, M., Toyonaga, T., Dias, M., Henry, S., Pittman, B., Ropchan, J., Nabulsi, N., Suridjan, I., Comley, R.A., Huang, Y., Finnema, S.J., Carson, R.E., 2020. Synaptic Changes in Parkinson Disease

Assessed with in vivo Imaging. Ann. Neurol. 87, 329–338. https://doi.org/10.1002/ana.25682

McNeill, T.H., Brown, S.A., Rafols, J.A., Shoulson, I., 1988. Atrophy of medium spiny I striatal dendrites in advanced Parkinson's disease. Brain Res. 455, 148–152. https://doi.org/10.1016/0006-8993(88)90124-2

Melki, R., 2015. Role of Different Alpha-Synuclein Strains in Synucleinopathies, Similarities with other Neurodegenerative Diseases. J. Parkinsons. Dis. 5, 217–227. https://doi.org/10.3233/JPD-150543

Middleton, E.R., Rhoades, E., 2010. Effects of Curvature and Composition on α-Synuclein Binding to Lipid Vesicles. Biophys. J. 99, 2279–2288. https://doi.org/10.1016/j.bpj.2010.07.056

Mishra, V.R., Sreenivasan, K.R., Yang, Z., Zhuang, X., Cordes, D., Mari, Z., Litvan, I., Fernandez, H.H., Eidelberg, D., Ritter, A., Cummings, J.L., Walsh, R.R., 2020. Unique white matter structural connectivity in early-stage drug-naive Parkinson disease. Neurology 94, e774–e784. https://doi.org/10.1212/WNL.0000000000008867

Miyoshi, J., Takai, Y., 2004. Dual role of DENN/MADD (Rab3GEP) in neurotransmission and neuroprotection. Trends Mol. Med. 10, 476–480. https://doi.org/10.1016/j.molmed.2004.08.002

Mizuno, Y., Ohta, S., Tanaka, M., Takamiya, S., Suzuki, K., Sato, T., Oya, H., Ozawa, T., Kagawa, Y., 1989. Deficiencies in Complex I subunits of the respiratory chain in Parkinson's disease. Biochem. Biophys. Res. Commun. 163, 1450–1455. https://doi.org/10.1016/0006-291X(89)91141-8

Moghaddam, H.S., Zare-Shahabadi, A., Rahmani, F., Rezaei, N., 2017. Neurotransmission systems in Parkinson's disease. Rev. Neurosci. 28, 509–536. https://doi.org/10.1515/revneuro-2016-0068

Motley, S.E., Grossman, Y.S., Janssen, W.G.M., Baxter, M.G., Rapp, P.R., Dumitriu, D., Morrison, J.H., 2018. Selective Loss of Thin Spines in Area 7a of the Primate Intraparietal Sulcus Predicts Age-Related Working Memory Impairment. J. Neurosci. 38, 10467–10478. https://doi.org/10.1523/JNEUROSCI.1234-18.2018

Nakamura, K., 2013. α-Synuclein and Mitochondria: Partners in Crime? Neurotherapeutics 10, 391–399. https://doi.org/10.1007/s13311-013-0182-9

Nakamura, K., Nemani, V.M., Azarbal, F., Skibinski, G., Levy, J.M., Egami, K., Munishkina, L., Zhang, J., Gardner, B., Wakabayashi, J., Sesaki, H., Cheng, Y., Finkbeiner, S., Nussbaum, R.L., Masliah, E., Edwards, R.H., 2011. Direct membrane association drives mitochondrial fission by the Parkinson disease-associated protein α-synuclein. J. Biol. Chem. 286, 20710–20726. https://doi.org/10.1074/jbc.M110.213538

Nemani, V.M., Lu, W., Berge, V., Nakamura, K., Onoa, B., Lee, M.K., Chaudhry, F.A., Nicoll, R.A., Edwards, R.H., 2010. Increased Expression of α-Synuclein Reduces Neurotransmitter Release by Inhibiting Synaptic Vesicle Reclustering after Endocytosis. Neuron 65, 66–79. https://doi.org/10.1016/j.neuron.2009.12.023

Nguyen, M., Wong, Y.C., Ysselstein, D., Severino, A., Krainc, D., 2019. Synaptic, Mitochondrial, and Lysosomal Dysfunction in Parkinson's Disease. Trends Neurosci. 42, 140–149. https://doi.org/10.1016/j.tins.2018.11.001

Nieto-Sampedro, M., Hoff, S.F., Cotman, C.W., 1982. Perforated postsynaptic densities: probable intermediates in synapse turnover. Proc. Natl. Acad. Sci. 79, 5718–5722. https://doi.org/10.1073/pnas.79.18.5718

Nikoletopoulou, V., Tavernarakis, N., 2018. Regulation and Roles of Autophagy at Synapses. Trends Cell Biol. 28, 646–661. https://doi.org/10.1016/j.tcb.2018.03.006

Nilsson, L., Pamrén, A., Islam, T., Brännström, K., Golchin, S.A., Pettersson, N., Iakovleva, I., Sandblad, L., Gharibyan, A.L., Olofsson, A., 2018. Transthyretin Interferes with Aβ Amyloid Formation by Redirecting Oligomeric Nuclei into Non-Amyloid Aggregates. J. Mol. Biol. 430, 2722–2733. https://doi.org/10.1016/j.jmb.2018.06.005

Noyce, A.J., Bestwick, J.P., Silveira-Moriyama, L., Hawkes, C.H., Giovannoni, G., Lees, A.J., Schrag, A., 2012. Meta-analysis of early nonmotor features and risk factors for Parkinson disease. Ann. Neurol. 72, 893–901. https://doi.org/10.1002/ana.23687

O'Regan, G., DeSouza, R.-M., Balestrino, R., Schapira, A.H., 2017. Glucocerebrosidase Mutations in Parkinson Disease. J. Parkinsons. Dis. 7, 411–422. https://doi.org/10.3233/JPD-171092

Obeso, J.A., Rodríguez-Oroz, M.C., Rodríguez, M., Arbizu, J., Giménez-Amaya, J.M., 2002. The Basal Ganglia and

Disorders of Movement: Pathophysiological Mechanisms. Physiology 17, 51–55. https://doi.org/10.1152/nips.01363.2001

Olanow, C.W., Brundin, P., 2013. Parkinson's Disease and Alpha Synuclein: Is Parkinson's Disease a Prion-Like Disorder? Mov. Disord. 28, 31–40. https://doi.org/10.1002/mds.25373

Oliveras-Salvá, M., Van der Perren, A., Casadei, N., Stroobants, S., Nuber, S., D'Hooge, R., Van den Haute, C., Baekelandt, V., 2013. rAAV2/7 vector-mediated overexpression of alpha-synuclein in mouse substantia nigra induces protein aggregation and progressive dose-dependent neurodegeneration. Mol. Neurodegener. 8, 44. https://doi.org/10.1186/1750-1326-8-44

Olsson, M., Nikkhah, G., Bentlage, C., Bjorklund, A., 1995. Forelimb akinesia in the rat Parkinson model: differential effects of dopamine agonists and nigral transplants as assessed by a new stepping test. J. Neurosci. 15, 3863–3875. https://doi.org/10.1523/JNEUROSCI.15-05-03863.1995

Oughtred, R., Stark, C., Breitkreutz, B.J., Rust, J., Boucher, L., Chang, C., Kolas, N., O'Donnell, L., Leung, G., McAdam, R., Zhang, F., Dolma, S., Willems, A., Coulombe-Huntington, J., Chatr-Aryamontri, A., Dolinski, K., Tyers, M., 2019. The BioGRID interaction database: 2019 update. Nucleic Acids Res. 47, D529–D541. https://doi.org/10.1093/nar/gky1079

Ozelius, L.J., Senthil, G., Saunders-Pullman, R., Ohmann, E., Deligtisch, A., Tagliati, M., Hunt, A.L., Klein, C., Henick, B., Hailpern, S.M., Lipton, R.B., Soto-Valencia, J., Risch, N., Bressman, S.B., 2006. LRRK2 G2019S as a cause of Parkinson's disease in Ashkenazi Jews [14]. N. Engl. J. Med. 354, 424–425. https://doi.org/10.1056/NEJMc055509

Pagonabarraga, J., Martinez-Horta, S., Fernández de Bobadilla, R., Pérez, J., Ribosa-Nogué, R., Marín, J., Pascual-Sedano, B., García, C., Gironell, A., Kulisevsky, J., 2016. Minor hallucinations occur in drug-naive Parkinson's disease patients, even from the premotor phase. Mov. Disord. 31, 45–52. https://doi.org/10.1002/mds.26432

Pang, S.Y.-Y., Ho, P.W.-L., Liu, H.-F., Leung, C.-T., Li, L., Chang, E.E.S., Ramsden, D.B., Ho, S.-L., 2019. The interplay of aging, genetics and environmental factors in the pathogenesis of Parkinson's disease. Transl. Neurodegener. 8, 23. https://doi.org/10.1186/s40035-019-0165-9

Parajuli, L.K., Wako, K., Maruo, S., Kakuta, S., Taguchi, T., Ikuno, M., Yamakado, H., Takahashi, R., Koike, M., 2020. Developmental changes in dendritic spine morphology in the striatum and their alteration in an a53t α-synuclein transgenic mouse model of parkinson's disease. eNeuro 7, 1–14. https://doi.org/10.1523/ENEURO.0072-20.2020

Parkinson, J., 1817. An Essay on the Shaking Palsy. J. Neuropsychiatry Clin. Neurosci. 14, 223–236. https://doi.org/10.1176/jnp.14.2.223

Patterson, J.R., Duffy, M.F., Kemp, C.J., Howe, J.W., Collier, T.J., Stoll, A.C., Miller, K.M., Patel, P., Levine, N., Moore, D.J., Luk, K.C., Fleming, S.M., Kanaan, N.M., Paumier, K.L., El-Agnaf, O.M.A., Sortwell, C.E., 2019. Time course and magnitude of alpha-synuclein inclusion formation and nigrostriatal degeneration in the rat model of synucleinopathy triggered by intrastriatal α-synuclein preformed fibrils. Neurobiol. Dis. 130, 104525. https://doi.org/10.1016/j.nbd.2019.104525

Paumier, K.L., Luk, K.C., Manfredsson, F.P., Kanaan, N.M., Lipton, J.W., Collier, T.J., Steece-Collier, K., Kemp, C.J., Celano, S., Schulz, E., Sandoval, I.M., Fleming, S., Dirr, E., Polinski, N.K., Trojanowski, J.Q., Lee, V.M., Sortwell, C.E., 2015. Intrastriatal injection of pre-formed mouse α-synuclein fibrils into rats triggers α-synuclein pathology and bilateral nigrostriatal degeneration. Neurobiol. Dis. 82, 185–199. https://doi.org/10.1016/j.nbd.2015.06.003

Pavlou, M.A.S., Outeiro, T.F., 2017. Neuroepigenomics in Aging and Disease, Advances in Experimental Medicine and Biology. Springer International Publishing, Cham. https://doi.org/10.1007/978-3-319-53889-1

Paxinos, G., Watson, C., Pennisi, M., Topple, A., 1985. Bregma, lambda and the interaural midpoint in stereotaxic surgery with rats of different sex, strain and weight. J. Neurosci. Methods 13, 139–143. https://doi.org/10.1016/0165-0270(85)90026-3

Peelaerts, W., Bousset, L., Baekelandt, V., Melki, R., 2018. α-Synuclein strains and seeding in Parkinson's disease, incidental Lewy body disease, dementia with Lewy bodies and multiple system atrophy: similarities and

differences. Cell Tissue Res. 373, 195–212. https://doi.org/10.1007/s00441-018-2839-5

Peelaerts, W., Bousset, L., Van Der Perren, A., Moskalyuk, A., Pulizzi, R., Giugliano, M., Van Den Haute, C., Melki, R., Baekelandt, V., 2015. α-Synuclein strains cause distinct synucleinopathies after local and systemic administration. Nature 522, 340–344. https://doi.org/10.1038/nature14547

Peng, X.M., 2005. -Synuclein activation of protein phosphatase 2A reduces tyrosine hydroxylase phosphorylation in dopaminergic cells. J. Cell Sci. 118, 3523–3530. https://doi.org/10.1242/jcs.02481

Pfeiffer, R.F., 2020. Autonomic Dysfunction in Parkinson's Disease. Neurotherapeutics 1, 79–98. https://doi.org/10.1007/s13311-020-00897-4

Phan, J.-A., Stokholm, K., Zareba-Paslawska, J., Jakobsen, S., Vang, K., Gjedde, A., Landau, A.M., Romero-Ramos, M., 2017. Early synaptic dysfunction induced by α-synuclein in a rat model of Parkinson's disease. Sci. Rep. 7, 6363. https://doi.org/10.1038/s41598-017-06724-9

Picard, M., White, K., Turnbull, D.M., 2013. Mitochondrial morphology, topology, and membrane interactions in skeletal muscle: A quantitative three-dimensional electron microscopy study. J. Appl. Physiol. 114, 161–171. https://doi.org/10.1152/japplphysiol.01096.2012

Pickel, V.M., Johnson, E., Carson, M., Chan, J., 1992. Ultrastructure of spared dopamine terminals in caudate-putamen nuclei of adult rats neonatally treated with intranigral 6-hydroxydopamine. Dev. Brain Res. 70, 75–86. https://doi.org/10.1016/0165-3806(92)90105-6

Plotegher, N., Berti, G., Ferrari, E., Tessari, I., Zanetti, M., Lunelli, L., Greggio, E., Bisaglia, M., Veronesi, M., Girotto, S., Dalla Serra, M., Perego, C., Casella, L., Bubacco, L., 2017. DOPAL derived alpha-synuclein oligomers impair synaptic vesicles physiological function. Sci. Rep. 7, 40699. https://doi.org/10.1038/srep40699

Poewe, W., Seppi, K., Tanner, C.M., Halliday, G.M., Brundin, P., Volkmann, J., Schrag, A.E., Lang, A.E., 2017. Parkinson disease. Nat. Rev. Dis. Prim. 3, 1–21. https://doi.org/10.1038/nrdp.2017.13

Polymeropoulos, M.H., Lavedan, C., Leroy, E., Ide, S.E., Dehejia, A., Dutra, A., Pike, B., Root, H., Rubenstein, J., Boyer, R., Stenroos, E.S., Chandrasekharappa, S., Athanassiadou, A., Papapetropoulos, T., Johnson, W.G., Lazzarini, A.M., Duvoisin, R.C., Di Iorio, G., Golbe, L.I., Nussbaum, R.L., 1997. Mutation in the α-synuclein gene identified in families with Parkinson's disease. Science (80-.). 276, 2045–2047. https://doi.org/10.1126/science.276.5321.2045

Postuma, R.B., Aarsland, D., Barone, P., Burn, D.J., Hawkes, C.H., Oertel, W., Ziemssen, T., 2012. Identifying prodromal Parkinson's disease: Pre-Motor disorders in Parkinson's disease. Mov. Disord. 27, 617–626. https://doi.org/10.1002/mds.24996

Postuma, R.B., Berg, D., 2019. Prodromal Parkinson's Disease: The Decade Past, the Decade to Come. Mov. Disord. 34, 665–675. https://doi.org/10.1002/mds.27670

Postuma, R.B., Berg, D., Stern, M., Poewe, W., Olanow, C.W., Oertel, W., Obeso, J., Marek, K., Litvan, I., Lang, A.E., Halliday, G., Goetz, C.G., Gasser, T., Dubois, B., Chan, P., Bloem, B.R., Adler, C.H., Deuschl, G., 2015. MDS clinical diagnostic criteria for Parkinson's disease. Mov. Disord. 30, 1591–1601. https://doi.org/10.1002/mds.26424

Pringsheim, T., Jette, N., Frolkis, A., Steeves, T.D.L., 2014. The prevalence of Parkinson's disease: A systematic review and meta-analysis. Mov. Disord. 29, 1583–1590. https://doi.org/10.1002/mds.25945

Rajput, A.H., Rozdilsky, B., Ang, L., 1991. Occurrence of resting tremor in parkinson's disease. Neurology 41, 1298–1299. https://doi.org/10.1212/wnl.41.8.1298

Rao, A., Simmons, D., Sorkin, A., 2011. Differential subcellular distribution of endosomal compartments and the dopamine transporter in dopaminergic neurons. Mol. Cell. Neurosci. 46, 148–158. https://doi.org/10.1016/j.mcn.2010.08.016

Recasens, A., Dehay, B., Bove, J., Caraballo, I., Dovero, S., Perez, A., Fernagut, P., Blesa, J., Parent, A., Perier, C., Fariñas, I., Obeso, J., Berzard, E., Vila, M., 2014. Lewy Body extracts from Parkinson's Disease Brains trigger α-Synuclein Pathology. Ann. Neurol. 75, 351–362.

Redgrave, P., Prescott, T.J., Gurney, K., 1999. The basal ganglia: a vertebrate solution to the selection problem? Neuroscience 89, 1009–1023. https://doi.org/10.1016/S0306-4522(98)00319-4

Reeve, A.K., Grady, J.P., Cosgrave, E.M., Bennison, E., Chen, C., Hepplewhite, P.D., Morris, C.M., 2018. Mitochondrial dysfunction within the synapses of substantia nigra neurons in Parkinson's disease. Parkinsons. Dis. 4, 9. https://doi.org/10.1038/s41531-018-0044-6

Reish, H.E.A., Standaert, D.G., 2015. Role of α-synuclein in inducing innate and adaptive immunity in Parkinson disease. J. Parkinsons. Dis. 5, 1–19. https://doi.org/10.3233/JPD-140491

Rochefort, N.L., Konnerth, A., 2012. Dendritic spines: from structure to in vivo function. EMBO Rep. 13, 699–708. https://doi.org/10.1038/embor.2012.102

Rodríguez-Chinchilla, T., Quiroga-Varela, A., Molinet-Dronda, F., Belloso-Iguerategui, A., Merino-Galan, L., Jimenez-Urbieta, H., Gago, B., Rodriguez-Oroz, M.C., 2020. [18F]-DPA-714 PET as a specific in vivo marker of early microglial activation in a rat model of progressive dopaminergic degeneration. Eur. J. Nucl. Med. Mol. Imaging 47, 2602–2612. https://doi.org/10.1007/s00259-020-04772-4

Rodriguez-Oroz, M.C., 2010. Deep brain stimulation for advanced Parkinson's disease. Lancet Neurol. 9, 558–559. https://doi.org/10.1016/S1474-4422(10)70108-3

Rodriguez-Oroz, M.C., Jahanshahi, M., Krack, P., Litvan, I., Macias, R., Bezard, E., Obeso, J.A., 2009. Initial clinical manifestations of Parkinson's disease: features and pathophysiological mechanisms. Lancet Neurol. 8, 1128–1139. https://doi.org/10.1016/S1474-4422(09)70293-5

Rodriguez, A., Ehlenberger, D.B., Dickstein, D.L., Hof, P.R., Wearne, S.L., 2008. Automated Three-Dimensional Detection and Shape Classification of Dendritic Spines from Fluorescence Microscopy Images. PLoS One 3, e1997. https://doi.org/10.1371/journal.pone.0001997

Rosenbusch, K.E., Kortholt, A., 2016. Activation Mechanism of LRRK2 and Its Cellular Functions in Parkinson's Disease. Parkinsons. Dis. 1–8. https://doi.org/10.1155/2016/7351985

Ruiz-Martínez, J., Gorostidi, A., Ibañez, B., Alzualde, A., Otaegui, D., Moreno, F., de Munain, A.L., Bergareche, A., Gómez-Esteban, J.C., Massó, J.F.M., 2010. Penetrance in Parkinson's disease related to the LRRK2 R1441G mutation in the Basque country (Spain). Mov. Disord. 25, 2340–2345. https://doi.org/10.1002/mds.23278

Ryan, S.D., Dolatabadi, N., Chan, S.F., Zhang, X., Akhtar, M.W., Parker, J., Soldner, F., Sunico, C.R., Nagar, S., Talantova, M., Lee, B., Lopez, K., Nutter, A., Shan, B., Molokanova, E., Zhang, Y., Han, X., Nakamura, T., Masliah, E., Yates, J.R., Nakanishi, N., Andreyev, A.Y., Okamoto, S., Jaenisch, R., Ambasudhan, R., Lipton, S.A., 2013. Isogenic Human iPSC Parkinson's Model Shows Nitrosative Stress-Induced Dysfunction in MEF2-PGC1α Transcription. Cell 155, 1351–1364. https://doi.org/10.1016/j.cell.2013.11.009

Saheki, Y., De Camilli, P., 2012. Synaptic Vesicle Endocytosis. Cold Spring Harb. Perspect. Biol. 4, a005645–a005645. https://doi.org/10.1101/cshperspect.a005645

Sanchez-Guajardo, V., Febbraro, F., Kirik, D., Romero-Ramos, M., 2010. Microglia Acquire Distinct Activation Profiles Depending on the Degree of α-Synuclein Neuropathology in a rAAV Based Model of Parkinson's Disease. PLoS One 5, e8784. https://doi.org/10.1371/journal.pone.0008784

Schapira, A.H.V., 2009. Neurobiology and treatment of Parkinson's disease. Trends Pharmacol. Sci. 30, 41–47. https://doi.org/10.1016/j.tips.2008.10.005

Schapira, A.H. V., Cooper, J.M., Dexter, D., Clark, J.B., Jenner, P., Marsden, C.D., 1990. Mitochondrial Complex I Deficiency in Parkinson's Disease. J. Neurochem. 54, 823–827. https://doi.org/10.1111/j.1471-4159.1990.tb02325.x

Schechter, M., Grigoletto, J., Abd-Elhadi, S., Glickstein, H., Friedman, A., Serrano, G.E., Beach, T.G., Sharon, R., 2020. A role for α-Synuclein in axon growth and its implications in corticostriatal glutamatergic plasticity in Parkinson's disease. Mol. Neurodegener. 15, 24. https://doi.org/10.1186/s13024-020-00370-y

Scheckel, C., Aguzzi, A., 2018. Prions, prionoids and protein misfolding disorders. Nat. Rev. Genet. 19, 405–418. https://doi.org/10.1038/s41576-018-0011-4

Scheperjans, F., Pekkonen, E., Kaakkola, S., Auvinen, P., 2015. Linking Smoking, Coffee, Urate, and Parkinson's Disease – A Role for Gut Microbiota? J. Parkinsons. Dis. 5, 255–262. https://doi.org/10.3233/JPD-150557

Schneider, S.A., Alcalay, R.N., 2017. Neuropathology of genetic synucleinopathies with parkinsonism: Review of the literature. Mov. Disord. 32, 1504–1523. https://doi.org/10.1002/mds.27193

Schulz-Schaeffer, W.J., 2010. The synaptic pathology of α-synuclein aggregation in dementia with Lewy bodies, Parkinson's disease and Parkinson's disease dementia. Acta Neuropathol. 120, 131–143. https://doi.org/10.1007/s00401-010-0711-0

Scott, D., Roy, S., 2012. -Synuclein Inhibits Intersynaptic Vesicle Mobility and Maintains Recycling-Pool Homeostasis. J. Neurosci. 32, 10129–10135. https://doi.org/10.1523/JNEUROSCI.0535-12.2012

Scott, H., Panin, V.M., 2014. The role of protein N-glycosylation in neural transmission. Glycobiology 24, 407–417. https://doi.org/10.1093/glycob/cwu015

Shahmoradian, S.H., Lewis, A.J., Genoud, C., Hench, J., Moors, T.E., Navarro, P.P., Castaño-Díez, D., Schweighauser, G., Graff-Meyer, A., Goldie, K.N., Sütterlin, R., Huisman, E., Ingrassia, A., Gier, Y. de, Rozemuller, A.J.M., Wang, J., Paepe, A. De, Erny, J., Staempfli, A., Hoernschemeyer, J., Großerüschkamp, F., Niedieker, D., El-Mashtoly, S.F., Quadri, M., Van IJcken, W.F.J., Bonifati, V., Gerwert, K., Bohrmann, B., Frank, S., Britschgi, M., Stahlberg, H., Van de Berg, W.D.J., Lauer, M.E., 2019. Lewy pathology in Parkinson's disease consists of crowded organelles and lipid membranes. Nat. Neurosci. 22, 1099–1109. https://doi.org/10.1038/s41593-019-0423-2

Sharma, M., Khan, S., Rahman, S., Singh, L.R., 2019. The Extracellular Protein, Transthyretin Is an Oxidative Stress Biomarker. Front. Physiol. 10. https://doi.org/10.3389/fphys.2019.00005

Shen, W., Flajolet, M., Greengard, P., Surmeier, D.J., 2008. Dichotomous Dopaminergic Control of Striatal Synaptic Plasticity. Science (80-.). 321, 848–851. https://doi.org/10.1126/science.1160575

Sheng, M., Hoogenraad, C.C., 2007. The Postsynaptic Architecture of Excitatory Synapses: A More Quantitative View. Annu. Rev. Biochem. 76, 823–847. https://doi.org/10.1146/annurev.biochem.76.060805.160029

Sheng, M., Kim, E., 2011. The Postsynaptic Organization of Synapses. Cold Spring Harb. Perspect. Biol. 3, a005678–a005678. https://doi.org/10.1101/cshperspect.a005678

Shevchenko, A., Tomas, H., Havliš, J., Olsen, J. V., Mann, M., 2007. In-gel digestion for mass spectrometric characterization of proteins and proteomes. Nat. Protoc. 1, 2856–2860. https://doi.org/10.1038/nprot.2006.468

Shilov, I. V., Seymourt, S.L., Patel, A.A., Loboda, A., Tang, W.H., Keating, S.P., Hunter, C.L., Nuwaysir, L.M., Schaeffer, D.A., 2007. The paragon algorithm, a next generation search engine that uses sequence temperature values sequence temperature values and feature probabilities to identify peptides from tandem mass spectra. Mol. Cell. Proteomics 6, 1638–1655. https://doi.org/10.1074/mcp.T600050-MCP200

Siderowf, A., Lang, A.E., 2012. Premotor Parkinson's disease: Concepts and definitions. Mov. Disord. 27, 608–616. https://doi.org/10.1002/mds.24954

Sidransky, E., Lopez, G., 2012. The link between the GBA gene and parkinsonism. Lancet Neurol. 11, 986–998. https://doi.org/10.1016/S1474-4422(12)70190-4

Simon, D.K., Tanner, C.M., Brundin, P., 2020. Parkinson Disease Epidemiology, Pathology, Genetics, and Pathophysiology. Clin. Geriatr. Med. 36, 1–12. https://doi.org/10.1016/j.cger.2019.08.002

Singh, P.K., Muqit, M.M.K., 2020. Parkinson's: A Disease of Aberrant Vesicle Trafficking. Annu. Rev. Cell Dev. Biol. 36, 237–264. https://doi.org/10.1146/annurev-cellbio-100818-125512

Singleton, A.B., 2003. -Synuclein Locus Triplication Causes Parkinson's Disease. Science (80-.). 302, 841. https://doi.org/10.1126/science.1090278

Sisková, Z., Mahad, D.J., Pudney, C., Campbell, G., Cadogan, M., Asuni, A., O'Connor, V., Perry, V.H., 2010. Morphological and functional abnormalities in mitochondria associated with synaptic degeneration in prion disease. Am. J. Pathol. 177, 1411–1421. https://doi.org/10.2353/ajpath.2010.091037

Smith, A.M., Depp, C., Ryan, B.J., Johnston, G.I., Alegre-Abarrategui, J., Evetts, S., Rolinski, M., Baig, F., Ruffmann, C., Simon, A.K., Hu, M.T.M., Wade-Martins, R., 2018. Mitochondrial dysfunction and increased glycolysis in prodromal and early Parkinson's blood cells. Mov. Disord. 33, 1580–1590. https://doi.org/10.1002/mds.104

Soler-López, M., Badiola, N., Zanzoni, A., Aloy, P., 2012. Towards Alzheimer's root cause: ECSIT as an integrating hub between oxidative stress, inflammation and mitochondrial dysfunction: Hypothetical role of the adapter protein ECSIT in familial and sporadic Alzheimer's disease pathogenesis. BioEssays 34, 532–541. https://doi.org/10.1002/bies.201100193

Song, D.D., Shults, C.W., Sisk, A., Rockenstein, E., Masliah, E., 2004. Enhanced substantia nigra mitochondrial pathology in human α-synuclein transgenic mice after treatment with MPTP111-Methyl-4-phenyl-1,2,3,6-tetrahydropyridine. Exp. Neurol. 186, 158–172. https://doi.org/10.1016/S0014-4886(03)00342-X

Soukup, S., Vanhauwaert, R., Verstreken, P., 2018. Parkinson's disease: convergence on synaptic homeostasis. EMBO J. 37, 1–16. https://doi.org/10.15252/embj.201898960

Spillantini, M.G., Crowther, R.A., Jakes, R., Hasegawa, M., Goedert, M., 1998. -Synuclein in filamentous inclusions of Lewy bodies from Parkinson's disease and dementia with Lewy bodies. Proc. Natl. Acad. Sci. 95, 6469–6473. https://doi.org/10.1073/pnas.95.11.6469

Sreenivasan, K., Mishra, V., Bird, C., Zhuang, X., Yang, Z., Cordes, D., Walsh, R.R., 2019. Altered functional network topology correlates with clinical measures in very early-stage, drug-naïve Parkinson's disease. Parkinsonism Relat. Disord. 62, 3–9. https://doi.org/10.1016/j.parkreldis.2019.02.001

Stichel, C.C., Zhu, X.-R., Bader, V., Linnartz, B., Schmidt, S., Lubbert, H., 2007. Mono- and double-mutant mouse models of Parkinson's disease display severe mitochondrial damage. Hum. Mol. Genet. 16, 2377–2393. https://doi.org/10.1093/hmg/ddm083

Suarez, L.M., Solis, O., Aguado, C., Lujan, R., Moratalla, R., 2016. L-DOPA Oppositely Regulates Synaptic Strength and Spine Morphology in D1 and D2 Striatal Projection Neurons in Dyskinesia. Cereb. Cortex 26, 4253–4264. https://doi.org/10.1093/cercor/bhw263

Subramaniam, S.R., Vergnes, L., Franich, N.R., Reue, K., Chesselet, M.F., 2014. Region specific mitochondrial impairment in mice with widespread overexpression of alpha-synuclein. Neurobiol. Dis. 70, 204–213. https://doi.org/10.1016/j.nbd.2014.06.017

Südhof, T.C., 2013. Neurotransmitter Release: The Last Millisecond in the Life of a Synaptic Vesicle. Neuron 80, 675–690. https://doi.org/10.1016/j.neuron.2013.10.022

Südhof, T.C., 2012. The Presynaptic Active Zone. Neuron 75, 11–25. https://doi.org/10.1016/j.neuron.2012.06.012

Sudhof, T.C., Rizo, J., 2011. Synaptic Vesicle Exocytosis. Cold Spring Harb. Perspect. Biol. 3, a005637–a005637. https://doi.org/10.1101/cshperspect.a005637

Sulzer, D., Surmeier, D.J., 2013. Neuronal vulnerability, pathogenesis, and Parkinson's disease. Mov. Disord. 28, 41–50. https://doi.org/10.1002/mds.25095

Sun, A.G., Wang, J., Shan, Y.Z., Yu, W.J., Li, X., Cong, C.H., Wang, X., 2014. Identifying distinct candidate genes for early Parkinson's disease by analysis of gene expression in whole blood. Neuroendocrinol. Lett. 35, 389–404.

Surmeier, D.J., Graves, S.M., Shen, W., 2014. Dopaminergic modulation of striatal networks in health and Parkinson's disease. Curr. Opin. Neurobiol. 29, 109–117. https://doi.org/10.1016/j.conb.2014.07.008

Surmeier, D.J., Obeso, J.A., Halliday, G.M., 2017. Selective neuronal vulnerability in Parkinson disease. Nat. Rev. Neurosci. 18, 101–113. https://doi.org/10.1038/nrn.2016.178

Surmeier, D.J., Song, W.J., Yan, Z., 1996. Coordinated expression of dopamine receptors in neostriatal medium spiny neurons. J. Neurosci. 16, 6579–6591. https://doi.org/10.1523/jneurosci.16-20-06579.1996

Tagliaferro, P., Burke, R.E., 2016. Retrograde Axonal Degeneration in Parkinson Disease. J. Parkinsons. Dis. 6, 1–15. https://doi.org/10.3233/JPD-150769

Tang, W.H., Shilov, I. V., Seymour, S.L., 2008. Nonlinear fitting method for determining local false discovery rates from decoy database searches. J. Proteome Res. 7, 3661–3667. https://doi.org/10.1021/pr070492f

Tanji, K., Mori, F., Mimura, J., Itoh, K., Kakita, A., Takahashi, H., Wakabayashi, K., 2010. Proteinase K-resistant α-synuclein is deposited in presynapses in human Lewy body disease and A53T α-synuclein transgenic mice. Acta Neuropathol. 120, 145–154. https://doi.org/10.1007/s00401-010-0676-z

Tatulli, G., Mitro, N., Cannata, S.M., Audano, M., Caruso, D., D'Arcangelo, G., Lettieri-Barbato, D., Aquilano, K., 2018. Intermittent fasting applied in combination with rotenone treatment exacerbates dopamine neurons degeneration in mice. Front. Cell. Neurosci. 12, 1–10. https://doi.org/10.3389/fncel.2018.00004

Thakur, P., Breger, L.S., Lundblad, M., Wan, O.W., Mattsson, B., Luk, K.C., Lee, V.M.Y., Trojanowski, J.Q., Björklund, A., 2017. Modeling Parkinson's disease pathology by combination of fibril seeds and α-synuclein overexpression in the rat brain. Proc. Natl. Acad. Sci. 114, E8284–E8293. https://doi.org/10.1073/pnas.1710442114

Theillet, F.-X., Binolfi, A., Bekei, B., Martorana, A., Rose, H.M., Stuiver, M., Verzini, S., Lorenz, D., van Rossum, M., Goldfarb, D., Selenko, P., 2016. Structural disorder of monomeric α-synuclein persists in mammalian cells. Nature 530, 45–50. https://doi.org/10.1038/nature16531

Theodore, S., Cao, S., McLean, P.J., Standaert, D.G., 2008. Targeted Overexpression of Human α-Synuclein Triggers Microglial Activation and an Adaptive Immune Response in a Mouse Model of Parkinson Disease. J. Neuropathol. Exp. Neurol. 67, 1149–1158. https://doi.org/10.1097/NEN.0b013e31818e5e99

Tozzi, A., de Iure, A., Bagetta, V., Tantucci, M., Durante, V., Quiroga-Varela, A., Costa, C., Di Filippo, M., Ghiglieri, V., Latagliata, E.C., Wegrzynowicz, M., Decressac, M., Giampà, C., Dalley, J.W., Xia, J., Gardoni, F., Mellone, M., El-Agnaf, O.M., Ardah, M.T., Puglisi-Allegra, S., Björklund, A., Spillantini, M.G., Picconi, B., Calabresi, P., 2016. Alpha-Synuclein Produces Early Behavioral Alterations via Striatal Cholinergic Synaptic Dysfunction by Interacting With GluN2D N-Methyl-D-Aspartate Receptor Subunit. Biol. Psychiatry 79, 402–414. https://doi.org/10.1016/j.biopsych.2015.08.013

Ulusoy, A., Bjorklund, T., Hermening, S., Kirik, D., 2008. In vivo gene delivery for development of mammalian models for Parkinson's disease. Exp. Neurol. 209, 89–100. https://doi.org/10.1016/j.expneurol.2007.09.011

Ulusoy, A., Decressac, M., Kirik, D., Björklund, A., 2010. Viral vector-mediated overexpression of α-synuclein as a progressive model of Parkinson's disease, in: Progress in Brain Research. pp. 89–111. https://doi.org/10.1016/S0079-6123(10)84005-1

Uversky, V.N., 2007. Neuropathology, biochemistry, and biophysics of a-synuclein aggregation. J. Neurochem. 103, 17–37. https://doi.org/10.1111/j.1471-4159.2007.04764.x

Van der Perren, A., Toelen, J., Casteels, C., Macchi, F., Van Rompuy, A.S., Sarre, S., Casadei, N., Nuber, S., Himmelreich, U., Osorio Garcia, M.I., Michotte, Y., D'Hooge, R., Bormans, G., Van Laere, K., Gijsbers, R., Van den Haute, C., Debyser, Z., Baekelandt, V., 2015. Longitudinal follow-up and characterization of a robust rat model for Parkinson's disease based on overexpression of alpha-synuclein with adeno-associated viral vectors. Neurobiol. Aging 36, 1543–1558. https://doi.org/10.1016/j.neurobiolaging.2014.11.015

Van Der Putten, H., Wiederhold, K.H., Probst, A., Barbieri, S., Mistl, C., Danner, S., Kauffmann, S., Hofele, K., Spooren, W.P.J.M., Ruegg, M.A., Lin, S., Caroni, P., Sommer, B., Tolnay, M., Bilbe, G., 2000. Neuropathology in mice expressing human α-synuclein. J. Neurosci. 20, 6021–6029. https://doi.org/10.1523/jneurosci.20-16-06021.2000

Van Kampen, J.M., Robertson, H.A., 2017. The BSSG rat model of Parkinson's disease: progressing towards a valid, predictive model of disease. EPMA J. 8, 261–271. https://doi.org/10.1007/s13167-017-0114-6

Vanni, S., Colini Baldeschi, A., Zattoni, M., Legname, G., 2020. Brain aging: A Ianus -faced player between health and neurodegeneration. J. Neurosci. Res. 98, 299–311. https://doi.org/10.1002/jnr.24379

Vargas, K.J., Makani, S., Davis, T., Westphal, C.H., Castillo, P.E., Chandra, S.S., 2014. Synucleins regulate the kinetics of synaptic vesicle endocytosis. J. Neurosci. 34, 9364–9376. https://doi.org/10.1523/JNEUROSCI.4787-13.2014

Vargas, K.J., Schrod, N., Davis, T., Fernandez-Busnadiego, R., Taguchi, Y. V., Laugks, U., Lucic, V., Chandra, S.S., 2017. Synucleins Have Multiple Effects on Presynaptic Architecture. Cell Rep. 18, 161–173.

https://doi.org/10.1016/j.celrep.2016.12.023

Vermilyea, S.C., Emborg, M.E., 2015. α-Synuclein and nonhuman primate models of Parkinson's disease. J. Neurosci. Methods 255, 38–51. https://doi.org/10.1016/j.jneumeth.2015.07.025

Vermilyea, S.C., Guthrie, S., Hernandez, I., Bondarenko, V., Emborg, M.E., 2019. α-Synuclein Expression Is Preserved in Substantia Nigra GABAergic Fibers of Young and Aged Neurotoxin-Treated Rhesus Monkeys. Cell Transplant. 28, 379–387. https://doi.org/10.1177/0963689719835794

Videira, P.A.Q., Castro-Caldas, M., 2018. Linking Glycation and Glycosylation With Inflammation and Mitochondrial Dysfunction in Parkinson's Disease. Front. Neurosci. 12, 381. https://doi.org/10.3389/fnins.2018.00381

Vila, M., 2019. Neuromelanin, aging, and neuronal vulnerability in Parkinson's disease. Mov. Disord. 34, 1440–1451. https://doi.org/10.1002/mds.27776

Villalba, R.M., Mathai, A., Smith, Y., 2015. Morphological changes of glutamatergic synapses in animal models of Parkinson's disease. Front. Neuroanat. 9, 1–16. https://doi.org/10.3389/fnana.2015.00117

Villalba, R.M., Smith, Y., 2018. Loss and remodeling of striatal dendritic spines in Parkinson's disease: from homeostasis to maladaptive plasticity? J. Neural Transm. 125, 431–447. https://doi.org/10.1007/s00702-017-1735-6

Villalba, R.M., Smith, Y., 2013. Differential striatal spine pathology in Parkinson's disease and cocaine addiction: A key role of dopamine? Neuroscience 251, 2–20. https://doi.org/10.1016/j.neuroscience.2013.07.011

Villalba, R.M., Smith, Y., 2010. Striatal Spine Plasticity in Parkinson's Disease. Front. Neuroanat. 4, 133. https://doi.org/10.3389/fnana.2010.00133

Volpicelli-Daley, L.A., Gamble, K.L., Schultheiss, C.E., Riddle, D.M., West, A.B., Lee, V.M.Y., 2014. Formation of α-synuclein Lewy neurite–like aggregates in axons impedes the transport of distinct endosomes. Mol. Biol. Cell 25, 4010–4023. https://doi.org/10.1091/mbc.e14-02-0741

Volpicelli-Daley, L.A., Kirik, D., Stoyka, L.E., Standaert, D.G., Harms, A.S., 2016. How can rAAV-α-synuclein and the fibril α-synuclein models advance our understanding of Parkinson's disease? J. Neurochem. 139, 131–155. https://doi.org/10.1111/jnc.13627

Volpicelli-Daley, L.A., Luk, K.C., Patel, T.P., Tanik, S.A., Riddle, D.M., Stieber, A., Meaney, D.F., Trojanowski, J.Q., Lee, V.M.Y., 2011. Exogenous α-Synuclein Fibrils Induce Lewy Body Pathology Leading to Synaptic Dysfunction and Neuron Death. Neuron 72, 57–71. https://doi.org/10.1016/j.neuron.2011.08.033

Vukoja, A., Rey, U., Petzoldt, A.G., Ott, C., Vollweiter, D., Quentin, C., Puchkov, D., Reynolds, E., Lehmann, M., Hohensee, S., Rosa, S., Lipowsky, R., Sigrist, S.J., Haucke, V., 2018. Presynaptic Biogenesis Requires Axonal Transport of Lysosome-Related Vesicles. Neuron 99, 1216-1232.e7. https://doi.org/10.1016/j.neuron.2018.08.004

Wang, B., Underwood, R., Kamath, A., Britain, C., McFerrin, M.B., McLean, P.J., Volpicelli-Daley, L.A., Whitaker, R.H., Placzek, W.J., Becker, K., Ma, J., Yacoubian, T.A., 2018. 14-3-3 Proteins Reduce Cell-to-Cell Transfer and Propagation of Pathogenic α-Synuclein. J. Neurosci. 38, 8211–8232. https://doi.org/10.1523/JNEUROSCI.1134-18.2018

Wang, C., Zhao, C., Li, D., Tian, Z., Lai, Y., Diao, J., Liu, C., 2016. Versatile Structures of α-Synuclein. Front. Mol. Neurosci. 9, 1–8. https://doi.org/10.3389/fnmol.2016.00048

Wefelmeyer, W., Puhl, C.J., Burrone, J., 2016. Homeostatic Plasticity of Subcellular Neuronal Structures: From Inputs to Outputs. Trends Neurosci. 39, 656–667. https://doi.org/10.1016/j.tins.2016.08.004

West, M.J., 1999. Stereological methods for estimating the total number of neurons and synapses: issues of precision and bias. Trends Neurosci. 22, 51–61. https://doi.org/10.1016/S0166-2236(98)01362-9

Wilson, H., Pagano, G., de Natale, E.R., Mansur, A., Caminiti, S.P., Polychronis, S., Middleton, L.T., Price, G., Schmidt, K.F., Gunn, R.N., Rabiner, E.A., Politis, M., 2020. Mitochondrial Complex 1, Sigma 1, and Synaptic Vesicle 2A in Early Drug-Naive Parkinson's Disease. Mov. Disord. 35, 1416–1427. https://doi.org/10.1002/mds.28064

Wong, Y.C., Luk, K., Purtell, K., Burke Nanni, S., Stoessl, A.J., Trudeau, L.E., Yue, Z., Krainc, D., Oertel, W., Obeso, J.A., Volpicelli-Daley, L.A., 2019. Neuronal vulnerability in Parkinson disease: Should the focus be on axons and synaptic terminals? Mov. Disord. 34, 1406–1422. https://doi.org/10.1002/mds.27823

Yacoubian, T.A., Slone, S.R., Harrington, A.J., Hamamichi, S., Schieltz, J.M., Caldwell, K.A., Caldwell, G.A., Standaert, D.G., 2010. Differential neuroprotective effects of 14-3-3 proteins in models of Parkinson's disease. Cell Death Dis. 1, e2. https://doi.org/10.1038/cddis.2009.4

Yang, X., Yan, F., He, Z., Liu, S., Cheng, Y., Wei, K., Gan, S., Yuan, J., Wang, S., Xiao, Y., Ren, K., Liu, N., Hu, Xiang, Ding, X., Hu, Xingwang, Xiang, S., 2015. ITSN2L Interacts with and Negatively Regulates RABEP1. Int. J. Mol. Sci. 16, 28242–28254. https://doi.org/10.3390/ijms161226091

Yang, Y., Wang, X. -b., Frerking, M., Zhou, Q., 2008. Spine Expansion and Stabilization Associated with Long-Term Potentiation. J. Neurosci. 28, 5740–5751. https://doi.org/10.1523/JNEUROSCI.3998-07.2008

Yao, W.D., Spealman, R.D., Zhang, J., 2008. Dopaminergic signaling in dendritic spines. Biochem. Pharmacol. 75, 2055–2069. https://doi.org/10.1016/j.bcp.2008.01.018

Zabel, C., Chamrad, D.C., Priller, J., Woodman, B., Meyer, H.E., Bates, G.P., Klose, J., 2002. Alterations in the Mouse and Human Proteome Caused by Huntington's Disease. Mol. Cell. Proteomics 1, 366–375. https://doi.org/10.1074/mcp.M200016-MCP200

Zaichick, S. V., McGrath, K.M., Caraveo, G., 2017. The role of Ca 2+ signaling in Parkinson's disease. Dis. Model. Mech. 10, 519–535. https://doi.org/10.1242/dmm.028738

Zaja-Milatovic, S., Milatovic, D., Schantz, A.M., Zhang, J., Montine, K.S., Samii, A., Deutch, A.Y., Montine, T.J., 2005. Dendritic degeneration in neostriatal medium spiny neurons in Parkinson disease. Neurology 64, 545–547. https://doi.org/10.1212/01.WNL.0000150591.33787.A4

Zambon, F., Cherubini, M., Fernandes, H.J.R., Lang, C., Ryan, B.J., Volpato, V., Bengoa-Vergniory, N., Vingill, S., Attar, M., Booth, H.D.E., Haenseler, W., Vowles, J., Bowden, R., Webber, C., Cowley, S.A., Wade-Martins, R., 2019. Cellular α-synuclein pathology is associated with bioenergetic dysfunction in Parkinson's iPSC-derived dopamine neurons. Hum. Mol. Genet. 28, 2001–2013. https://doi.org/10.1093/hmg/ddz038

Zhai, S., Tanimura, A., Graves, S.M., Shen, W., Surmeier, D.J., 2018. Striatal synapses, circuits, and Parkinson's disease. Curr. Opin. Neurobiol. 48, 9–16. https://doi.org/10.1016/j.conb.2017.08.004

Zhao, Y., Perera, G., Takahashi-Fujigasaki, J., Mash, D.C., Vonsattel, J.P.G., Uchino, A., Hasegawa, K., Jeremy Nichols, R., Holton, J.L., Murayama, S., Dzamko, N., Halliday, G.M., 2018. Reduced LRRK2 in association with retromer dysfunction in post-mortem brain tissue from LRRK2 mutation carriers. Brain 141, 486–495. https://doi.org/10.1093/brain/awx344

Zhou, Y., Zhou, B., Pache, L., Chang, M., Khodabakhshi, A.H., Tanaseichuk, O., Benner, C., Chanda, S.K., 2019. Metascape provides a biologist-oriented resource for the analysis of systems-level datasets. Nat. Commun. 10, 1523. https://doi.org/10.1038/s41467-019-09234-6

ANNEX

Antibodies

The antibodies used for the detection of proteins in immunohistochemistry and immunofluorescence studies are listed in Tables 16 and 17, and those used in Western blots in Tables 18 and 19. All of them specify the antigen against which they react, the host species, the species reactivity, the clone, the isotype, the fluorophore or the conjugated protein, the reference, the corresponding commercial company and the dilution used in the experiments.

Table 16. Primary antibodies used for immunohistochemistry and immunofluorescence.

Antigen	Host Species	Species reactivity*	Clon	Isotype	Reference	Producer	Dilution
DAT	Goat	H, M, R	Polyclonal	IgG	Sc-1433	Santa Cruz Biotechnology	1:100
Lamp1	Rat	H, M, R	Monoclonal (1D4B)	IgG2a	sc-19992	Santa Cruz	1:50
LC3B	Rabbit	H, M, R	Polyclonal	IgG	L7543	Sigma Aldrich	1:250
Rab5	Goat	H, M, R	Polyclonal	IgG	ABIN144056	Antibodies-online	1:100
Rab7	Rabbit	H, R	Polyclonal	IgG	ab77993	Abcam	1:100
TH	Mouse	H, M, R	Monoclonal (2/40/15)	IgG2a	MAB5280	Merck Millipore	1:1.000
α-synuclein	Mouse	H	Monoclonal (LB509)	IgG1, kappa	180215	ThermoFischer Scientific	1:500

*We only show the following species: H, human; M, mouse; R, rat.

Table 17. Secondary antibodies used for immunohistochemistry and immunofluorescence.

Target	Production Specie	Fluorophore/Conjugated	Isotype	Reference	Producer	Dilution
Anti-goat	Rabbit	Biotinylated	IgG	BA-5000	Vector Laboratories	1:500
Anti-mouse	Horse	Biotinylated	IgG	BA-2000	Vector	1:500
Anti-mouse	Goat	Alexa Fluor 633*	IgG	A21052	Invitrogen	1:500
Anti-rabbit	Goat	Alexa Fluor 488*	IgG	A11034	Invitrogen	1:500
Anti-rat	Goat	Alexa Fluor 546*	IgG	A11081	Invitrogen	1:500
Anti-goat	Donkey	Alexa Fluor 488*	IgG	A11055	Invitrogen	1:500
Anti-mouse	Donkey	Alexa Fluor 647*	IgG	A31571	Invitrogen	1:500
Anti-rabbit	Donkey	Alexa Fluor 546*	IgG	A10040	Invitrogen	1:500

Table 18. Primary antibodies used for western blot.

Antigen	Host Species	Species reactivity*	Clone	Isotype	Reference	Producer	Dilution
α-synuclein	Mouse	H	Monoclonal (Syn211)	IgG1, kappa	328100	ThermoFisher Scientific	1:1.000
β-actin	Rabbit	H, M, R	Monoclonal (13E5)	IgG	4970	Cell Signaling	1:5.000

*We only show the following species: H, human; M, mouse; R, rat.

Table 19. Secondary antibodies used for western blot.

Target	Production Specie	Fluorophore/Conjugated	Isotype	Reference	Producer	Dilution
Anti-mouse	Horse	HRP	IgG	7076	Cell Signaling	1:2.000
Anti-rabbit	Goat	HRP	IgG	7074	Cell Signaling	1:2.000

Buffers

The following section summarizes the composition of buffers used in the different experiments of this work, arranged alphabetically.

Blocking solution

Skim milk	0.05 g/ml
TBS-T	

Buffer A

HEPES	10 mM
Sucrose	0.32 M
$MgCl_2$	1 mM
$CaCl_2$	0.5 mM
EGTA	1 mM
Cocktail of protease inhibitors	
pH 7.4	

Buffer B

HEPES	10 mM
Sucrose	1.4 M

Cryoprotective solution

Sucrose	0.87 M
PBS 0.1 M pH 7.4	

DAB

DAB	27 mM
PBS 0.1 M pH 7.4	

Electrophoresis Buffer

Tris base	25 mM
Glycine	191 mM
SDS	3.5 mM

Ionic Medium

HEPES	20 mM
D-glucose	10 mM
Na_2HPO_4	1.2 mM
$MgCl_2$	1 mM
$NaHCO_3$	5 mM
KCl	5 mM
NaCl	140 mM
pH 7.4	

Incubation Medium

KCl	3.5 mM
NaCl	120 mM
$CaCl_2$	1.3 mM
KH_2PO_4	0.4 mM
Na_2SO_4	1.2 mM
$MgSO_4$	2 mM
D-Glucose	15 mM
Pyruvate	10 mM
TES	10 mM
BSA	4 mg/ml
pH 7.4, 37°C	

Loading Buffer 4X

Tris-HCl (pH 6.8)	1.25 M
Glycerol	40%
SDS	0.27 M
Bromophenol blue	0.5 mM
2-Mercaptoetanol	5%

Lysis buffer

HEPES (pH 7.4)	25 mM
NaCl	150 mM
Triton™ X-100	1%

EDTA	5 mM

PB 0.1 M pH 7.4

Sodium dihydrogen phosphate monohydrate (NaH_2PO_4-H_2O)	25 mM
Disodium hydrogen phosphate dihydrate (Na_2HPO_4-$2H_2O$)	85 mM

PBS 0.1 M pH 7.4

Sodium chloride (NaCl)	154 mM
PB 0.1 M pH 7.4	

Preservative solution

Sodium azide (NaN_3)	3 mM
PBS 0.1 M pH 7.4	

TBS

Tris base	20 mM
NaCl	136 mM
pH 7.6	

TBS-T (0.1%)

Tween-20	0.1%
TBS	

4% PFA

PFA	1.33 M
PB 0.1 M pH 7.4	

** All buffers were diluted in distilled water, unless otherwise specified.*